University
of Southampton

School of
Engineering
Sciences

Acoustic emission characterisation of damage in CFRP composites

Marco Rosario Venturini Autieri

Thesis submitted for the title of Doctor of Philosophy
June 2007

Abstract

Acoustic Emission (AE) is a well established Non-Destructive Testing and Evaluation technique for damage monitoring and flaw location and has been used in a wide variety of fields, such as the aerospace and nuclear industry. The material studied here is fibre reinforced composites, which are not monolithic and therefore can fail in different modes. The research determines whether a characterisation of the damage is possible in terms of AE. This is accomplished by studying classic AE features (such as duration, counts, etc) and the frequency content.

This thesis describes some basic wave theory and the type of sensors and equipment used in modern AE systems, and includes a review of recent publication on the use of AE to detect, locate and characterise damage in composites.

The experimental work described here, by using pencil lead breaks, assesses the suitability of the AE parameters to characterise a source. The work shows that a characterisation must deal with the effects of the material and lay-up, shows the effects that the dimensions of the sample have on the internal reflections of the elastic waves and ultimately on the recorded signals, analyses how the accumulation of the signal with the time can provide useful information, illustrates a compact way to present the typically large number of AE data coming from the testing of composites and shows that the signals coming from a single sensor can carry information on the geometry of the structure. Studies on tensile tests in CFRP strips of different lay-ups and one panel loaded with a four-point bending are also included, to test the performance and the feasibility of AE in characterising actual sources of damage.

The novelty of this work consists of the following points:

- The difference between a *description* and a *characterisation* was defined
- It was shown that the characteristics of the sensors largely affect the *description*
- The variability introduced by the system and the testing parameters were investigated
- The importance of the non-stationarity of the signals was illustrated, together with how this can yield to new information

It was concluded that a characterisation can only have a weak meaning

CONTENTS

Contents I

List of tables VI

List of figures VII

Nomenclature XVIII

1 Introduction 1

1.1 Background 1

1.2 Acoustic Emission (AE) 4

1.3 Aims and objectives 7

1.4 Thesis organization 8

2 Elastic waves in homogeneous media 10

2.1 Structure-borne sound 10

2.2 A summary of the theory of elasticity 11

2.3 Wave equation in three dimensions 15

2.4 Rayleigh waves 17

2.5 Lamb waves 18

2.6 Dispersion 23

2.7 Attenuation of Lamb waves 24

2.8 Anisotropy and inhomogeneity 27

2.9 Summary 28

3 Acoustic Emission 29

3.1 Sensors 31

3.2 Couplants 35

3.3 Preamplifiers 36

3.4 Definitions of AE terminology 36

3.5 A generic AE system 39

3.6 System sensitivity check 40

3.7 Data analysis 41

3.8 A physical model 42

3.9 Localisation capabilities 43

3.10 Noise interference in AE 44

3.11 Summary 45

4 Review of AE studies in composite materials 47

4.1 AE features 48

4.2 Frequency analysis 56

4.2.1 Classification in frequency bands 56

4.2.2 Frequency spectra 57

4.2.3 Wavelet analysis and other techniques 59

4.3 Neural networks 62

4.4 Validation against a mathematical model 63

4.5 Source location on composite panels 64

4.6 In-flight AE sensing 65

4.7 Summary 67

5 System and sensors used in this work 69

5.1 Physical Acoustics' AE System 69

5.1.1 General experimental procedure 70

5.2 PAC sensors 71

5.3 PAC AEWin 2.0 software 76

5.3.1 General set-up procedure for AEWin software 77

5.3.2 Procedure to measure wave speed with PAC system 78

5.3.3 Location filtering with PAC AEWin 79

5.3.3.1 Guard sensors 79
5.3.3.2 Spatial filtering 80
5.3.3.3 Implementation in AEWin 80
5.3.3.4 Description of a typical set-up 82
5.3.4 Frequency calculations 83
5.4 The preamplifiers 85
5.5 Summary 86

6 Consistency of AE parameters 87
6.1 The pencil lead break source 88
6.2 The response of the sensors 88
6.3 Absolute energy 90
6.4 Frequency spectra 97
6.5 Hit amplitudes 98
6.6 Time-related features (duration, counts) 99
6.7 Dependence of hit durations on threshold settings 100
6.7.1 Results and analysis 101
6.8 Location capabilities 105
6.8.1 Results and analysis 105
6.9 Overall considerations 108

7 Frequency analysis 110
7.1 Effect of different media on AE signals 110
7.1.1 Test specimens 110
7.1.2 Sensor placement and test procedure 111
7.1.3 Description of the tests 111
7.1.4 Results and analysis 114
7.1.5 Standard deviation of the spectrum 116
7.1.6 Summary 117
7.2 Effect of anisotropy and position of sensor and sources relative to the edges on the waveforms 121
7.2.1 Descriptions of the tests 121
7.2.2 Results and discussion 123

7.3 PLBs on a carbon strip at different distances from the sensor 126
7.3.1 Testing setup 126
7.3.2 Results and discussion 127
7.3.3 Analysis: development and building-up of the waveform 128
7.3.4 Overall comments 133
7.4 PLBs distributed on a steel plate 134
7.4.1 Test setup 134
7.4.2 Results and analysis 135
7.4.2.1 Mathematical model for the reflections 137
7.4.2.2 Conclusions 140
7.4.3 Comments 141
7.5 Relationship between spectral features and position of the source on the panel 143
7.5.1 Test setup 143
7.5.2 Results 144
7.5.3 Discussion 145
7.6 Conclusions 149
7.6.1 Suitability of a frequency analysis 149
7.6.2 Characterising a source only 149
7.6.3 Compacting the spectral information 150
7.6.4 Positional information contained in the signals 150

8 Acoustic emissions from composite tensile test specimens 151
8.1 Test specimens 152
8.2 Test procedure 153
8.3 Unidirectional specimens 155
8.3.1 Description of the tests and basic AE features 155
8.3.2 Spectral analysis 163
8.3.3 Comparison of the frequency peaks and overall comments 170
8.4 Cross-ply specimens 174
8.4.1 Description of the tests and basic AE features 174
8.4.2 Spectral analysis 180
8.4.3 Comparison of the frequency peaks and overall comments 183
8.5 Angle-ply specimen 187

8.5.1 Description of the test and basic AE features 187
8.5.2 Comparison of the frequency peaks and overall comments 190
8.6 Transverse specimen 196
8.7 Conclusions 197

9 Acoustic emissions from a composite panel **199**
9.1 Test set-up 200
9.2 Setup and results 203
9.3 Comments 210

10 Conclusions and future work **212**

References **227**

Appendices **229**

A Mathematical derivations from chapter 7 **229**

B Matlab code **232**

C Technical drawings **250**

LIST OF TABLES

2.1 Conversion to engineering notation 13

4.1 Tabular summary of numerical results in literature; "f.c." stands for *frequency centroid*, "Gl" for *glass*, "Pp" for *polypropylene*, "Po" for *polyester*, "Gr" for *graphite*, "Ca" for *carbon*, "Ep" for *epoxy*, "Ten" for *tensile specimen*, "Tra" for *traction* 51

5.1 PAC WD sensor's features (PAC, 2003) 71

5.2 Sensors labels 72

5.3 Preamplifiers labels 86

6.1 Y tests layout 90

6.2 J tests layout 90

6.3 Results for "Y" tests (Absolute energy, aJ) 91

6.4 Results for "J" tests (Absolute energy, aJ) 92

6.5 Comparison between hits I and II 93

6.6 Frequency centroids (kHz, averaged over the four pencil lead breaks of each test) from Y tests, together with the average over all tests for each sensor . . 97

6.7 Minimum and maximum recorded amplitudes over the four breaks of each Y test 98

6.8 "Y" tests results (Amplitude, dB) 99

6.9 Average duration (1st row, μs), ring-down counts (2nd row) and their ratio (μs), on the right, for each sensor/test 100

6.10 Average rise times (μs) for each Y test / sensor 100

6.11 Amplitudes and durations in test T1 102

6.12 Positions located for test T2 105

6.13 Arrival time differences Δt in test T2 (a positive difference means an arrival at S3 before S1); the last row reports the average and the standard deviation σ 107

7.1 Parameters adopted for tests Comp1, Comp2, Comp3 112

7.2 Wave speed measured for the five tests 114

7.3 Frequency centroids (Hz) for all the tests: μ is the average frequency centroid of all the twenty waveforms; σ is the standard deviation of the frequency centroids; GMS is the frequency centroid of the geometric mean spectrum; AMS is the frequency centroid of the arithmetic mean spectrum 116

7.4 Acquisition parameters for tests O and E 122

7.5 Frequency centroids (kHz) of the ten events for test O 125

7.6 Parameters adopted for the test in the positions A and B 127

7.7 Parameters adopted for test S 135

7.8 Frequency centroids (f.c., kHz) for each position at two different partial waveform lengths, and distance sensor–source (cm) 138

7.9 Parameters adopted 143

8.1 Tensile tests — Notes: † notched, 15 cm intra-sensors distance; ‡ notched, 25 cm intra-sensors distance — E: Young's modulus (GPa) in the direction of the load, σ_u: Ultimate stress (MPa) in the direction of the load 152

8.2 Test parameter summary for tests Zero 155

8.3 AE setup summary 155

8.4 Test parameter summary for tests CP 175

8.5 Test summary for sample AP1 187

8.6 Test summary for sample Ninety 197

9.1 Parameters adopted for the test of the panel 204

LIST OF FIGURES

2.1 State of stress at a point of a continuum 14

2.2 Surface waves as a combination of longitudinal and transverse waves. The wave vector is parallel to the polarisation in longitudinal waves, orthogonal in shear waves. From Filipczynski *et al.* (1966) 17

2.3 Schematic of the plate 19

2.4 Lamb waves 21

2.5 Typical waveform detected on graphite/epoxy tube from lead break source on surface of tube. Source to receive distance is 0.1524 meters. From Prosser *et al.* (1992) 22

2.6 Group velocities (dispersion curves) for aluminium (Chahbaz *et al.*, 1996) . . 24

2.7 Schematic of scattering of waves 26

3.1 Schematic of a typical AE sensor (NDTRC, 2007) 32

3.2 Simple frequency response function 34

3.3 Effect of backing masses on the FRF: ω_{1--4} are the individual resonant frequencies (adapted from Coleman, 2006) 35

3.4 An idealized AE waveform for a single "hit" (PAC, 2003) 38

3.5 Schematic set-up of AE sensing 40

3.6 Hsu-Nielsen source (NDT.net, 2007) 41

3.7 Triangulation for an earthquake and intersection of the hyperbolae for AE . . 43

4.1 Graphical comparison of some of the numerical results shown in Tab. 4.1 (extended from de Groot *et al.*) 52

5.1 Simple schematic of PAC system 70

5.2 Calibration certificate for S1 73
5.3 Calibration certificate for S2 73
5.4 Calibration certificate for S3 74
5.5 Calibration certificate for S4 74
5.6 All the four calibration certificates are superimposed and shown here in different colours 75
5.7 Two examples of histograms 77
5.8 An example of a point plot 77
5.9 Graph setup window 78
5.10 Guard sensor principle (Diederichs and Ginzel, 1999) 80
5.11 Location Setup window in PAC AEWin 1.53 81
5.12 Location example: the events located in an amplitude versus position point-plot 83
5.13 Location example: the location setup window 83
5.14 Location example: the sensor placement window 84
5.15 Location example: the graph setup window 85

6.1 Modified pencil lead break test: starting position and indication of the movement 88
6.2 Simple layout for tests J and Y 89
6.3 Normalised power vs frequency (kHz) for the very same event detected as hits I and II by sensors S1 and S3, as generated by AEWin 94
6.4 Hit I over S1's calibration certificate, normalised power vs frequency (kHz) . 95
6.5 Hit II over S3's calibration certificate, normalised power vs frequency (kHz) . 95
6.6 An acoustic emission from test Y1 truncated after 25, 50, 100 and 300 μs, displayed in time (V,μs) and frequency domain (normalised spectra) 96
6.7 Simple geometry lay-out for test T1 101
6.8 Waveforms from sensors S1 and S3 corresponding to the same event. Time (μs) vs. voltage (mV). The threshold (1000 mV) is shown, and the amplitude and duration reported by the system is indicated. The scale is different for the two waveforms. 104
6.9 Half of the same waveform from Fig. 6.8b with a new threshold 10 dB bigger 104
6.10 Amplitude versus position plot for test T2 106

7.1 General sensor setup 112
7.2 Set-up for test Comp1 113
7.3 Set-up for test Comp2 113
7.4 Set-up for test Comp3 113
7.5 The geometric means of the power spectra coming from all the five tests, normalised 115
7.6 The geometric mean of the power spectra from the twenty hits of Al test, normalised 116
7.7 The geometric mean of the power spectra from the twenty hits of Steel test, normalised 117
7.8 The geometric mean of the power spectra from the twenty hits of Comp1 test, normalised 118
7.9 The geometric mean of the power spectra from the twenty hits of Comp2 test, normalised 119
7.10 The geometric mean of the power spectra from the twenty hits of Comp3 test, normalised 119
7.11 Spectral arithmetic mean (μ) and standard deviation ($\mu+\sigma$, $\mu-\sigma$), normalized, of data from Comp3 separated over the two channel 120
7.12 Spectral geometric means for Comp3, with the data separated over the two channels S3 and S4 120
7.13 Positions A, B, C, D for test O (not in scale) 122
7.14 Positions α, β, γ, δ for test E (not in scale) 122
7.15 Normalised geometric mean of power spectra from tests O and E 123
7.16 Normalised geometric mean of power spectra from tests O and E 124
7.17 Schematic of the specimen and test setup, not in scale 127
7.18 Waveforms "A" and "B" 128
7.19 Normalised spectra for the two waves A and B; the normalisation point corresponding with the very-low frequency peak 129
7.20 Zoom on Figure 7.19 130
7.21 Subpart of waveform B and its corresponding normalised power spectrum, after: 30, 160, 270, 450, 800, 2000 μs 131

7.22 Three sections of the waveform from position B with relative normalised power spectrum 132
7.23 Different zoom and scale on the waveform from position B 133
7.24 Plot of the frequency centroid (kHz) VS the length of the waveform considered (μs, logarithmic), for waves A and B 133
7.25 Schematic of the steel plate with the identification of the positions 134
7.26 Typical waveform for test S as detected in A 135
7.27 Spectrum from position A ("single") plus the geometric mean spectrum for all the twenty signals, both normalised 136
7.28 Frequency centroids (kHz, logarithmic) VS partial waveform length (μs, linear) for test S 137
7.29 Graphs of the frequency centroids versus the partial waveform length for two PLBs detected respectively in positions G, H, L 138
7.30 Schematic of a sensor and a source on an open plate 139
7.31 Schematic of a side reflection 139
7.32 Time windows (microseconds) for a narrow strip: schematic and contour map (not in scale) 140
7.33 Time windows for a panel (microseconds): schematic and contour map 141
7.34 Reflection-free times (μs) on half of the plate of test S 142
7.35 Schematic of the aluminium plate and the positions 144
7.36 Superimposition of power spectra calculated at different sampling times (in the legend, in microseconds) and normalised, for a single signal detected in position F, with the indication of the local maxima and of the threshold. The semi-logarithmic scale makes the threshold clearly visible at $10^{-2} = 0.01$ . . . 147
7.37 Summary of all the signals from this experiment — abscissa: frequency, ordinate: position of the sensor 148

8.1 Power spectra (dB VS kHz) for sensors S3 (top grip) and S4 (bottom grip) . 154
8.2 Power spectra (dB VS kHz) for sensors S3 (bottom grip) and S4 (top grip) . 154
8.3 Overall AE activity for test Zero1, expressed as event amplitude, superimposed to the stress/strain (a) and stress/time (b) curves 156
8.4 Event amplitude (dB) versus position on the length of the sensor (m) for sample Zero1 157

8.5 Normalised power spectrum, as displayed by AEWin, for a typical waveform from test Zero1 157
8.6 Histograms of hits (grey) and events (black) versus time, for sample Zero1 . . 158
8.7 Overall AE activity for test Zero2, expressed as event amplitude, superimposed to the stress/strain (a) and stress/time (b) curves 158
8.8 Event amplitude (dB) versus position on the length of the sensor (m) for sample Zero2 159
8.9 Typical spectrum (normalised) for the events from sample Zero2, as displayed by AEWin 159
8.10 Histograms of hits (grey) and events (black) versus time, for sample Zero2 . . 160
8.11 Overall AE activity for test Zero3, expressed as event amplitude, superimposed to the stress/time curve 160
8.12 Event amplitude (dB) versus position on the length of the sensor (m) for sample Zero3 161
8.13 Normalised power spectrum, as displayed by AEWin, for two typical waveforms from test Zero3 161
8.14 Frequency centroid (kHz) versus sample time (μs) for ten waveforms from test Zero1 163
8.15 Normalised power spectra superimposed to the respective part of the waveform 2, for different sampling times — the lower abscissa is the sampling time (μs) and refers to the waveforms, measured on the ordinate in V; the upper abscissa is the frequency of the spectral density, nondimensional 164
8.16 Spectral densities for different sampling times (in μs in the legend) for waveform 1 from test Zero1. A threshold of 0.20 identifies the local maxima as indicated by the upper bands 165
8.17 Frequency centroid (kHz) versus sample time (μs) for ten waveforms from test Zero2 166
8.18 Spectral densities for different sampling times (in μs in the legend) for two waveforms from test Zero2. A threshold of 0.20 identifies the local maxima . 167
8.19 Frequency centroid (kHz) versus sample time (μs) for the selected waveforms from test Zero3 168

8.20 Spectral densities for different sampling times (in μs in the legend) for waveform 1 from group Centre, test Zero3. A threshold of 0.2 identifies the local maxima as indicated by the upper bands 169
8.21 Waveform from a PLB on a specimen like Zero1; modes A_0 and S_0 are indicated 170
8.22 Beginning of a waveform collected from Zero1 171
8.23 Spectral maxima for the waveforms selected, threshold = 0.20 172
8.24 Spectral maxima for test Zero2, threshold = 0.25 173
8.25 Overall AE activity for test CP1, expressed as event amplitude, superimposed to the stress/strain (a) and stress/time (b) curves 175
8.26 Normalised power spectrum, as displayed by AEWin, for a typical waveform from test CP1 176
8.27 Event amplitude (dB) versus position on the length of the sensor (m) for sample CP1 176
8.28 Event amplitude (dB) versus position on the length of the sensor (m) for samples CP3 and CP4 178
8.29 Histograms of hits (grey) and events (black) versus time, for samples CP3 and CP4 179
8.30 Histograms of hits (grey) and events (black) versus time, for sample CP1 . . 179
8.31 Frequency centroid (kHz) versus sample time (μs) for ten waveforms from test CP1 180
8.32 Frequency centroid (kHz) versus sample time (μs) for ten waveforms from tests CP3 and CP4 181
8.33 Spectral densities for different sampling times (in μs in the legend) for waveform 1 from test CP1. A threshold of 0.25 identifies the local maxima as indicated by the upper bands 182
8.34 Spectral densities for different sampling times (in μs in the legend) for waveform 2 from test CP3. A threshold of 0.25 identifies the local maxima as indicated by the upper bands 182
8.35 Spectral maxima for CP tests, threshold = 0.25 185
8.36 Spectral maxima for CP3 and CP4 tests, threshold = 0.40 186
8.37 Overall AE activity for test AP1, expressed as event amplitude, superimposed to the stress/strain (a) and stress/time (b) curves 188

8.38 Histograms of hits (grey) and events (black) versus time, for sample AP1 . . 189
8.39 Event amplitude (dB) versus position on the length of the sensor (m) for sample AP1 189
8.40 Normalised power spectrum, as displayed by AEWin, for two typical waveforms from test AP1 190
8.41 Frequency centroid (kHz) versus sample time (μs) for the selected waveforms from test AP1 191
8.42 Spectral densities for different sampling times (in μs in the legend) for three waveforms from test AP1. A threshold of 0.25 identifies the local maxima as indicated by the upper bands 193
8.43 Spectral maxima for AP1 test, threshold = 0.25 194
8.44 Spectral maxima for AP1 test, threshold = 0.60 195

9.1 Schematic of the panel and the forces involved 201
9.2 The four-point bending test rig — the main dimensions are quote in millimeters 202
9.3 Sensor, panel and rig setup 203
9.4 Located events, subdivided in two "horizontal" groups, for the panel 204
9.5 Amplitude vs X Position for events coming from the panel 205
9.6 Power spectra of two waveforms collected during the test of the panel 206
9.7 Frequency centroid (kHz) versus sample time (μs) for the waveforms from the test on the panel 207
9.8 Spectral densities for different sampling times (in μs in the legend) for waveform number 5 from group α. A threshold of 0.25 identifies the local maxima as indicated by the upper bands 208
9.9 Spectral maxima for the waveforms from the test on the panel, threshold = 0.25 209

Appendices figures

1 Schematic of a rear reflection 230
2 Transforming to cartesian coordinates 231
3 Central pin (interface with Instron machine) 250
4 Roller 251
5 Lower half: plate 251

6 Upper half: plate 252
7 Vertical plates 252
8 Upper half 253
9 Lower half 253

Grazie a...

Beggar that I am, I am even poor in thanks.

William Shakespeare, Hamlet. Act II. Sc. 2.

Mum and dad for ontological reasons, first,

and for not killing me, after

My supervisor Janice Barton for choosing me, first,

and for her help with the thesis, after

Those people who became my friends in Southampton

for not discarding me, first,

and for not discarding me, after

My past supervisor in Italy, Luca d'Agostino,

for the constant and friendly encouragement,

which has no first nor after

I am most grateful to BAE Systems

that sponsored this research.

Nomenclature

A	Antisymmetrical mode
b	Half plate thickness
c_{ijkl}	Elastic costant tensor
d	Distance
e	Distance from source to edge
E	Young's modulus
h	Distance from sensor to edge
I, J, i, j, k, l	Indices
k	Wave number
l	Distance between two points
L	Longitudinal (subscript)
P	Pressure
S	Strain Tensor and Symmetrical mode
t	Time
T	Transverse (subscript)
$\mathbf{u}$	Displacement vector
v	Wave velocity
x_i	Cartesian coordinate

α	Phase angle and Attenuation constant
β	Attenuation constant
δ_{ik}	Kronecker's delta
ϵ	Strain
ϕ	Scalar potential of displacement vector
λ_e	First Lamé constant
κ	Bulk modulus
μ	Modulus of rigidity
ν	Frequency
ρ	Density
σ	Stress
ψ	Vector potential of displacement vector
ω	Angular frequency

CHAPTER

ONE

Introduction

Every new beginning comes from some other beginning's end.

Semisonic, Closing Time

1.1 Background

Composite materials are among the strongest, lightest and stiffest corrosion-resistant materials known to man. They are engineered materials which consist of more than one material type, designed to display a combination of the best characteristics of each of the component materials (Daniel and Ishai, 1994). Most composites have strong, stiff fibres in a matrix which is weaker and less stiff. The objective is usually to make a component which is strong and stiff, often with a low density. Commercial material commonly has glass or carbon fibres in matrices based on thermosetting polymers, such as epoxy or polyester resins. There are further classes of composite in which the matrix is a metal or a ceramic. For the most part, these are still in a developmental stage, with problems of high manufacturing costs yet to be overcome, and the reasons for adding the fibres (or, in some cases, particles) are often rather complex; for example, improvements may be sought in creep, wear, fracture toughness, thermal stability, etc. High stiffness and strength usually require a high proportion of fibres in the composite. This is achieved by aligning a set of long fibres in a thin sheet (a *lamina* or *ply*). However, such material is largely anisotropic, generally being weak in the transverse

direction. Commonly, high strength and stiffness are required in various directions within a plane. The solution is to stack and consolidate a number of sheets, each having the fibres oriented in different directions. Such a stack is termed a *laminate.*

Some composite materials are capable of operating at extremely high temperatures and in the vacuum of space (Rawal, 2001); others are very tough and durable. In spite of their enhanced material properties that have facilitated their wide-spread use in modern aircraft, the mechanics of composite material failure is not straightforward, and inspection and identification of such damage is an issue of current importance. The National Transportation Safety Board (NTSB, 2003) recommended more strict non-destructive inspections on aircraft and stated that current inspection methods "may be inadequate" for damage detection and identification purposes.

Damage in composite materials can come from a number of sources, both during initial processing and in service, that can lead to a serious degradation in their load carrying capacity. Even seemingly minor impact events can result in significant damage, especially in thin-walled structures. In order to ensure the safety of the structure, it is often necessary to carry out expensive and extremely time-consuming inspections (Matthews, 1999). If undetected, damage can grow to a critical size and lead to catastrophic failure of the structure. Because of this, damage monitoring systems in aircraft and aerospace structures can be extremely helpful in improving their safety and reducing maintenance cost by a significant amount (Mal, 2000).

Damage in composite materials can be divided into the following six categories (Tatiparthi, 2004):

(i) **Fibre-matrix debonding:** this occurs because of poor interface bonding between the fibers and the matrix.

(ii) **Matrix cracking:** this occurs as a result of multiple debonding between the fibres and the matrix so that individual debonds become connected in the matrix material. Under continuous loading, more matrix cracks develop until a large area is damaged and results in reduced stiffness and strength.

(iii) **Delamination:** this occurs on a plane between adjacent layers within a laminate. Microcracks introduce multiple stress concentration points at the crack tips as the microcracks are restrained by the adjacent layers. These crack tips exist at the interface

between piles of a laminated composite and thus lead to delamination which is a large scale damage.

(iv) **Fibre breakage:** usually occurs after gross delamination and matrix cracking. Since the load transfer in the structure is inhibited because of the matrix cracking, fewer fibres are able to carry load and hence fibre breakage occurs.

(v) **Fibre pull-out:** this occurs along with breakage, particularly under tensile load, when the fibres are simply pulled from the matrix.

(vi) **Fracture:** This is the final stage of failure where the material breaks and separates out.

Defects of materials and manufacturing anomalies are inherent in composite materials and structures, so the introduction of composites into large scale production depends in large measure on the successful application of non-destructive testing (NDT) techniques for damage detection and monitoring (Farrar *et al.*, 2003), that often have to be specifically tailored for composites, for issues regarding the applicability of the physics of some of the techniques. In fact some physical properties of metals differ substantially from those of composites: thermal conductivity and electrical conductance are much larger in metals than in composites, the acoustic attenuation of composites is larger, and the elastic behaviour differs significantly. Secondly, composites are anisotropic, whereas metallic structures are fabricated from feedstock, e.g. plate, bar and section, homogeneous in nature and of known property, composition and quality. Most of the difficulties in the successful detection of damage in composite materials arise from the inherent inhomogeneity and anisotropy of composite materials (Guild and Adams, 1981). All this means that some of the classic non-destructive inspection techniques of metals (Chalmers, 1944) cannot always be used with composites.

For translucent GRP composites, visual inspection methods can be the most useful of the available techniques. Where there is access to both surfaces, use of a strong light source and observing transmission through the laminate thickness can be particularly effective. Porosity, poor impregnation, delamination and inclusions can all be detected as well as surface flaws.

Radiography and ultrasound for non-destructive inspection of fibre-reinforced polymer composites, although not straightforward as for simpler structures, are the generally selected methods used in high-performance applications such as aircraft and space structures (Birt,

2000). For structural composites as a whole, ultrasonic inspection methods are probably the most widely used form of NDT. Active ultrasonic methods interrogate the structure through the application of ultrasonic pulses. The greatest difficulty here is that the sound attenuates more quickly in composites than traditional materials such as metals. Furthermore, sound attenuation is more dramatic in a damaged material than that in the same whole material; thus as a material becomes more damaged, the sound attenuates more rapidly (Cheeke, 2002). X-radiography techniques are available and can be used to determine foreign inclusions, interlaminar cracks and voids although problems with low contrast may occur. This can be improved by the use of radio-opaque penetrants such as sulphur, trichlorethylene, carbon tetrachloride or methyl or zinc iodide. In this way very fine cracks can be resolved.

Eddy current methods can be used, but the electrical properties of composites lead to modifications of current methods applied to metals. For composites where the fibres are conductive, eddy current techniques can be used to determine resin content and lay-up geometry (De Goeje and Wapenaar, 1992).

Electrical resistance damage detection (Chung, 2001) is valuable for evaluating composites and joints, provided that the materials involved are not all electrically insulating. The electrical resistance will increase with increasing strain, and an important change can be seen at the transition point where the carbon fibre bundles fracture, since stiffness and electric resistance usually show a similar trend (Seo and Lee, 1999).

Some success has been obtained using dye penetrants, but this method can only detect surface cracks; in addition, the dye penetrant may itself affect the material properties and result in degradation (Vipond and Daniels, 1985). Other, less used, NDT techniques for composites are x-ray diffractometry (Prakash, 1980), and pulsed thermography (Avdelidis *et al.*, 2004).

1.2 Acoustic Emission (AE)

AE[1] is a naturally occurring phenomenon within materials. The term "acoustic emission" is used to define the transient elastic waves than result from a sudden strain energy release resulting from microstructural changes. If loading causes damage such as cracking, dislocation motion or the formation or collapse of internal voids, energy will be liberated in the

[1]Throughout this report, "AE" will be used to indicate the NDT technique, whereas "acoustic emission" will denote the actual physical process which consists of the release of energy as elastic wave.

form of vibrations that travel through the material, which can be detected at its surface by suitably sensitive transducers (Williams, 1980). AE can be distinguished from the other methods used for damage detection (described above) as it utilizes information supplied by the process *while* it occurs. Because of that, the AE technique stands out amongst the other NDT techniques in a category of its own: it is a *continuous monitoring technique* rather than a tool for non-destructive inspection; in fact, the structure must be loaded, and eventually damaged, in order to collect acoustic emissions.

The release of enough energy will produce audible sounds; the AE technique permits the detection of higher frequency and low intensity sound. Today, AE measurements are carried out in the range between 1 kHz and 2 MHz (Carlos, 2003), although more typically between 100 and 1000 kHz. Higher frequencies are usually too easily absorbed by the material to be detected at a significant level. On the other extreme, lower frequencies would mix with background extraneous noise (that is generally characterised by frequencies below 50 kHz) that would interfere with the measurement of the useful acoustic emissions.

Perhaps the main advantage of AE is that, under continuous monitoring, events may be detected as they occur and from any location in the body. On the other hand, the major disadvantage is that great skill is needed on the part of the operator to interpret the information from the structure, and to relate it objectively to possible damage sources (Wevers and Surgeon, 2000).

In summary, the AE technique has the following features which, all together, make it unique:

- it is a passive method for *in situ* monitoring of the response of a material to an applied load,
- it is a global monitoring technique where it is possible to detect damage remote from the sensor,
- it is nondirectional, in such the emitting sources radiate the energy in every direction, although important anisotropic effects must be taken into account for composites,
- it is sensitive to defect growth and changes in the material rather than to the static presence of defects,
- AE is noninvasive.

Among the phenomena that can be detected by AE are (Nichols, 1976) (i) plastic deformation i.e. dislocations, (ii) phase transformations, in particular those which occur very rapidly, i.e., martensitic transformation, (iii) crack formation and growth of fracture phenomena, and (iv) friction phenomena in a crack.

Halmshaw (1991) summarizes many of the achievements of AE with metal structures. A particular example was cited, that of the use of AE during a hydrotest of a pressure vessel; typically the proof pressure of a vessel is 150% of the designed working pressure, and because this is likely to cause some local yielding and stress relief, the vessel is routinely loaded several times to proof pressure and, due to the Kaiser effect (no new emissions will occur until the previous maximum stress has been exceeded), if no damage occurred on the first proof there should be no acoustic emission on subsequent loadings; whereas, if there are flaws causing significant damage, there should be acoustic emission on subsequent loadings.

The detection of in-service stress corrosion cracking appears to be a relatively straightforward application: stress corrosion produces copious acoustic emissions, and several successful applications have been reported (Ferrer *et al.*, 2002). Process monitoring — cutting, grinding, forming, curing — all cause acoustic emissions, and so AE monitoring can be used either to characterise the process, or detect abnormalities in situ after the process completion (Tsai and Hocheng, 2002). By using a so-called intelligent system, a feed-back loop can be used to stop the equipment if a pre-chosen AE threshold is exceeded.

It is sometimes the case that AE can provide information on the nature of a defect, and much work has been done in attempting to relate the acoustic emission to metallurgic conditions (Mukhopadhyay *et al.*, 2002). It is now generally accepted that in steel the predominant source of acoustic emissions is plastic yield, which is enhanced at regions of stress concentrations (Singh *et al.*, 2003). It is also known that acoustic emissions have a close relationship with material behaviour at the tip of a crack under load, so that it seems possible to obtain a correlation between acoustic emissions and fracture toughness parameters (Dunegan, 1969). There is a rapid increase of acoustic emission activity when the stress intensity factor at the crack tip approaches the fracture toughness of the material.

As it has been mentioned, final failure of laminated composite components is often preceded by significant damage of the material in the component, for example by matrix cracking, fibre fracture and delamination. These events correspond to actual acoustic emissions, which can thus be monitored through AE and, if understood, can become a valuable tool in

the integrity assessment of such structures. The damage events are often very localised in space and time (for example, the breakage of a single fibre); this means that each damage event will produce a distinct stress pulse in the specimen and consequently, each signal can be considered as the acoustic signature of the different damage modes (Âberg, 2001; Huguet *et al.*, 2002). Measuring acoustic emission is therefore potentially a good way of monitoring damage evolution in composite materials, because the acoustic emissions are potentially a powerful source of information about internal processes of deformation.

AE offers the capability of *continuous* monitoring of the structure, which is necessary for real-time operation. In fact, modern commercial and military aircraft are being constructed using substantial amounts of advanced light-weight composite materials, and the use of composite materials in the secondary structures of aircraft in order to keep deadweight down is significant. A reliable health monitoring system can enable condition-based maintenance and significantly reduce life cycle costs by minimizing inspection time and effort, and by extending the useful life of new and aging aerospace structural components. In other words, composite materials would gain substantial added value if it were possible to equip them with a system that could continuously monitor their damage state. AE clearly has the potential to provide the basis of such a system.

1.3 Aims and objectives

Damage in composite materials can be localised to one of the constituent parts or affect the structure as a whole. *The overall goal of this thesis is to develop an approach that allows a characterisation of the damage in composites using AE.* The need for such a characterisation is essential if real-time in-service damage monitoring system is to be developed.

There are essentially two experimental approaches to damage characterisation using AE: using the AE features derived from the AE system, and using the frequency content of the acoustic emission. In turn, these approaches can resort to a variety of techniques which can further increase the assortment of the tasks which have all the same goal of identifying the damage mode.

In this work, acoustic emissions from known damage sources will be detected, located in order to eliminate spurious noise, recorded, and their frequency content analysed. The

usefulness of the AE features in this context will be examined (§6). The issues related to the anisotropy of the composites will be considered, both in relation to the source location and the way the anisotropy affects the waveforms as they progress through the structure (§7.2).

As the work focuses on aircraft structures, the materials used throughout the work is a carbon/epoxy composite system. They will be cut in form of strips, loaded in tension, and the acoustic emission data will be obtained using a commercially available AE system (§8). Panels will also be tested, in order to attempt a two-dimensional location and filter out the reflections coming from the edges of the strips (§9). A series of tests are developed that ensure preferential damage types are initiated and the AE response is analysed.

Some words are needed here to explain better the scope of this research, by defining in more detail what is meant by *characterisation*, and what has (and has not) been already achieved by other researchers. In the literature there are a large number of papers undertaking a characterisation that end up with what merely is a *description* of the failure of a component in terms of AE parameters, and *not* a full relationship between the actual damage and the acoustic emissions. This means that it is unlikely that the same structure tested in different conditions will generate the same acoustic emissions, or a different structure made from the same material will produce the same signals. Therefore it is necessary to determine if the acoustic emissions collected are exclusive of the structures examined, or if different sources may provide identical signals. Without generality and uniqueness, a characterisation does not permit an *identification*, i.e. "the making, regarding, or treating of a thing as identical with another, or of two or more things as identical with one another" (O.U.P., 1989). It is this possibility of abstracting a set of data and applying it to a different structure ("another" thing) with something in common that is the focus of the work in this thesis. Therefore this work, before concentrating on a systematic collection of AE data from tensile specimens with different lay-ups, will investigate on the conditions that may attribute validity to such collection.

1.4 Thesis organization

The underlying physics of acoustic emission is based on the propagation of elastic waves. As background an overview of this is provided in §2.

A description and an introduction to AE technique is given in §3, together with an

explanation of how the physics of the waves interact with the sensors, and how such AE systems are constructed.

A critical review of the literature on the AE characterisation of damage in composites is provided in §4, where the review of the works is subdivided according to the main AE analysis technique, and is followed by studies on the source location on composites, and on the in-flight operation in aircrafts. A summary will then describe what yet is to be achieved in AE characterisation of damage in composites, and will explain the points where the existing works fail to fully address the issues raised in this chapter.

Chapter §5 is devoted to a detailed description of the equipment used in this work.

After the description of the general experimental and analysis procedure, Chapters §6 and §7 will describe experiments conducted with pencil lead breaks (PLBs) in tests designed to show the variability of the collected signals with parameters such as equipment, geometry, position, etc., and suggest testing parameters for the subsequent tests. Whereas §6 will focus on the "AE parameters", §7 will show how a frequency description can account for these variations. These tests will involve strips and plates, composites and metals, and will leave damage aside, concentrating on the acoustic emission considered as a signal independent from the originating causes. Considerations will be drawn about the subjectivity of the results due to the different acquisition systems and parameters used; emphasis will be given to the sensitivity of the sensors and the sampling time of the signals.

Tests to collect acoustic emissions from failing composites are described in §8 and §9, where it shall be explained that the motivation of these tests is collecting data from lay-ups designed to produce preferential damage. They will mostly consist of tensile tests on strips (§8), but an analysis of the emissions from one panel will be presented as well (§9). The tests will allow a comparison of the acoustic emissions from specimens varying for one dimensional parameter only. The acquisition will make use of two sensors at least, in order to locate the AE events and exclude the spurious data. Finally, overall conclusions are drawn in §10, that will summarise the outcomes of this work in the context of the aims and objectives given in this introductory chapter.

CHAPTER

TWO

Elastic waves in homogeneous media

You can't stop the waves, but you can learn to surf.

Jon Kabat Zinn

Waves propagating in elastic material are termed *elastic waves.* Unlike acoustic waves in air, waves in solids are inaudible to human ears, and unlike surface waves in water, waves in solids are invisible to human eyes. Yet, waves in solids are real, physical, and of the utmost importance in engineering applications, and useful in nondestructive evaluation (Liu and Xi, 2002). A short summary of elastic waves is given here, because they underlie the generation and the transmission of the acoustic emission from the material to the sensor.

Composites are not homogeneous, but a description of the wave transmission in inhomogeneous media can be built illustrating how the inhomogeneity of the material affects and modifies those waves which are present in a simpler material. The theory of elastic waves in homogeneous media is the basis over which a more exact theory can be built.

2.1 Structure-borne sound

The propagation of waves in solids may be divided roughly into three categories. The first is elastic waves, where the stresses in the material obey the Hooke's law; the considerations contained in this thesis will assume such elastic behaviour. The two other main categories, visco-elastic waves, where viscous as well as elastic stresses act, and plastic waves in which

the yield stress of the material is exceeded, are not of interest here (Graff, 1991).

Structure-borne sound must travel through many different structures and materials, whereas air-borne sound only travels in one medium. In gases and liquids only compression waves are of importance, in solid bodies two types of waves occur (in many different combinations; Cremer and Heckl, 1973). Acoustics studies the macroscopic phenomena caused by sound waves and is formulated as if matter were a continuum (Auld, 1973).

The low-amplitude waves dealt with in this thesis fall in the field of ultrasound, with frequencies higher than those to which the human ear can respond (about 16–20 kHz). Reasons for this are: 1. shorter wavelengths occur at higher frequencies, where plane wave conditions are more easily realized (this is especially true with small specimens); 2. frequencies associated with relaxation phenomena often fall within the ultrasonic range. Waves of lower frequencies are called acoustic.

2.2 A summary of the theory of elasticity

A brief summary of the theory of elasticity is given here to introduce the notation (Dieulesaint and Royer, 1980). The theory described here will not be used in full for the subsequent work, but only to present the phenomenon of the dispersion of the waves.

The strain tensor S_{ij} is a linearised second-order tensor describing the mechanical strain at a point. The strain tensor is symmetric:[1]

$$\varepsilon_{ij} = \frac{1}{2}\left(\frac{\partial u_i}{\partial x_k} + \frac{\partial u_k}{\partial x_i}\right) \tag{2.1}$$

so that the distance dl' between two points close together after a deformation with small strain is related to the distance dl before the deformation through

$$dl'^2 = dl^2 + 2S_{ij}dx_i dx_j \tag{2.2}$$

where $dl^2 = dx_i^2$ and $dl'^2 = (dx_i + du_i)^2$, $\mathbf{du}$ being the displacement vector.

The stress tensor σ_{ij} is a second-order symmetric tensor describing the local stress. The first index gives the direction of the force, the second gives the direction of the normal to

[1]The usual tensor summation convention is assumed, of summation over repeated indices:

$$x_{i,j}y_j = x_{i,1}y_1 + x_{i,2}y_2 + x_{i,3}y_3$$

the surface on which it acts (Fig. 2.1).

The bulk modulus κ (or modulus of compression) is the elastic constant corresponding to hydrostatic compression:

$$\varepsilon_{ii} = -\frac{P}{\kappa} \tag{2.3}$$

where $\kappa = \lambda_e + \frac{2}{3}\mu$. The bulk modulus κ gives the change in volume V of a solid substance as the pressure P on it is changed,

$$\kappa = -V\frac{dP}{dV} \tag{2.4}$$

$$= -\rho\frac{\partial P}{\partial \rho} \tag{2.5}$$

The bulk modulus has units of pressure.

Lamé constants λ_e and μ are the constants historically chosen to describe the classic properties of an isotropic solid[2] that arise in strain-stress relationships. They are given in terms of other solid properties, as follows.

The coefficient μ is termed "modulus of rigidity" because the equation

$$\sigma_{ik} = \kappa\varepsilon_{ll}\delta_{ik} + 2\mu\left(\varepsilon_{ik} - \frac{1}{3}\varepsilon_{ll}\delta_{ik}\right) \tag{2.6}$$

shows that pure compression and shear deformation give rise to stress components proportional to κ and μ, respectively. It is also a manifestation of Hooke's law as, in both cases, stress is proportional to strain.

Another approach to Hooke's law of more practical use sees σ_{ij} expanded as a Taylor's series in ε_{kl}; in linear elasticity, the series is truncated after the second term, leading to

$$\sigma_{ij} = c_{ijkl}\varepsilon_{kl} \tag{2.7}$$

where

$$c_{ijkl} \equiv \left(\frac{\partial\sigma_{ij}}{\partial\varepsilon_{kl}}\right)_{\varepsilon_{kl}=0} \tag{2.8}$$

is known as the elastic constant tensor, a fourth-order symmetric tensor.

Young's modulus E is the elastic constant corresponding to the stretching of a free-

[2]The symbol λ is conventionally used for the first Lamé constant, but in this text, to avoid confusion with the more used wavelength symbol, λ_e shall be used.

standing bar and is related to Lamé constants by

$$E = \frac{\mu}{\lambda_e + \mu}(3\lambda_e + 2\mu) \tag{2.9}$$

Since each of σ_{ij} and ε_{kl} has six independent components, the c_{ijkl} tensor has a maximum of 36. This leads to the engineering notation where $c_{IJ} \equiv c_{ijkl}$, with ij and kl going in pairs, as in Table 2.1.

Table 2.1: Conversion to engineering notation

I, J	ij, kl
1	11
2	22
3	33
4	23=32
5	31=13
6	12=21

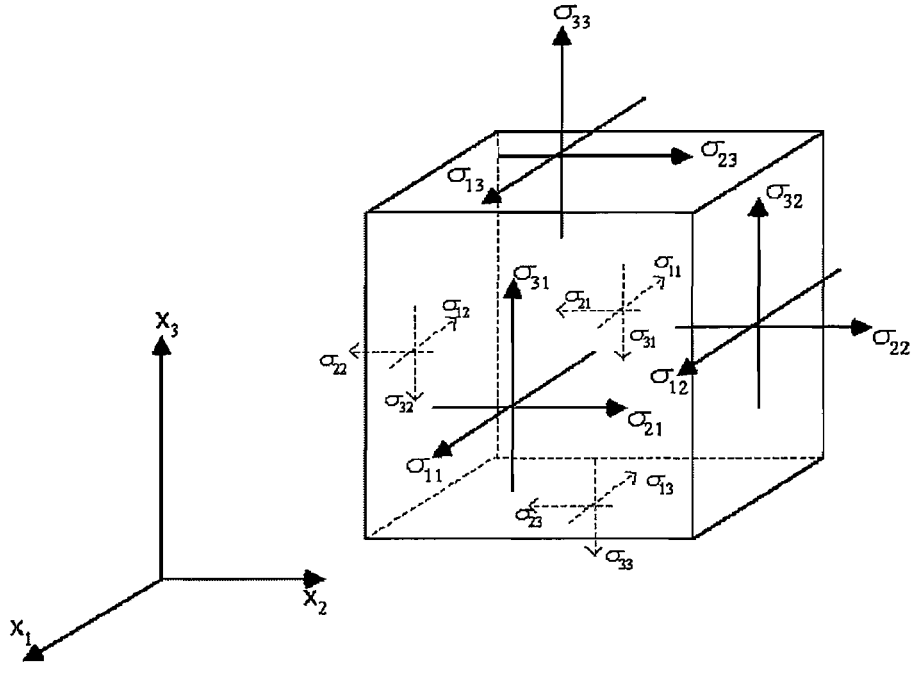

Figure 2.1: State of stress at a point of a continuum

2.3 Wave equation in three dimensions

The wave equation in three dimensions can be obtained by combining (2.7) with the following equation

$$\frac{\partial \sigma_{ij}}{\partial x_j} = \rho \frac{\partial^2 u_i}{\partial t^2} \tag{2.10}$$

where ρ is the density. This equation of motion comes from the fundamental law of dynamics $\mathbf{F} = m\mathbf{a}$, where the force density per unit volume of stressed material is given by

$$f_i = \frac{\partial \sigma_{ij}}{\partial x_j} \tag{2.11}$$

giving rise to an acceleration $\partial^2 u_i / \partial t^2$ along the i-th axis for the unit volume mass ρ.

Now, for better management of the equations, an isotropic solid will be considered, for which

$$c_{ijkl} = \lambda_e \delta_{ij} \delta_{kl} + \mu(\delta_{ik}\delta_{jl} + \delta_{il}\delta_{jk}) \tag{2.12}$$

Rearranging using the engineering notation, (2.7) can be written, for an isotropic solid:

$$\sigma_{ij} = (c_{11} - 2c_{44})\, \varepsilon\, \delta_{ij} + 2c_{44}\varepsilon_{ij} \tag{2.13}$$

where

$$\varepsilon = \varepsilon_{ii} = \nabla \cdot \mathbf{u} = \frac{\partial u_i}{\partial x_i} \tag{2.14}$$

Thus the equations (2.7) and (2.10) can be written as

$$\frac{\partial}{\partial x_i}\left[(c_{11} - 2c_{44})\frac{\partial u_i}{\partial x_i}\right] + c_{44}\frac{\partial^2 u_i}{\partial x_j^2} + c_{44}\frac{\partial}{\partial x_i}\left(\frac{\partial u_i}{\partial x_j}\right) = \rho \frac{\partial^2 u_i}{\partial t^2} \tag{2.15}$$

Traditionally, the displacement vector is written in terms of the scalar (ϕ) and vector (ψ) potentials:

$$\mathbf{u} = \nabla\phi + \nabla \times \boldsymbol{\psi} \tag{2.16}$$

In vector notation, equation (2.15) becomes then:

$$\nabla\left(\rho\frac{\partial^2\phi}{\partial t^2} - c_{11}\nabla^2\phi\right) + \nabla \times \left(\rho\frac{\partial^2\boldsymbol{\psi}}{\partial t^2} - c_{44}\nabla^2\boldsymbol{\psi}\right) = 0 \tag{2.17}$$

which is the sum of a scalar and a vector quantity, both equal to zero:

$$\rho \frac{\partial^2 \phi}{\partial t^2} = c_{11} \nabla^2 \phi \tag{2.18}$$

$$\rho \frac{\partial^2 \psi}{\partial t^2} = c_{44} \nabla^2 \psi \tag{2.19}$$

Since $c_{11} = \lambda_e + 2\mu$ and $c_{44} = \mu$, ϕ is associated with longitudinal waves (L) and ψ with transverse waves (T):

$$\mathbf{u} = \mathbf{u}_L + \mathbf{u}_T \tag{2.20}$$

$$\mathbf{u}_L = \nabla \phi \tag{2.21}$$

$$\mathbf{u}_T = \nabla \times \psi \tag{2.22}$$

The two equations are decoupled, which has the consequence that longitudinal and shear waves are independent modes of propagation in bulk solids.

Finally:

$$\frac{\partial^2 \mathbf{u}_L}{\partial t^2} = V_L^2 \nabla^2 \mathbf{u}_L \tag{2.23}$$

$$\frac{\partial^2 \mathbf{u}_T}{\partial t^2} = V_T^2 \nabla^2 \mathbf{u}_T \tag{2.24}$$

where

$$V_L = \sqrt{\frac{\lambda_e + 2\mu}{\rho}} \tag{2.25}$$

$$V_T = \sqrt{\frac{\mu}{\rho}} \tag{2.26}$$

are the wave speeds of the two modes, of order of few kilometers per second in most materials. The fact that $\nabla \cdot \mathbf{u}_T = 0$ confirms that there is no change in volume for transverse waves, whereas $\nabla \times \mathbf{u}_L = 0$ means that there is no rotation associated with longitudinal waves.

Although these formulae refer to an ideal three dimensional solid, and are not specific of plates (which will be dealt with in the next sections), they already present the issue of different travelling speed for different modes, that can importantly affect the way such waves are detected by a sensor at different distances.

2.4 Rayleigh waves

Waves travelling through an extended medium (one the dimensions thereof are much larger than the acoustic wavelength) are called *bulk waves.* As anticipated with the scalar and vector potentials, only two types of them exist, in an ideal unbounded isotropic solid (Dieulesaint and Royer, 1980):

(i) **longitudinal waves**, or compression waves, or extensional mode. They are characterised by a particle displacement parallel to the direction of propagation. A compression wave creates a variation in the distance between parallel planes containing given particles, thus the volume occupied by a given number of particles is not a constant. The restoring force for compression waves is provided by the medium's bulk modulus.

(ii) **transverse waves**, or shear waves, or flexural mode. The particle displacement is perpendicular to the wave vector and the gliding of parallel planes causes no variation in volume. An S-wave is a wave in an elastic medium in which the restoring force is provided by shear. Shear waves are divergenceless, $\nabla \cdot \mathbf{u} = 0$, where $\mathbf{u}$ is the displacement of the wave, and come in two polarizations: vertical or horizontal.

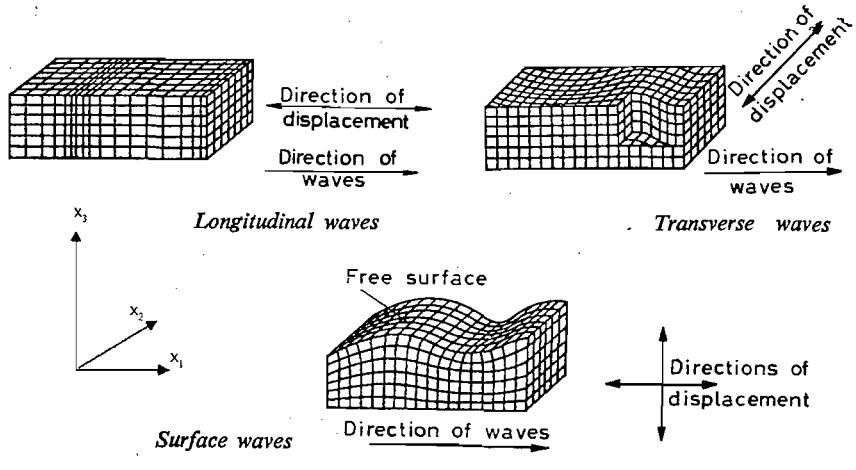

Figure 2.2: Surface waves as a combination of longitudinal and transverse waves. The wave vector is parallel to the polarisation in longitudinal waves, orthogonal in shear waves. From Filipczynski *et al.* (1966)

In more general cases (bounded, anisotropic solids), the waves may be much more complex (Fig. 2.2). Waves can be propagated over the plane boundary between an elastic half-space and a vacuum or sufficiently rarefied medium (for example, air), where the amplitude

of the waves decays rapidly with depth. These waves, named Rayleigh or surface waves, comprise the principal type of wave observed in earth tremors (Viktorov, 1967).

A surface wave has its maximum amplitude at the surface of the solid, with the amplitude decreasing with distance from the surface. The plane of the particle motion ellipse can be either parallel (Love waves) or perpendicular (Rayleigh waves) to the surface. However, because most AE sensors detect motion perpendicular to the surface, the parallel component is seldom seen.

The velocity of Rayleigh waves is slightly lower than the shear velocity.[3] Lord Rayleigh first described in 1885 the acoustic waves that travel along the earth's surface after an earthquake. But this kind of wave may be studied for different purposes; for instance, to process signals in communication systems (Kino and Shaw, 1972) and, as described in this thesis, for damage detection via AE.

Rayleigh waves are a simple case of guided waves. They are confined to within a wavelength or so of the surface[4] along which they propagate and contain both longitudinal and shear displacements so that the particle displacement is ellipsoidal. Strictly the Rayleigh wave propagates only on the boundary between an isotropic solid and a vacuum. If the solid is bounded by a fluid the properties of the interface wave may change significantly, and if the boundary is between two solids the conditions become very complex (Silk, 1984). In Rayleigh waves, the longitudinal and shear motions are intimately coupled together and they travel at a common velocity.

2.5 Lamb waves

When the medium is bounded by two parallel plates, and the thickness of the medium is of the order of λ, the type of wave is termed *Lamb wave* (synonymous terms are *guided waves* and *plate waves*), which can be either symmetric or antisymmetric (Pollock, 1986). The model of Lamb waves has a key relevance in this work because it is the best useful approximation to the shape and boundary conditions of composite laminates and strips.

Lamb waves are the vibrations of an elastic plate of finite thickness imbedded in vacuum, corresponding to the eigenvalues of the wave equation.[5] Lamb waves always contain com-

[3]Rayleigh waves have a speed slightly lesser than that of shear waves: $V_{\text{Rayleigh}} \approx 0.9\sqrt{\frac{\mu}{\rho}}$ (Szilard, 1982a). However, it depends on the material. For the speed of Lamb waves, see page 23.

[4]The amplitude of surface waves decreases rapidly with depth; by one wavelength it is down to 0.37 times its maximum value.

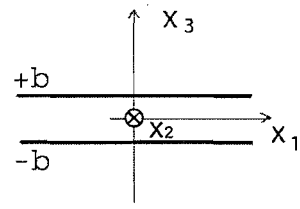

Figure 2.3: Schematic of the plate

ponents of the particle oscillation at right angles to the surface: this means that they can always be easily detected by the sensors commonly used in AE, usually not or little sensitive to in-plane oscillations. They occur in two different basic modes, symmetric and antisymmetric. The particles of the middle zone (the neutral axis, not in tension nor in extension) perform in the symmetric mode purely longitudinal oscillations, and in antisymmetric mode purely transverse oscillations.[6] The other particles oscillate, for both types, elliptically. For each kind there is an arbitrary number of harmonics which can be characterised briefly by the existence of more than one neutral fibre (Krautkrämer and Krautkrämer, 1983). Lamb waves are polarized in the sagittal (x_1x_3) plane,[7] with surface normal along x_3 (Fig. 2.3) and propagation along a thin plate in the x_1 direction. As long as the wave is plane and the motion does not depend on the coordinate x_2, the vector potential ψ has a non zero magnitude only in the direction of the x_2 axis.

The x_2 component of ϕ and ψ are represented in the following form:

$$\phi = A\cosh(k_{tl}x_3) + B\sinh(k_{tl}x_3) \tag{2.27}$$

$$\psi = D\sinh(k_{ts}x_3) + C\cosh(k_{ts}x_3) \tag{2.28}$$

The factor $e^{\imath(kx-\omega t)}$ is dropped for brevity, A, B, C, D are arbitrary constants, k is the Lamb wave number, $k_{tl} = \sqrt{k^2 - \frac{\omega^2}{V_L^2}}$ and $k_{ts} = \sqrt{k^2 - \frac{\omega^2}{V_T^2}}$ are the wave numbers for longitudinal and shear modes.

The eigenvibrations of an elastic plate in vacuum are obtained by solving the elastic wave equations subject to the conditions of free plate boundaries. This leads to Lamb's secular equation, whose eigenvalues (which are found to be real) may be taken as the phase

[5]These vibrations are sometimes called *eigenvibrations*.

[6]This theoretical description of the mechanics of the two different kinds of waves must not mean that these two modes can actually exist and be observed *separately*; on the opposite, they usually travel together.

[7]The plane which contains the wave vector and is normal to the boundary is termed sagittal plane; see Fig. 2.3.

velocities of the various Lamb wave modes propagating along the plane of the plate; they are obtained as functions of the frequency (Überall, 1973).

The expressions (2.27) and (2.28) satisfy the wave equations (2.18) and (2.19). Moreover, they must cause the stresses σ_{13} and σ_{33} on the planes $x_3 = \pm b$ to go to zero. Using Hooke's law and

$$u_1 = \frac{\partial \phi}{\partial x_1} + \frac{\partial \psi}{\partial x_3} \tag{2.29}$$

$$u_3 = \frac{\partial \phi}{\partial x_3} - \frac{\partial \psi}{\partial x_1} \tag{2.30}$$

the following is obtained

$$\sigma_{33} = \lambda_e \left(\frac{\partial^2 \phi}{\partial x_1^2} + \frac{\partial^2 \phi}{\partial x_3^2} \right) + 2\mu \left(\frac{\partial^2 \phi}{\partial x_3^2} + \frac{\partial^2 \psi}{\partial x_1 \partial x_3} \right) \tag{2.31}$$

$$\sigma_{13} = \mu \left(2\frac{\partial^2 \phi}{\partial x_1 \partial x_3} + \frac{\partial^2 \psi}{\partial x_1^2} - \frac{\partial^2 \psi}{\partial x_3^2} \right) \tag{2.32}$$

The boundary conditions lead to two characteristic equations for the determination of the eigenvalues of the wave number k:

$$(k^2 + k_{ts}^2)^2 \cosh(k_{tl} b) \sinh(k_{ts} b) - 4k^2 k_{tl} k_{ts} \sinh(k_{tl} b) \cosh(k_{ts} b) = 0 \tag{2.33}$$

$$(k^2 + k_{ts}^2)^2 \sinh(k_{tl} b) \cosh(k_{ts} b) - 4k^2 k_{tl} k_{ts} \cosh(k_{tl} b) \sinh(k_{ts} b) = 0 \tag{2.34}$$

For stress-free boundary conditions at the free surfaces, the potentials ϕ and ψ must be of opposite parity, so that

$$\phi = A \cosh(k_{tl} x_3 + \alpha) \tag{2.35}$$

$$\psi = D \sinh(k_{ts} x_3 + \alpha) \tag{2.36}$$

When $\alpha = 0$ to σ_{33} is even and σ_{13} is odd; and when $\alpha = \pi/2$, σ_{33} is odd and σ_{13} is even. Thus the displacement becomes, from (2.29) and (2.30):

$$u_1 = \imath k A \cosh(k_{tl} x_3 + \alpha) + k_{ts} D \cosh(k_{ts} x_3 + \alpha) \tag{2.37}$$

$$u_3 = k_{tl} A \sinh(k_{tl} x_3 + \alpha) - k D \sinh(k_{ts} x_3 + \alpha) \tag{2.38}$$

These solutions divide up into two groups according to whether $\alpha = 0$ or $\alpha = \pi/2$:

1. $\alpha = 0$: these are symmetric with respect to x_3

2. $\alpha = \pi/2$: these are antisymmetric with respect to x_3

In a plate of thickness 2b at a frequency ω there can exist a finite number of symmetrical and antisymmetrical Lamb waves (Fig. 2.4). The symmetrical modes occur on both sides of the meridian plane;[8] the longitudinal components are equal and the shear components have opposite signs. The antisymmetrical mode also occurs on both sides of the meridian plane, however the longitudinal component changes sign whereas the shear component does not. The number of symmetrical waves is determined by the number of real roots of (2.33), the number of antisymmetrical waves by the real roots of (2.34). For $\omega b \to 0$, (2.33) and (2.34) have only one root each. The root of equation (2.33) corresponds to the so-called zeroth symmetrical normal mode, designated S_0, while the root of (2.34) represents the zeroth antisymmetrical mode A_0. As ωb increases, their roots k_{S_0} and k_{A_0} vary in magnitude and for definite ratios between ω and b new roots appear, corresponding to the first, second, and higher symmetrical (S_1, S_2,...,S_n) and antisymmetrical (A_1, A_2,...,A_n) Lamb waves. The values of ω and b at which new roots appear are called the "critical" thicknesses and frequencies. The cutoffs of the symmetric and antisymmetric modes are given by the plate thickness corresponding to a half-integer number of wavelengths of longitudinal, and to an integer number of wavelengths of transverse waves, for the symmetric modes — and vice versa for the antisymmetric modes.

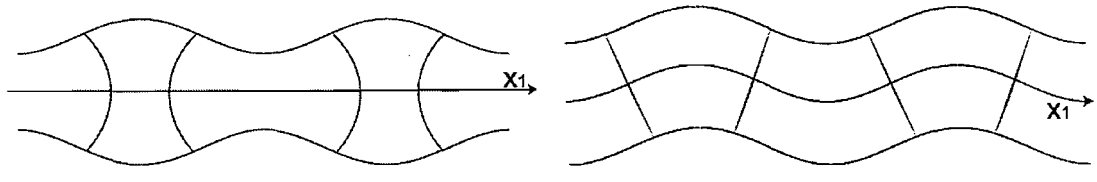

(a) Symmetric (b) Antisymmetric

Figure 2.4: Lamb waves

The simple physics of the S_0 and A_0 modes at low frequencies can be understood by considering the deformation of a thin sheet of paper. If it is gripped uniformly across the ends and stretched, this corresponds to an S_0 type deformation. There is evidently a high resistance to stretching. When the paper is bent, there is almost no resistance. This is a function of the modulus of elasticity.

[8]The middle or meridian plane is the x_1x_2 plane in Fig. 2.3

In composite panels and thin bodies in general, the elastic waves are Lamb waves. So, the AE applied to composite laminates deals with Lamb waves. If the body is thick, the waves will be different, but the surface-mounted AE sensors detect "surface waves". Both Rayleigh and Lamb waves, from a mathematical point of view, are solutions of the wave equation. Assuming that the body is thin, this signifies that the wave equation is simplified knowing that the problem becomes an eigenvalue problem, that its solutions are eigensolutions, and that these yield to eigenvibrations which are named Lamb waves.

The S_0 and A_0 modes of the Lamb waves are the most easily observable in AE measurements in thin plates. A typical acoustic emission signal generated by an out of plane deformation, such as a pencil lead break, will contain two separate components: extensional and flexural. The flexural mode has a much greater amplitude than the extensional mode because the emission is generated by an out-of-plane source motion (Fig. 2.5). The extensional mode travels faster: the flexural mode is highly dispersive with higher frequencies travelling at higher velocity, while the extensional mode suffers little dispersion except at high frequencies. Also, the attenuation of the extensional mode is less than that of the flexural mode, and only slightly dependent on the plate thickness (Prosser, 1996). In a sense, then, a transient recording of the waveforms is deceiving, inasmuch it portrays the emissions as they were from a continuous event.

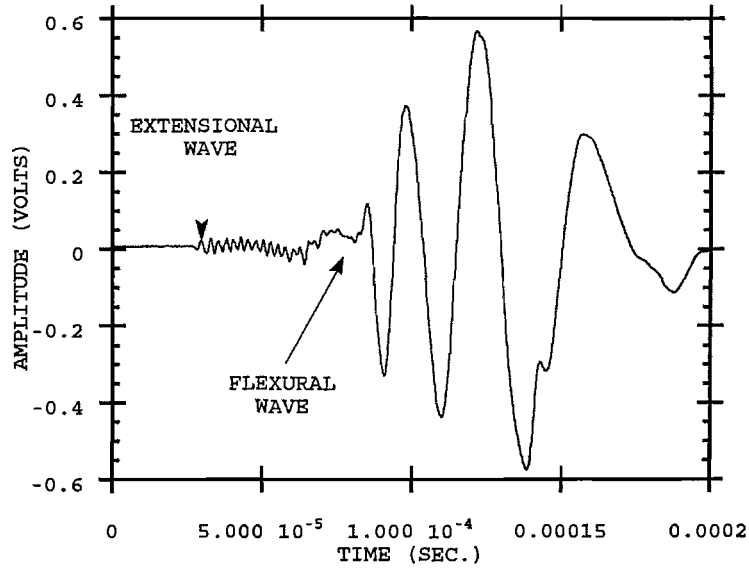

Figure 2.5: Typical waveform detected on graphite/epoxy tube from lead break source on surface of tube. Source to receive distance is 0.1524 meters. From Prosser *et al.* (1992)

2.6 Dispersion

A very generic equation for a wave can be of the form:

$$Y = A_0 \sin(\omega t - kx) \tag{2.39}$$

where A_0 is the amplitude, ω is the frequency in rad/s, and k is 2π over the wavelength λ. The frequency, wavelength and wave velocity v are related by:

$$v = \lambda\omega \tag{2.40}$$

This wave velocity is known as the phase velocity, at which the waves travel through the medium. In general, acoustic waves propagating through solids have a multiple frequency. In bounded media the phase velocity is a function of frequency. Therefore different frequencies propagate at different speeds; this is called dispersion. Dispersion has little effect on continuous waves; however, acoustic emissions are packets of waves (see §3.8) which can be thought of as a superposition of continuous waves of different frequency. If each wave train making up the packet travels at a different velocity, *the wave packet will change as it travels through the medium.* The result is that the same acoustic emission produces a different response when detected in different positions.

For Lamb waves the velocity cannot be found as easily as for longitudinal and transverse waves. It depends not only on the elastic constants of the material, but also on the plate thickness and on the frequency. The symmetric mode (S_0) generally travels at the highest velocity and is non-dispersive in nature, meaning that all frequency components of this mode travel at the same velocity. The antisymmetric mode (A_0) travels at a lower velocity and is dispersive with the square root of frequency, meaning that the higher frequency components propagate faster than the lower frequency components. In practice, this will lead to a gradual decrease in the amplitude of A_0 as it propagates, owing to the spatial separation of the different frequency components (Surgeon and Wevers, 1999). This aspect, anticipated in §2.3 for an ideal solid, has a very important technical relevance, the consequences thereof will be examined in §7.3.

The values of the group velocities for the different Lamb modes are generally given in *dispersion curves* such as those in Fig. 2.6, presented as a plot of group velocity versus the

frequency×thickness product of the structure. These curves can be simulated with dedicated

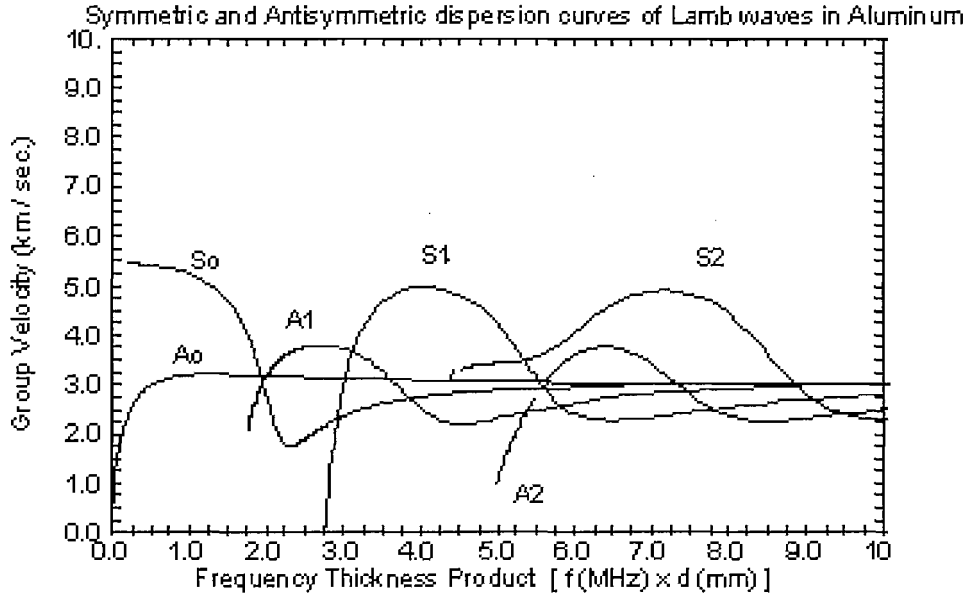

Figure 2.6: Group velocities (dispersion curves) for aluminium (Chahbaz *et al.*, 1996)

software. Although the numerical values presented in Fig. 2.6 do not coincide exactly with those of a composite laminate, that must be calculated accordingly to its specific geometry and layup, they are explicative of their technical relevance. For example, the graph would suggest that for values of 1 MHz mm or below, only the S_0 and A_0 modes are observed. The same actually happens for composite laminates, where the frequencies detected by the sensors never exceed 1 MHz and the thickness are around 1 mm, and so the higher modes are not observed. The graph also indicates that the symmetric mode is much faster and so it would arrive at the sensor before the antisymmetric one; nevertheless, the AE system can be triggered by the antisymmetric mode, if it happens that the symmetric mode has a too low amplitude, below the triggering threshold.

2.7 Attenuation of Lamb waves

During the propagation of a wave through a solid from its source, it can suffer attenuation from a number of mechanisms, such as dislocation damping, internal friction, deformation hysteresis, relaxation and micro-creep. The intensity of an ultrasonic wave decreases as the distance from the source increases. It is evident that the attenuation undergone by the wave system generated by the dynamic disturbance will affect the wave form of the source signal.

The higher frequencies will be most affected.

The attenuation of plane waves arises from (Blitz, 1963; Prosser, 1996):

1. deviation of energy from the parallel beam by reflection, refraction, diffraction and scattering,
2. absorption, for which mechanical energy is converted into heat by internal friction,
3. geometric spreading of the wave,
4. internal friction,
5. dissipation of the wave into adjacent media,
6. losses related to velocity dispersion.

In a homogeneous medium, these losses usually occur as a fixed percentage of the wave packet energy per unit length of travel. Mathematically this is an exponential decrease in the wave amplitude with distance and can be expressed as

$$A = A_0 \exp(-\alpha x) = A_0 \exp(-\beta t) \tag{2.41}$$

where α is an attenuation constant per unit length and β is an attenuation constant per unit time. The two constants are related by the acoustic velocity

$$\beta = \alpha v \tag{2.42}$$

In fact, since the relative motions of the particles in these waves are different, the elastic constants and therefore the wave velocities also differ. Usually the shear velocity is slightly greater than one half of the longitudinal velocity. But generally waves have both shear and longitudinal components, each travelling at their own velocity, so that in an ideal nonattenuating, nondispersive medium, a transient wave, detected at some distance from its point of origin, may appear to be two separate waves, one longitudinal and one shear. In a real material, this just means that *a waveform may appear different according to the distance it travelled before the detection.* This of course poses a serious problem for a characterisation.

For two dimensional wave propagation in geometries such as plates, the amplitude decrease due to geometric spreading (point 3 in §2.7) is inversely proportional to the square

root of the distance of propagation. In few centimeters of propagation the attenuation can be large enough so that some weak events detected by one sensor may not be detected by another one, further from the source.

The largest component of the flexural mode particle displacement is out of the plane of the plate, while a source motion with predominantly in-plane components and symmetric about the midplane generates acoustic emissions with large symmetric modes components. Moreover, out of plane source motion such as delamination or impact damage produces acoustic emissions with large antisymmetric mode components, and this knowledge is useful to discriminate acoustic signatures. In fact, in composites, fibre breaks excite preferentially the symmetric mode associated with AE signals of high amplitude, whereas matrix fractures rather excite the antisymmetric undulatory mode and the low amplitudes (Frederick, 1965; Prosser, 1998).

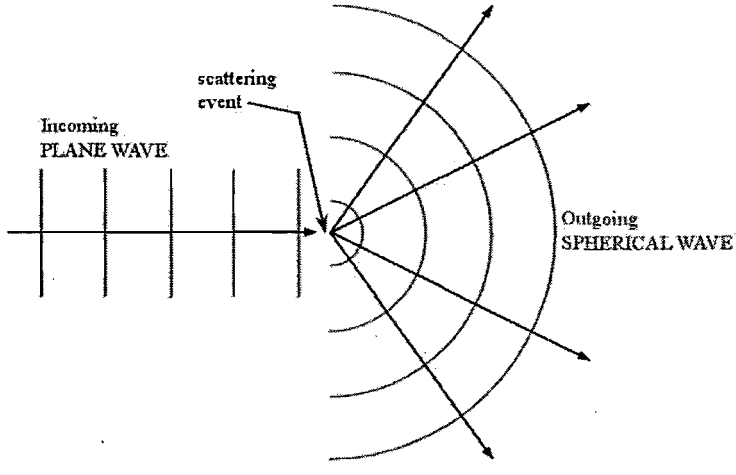

Figure 2.7: Schematic of scattering of waves

Losses due to reflection, refraction and diffraction depend on the geometrical configuration of the system, but scattering losses are caused by the structure of the material. Although the physical mechanism is the same, while on a smooth boundary losses result from reflection, on the other hand on a rough boundary it is the scattering which deviates the waves. The loss from scattering at interior grain boundaries (or other internal irregularities) can be significant (Fig. 2.7). The interaction wave/irregularity is dominated by the relative dimensions wavelength/scattering element, so scattering is strongly frequency dependent, and thus a short pulse, with its inherent frequency band, will suffer an appreciable distortion during transmission. The existence of a difference of acoustic impedance on the two sides of

a boundary will give rise to a reflected wave and, furthermore, if the boundary is inclined to the wave direction, some mode conversion between longitudinal and transverse waves can occur.

Relaxation absorption can be described by considering a sound wave passing through a medium. During the positive half of the stress cycle energy is absorbed, and during the negative half of the cycle energy is given up. A finite period of time is required for this exchange of energy to take place. A simple case is that due to thermal conduction; here the flow of energy takes place from regions under compression at higher temperatures to those which have expanded and are consequently at lower temperatures. As the frequency increases the wavelength diminishes; the temperature gradients are thus increased and the rate of flow of heat from a compressed region to the next rarefied one becomes greater: this contributes towards increasing the entropy of the system and thus gives rise to energy losses.

2.8 Anisotropy and inhomogeneity

Understanding the propagation of elastic waves through inhomogeneous, anisotropic media and the scattering caused by the inhomogeneities is of potential benefit in several engineering fields. The mathematical complexity of the phenomenon, though, only allows a numerical treatment, always limited to single cases, where the inhomogeneities have a well specified form (for example, inclusions in austenitic steels) and the anisotropy has an "easy" directionality or symmetry.

Although no real material can be considered perfectly homogeneous, this approximation usually holds well for many cases (for example, ferritic steels); nevertheless, even in such cases, the presence of cracks or defects is itself an important source of inhomogeneity (Temple, 1988).

The case of composites is fairly complicated and not prone to be modelled in closed form. Apart from the strong anisotropy, that change with each single lay-up, the numerous inclusions (the fibres) generate complex scattering at inhomogeneities, greatly complex as the large number of relevant published papers bear witness.

The information contained in this chapter cannot have a direct and quantitative correspondence in the real world of composites, but they can explain concepts and describe them so that a similar qualitative trend can be expected in the AE testing of composite laminates.

2.9 Summary

§2.1 provided an explanation of the basic types of waves existing in a solid, and the waves of interest for AE. §2.2 explained the main parameters for describing the mechanical properties of a solid, as well as stress and strain relations. §2.3 provided the wave equation in three dimensions and its simplest solutions for longitudinal and transverse waves. A particular case is represented by the surface waves which are described in §2.4, and a particular case, the Lamb waves, is presented in more detail in §2.5. §2.6 illustrates the role of phase speed and of frequency in these waves. §2.7 is an introduction to the modifications that elastic waves must face when travelling through a real, non-idealized body, and finally §2.8 comments on the applicability of this theory to inhomogeneous and anisotropic media.

The information contained in this chapter will not be used directly to generate a mathematical model of the structures tested: the complexity of the equations themselves and the issues about inhomogeneity and anisotropy have suggested that this approach would not have a practical feasibility. The most immediate applicability of the theory just reviewed will become evident in the experimental chapters, where the concepts of modal separation and dispersion will be put to work to explain and interpret the differences in the recorded signals that are encountered when the positions and the distances in the experimental setup change. Dispersion and attenuation together will be shown to have a determinant effect on the very same concept of characterisation, in such it will be inevitably linked to the subjectivity introduced by the positions, distances, and times adopted.

CHAPTER

THREE

Acoustic Emission

Be not afeard: the isle is full of noises,
Sounds and sweet airs, that give delight, and hurt not.
William Shakespeare, The Tempest

Nondestructive Testing and Evaluation (NDT&E) techniques can potentially detect any defects present in a material, but without damaging or disturbing the material or the structure in any way. AE is a well established NDT&E tool, but has the peculiarity of needing to load the structure examined; for this reason, it is mainly used for continuous monitoring purposes. In fact, a significant difference between AE and other nondestructive evaluation (NDE) methods is that AE detects the *activities* inside the materials, while other NDE methods attempt to examine the internal structures of the materials.

AE has been widely used in industry (Drouillard, 1996; Holroyd, 2000). AE has also been widely researched in the past and at present has received much attention because of the increase in available computing power. It was not until the 1970's (Fuwa *et al.*, 1976) that a significant amount of work on the application of AE to composites began to appear in the literature.

AE works by detecting the acoustic emissions of a failing material. On a physical level, the proportion of energy that is released as elastic waves rather than as heat, when a micro failure occurs in a material, depends on the nature of the source, how localised it is and how rapidly the release takes place. An acoustic emission is associated with the local redistributions of

material, and consequently of energy. Localised, rapid energy releases give rise to elastic waves in the ultrasonic frequency regime that will behave as illustrated in §2 and can be detected by transducers attached to the surface of the specimen, provided the waves are of sufficient amplitude. The release of energy may be very small, and range in scale from the transient wave launched by the advancement of a subcritical crack, to material readjustment (Tatro, 1976). These same abrupt phenomena that generate the acoustic emissions may additionally excite the natural vibrational modes of the structure; this may be a problem if the size and rigidity of the structure lead to proper modes that are of high frequencies comparable to those typically investigated in AE.

AE is based on the detection of surface deformations caused by stress waves generated by fracture processes on a microscopic scale, using piezoelectric transducers. In ultrasonic testing an acoustic signature is input into a structure, and defects are detected by using a sensor that monitors the propagation of the wave around the defect; in AE the material must be undergoing a process for damage to be detectable. Therefore in AE the structure is "active" and the detection system "passive". Conversely in ultrasonic monitoring the structure is "passive" and the detection system is "active". Therefore, AE can be used to *continuously monitor* structural activity. An important aspect of AE is the "Kaiser effect", i.e. the absence of detectable acoustic emission at a fixed sensitivity level, until previously applied stress levels are exceeded.

In practice, AE generally falls within one of the following three categories:

- structural testing and surveillance;
- process monitoring and control;
- materials characterisation and testing.

Since its inception in the late 1960s, applications of AE have broadened to include the monitoring of various materials processes, and the list of the potential AE source events has grown in the past decades. In 1987 they were summarised by Scruby as follows:

(i) Materials degradation: defect growth, crack advance, plastic deformation, inclusion or precipitate fracture, surface degradation including corrosion and disbonding of coatings.

(ii) Reversible processes: crystallographic phase transformations, melting or solidification,

thermoelastic effects, ferromagnetic and ferroelectric domain wall motion, friction between surfaces.

(iii) Fabrication processes: welding noise, rolling, forging, machining, drilling, mixing, grinding, valve sequencing.

(iv) Leak and flow: flow of single- and two-phase fluids and particles, leaks, gas evolution, boiling.

The AE technique procedures have been standardised in several documents of the British Standard, that explain their general principles (BSI, 2002), the equipment description and characterisation (BSI, 2001a,b), the application for proof testing pressurised metal vessels (BSI, 2006), etc. More specific aspects, such as the AE testing of small components (ASTM, 1998) and the sensor response (ASTM, 2007) are also covered by ASTM standards.

3.1 Sensors

The single most important factor in AE testing is probably the selection of an AE sensor (transducer). Their main characteristics, as well as those of the other system components, are described in a British Standard (BSI, 2001a).

In order to detect AE events, a transducer or sensor is required to convert very small surface displacements (of the order of pm) into electrical signals that can be amplified and recorded. These transducers make use of the piezoelectric effect. Piezoelectricity is the ability of certain crystals to generate a voltage in response to applied mechanical stress. In a piezoelectric crystal, the positive and negative electrical charges are separated, but symmetrically distributed, so that the crystal overall is electrically neutral. In AE the elastic waves cause a surface deformation which in turn deforms the crystal. This deformation results in a charge which is a function of the applied force. In its operating region, a greater force will result in more surface charge. This charge results in a voltage $V = Q_f/C$, where Q_f is the charge resulting from a force f, and C is the capacitance of the device. These sensors detect a combination of wave types: compressional, shear, surface (Rayleigh), plate (Lamb), arriving from any direction.

After the sensing element produces a desirable output, this signal must be conditioned prior to being analyzed. The raw signal processing can be accomplished by two different methods: internal to the sensor by a microelectronic circuit or external to the sensor. These

analogue processing circuits serve the same general functions of (i) conversion to a useful, low impedance, voltage signal, (ii) signal amplification and attenuation, and (iii) filtering.

From a practical point of view, it is very useful if the sensors have built-in microelectronics, which produce a low impedance, voltage signal compatible with most readout equipment, capable of being transmitted over long cables through harsh environments with no loss in signal quality. Sensors with the signal processing electronics placed externally are usually referred to as "charge mode" sensors. They output a high impedance signal which requires conditioning prior to being analyzed and has the potential to be contaminated by environmental influences such as cable movement, electro-magnetic signals and radio frequency interference.

The first AE systems used resonant transducers, having a resonant peak in the frequency range of 150-500 kHz. The rapid development of computers with increasing speed and extended memory capacity have, however, enabled digital acquisition using broad-band transducers.[1] These transducers are sensitive in a wider frequency range, typically from 50 kHz up to 1.5 MHz, but not necessarily have high-fidelity (i.e. a flat characteristic curve).

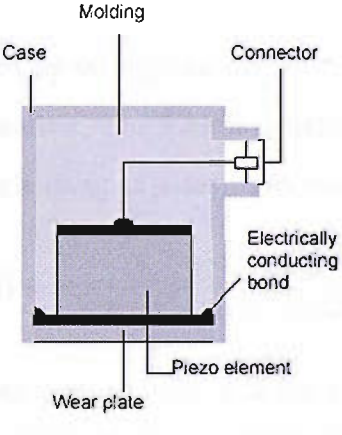

Figure 3.1: Schematic of a typical AE sensor (NDTRC, 2007)

The specific type of sensor used in an application, whether resonant or wide-band, would depend on the type of information desired from a test. Resonant sensors have the advantage of being more sensitive and are thus used when detection and quantification of AE activity is the primary objective. Broad-band sensors detect a wider range of signal frequencies and are therefore more accurate in reproducing the actual signal; they are advantageous when performing characterisation studies to identify different AE source mechanisms.

[1] "Broad-band" and "wide-band" are synonymous terms that can be used interchangeably.

It is normally convenient to employ a resonant transducer to improve sensitivity: because of the low level of the acoustic signals involved, it is conventional to use undamped piezoelectric transducers to detect the acoustic emissions. Most piezoelectric transducers (Fig. 3.1), as used for AE measurement, have the sensing element in the form of a disc of the piezoelectric material, which is usually lead zirconate titanate (PZT). If the disc is unbacked and undamped in any way, it acts as a resonator for incident and elastic waves so that the output voltage is typically a decaying sinusoid, the principal frequency of which is determined by the thickness of the element. Such resonant peaks may be very strong. Backing the element with an attenuating medium produces a heavily damped transducer with a more broad-band response.

The basic theory underlying the design of acoustic emission sensors is the single-degree-of-freedom (SDOF) vibration theory, where a vibratory force is applied to a simple mass, spring, and damper system. The frequency response function (FRF) results from the solution of the differential equation of motion for the SDOF system. This equation is obtained by setting the sum of forces acting on the mass equal to the product of mass times acceleration. The FRF results from the solution of the differential equation of motion for the SDOF system. This equation is obtained by setting the sum of forces acting on the mass equal to the product of mass times acceleration. The FRF is usually indicated by the notation $h(\omega)$ and, for a simple case of of a single damped mass, is expressed by:

$$h(\omega) = \frac{(1-\beta^2) - 2\imath\zeta\beta}{-m\omega_r^2[(1-\beta^2)^2 + 4\zeta^2\beta^2]} \tag{3.1}$$

where ω is the circular frequency (radians/s), m is the system mass, ω_r is the resonant frequency, $\beta = \omega/\omega_r$, ζ is the damping factor. An FRF of such a simple case usually looks like in Fig. 3.2. The process of obtaining a non-resonant, wideband sensor can be exemplified by the superimposition of several peaked FRFs, by adding backing masses. Schematically, the resultant FRF looks like in Fig. 3.3.

Resonant sensors are used in a wide range of practical applications and broad-band sensors are employed more in research activity. This usually happens because industrial applications include well known and specific cases (e.g. pressurized vessels, bridges) where the acoustic emission footprint ranges within relatively narrow bands of frequencies; this not only increases the sensitivity to the useful signals, but also greatly reduces the inconvenience

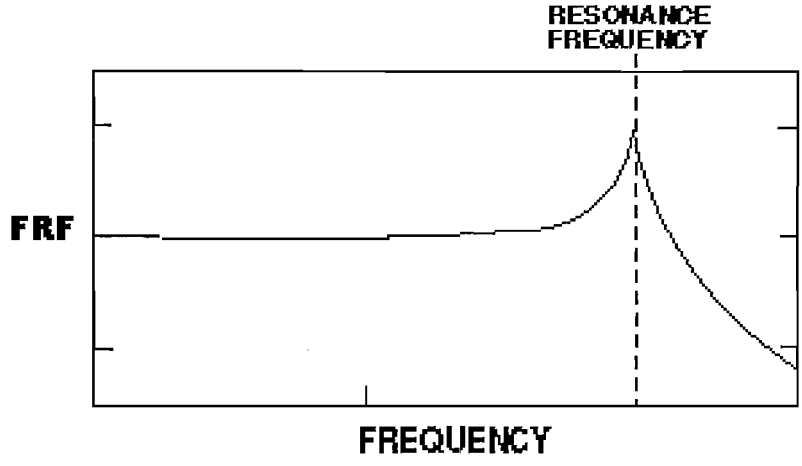

Figure 3.2: Simple frequency response function

of picking up extraneous noise, which possibly falls in a different frequency band. However, this trend is today more blurred than yesterday, because the higher computational power available means that the signals can be conveniently post-processed to exclude noise. The frequencies chosen for most resonant AE transducers lie in the range 100 kHz to 1 MHz. The impulsive nature of the acoustic emissions means that a "burst" signal is produced by the transducer which is the convolution of the acoustic pulse frequency spectrum and the transducer transfer function: all this results in a strong distortion of the recorded signal.

The physical size of the sensor has some importance because it can lead to two main effects. The first is resonance and the second is averaging. Both can become important when the physical dimensions of the sensor approach or exceed the wavelength of the acoustic wave.

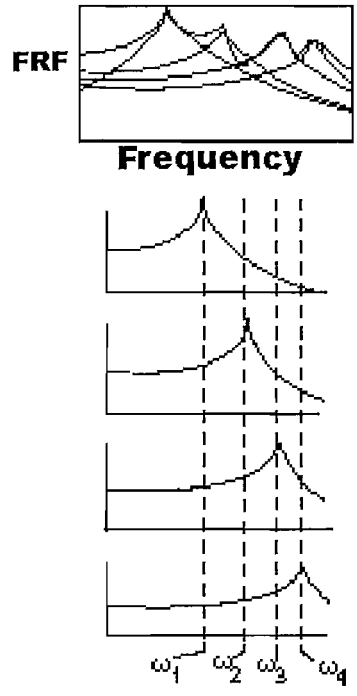

Figure 3.3: Effect of backing masses on the FRF: ω_{1--4} are the individual resonant frequencies (adapted from Coleman, 2006)

3.2 Couplants

When the sensor is simply placed on the surface of the material containing the acoustic wave, it is found that the sensor produces a very weak signal. If a thin layer of a fluid is placed between the sensor and the surface, a much larger signal is obtained.[2] Physically, this can be explained by considering the acoustic wave as a pressure wave transmitted across two surfaces in contact. On a microscopic scale, the surfaces of the sensor and the material are quite rough so that only a few spots actually touch. Stress is force per unit area and the actual area transmitting the force is very small. If the microscopic gaps are filled with a fluid, the pressure will be uniformly transferred between the surfaces. Filling the gaps with a low viscosity liquid will not help much since it will not support a shear stress. However, a high viscosity liquid or a solid will help transmit the parallel strain between the surfaces. On the other hand, for a compressional wave, any fluid will act as a couplant. Vaseline is a common and convenient choice.

[2]Incidentally, this adds to the relativeness of some AE features discussed in more detail in §4.1.

3.3 Preamplifiers

In conjunction with the piezoelectric sensors, preamplifiers must be used before the signal is conveyed to the rest of the system. According to the type of the sensor, and to whether it has or not an integrated circuit, the preamplifiers can be either voltage or charge amplifiers.

The purpose of a charge preamplifier is to convert the extremely high output impedance of the sensor to a low value suitable for transmitting the signal over cables to other signal processing instruments. The charge amplifier is sensitive to the amount of electric charge generated by the sensor rather than the voltage the sensor generates. Because the charge is independent of the cable attached to the sensor, the sensitivity of the sensor does not vary with cable length as it does when using a voltage amplifier. When connecting a sensor to an external charge amplifier, low capacitance cables should be used and mounted to minimize vibration pickup by the cables.

Many of the AE sensors with built-in preamplifiers were originally designed for the traditional applications of non-destructive material testing, and may not be suitable for use in some applications, like metal cutting, as the signals originating can be considerably strong; Jemielniak (2001) reports about some aspects of AE signal pre-processing.

3.4 Definitions of AE terminology

The following are some AE definitions largely used in this report. A larger listing of AE terms and definitions can be found in the British Standards (BSI, 2000). Fig. 3.4 shows an idealized AE waveform; the following description of the terminology focuses on this figure.

Amplitude The maximum peak in the AE signal waveform, expressed usually in dB.

Burst A qualitative description of the discrete signal related to an *individual* emission event occurring within the material. The terms AE event and AE burst are often used interchangeably; however, the distinction is apparent with large structures, where a single event can give rise to a number of *discernible* bursts due to large differences in propagation times between different paths and wave modes.

Count The number of times the oscillatory AE signal exceeds a pre-set threshold level. Also known as "ring down counts".

Duration The time a single-hit signal exceeds the threshold level.

Event A *single* source occurrence (micro-displacement, material change) giving rise to acoustic emission.

Hit In multi-channel event based AE systems, a hit is the detection and measurement of an AE signal on a channel.

Hit definition time (HDT) The function of the HDT is to enable the system to determine the end of the hit, close out the measurement process and store the measured attributes of the signal as belonging to one hit. If the HDT is too short, the end of hit is defined prematurely, and results in the remaining part of the waveform being recorded as separate hits. If the HDT is too long, there is the risk that two separate hits will be treated as a single hit. Basically, the hit ends HDT after the last passing of the threshold.

Hit lockout time (HLT) Only after the HLT the system is rearmed for the next hit.

Peak definition time (PDT) The system identifies in the waveform a local maximum as the global maximum (peak) within this time range. If it is too short, the system is not allowed to wait further for a potential higher peak which comes later.

Rise time The time from an AE signal's first threshold crossing to its peak.

Source The small region of the material the elastic waves emanate from.

Threshold level A reference voltage level which the AE signal is compared with in order to determine whether or not the signal magnitude exceeds it. Setting a threshold is necessary in order to filter out weak signals. They could either be "noise" (i.e. events not coming from damages in the structure) or real damage events, but too weak and then insignificant, and susceptible to overflow the digital acquisition system.

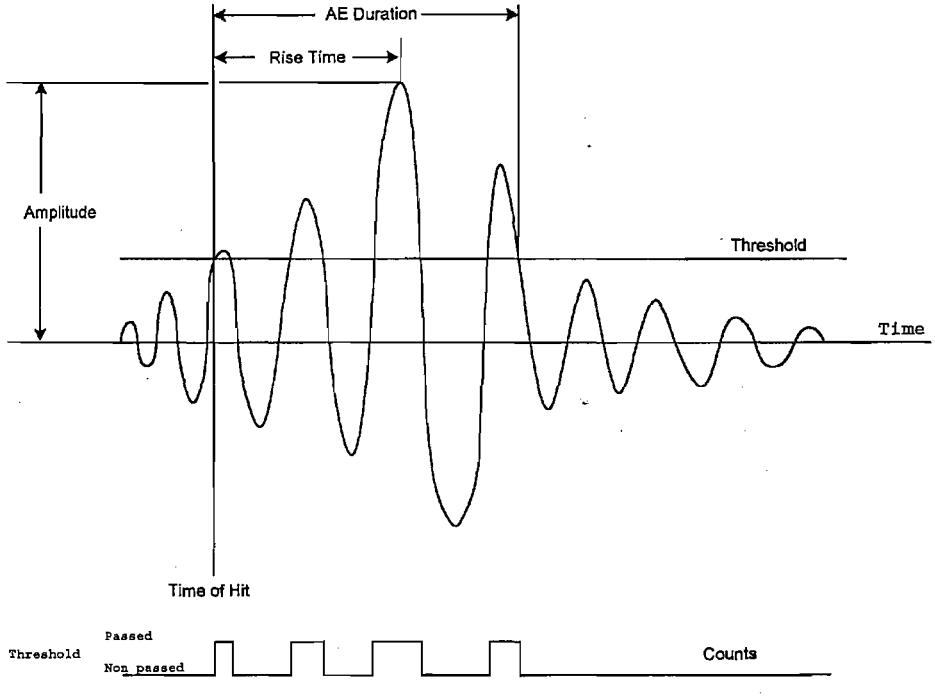

Figure 3.4: An idealized AE waveform for a single "hit" (PAC, 2003)

3.5 A generic AE system

A schematic of an acoustic emission and its detection is represented in Fig. 3.5. The process chain basically consists of the following links:

(i) **Testing of object and application of load** to produce mechanical tensions and eventually damage. A peculiarity of AE is that a load must be applied to the component so that some damage occurs.

(ii) **Release of elastic energy** Part of the energy due to the failure of of the material is released as heat, part as elastic waves.

(iii) **Wave propagation from the source to the sensor** The waves travel through the material (as Lamb waves in thin specimens, as described in chapter 2) and undergo strong modifications, reflections, damping, dispersion.

(iv) **Sensing** Converting a mechanical wave into an electrical AE signal using piezoelectric transducers.

(v) **Amplification** Increasing the voltage output, by converting the high-impedance output of the sensor to a low impedance suitable for transmitting the signal over cables to the acquiring system.

(vi) **Filtering** Providing the flexibility to optimize sensor selectivity and noise rejection.

(vii) **Acquisition of measurement data** Converting the electrical AE signal (voltage, analogue) into an electronic data set (digital). The signal voltage is first squared, and then the area under the curve of voltage squared against time is measured. This area is proportional to the signal energy with the constants of proportionality being the amplifier gain and input impedance. In addition, so-called parametric channels or inputs measure the environmental conditions as well as the external load as reference parameters for the detected AE. One of the very important tasks of an AE systems is to convert the AE bursts into compact data sets and to eliminate the background noise (which is more or less continuous). For this, modern AE systems use detection thresholds.

(viii) **Display of measured data** Typically the user can choose from a wide variety of combinations of independent parameters/features (such as duration, counts, hit amplitude), in order to visualize a meaningful trend in the process.

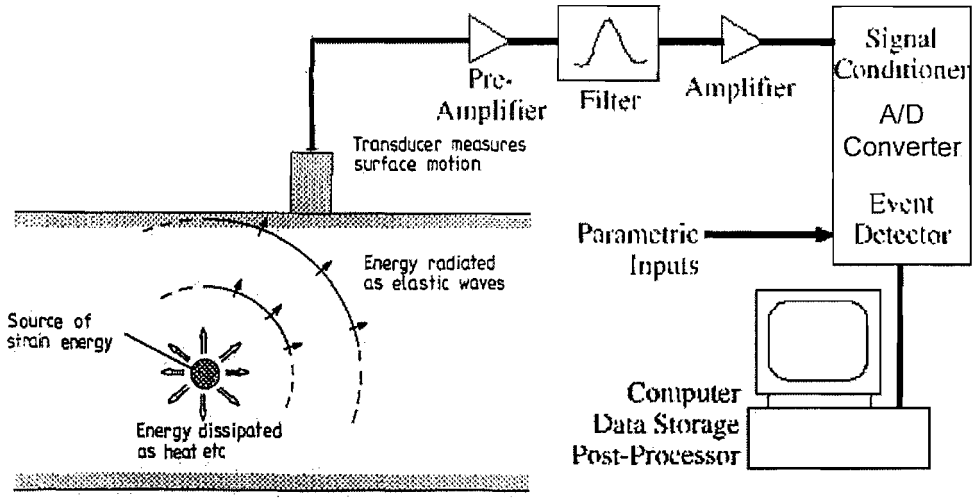

Figure 3.5: Schematic set-up of AE sensing

3.6 System sensitivity check

There is often the necessity to simulate in a simple way a repeatable AE source. A Hsu-Nielsen source consists of a pencil lead break (Nielsen, 1980) (Fig. 3.6) that works as an aid to simulate an acoustic emission event using the fracture of a brittle graphite lead in a suitable fitting. This test consists of breaking a 0.5 mm (alternatively 0.3 mm) diameter pencil lead approximately 2–3 mm (±0.5mm) from its tip by pressing it against the surface of the piece. This generates an intense acoustic signal, quite similar to a natural AE source, that the sensors detect as a strong burst. The purpose of this test is twofold. First, it ensures that the transducers are in good acoustic contact with the part being monitored. Generally, the lead breaks should register amplitudes of at least 80 dB for a reference voltage of 1 mV and a total system gain of 80 dB. Second, it checks the accuracy of the source location setup. This last purpose involves indirectly determining the actual value of the acoustic wave speed for the object being monitored. The topic of reproducibility is covered by a British Standard (BSI, 2001b) and an ASTM Standard (ASTM, 2007), whereas that of calibration in an ASTM Standard (ASTM, 2002).

It must be mentioned that the standard calibration carried out with the Hsu-Nielsen source is *not a proper calibration:* as Jones and Yan (2005) observe, the detected AE signals are significantly affected by the positioning of the sensor on a structure and by the variability of the sensor-structure interface, resulting in AE measurements with poor repeatability, since all that is actually measured is the voltage of the AE sensor system output, whereas what is desired is the measurement of the actual AE source.

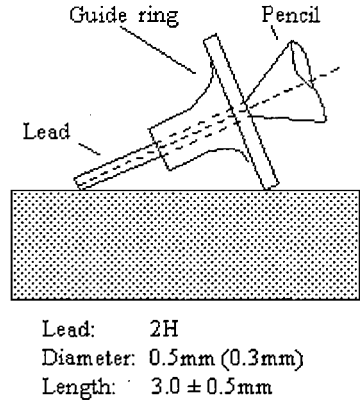

Figure 3.6: Hsu-Nielsen source (NDT.net, 2007)

3.7 Data analysis

Several main types of AE data analysis have been extensively explored so far: activity analysis, feature analysis, frequency analysis, modal analysis.

An **activity analysis** focuses on measuring the amount of AE signals produced by a specimen or a structure. It primarily results in information about the initiation and the evolution of damage throughout a test or during the service life of a component. Its purpose is the health monitoring of a structure.

A **feature analysis** makes use of signal parameters like ring down counts, amplitude, energy and duration. During the first two decades of instrumented AE testing, AE activity was measured mainly by counting the number of times an oscillating signal exceeded a preset threshold. Ringdown counts were correlated to load, strain, fatigue cycles, stress intensity factors and other measurable parameters to get an understanding of how damaged materials emit acoustic emissions. Other AE parameters such as RMS voltage and amplitude were also used in characterising material failures.

A valid alternative can be an **AE frequency analysis.** This uses Fast Fourier Transform (FFT) techniques to calculate the frequency spectrum of AE waves and uses the frequency spectra of AE waves for discrimination purposes, based on the assumption that different damage phenomena will produce signals with different frequency contents. Although the signal delivered by the sensor is a strongly modified representation of the original source, it is realistic to consider that this signal contains some features representative of the source in such a manner that direct correlation exists between the damage mechanisms and the magnitude of the various AE parameters. Consequently, each signal may be considered as the acoustic signature of the different damage modes.

Modal analysis is a waveform based AE. This works on the assumption that, in thin plates, the two observed modes of propagation in AE signals are the symmetric and antisymmetric plate modes (lowest orders symmetric S_0 and antisymmetric A_0 Lamb modes respectively; Dunegan, 1997), and can then be considered separately (see §2.7). Usually, considering the waveforms as formed by two different components can lead to a more sophisticated analysis (Prosser, 1998; Surgeon and Wevers, 1999).

3.8 A physical model

A good physical working model of AE is presented by Beattie (1983) in his review. All real materials are inhomogeneous on a microscopic scale. A real metal is composed of crystallites with random orientations and a range of sizes, and possibly of various phases and compositions. When a fracture occurs, to allow for a reduced stress field, the stress will propagate away as an acoustic wave; the amplitude, directionality and polarisation thereof will depend both upon the size and orientation of the crystallites. An important point in this model is that the acoustic emission is produced by the fracture of *individual* crystallites and therefore occurs in the form of *discrete* packets of acoustic waves. These two characteristics, discrete packets of acoustic energy with no correlation either in time or in the characteristics of the packets, are the fundamental nature of acoustic emission. As such they are the reason for *the primarily statistical approach of AE analysis.*

The discrete packets of acoustic energy are known as *burst emission* and their lack of correlation in time precludes the concept of a repetition rate, or frequency. However, it is possible to define an *average* repetition rate as the average rate of occurrence of the bursts

over some period of time. These frequencies differ widely for different systems. While for earthquakes the lowest measured rates are at a century apart on a given fault, the highest measurable rate is around 50 kHz (so, usually below the sensitivity of common AE sensors). Above 50 kHz, the length of the bursts usually exceeds the time interval between them, and the superposition of the bursts produces continuous occurring acoustic waves which are called *continuous emission.* In most AE systems the sampling rate is not high enough so that it is only possible to detect continuous emissions and not the single bursts. All this means that what the AE systems can detect as continuous acoustic signal, is not physically continuous. A real acoustic signal, similar to continuous emission, is produced by a gas or a fluid passing through a small opening (of course, a fluid is not made of crystallites).

3.9 Localisation capabilities

The determination of the source location of each event is an essential element of AE testing. AE has inherited more than just one aspect from seismography: apart from the surface waves, which were studied for the first time with respect to wave propagation in the earth's crust (the Rayleigh waves), the damage location works with the principle of triangulation, which is the same technique used to determine the epicentre of an earthquake (Fig. 3.7a) calculating the travelling distances from the arrival times.

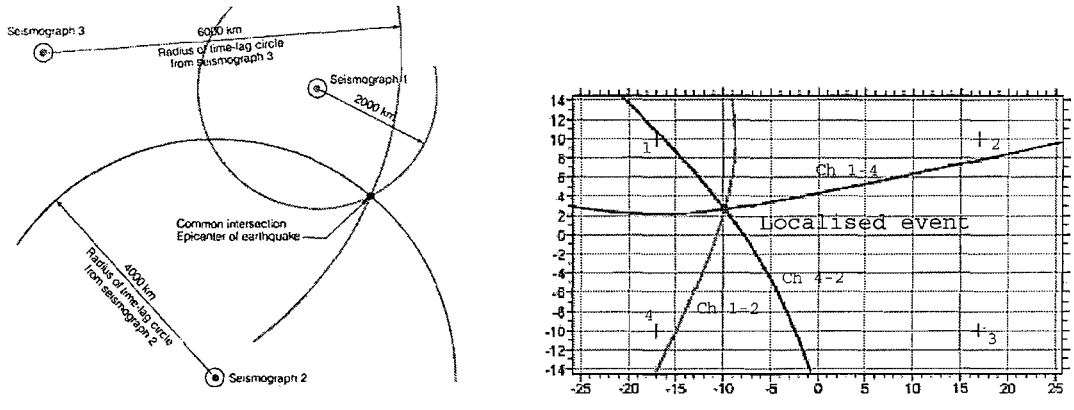

(a) Triangulation for an earthquake: the radii are computed from the arrival time

(b) Hyperbolae intersecting

Figure 3.7: Triangulation for an earthquake and intersection of the hyperbolae for AE

All points having a constant difference between their distances to two fixed generic points form a hyperbola. Fig. 3.7b is an example where a signal arrives only at three out of four sensors. The hyperbolae represent here the loci of the points equidistant from two sources,

i.e. the intersections of the circles represented in Fig. 3.7a. Three hyperbolae are plotted, each representing all the points having the distance difference to two given sensors (for example, "Ch 1-4" is the locus of the intersections of the circles centered in sensors 1 and 4). At the point of intersection of the three hyperbolae, the three distance differences are equivalent to the measured time differences. So, this identifies the source position. As can be seen in this example, the arrival time at three sensors is required to find the point of intersection in a plane. If an AE event only arrives at two sensors, there is only one couple of sensors and, thus, only one hyperbola, which is not sufficient for this method to calculate the planar location (Vallen, 2002).

The distance difference between a source and different sensors are equal to Arrival Time Difference $\times$ Wave Velocity.[3] The computing of the location is based on the evaluation of the differences in the arrival times of the AE signals propagating from their sources to the sensors (two at least for a linear case; Pollock 1976). In isotropic media, an AE wave propagates in concentric circles from its source and arrives at different sensors with certain delays. The delays are proportional to the distance between the sensor and the source. Unfortunately, this is not perfectly true with inhomogeneous materials, like composites; this is examined in §4.5.

3.10 Noise interference in AE

Two types of noise exist in AE: electrical noise, which does not involve sensor response, and acoustic noise, which does. The former can be reduced, although not eliminated, by good connections (short, well-insulated cables especially between the transducer and the preamplifier) and good instrument grounding. The latter consists of real sounds which are not useful for the damage monitoring, and may include the gripping of the specimen in a laboratory, the engine fan in an aircraft, etc. Part of the acoustic noise is generally managed by frequency filtering, location filtering or more sophisticated filtering based on signal characteristics.

[3]The wave velocity, depending on the specific problem, may be an unknown of the problem. Also, although this very simple formula illustrates the basic principle, the real algorithms used for source location are more complicated and use different formulae.

3.11 Summary

In this chapter all of the necessary equipment to conduct an AE investigation has been described along with the terminology of the standard data processing associated with AE.

The sensors, the most important elements in any AE system, were treated in §3.1, together with some observations on their correct use and choice. How they are placed on the structure and then transmit the signals to the system through the preamplifiers is explained in §3.2 and §3.3. After a brief glossary of the technical terminology presented in §3.4, a generic AE system and its way to process incoming data is illustrated in §3.5. A common way of calibrating an AE test, in order to ensure some repeatability, is described in §3.6. The traditionally four modes of AE data analysis are presented in §3.7. The description of a realistic working model for acoustic emissions, given in §3.8, makes clearer what can and what cannot be achieved by AE sensing, with special stress on the limitations of the technique. The similarities and common features with seismology, which permit a location of the acoustic emissions, were described in §3.9. Finally, the two types of noise encountered in AE are listed in §3.10

The AE technique offers a number of inherent **advantages**, over other NDT&E techniques, because of the following capabilities:

- continuous and in situ monitoring;
- examining the whole volume of a structure simultaneously with a limited number of sensors, localising the source;
- observing damage processes during the entire load history without any disturbance to the specimen;
- following the dynamics of internal damage;
- detecting only defects that are actively growing under stress, i.e. it selects the potentially most harmful defects.

Among the limitations that emerge from a survey of the technique, the following are important for a damage characterisation:

(i) given the "passive" nature of AE, it is impossible to intensify the sound field generated by the process to improve the response from the sensors, so that weak events may not be detected,

(ii) depending on the transducer range, not all the energy incident upon the receiving plate will be recorded, although this can be minimized with "wide-band" sensors,

(iii) the signals, not stationary and often comprising overlapping transients, are subjected to attenuation which will make the detected waveform different from the one produced by the source,

(iv) all the above means that expecting a deterministic, constant, unique acoustic emission from the "same" damage is unrealistic, and the only possible approach can be statistical over large data sets.

From what seen in this chapter, it is clear that the experimental work will have to be preceded by a careful examination and evaluation of the actual system in use, for a disambiguation of the results that will actually be obtained. Particular care shall be addressed to assess the sensors that, as ASTM (2007) confirms explicitly, are the component most subject to variation in an AE system.

Given the nature of the Lamb waves (explained in the previous chapter), always containing displacements normal to the surface, the choice of the acoustic couplant will lead to Vaseline, that although cannot transmit effectively shear stresses, is easy to use and effective for transmitting compressions.

There are not standards for calibrating an AE system but, yet, the research scope of this work, this would be of the utmost importance. Therefore in the analysis and planning of the experimental work, attention will be given to the interpretation of the data in view of this lack.

The localisation capabilities of the AE system will be used extensively to address the problem of identifying only the useful signals. Of course, the difficulties of doing so in an anisotropic medium will be considered.

CHAPTER

FOUR

Review of AE studies in composite materials

Unlike other people, our reviewers are powerful because they believe in nothing.

Harold Clurman

The tasks attempted by studying composites with AE are several: detection of damage initiation, location of source of damage, monitoring damage accumulation, determining material quality, and identifying the failure mechanisms and processes, determining whether there is an acoustic emission "signature". All this would also enable predictions of the failure or residual life of a component.

Although many applications of AE to composites in the literature deal with the identification of the acoustic emission sources, some of them cover only damage evaluation of composite structures when treated as monolithic. Of course, the most interesting works for this research are those which regard the composites as, exactly, composite structures, and thus with a focus on the relationships existing between the different constituent materials and the identification of their failure.

During the deformation of a fibre reinforced composite material, acoustic emissions can be generated in the following ways (Fuwa *et al.*, 1976):

- plastic deformation or fracture of the fibres,
- plastic deformation or fracture of the matrix material, and
- debonding and/or pull-out of the fibre from the matrix.

However, whereas most deformation or failure processes within a material may yield acoustic emissions, they will only account for a fraction of the total energy involved. Plastic strain, heating, the creation of new surfaces, and frictional forces will all share in the overall dissipation of energy, and reflections at interfaces and boundaries of the specimen will complicate the interpretation of emissions recorded at the surface.

The sole statement "AE characterisation" may be meaningless, because there are several ways the AE can be used to describe and monitor a process. In order to define an optimal approach, an overview of the various possibilities will be described in this chapter.

These approaches are enormously disparate, but a first classification may be twofold:

1. the test specimens/structure (geometry, lay-ups, materials, etc.), which can be either standard or manufactured specifically in order to match testing requirements, in a shape that cannot be usually found in real structures (for example, a single fibre embedded in a matrix of resin);

2. the techniques employed to analyse the data (neural networks, Fourier transforms, etc.).

Mathematical models and simulations fall outside of this very broad classification, but are also discussed in this chapter.

The rest of the chapter is subdivided in sections, each one focusing on one approach to AE characterisation, yet it must be noted that often the approaches contained in each paper can be multiple, and so the insertion of its review in one section is not to be intended in a strict sense.

Usually (and this shall be noted case by case) the results presented do not produce a proper characterisation in the sense intended and described in §1.3, because: (i) *either* produce characterisations that are too specific of the structures involved, and as such are not likely to be extrapolated, (ii) *or* implement neural networks that perform excellently, but give no extrapolative information.

4.1 AE features

The historically first approach to AE analysis is based on the extraction of "features" or "parameters" from the signals: duration, ring-down counts, amplitude, etc. as described in §3.4. This kind of analysis is sometimes called *multiparametric.* "These parameters appear

to be only poorly understood" (Hill and Stephens, 1974), and this is sometimes still the case, a few decades later. In the same work, the authors suggest relationships between the acoustic emission stress wave and the measurement parameters such as count, amplitude and energy.

The great majority of studies have attempted to correlate modes of failure with the *event amplitude,* the event *energy* and its *duration.* Interestingly, as Awerbuch (1997) reports, this did not happen for reasons particularly well scientifically grounded, but because "it is relatively simple to measure".

The use of the AE parameters was the only way to record data when the computing power (Beattie, 1983) did not permit the recording of the whole waveforms, also termed "transient analysis" because it usually happens during a *transitory* period of time, during which the data are recorded. These parameters are effective for damage monitoring of conventional structures, but might be out of place in a more advanced context of damage characterisation. Many research papers (for example, those summarised in Table 4.1) are affected by the distortion of considering the AE features, which are intrinsically relative quantities, as absolute.

Table 4.1 and Fig. 4.1 can surely illustrate this point:[1] the AE parameters, too concise to correctly frame a complex phenomenon, yield to characterisations that spread over "typical" bands that are too wide to describe the physics effectively. These bands overlap and contradict each other amongst different authors, and in some cases overlap even within the results of the same author (different frequencies or amplitudes assigned to more than one damage). What is said refers both to the frequencies and hit amplitudes, but for the latter the confusion is more dramatic and the description less precise, since the logarithmic scale of decibels hides large factors within a few digits.

Part of the confusion seen in these results is also to be attributed to different ways of classifying the damage: for example, Haselback and Lauke did not include fibre pull-out in their analysis, but of course in the physical reality fibre pull-outs must have occurred during their tests, and might explain the large width of such bands.

In some cases (de Groot *et al.*; Komai et al.) the ranges indicated are open (do not include an upper or lower limit). A general trend can be easily seen, acknowledged by Ceysson *et al.*

[1]Table 4.1 only summarises those findings that can be expressed as numbers, or bands of values. Table 4.1 does not contain findings expressed as power spectra or other non tabulable data. Also, it must be kept in mind that the Table refers to works done on a variety of materials and testing conditions.

(1996) in their review: low amplitudes/frequencies are correlated with matrix cracking, medium amplitudes with delamination, high amplitudes/frequencies with fibre breakage. This trend is, exactly, just a trend, and is too weak to be used effectively to tell one damage from the other as well as a damage from the environmental noise; moreover, this trend is contradicted in some cases (for example by Haselback and Lauke, that reported very low amplitudes for fibre breakage). In one case (Haselback and Lauke, Table 4.1) the frequency values indicated are not expressed in terms of bands but of frequency centroids: while this approach nay be more accurate in some respects, it implies full-spectrum calculations that introduce a degree of subjectivity due to the choice of the sampling time, which for highly non-stationary signals like acoustic emissions may be overly important. This aspect will be examined in §7.

The differences encountered in the results summarised in Table 4.1 and Fig. 4.1 may be linked to one, or a combination, of the following reasons:

1. the AE parameters are greatly affected by the impossibility of conducting a proper calibration of the system. This is acknowledged by (Jones and Yan, 2005) and will be the subject of an investigation that will be reported in §6.

2. The variability of the samples tested (dimensions, lay-ups) combined with the fact that specific specimens were normally used to extrapolate general results.

Prosser *et al.* (1995) carried out experiments to study matrix cracking in cross-ply graphite/epoxy composites and conclude that their "measurements demonstrated that the same source mechanism can generate a wide range of acoustic emission signal amplitudes", that is another way to say that signal amplitudes cannot characterise a signal.

The *stability* of AE parameters is the topic of the theoretical analysis carried out by Tuikin and Ivanov (1985). They observed that these parameters are greatly affected by the measuring conditions and by the stability of the acoustic-electronic channels. Among the AE parameters, some of them may be more suitable for a given aim. For example, the "energy" might be found more apt than the "duration" to describe the physical size of the source. After questioning the suitability of the parameters, Tuikin and Ivanov stated that the chosen parameter must also be stable with respect to disturbing factors (changes in the experimental parameters: threshold, distance). Their work was continued by Shiryaev *et al.* (1990), who remarked that there is a significant lack of reliable quantitative characteristics

Authors	Matrix cracking	Fibre fracture	Debonding matrix/fibre	Longitudinal splitting	Pull-out	Delamination	Material	Test specimen	Loading
Ely and Hill		stronger signals		weaker signals			Gr/Ep	UD	Tra
de Groot *et al.*	90–180 kHz	above 300 kHz			180–240 kHz	240–310 kHz	Ca/Ep	Ten	Tra
Russel and Henneke	50–150 kHz	140–180 kHz					Gr/Ep		
Suzuki et al.	30–150 kHz	300–400 kHz	180–290 kHz		180–290 kHz	30–100 kHz	Gl/Po		
Komai et al.	under 300 kHz	above 500 kHz			about 300 kHz	under 300 kHz	Ca/Ep		
Suh et al.	60–80 Hz	1900 Hz	60–80 Hz		400 Hz		Ca/Ep		
Barré and Benzeggagh	40–55 dB	85–95 dB			65–85 dB	60–65 dB	Gl/Pp		
El Guerjouma *et al.*	50–70 dB					70–90 dB	Gl/Po	Pure resin, 45° and 90° off-axis	Tra
Barnes and Ramirez		high dur. & ampl.				high dur., 45–70 dB	Ca	Pipes	
Woo *et al.* (2004)	40–270 kHz	40–480 kHz	40–270 kHz		40–270 kHz		Gl/Ep	Various	Various
Haselback and Lauke	< 60 dB, f.c. 170 kHz	< 90 dB, f.c. 90–180 kHz	< 45 dB, f.c. 270–330 kHz				Gl	Single fibre in resin	Tra

Table 4.1: Tabular summary of numerical results in literature; "f.c." stands for *frequency centroid*, "Gl" for *glass*, "Pp" for *polypropylene*, "Po" for *polyester*, "Gr" for *graphite*, "Ca" for *carbon*, "Ep" for *epoxy*, "Ten" for *tensile specimen*, "Tra" for *traction*

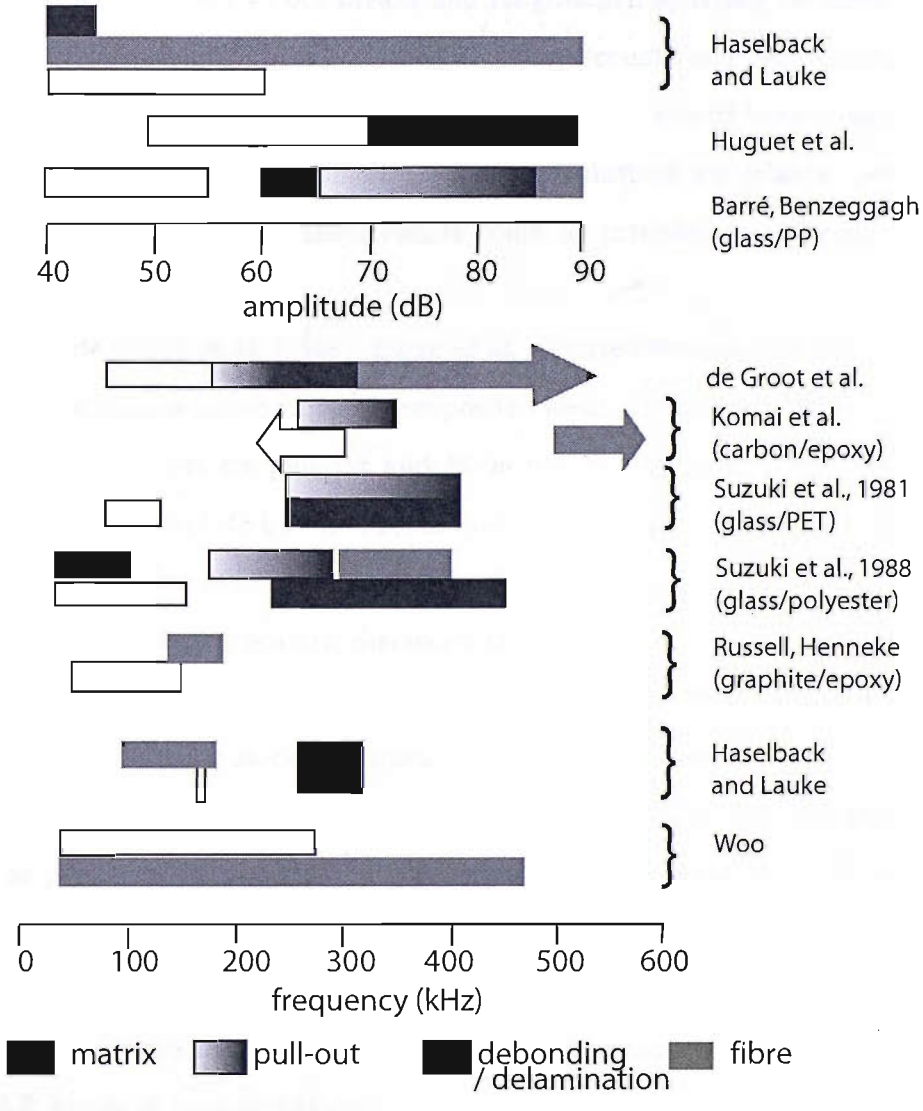

Figure 4.1: Graphical comparison of some of the numerical results shown in Tab. 4.1 (extended from de Groot *et al.*)

of the informativeness of AE parameters. They observed that applying the usual statistical evaluations to AE parameters is not well grounded in such they are not quantities following a Gaussian distribution.

Ely and Hill (1993) arbitrarily divided the data sets into a set having event amplitudes of 59 dB or less and one having event amplitudes of 60 dB or greater, and classify the events as "stronger signals" and the "weaker signals." They worked on standard graphite/epoxy composites, modified such that fibre breakage and longitudinal splitting occurs at a known position in the specimen, by means of cuts on the specimen filed with epoxy. They gathered a data set containing two discrete data intervals for amplitude, duration and counts; finally

it was determined that when fibre breaks and longitudinal splitting occurred at the same position, the stronger signals (high amplitude/energy/counts and long duration) resulted from fibre breakage and the weaker signals (low amplitude/energy/counts and short duration) resulted from longitudinal splitting.[2] Their conclusions are mainly speculative, and no mention is made to whether these results could be extended to different specimens or materials.

As cited by de Groot *et al.* (1995), Barré *et al.* reported measures for the energy content of AE signals from glass/polypropylene composite: 40–55 dB for matrix cracking, 60–65 dB for debonding, 65–85 dB for pull-out and 85-95 dB for fibre fracture. Here, amplitudes values are treated as absolute but are not, as no calibration was carried out that would yield comparable results. No mention was made in this work on how these measured amplitudes would change with different sensors, distances, or structures.

Joffe *et al.* (1995) designed glass fibre/epoxy strips in order to obtain mainly the desired failure mode. The laminate stacking sequence was $[0_2/90_n]_s$ where $n = 4, 8$ and thus, matrix cracking was the expected primary failure mode. A simple, non-waveform-based AE activity analysis was performed, and events with AE-amplitudes in excess of 0.5 V were correlated with formation of primary transverse cracks. The acoustic emissions were then related to strain, finding that cracks commenced at about 0.5% strain. This work did not present any kind of real characterisation useful for an in-service environment, where clearly there would be many AE events of high amplitude.

Hill *et al.* (1998), working on non-standard specimens, gave a basic characterisation in terms of ringdown count per event. They mechanically tested, with a transverse load, composites consisting of a bundle of fibres set in a polyester resin, to study the transverse cracking. The work aimed at characterising material changes by detecting general changes within the AE profile and the statistics of these AE parameters. They reported that in the case of room-cured specimens, intense (late) AE activity was followed by material failure (quiet then noisy); while in the case of post-cured specimens, intense AE activity began at a relatively low strain (noisy then quiet). They concluded that the effect of post-curing the specimens had been to increase the stiffness of the resin, but also the toughness of the resin.

A substantially different approach to feature extraction is that by Iwamoto *et al.* (1999) who produced, for carbon fibre reinforced unidirectional DCB specimens, histograms by

[2]In line to the trend indicated by Ceysson *et al.* (1996).

accumulating (summing up) *frequency peaks* found in the power spectra above a threshold level. Furthermore, a linear relationship between crack length and normalized cumulative AE event count rate was obtained. The results depended strongly on the type of composite tested, and looked more like a simple listing of results found rather an interpretation of them.

Bohse (2000) clearly stated that, according to his experiments, "the AE amplitude and AE energy are not sufficient for distinguishing the failure mechanisms in fibre composites." Dzenis and Qian (2001) noted that "parametric analysis requires simpler and cheaper hardware", and understood that "attempts to apply single-parameter filters to separate damage mechanisms have been largely unsuccessful". Thus they tried a hybrid transient-parametric method, using the AE parameters without mentioning the issues of the sensitivity and setting of the hardware.

Ni *et al.* (2001) investigated the attenuation of AE signals in composites through the analysis of the amplitudes recorded at different distances. The attenuation of the signals was found to be significant: they are reduced by about 80% after a distance of just 30 mm. They concluded that such variations were too broad to characterise the source.

From ASTM (2007) it emerges that the classic AE features are of extreme relativity. "The procedures" — it can in fact be read — "are not capable of providing an absolute calibration of data sets between organisations", and quite clearly cannot provide an absolute characterisation. The Standard suggests that emphasis should be placed on the initial few cycles and on the "large amplitude" features, remarking that these might have a better chance of repeatability and could possibly represent better the major structural damages. Nevertheless, the Standard does not explain how it is effectively possible to define a "large amplitude" hit. The document

- explains that the attenuation of the acoustic emissions can be very high even for short distances, and yet suggests suggests to keep the sensors at least 10 cm away from the pencil lead breaks, to achieve good uniformity,

- explains why the commercially available AE systems cannot provide comparable results because of the lack of uniformity in the sensor response ("the acoustic emission is [...] subject to variation. This variation can be a result of damage or aging, or there can be variations between nominally identical sensors."),

- lists many factors which can lead to a non-reproducibility of the collected signals, not all of them easily controlled in laboratory, and even less in a real in-service environment,
- suggests a procedure (the pencil lead break test) that is often adopted as the only "calibration" procedure, and yet it also states that "these procedures in *no* way constitute a calibration of the sensor".

A rather weak "characterisation" is the one suggested by El Guerjouma *et al.* (2001); Huguet *et al.* (2002). They aimed to demonstrate the potential of AE to discriminate in real time the different types of damage occurring at the microscopic scale in a glass/polyester composite. They work on samples that they expected to produce preferential damage mechanisms (matrix fracture for resin samples, mainly matrix fracture with some decohesion for 90 ° off-axis, mainly decohesion with some matrix fracture for 45 ° off-axis). The AE data were collected through a PAC system, with a sampling rate of 8 MHz and a 80 dB total amplification; ambient noise was filtered using a threshold of 32 dB; two resonant sensors (200 kHz–1 MHz) were adopted. The authors finally identified matrix fracture and fibre-matrix decohesion (the signals had different peak amplitude, signal duration and energy distributions). The amplitude of the collected signals were mainly distributed in two zones exhibiting a bimodal behavior: about 70% of them had amplitudes in the range of 50 to 70 dB, with waveforms similar to those observed in the tests on pure resin ("A-type" signals); the 30% left signals had amplitudes in the range of 70 to 90 dB and waveforms quite different from those of A-type, with shorter decay time and higher energies ("B-type"). The similarities in waveforms found between A-type signals in 90 ° off-axis tests and signals from pure resin tests made them conclude that the source mechanism was the same in both cases, i.e. matrix fracture. For the tests on samples in the 45 ° direction to fibres, A-type and B-type signals could be observed in the same amplitude zones as previously and with very close parameters and waveforms. The authors suggested the need of a multiparameter analysis to improve the identification of damage modes, but understood that this is rather difficult when many damage mechanisms take place in the same composite material. In order to separate numerically the two types of signals that they had observed, they implemented a neural network.

Huguet *et al.* (2002) also cited results from Barré and Benzeggagh (who found for glass/polypropylene that matrix cracking has 40–55 dB, debonding 60–65 dB, pull-out 65–85 dB, and fibre fracture 85–95 dB amplitude hits) and Barnes and Ramirez (who, testing car-

bon fibre reinforced pipes, found for delamination and debonding "high duration and 45–70 dB" hits, and for fibre fracture "high duration and high amplitude" hits).

Finally, Lariviere *et al.* (2003) tested modified glass fibre/polypropylene plates (commingled yarn) in transverse tensile loading with one 200 kHz resonant sensor and found, for interface fractures, 59–66 dB. They also investigated the same material under a mode I delamination test, but could not find any characterisation for that case.

4.2 Frequency analysis

Because of the intrinsic limitations of a purely AE-features approach, many works take advantage of more advanced AE systems to look into the frequency content of the acoustic emissions. Although some of them merely summarize a whole waveform with some sort of average frequency (§4.2.1), the best works look at all the waveform, mostly using frequency spectra (§4.2.2) and wavelet decomposition (§4.2.3). In fact the identification of a full frequency spectrum is more complete and less arbitrary: it is not possible to effectively reduce a whole frequency spectrum to a mere frequency band, because doing this would signify a substantial loss of information.

The obstacles encountered in the AE signal analysis are mostly due to the typically non-stationary nature of the signals: the frequency and the statistical characteristics change with time. They are made of a series of decaying transient bursts occurring at irregular intervals and with random amplitudes; they contain discontinuities due to different reflections and are contaminated by noise emanating from various sources (Terchi and Au, 2001).

4.2.1 Classification in frequency bands

Many authors provided their results in the form of frequency bands the acoustic emissions fall within (see Table 4.1 and Fig. 4.1). This did not lead to an effective characterisation. A major limitation is that to specify a band underlies implicitly the choice of a sort of threshold, necessarily *arbitrary*.

Haselback and Lauke (2003) tested non-standard specimens consisting of a single glass fibre immersed in resin with a double V-notched in the middle. The transparency of the resin and the presence of a single fibre allowed inspections at the microscope to correlate the acoustic emissions to the damage. The V-notch would produce tensile forces perpendicular

to the applied load and thus debonding. No mention was made to whether and how these results could be applied to specimens different in size and shape, or to *real* composites.

De Groot *et al.* (1995) worked on several types of standard carbon/epoxy specimens, using a preamplification between 10 and 20 dB, filters from 100 to 1000 kHz, and broadband PAC WD sensors. They found matrix cracking in 90–180 kHz, fibre fracture above 300 kHz, debonding in 240–310 kHz, and pull-out in 180–240 kHz.[3] They also summarised other works: Russel and Henneke found for graphite/epoxy that matrix cracking happens in 50–150 kHz, fibre fracture in 140–180 kHz. Komai et al. found for carbon/epoxy that matrix cracking and debonding was under 300 kHz, fibre fracture above 500 kHz, pull-out and friction at about 300 kHz. Suh et al., in carbon/epoxy, found matrix cracking and fibre debonding in 60–80 Hz, fibre fracture at 1900 Hz, pull-out at 400 Hz; these being frequencies much lower than other researchers'.

Huguet *et al.* (2002) summarised the results of other researchers: Suzuki et al. found, for glass/polyester, matrix cracking in 30–150 kHz, delamination in 30–100 kHz, fibre fracture in 300–400 kHz, fibre debonding and pull-out in 180–290 kHz.

Woo *et al.* (2004) worked on glass fibre/epoxy and satin-weave glass-fabric/epoxy laminates, of various orientations, with two μ30 PAC sensors, with an operating range of 100–600 kHz and a peak at 275 kHz. They concluded that matrix fracture, fiber-matrix interfacial failure, and pull-out fell within 40–270 kHz, whereas fiber fracture and accompanying matrix fracture in 40–480 kHz. The classification of the kind of damage was aided by the analysis of other published works.[4]

4.2.2 Frequency spectra

As opposed to a multiparametric analysis, a more modern, different kind of analysis which heavily uses the computational power of digital computers is a "transient analysis", i.e. the study of the single waveforms, also with the aid of different kinds of transforms (Fourier, wavelet) and digital visualization. A transient analysis starts with the digitized acquisition of a waveform by mean of a transient recorder.

The works reviewed here, although dealing with the frequency content of the acoustic emissions, never use high-fidelity sensors, nor mention the problem of the response fidelity.

[3] Matrix cracking is classified in a band outside the operating range of the preamplifier.
[4] The identified frequency ranges fall again outside the sensor working frequencies.

Usually, the expressions "broad band," "wide band," and "resonant" are used, applied to a particular transducer performance. Broad-band and wide-band imply high sensitivity over a large frequency range; resonant implies high sensitivity over a narrow frequency range. High fidelity implies that there are no resonances over the frequency band of interest. Confusion may arise when the term "broad band" is used in the context of being high fidelity, and "resonant" is inferred as a transducer having sensitivity over a narrow range of frequencies. An AE transducer can have resonances but still be responsive to signals over a broad frequency range. A high fidelity transducer can have flat response with frequency, but be limited to a narrow range of frequency over which it exhibits the flat response (Dunegan, 1996).

Johnson and Gudmundson (2000) used different stacking sequences in order to trigger different crack mechanisms, with the purpose of studying transient recordings from broad-band transducers generated from matrix cracking, local delamination and fibre breakage, to see if characteristic features could be recognised and used to discriminate these different damages types. The specimens used were strips and had the edges wet sanded to prevent damage initiation from the edges; four sensors (two pairs) were used for the waveform detection and a couple of additional transducers (six in total) were mounted close to the end tabs to permit the exclusion of signals coming from damage or slipping in the gripping region. The authors separated extensional and flexural waves: they mounted the sensors in couple, on both the sides of the strips, and then added and subtracted the signals to obtain respectively the extensional and flexural waves alone. Different acoustic emissions were correlated to different strain levels. Differently from what was found by other authors, the amplitude of emissions generated from assumed fibre breakage were very small.

Qi (2000) found, with a series of pencil lead breaks and a couple of sensors, that for the same acoustic emissions the two power spectra, coming from each sensor, were different. Being the sensors at different distance from the source, he argued that the frequency spectrum could have been shifted as the wave propagated into the material, within a few millimeters distance. In fact a loss of energy at higher frequency occurred. This finding clearly poses some problems for a possible characterisation, since, in addition to the other variability factors, the distance at which the characterisation is done must always be specified. On the other hand, though, Ni *et al.* (2001) found that the frequency of their signals are almost unchanged for different distances (up to 30 mm) of signal propagation. They concluded that

"even in anisotropic medium, such as composite materials, frequency analysis is an effective way to process AE signals".

Bohse (2000) showed some typical power spectra for cracks in pure epoxy and carbon-fibre fragmentation in epoxy matrix. The author used specimens designed on purpose and also attempted some mathematical description of some AE features. He obtained averaged power spectra for: (i) fibre fragmentation and matrix cracking (separately) in pure epoxy, single glass fibre/epoxy, and single carbon fibre/epoxy, with a sampling frequency of 5 MHz, a PAC 1220A preamplifier with 60 dB gain and a 100–1200 kHz filter, and one PAC WD wide-band sensor, (ii) debonding in double cantilever beam specimens of glass fibre/polypropylene (multi-fibre), using two PAC WD wide-band sensors in linear location setup, PAC 1220A preamplifiers with 40 dB gain and 20–12100 kHz filter, and a sampling frequency of 4 MHz. The power spectra collected showed distinctive features, but they were in the form of "averaged power spectra of selected acoustic emissions"; it is not clear how much the single spectra differed from each other, nor how representative the selected signals were of all the collected ones.

Pappas *et al.* (2004) underlined that the acquisition of the waveforms cannot be a straightforward process, since the electric signals contain the information coming not only from the source of the event but also the medium they propagates through and the particular path. They also questioned the usefulness of a database of typical waveforms, wondering whether the obtained values could be used to evaluate the response of the same material in different structures and testing conditions, and whether a micro-scale approach (testing single filaments; see for example Giordano *et al.* (1998) that however do not present significant results) would be applicable to the macro-scale (plates, structures, and so on). Pappas *et al.* presented nevertheless a frequency analysis of acoustic emissions generated by several filament bundles of different fibre types (Nextel, Kevlar, etc.), not set in resin, detected through miniature sensors, and they found different frequencies for the different fibres, ranging over extremely large frequency bands (the peaks for the fibre failure are reported within 20–400 kHz). These results quite obviously cannot be effectively translated into generic composite structures.

4.2.3 Wavelet analysis and other techniques

Qi *et al.* (1997) tested some standard specimens (u.d. and cross-ply with a circular hole),

using PAC μ30 resonant (at 300 kHz) sensors, attached to PAC 1220A preamplifiers, with 40 dB gain, set with a 100–300 kHz filter, at a 8 MHz sampling frequency. They noted that 90% of AE activities were concentrated in the frequency range 100–300 kHz (not surprising considering the filter), then arbitrarily divided this range into a set of consecutive frequency bands. Observing that each band could be associated to various fracture modes, they decomposed the AE signal into different wavelet levels (discrete wavelet decomposition), each level representing a specific frequency range. AE energy was dominated by three wavelet levels, denoted with 7, 8 and 9. Frequency spectra levels 7, 8, and 9 were centered at about 110 kHz, 250 kHz, and 300 kHz. Among these, level 7 was associated to matrix failure because this is a low-energy, relatively low-frequency phenomenon. On the other hand, it was reported that the energy magnitude and frequency were the highest in level 9: the fibre fracture was reported to be a high-frequency phenomenon because of the high-intensity low-duration nature of the phenomenon. Finally, the energy magnitude and representative frequency in level 8 were placed between those in level 7 and 9, and it was therefore concluded that level 8 indicated the fracture associated with the debonding between matrix and fiber. The energy carried by the AE signal was analysed by considering the full waveform instead of only AE counts or event counts.

Mizutani *et al.* (2000) studied a sequence of 70 AE events in a locally loaded cross-ply CFRP. Various internal damages (fibre fracture, in the front layer, transverse matrix cracks in the midlamina, delamination and splitting) in cross-ply composite specimens were induced under local compressive loading. These signals are compared with laser-induced S_0 and A_0 Lamb waves of known source types, to simulate AE waveforms produced by various fracture mechanisms. The signals were then analyzed using FFTs and wavelet transforms. The events were finally visually classified into four types by their waveforms and wavelet maps. Internal damages of the specimen were identified as fibre fracture, transverse matrix cracks, delamination and splitting. The procedure had to rely on a comparison with signals from a non defective specimen; this would not be acceptable for an in-flight real-time diagnosis.

Johnson (2003) used epoxy/glassfibre prepregs and considered two types of damages, namely matrix cracking in the mid and the surface layers of a $[0_2; 90_3]_S$ and $[90_2; 0_3]_S$ specimen, respectively. His approach was original: numerically calculated AE-signals were generated to form a training set, which was used to classify experimentally measured AE-signals. Both the numerical and the experimental signals were first analysed by the continuous

discrete wavelet transform to explore the time-frequency content. Each signal was then represented by a wavelet coefficient matrix, and used in a Partial Least Squares Regression analysis, capable of visualizing the class belonging of the experimental AE signals. He used six DWC B1025 piezoelectric transducers, of broad-band type with an approximately flat frequency response in the range of 50 kHz to 1.5 MHz. The sensors were placed in such a way to split the signal into its extensional and flexural modes, following the approach by Johnson and Gudmundson (2000). To deal with dispersion, all signals were wavelet transformed, resulting in coefficient matrices representing the time-frequency content of each signal.

One of the best identifications of the waveforms is obtained by Ferreira (2000); Ferreira *et al.* (2004). They provided a visual representation of typical spectra and spectrograms for different types of E-glass/epoxy specimens (standard, in different lay-ups, with tensile and 3- and 4-point flexural tests) and damages. They used PAC S9220 sensors, sensitive in the 100–1000 kHz range, aiming at producing different damage mechanisms by combining different lay-ups (choosing from $[0°]_1$, $[0°]_2$ and $[90°]_1$) and loadings, subsequently verifying the obtained damages with a visual inspection in order to support the association of the frequency spectra groups obtained to the failure modes. Firstly, to characterise the failure modes, the AE signal was considered in the frequency domain, obtaining the mean spectra for each specimen. Secondly, the wavelet analysis was adopted, aiming at characterising failure mechanisms in the time-frequency domain. While FFT analysis showed some typical frequency ranges, the wavelet analysis did not, the highest differences being observed in the time domain. The work produced about three or four signals for each specimen, and only signals visually best represented were chosen for presentation and analysis. They were able to correlate only two frequency spectra with the respective failure mechanisms (matrix cracking and debonding fibre/matrix), and concluded that the other spectra were originated by interaction of more than one failure mechanism. No mention was given in the text to the problem represented by the size of the specimens, which are likely to modify a characterisation purely done on a frequency basis. The spectra were accompanied by the intervals of standard variation, which were quite narrow. Their work was then continued by Silva *et al.* (2005) who elaborated further on the same data with a fractal analysis.

4.3 Neural networks

If viewed from the point of view of a successful identification of the kind of damage on the basis of its acoustic emissions, the literature shows that a neural network approach has probably given the best results. Neural networks programmed and instructed on a *specific* structure are quite able to discern one type of damage from another in *that* structure.

Nevertheless, notwithstanding some successes, a neural network approach is to be discarded here. In fact, task of this work is not the identification of the damage in a given structure, but rather the characterisation (as broad and general as possible) of each kind of damage. For their specific nature, neural networks do not provide predictive or extrapolative information. In other words, well trained networks are well capable to distinguish the damages in a specific structure; nevertheless all that do not yield to a proper general characterisation which can be extrapolated from that particular case. The review of three representative works follows.

El Guerjouma *et al.* (2001); Huguet *et al.* (2002) (see also §4.1) separated the AE parameters and waveforms of the signals by means of *pattern recognition* techniques. They investigated the development of Kohonen's self-organising map for AE data and the use of the non-linear projection of self-organising map technique to identify classes of signals on the Kohonen map.

Bhat *et al.* (2003) attempted an elimination of noise from AE signals by characterising the noise sources in terms of their waveform parameters (rise time, ring count down, energy, event duration, frequency etc.) and grouping them into number of classes, thus creating a database of noise sources using ANN developed specifically for this purpose (Kohonen self organising feature map which learns in un-supervised manner and multi-layer perception which learns in supervised manner using back-propagation algorithm). In the next step, an AE database was created by collecting signals under laboratory conditions and characterised. Subsequently, an ANN was trained with input signals from both noise and AE signal databases. AE data corresponding to three different failure modes (fiber failure, fiber/matrix debond and matrix cracks) were identified with accuracy in standard CFRP specimens. Though the initial objective was only to separate the noise from AE signals, the method enabled the identification of AE signals belonging to three different failure modes (fibre failure, fibre/matrix debonding and matrix cracks). The authors suggested that this

approach could be adapted to actual situations like monitoring an aircraft in-flight; however, this would require the generation of a database for the failure mode signals obtained from actual CFRP structure of an aircraft.

4.4 Validation against a mathematical model

Some attempts were made to compare numerical calculations with experimental investigations of acoustic emission generated from microcracking in composites. A theoretical model must include the AE source, the propagation of the elastic wave field and the characteristics of the receiving system: a wave field generated by a microcrack will be influenced by dispersion, attenuation, reflections and other damages in the considered composite laminate. These effects make the transfer of discriminating features and classification criteria from a laboratory specimen level up to a real component level a very difficult job.

The topic of elastic wave propagation in solids has been described in §2. Complex geometries, such as an inhomogeneous, multi-layered, anisotropic composite, do not present a straightforward task. Only a few authors attempted to describe analytically the acoustic signatures of fractures and their propagation trough the material, limiting themselves to very basic cases, obtaining only some indication about the expected characteristics. Such efforts rely on large computation power to theoretically calculate AE signals from a theoretical model. If the specimen changes, different calculations have to be performed. These simple results do not correctly represent the real physics.

Enoki *et al.* (1997) represented the AE signals as the convolution integral of the source function due to microfracture of materials, the dynamic Green's function of the media and the transfer function of the measuring system. Rhian Green (1997) showed the calculated surface response of a cross-ply fiber composite plate due to buried impulsive sources, described mathematically as "line couples" and "line double couples without moment." Guo *et al.* (1997) theoretically modelled Lamb waves from microfractures in composite plates for different source types, to investigate the relationship between the waveform signatures and the source characteristics. They presented the solution of the three-dimensional wave propagation in transversely anisotropic plate, then validated it through experiments conducted with an aluminum plate.

Johnson and Gudmundson (2001) compared theoretical predictions for transient wave

propagation based on a finite element discretization of the cross section of the specimen, with experimental data from transverse matrix cracking in a cross-ply composite. The computations had only included the extensional mode. They pointed out that the transducers should be as small as possible to minimize wavelength effects.

Banerjee and Mal (2005) presented a semi-analytical method to calculate the elastodynamic field produced by localised dynamic loads (e.g. a pencil lead break) in a thick composite plate. The model represented correctly the low-frequency range due to the flexural waves; the extensional waves were described less accurately. Interestingly, the waveforms collected (and calculated) at the sensor showed dependence with the travelling direction from source to the sensor, in respect to the fibres orientation.

4.5 Source location on composite panels

For planar source location in isotropic media, at least three sensors are used. Analysis of arrival times at different sensors enables the emission source to be located by means of a triangulation method. A pair of differences in the arrival time from an array of three sensors defines two hyperbolae at which point of intersection the emission source is located. This is a mathematical problem, the solution thereof is embedded in modern AE systems, such as the PAC in use for these experiments. For anisotropic materials, the mathematical problem is different, and although a closed form solution can be found, this is not necessarily implemented in commercial AE systems.

The simple triangulation process, commonly used for source location in AE as described in §3.9, cannot be used in anisotropic media, such as composite laminates. Here, the waves travel in different directions with different velocities, whereas the triangulation implicitly needs uniform wave velocity: in orthotropic composite materials the velocity profile of an expanding stress wave is not circular. In addition to this, the source location is also impractical in composites because of the strong frequency dependence of wave velocities and large attenuation.

Jeong and Jang (2000) presented a new approach for the analysis of transient waves propagating in composite laminates, finalized at a better source location. They performed a planar source location using a triangulation method based on flexural waves, and used a frequency dependent arrival time of output signal and an angular dependence of group

velocity.

Castagnède (1990) described a method by which a pointlike source of acoustic emission could be located in a plate of composite material. The method was mathematical, and could not be implemented in a standard commercial AE system. Besides, the pointlike source used to validate the model was simulated by fracturing tiny glass capillaries — and this is definitely too much ideal for any practical purposes. Other algorithms were presented by Koo *et al.* (1998) and Yamada *et al.* (2001), which dealt specifically with the dispersive nature of Lamb waves, but again they were not something that could be implemented in a standard commercial system, and even so, the results obtained showed huge difficulties in source location on composites.

4.6 In-flight AE sensing

All types of aircraft suffer from structural cracking; and even though the location of the crack can often be predicted, the inspections required are costly, often requiring significant disassembly. A successful structural health monitoring system would lead to reduced life-cycle costs, improved aircraft reliability, improved maintainability, increased safety of flight, and maintenance on demand.

Structural damage may come either from **external** or **internal failure.** An example of the former may be provided by the damages caused by micrometeorite impacts on spacecrafts: with AE on-board, a vehicle can passively listen to the structure and locate where the impacts occur. But this research is devoted to the monitoring of *internal* failure noises, generated by a failure in the composite panels (matrix cracking, fibre fracture, delamination). These can be separated from the noise in two ways, basically: *spatial* and *parametric filtering.* If a **spatial filtering** aims at the elimination of the AE signals coming from outside an area of interest (in this case, a wing panel for instance), a **parametric filtering** requires characterisation of either the useful signals or the aircraft noise source on one or more combination of parameters (rise time, ring count down, energy etc.) range.

The main theoretical problem for an in-flight AE monitoring system is represented by the need to discern AE events from operational noise. To do this, either the operational noise or the damage noise must be identified. *This research aims at the latter.* Aircraft structures comprise a large number of bolts, fasteners and plates, which move relative to one

another — as very well explained Bhat *et al.* (2003). This leads to bolt hole rubbing (friction noise) as well as crack face rubbing and fretting. But whereas the former leads to undesirable frictional noise, crack face rubbing may be *useful noise* as it indicates the presence of a crack. This noise along with the structural flexural noise is termed as "airframe or structural born noise" and is due to load changes. On the other side, jet engines produce appreciable noise and so also the airflow; and landing gear operations and hydraulic system vibrations give rise to extraneous noises which can be grouped under "mechanical noises." Finally, another category of noise comes from electromagnetic interference, due to the avionics systems, relays and possible bus switching between AC and battery power sources, and also from switching ON/OFF of various other electronic and electrical systems.

Present day computer technologies make it possible to put a small computer and sensor system on an aircraft to monitor structural health at locations that are difficult and costly to inspect through more traditional techniques. The health of the monitored locations can be determined by the end user through normal operations (Standard Flight Data Recorder download), thereby providing a significant reduction in scheduled maintenance requirements. For such an onboard system to be successful, it must be capable of remotely detecting damage. In other words, it must be capable of detecting flaws that occur at distances from the sensors. Accordingly to Marantidis *et al.* (1994), the only passive technology capable of accomplishing this is AE. AE monitoring can also be achieved as a combination of active and passive techniques which lead to applications of "smart" CFRP structures (Pohl *et al.*, 2001).

AE is not a novel technique in aircraft testing, but is not routinely used during flight today; it is rather confined to a full-scale fatigue testing, for which the aircraft must be called out of service. Thus an in-flight sensing for the *continuous health monitoring* of the structure would be a completely different approach.

Few unsuccessful attempts of in-flight tests made AE gain a bad reputation and probably slowed down the research in the field (Carlyle *et al.*, 1999), although such topic continued to arouse interest even outside the technical field (Cohen, 1997). McBride *et al.* (1991) were able to detect a crack growth in flight, but the flaw was originated from a very simple specimen carried onboard an aircraft, and a very basic AE analysis was featured.

Haugse *et al.* (1999) presented results from proof-of-concept testing. They characterised the background noise level of an F-16, concluding that the noise from electronics, flight

actuators and engines should not interfere with the monitoring of crack growth using AE, because all the mechanical noise was 200 kHz or less, and the EMI noise was minimal and easily distinguishable from the crack growth signals.

Horvath and Cook (1982) studied algorithms to discriminate crack-growth acoustic emissions from other innocuous sources during an inflight operation. They reported successful results with an Adaptive Learning Network pattern recognition model.

Carlyle *et al.* (1999) reported about two successful applications of AE in an aeronautical environment, but these were not applied to a normal in-flight condition. The first one involved an F-111 cold proof testing to test the integrity of its steel components. With the aim of locating the damages with a 0.3 m accuracy, 28 narrowband 300 kHz sensors were used, with a sensor spacing varying from 0.5 m to 6.7 m over the aircraft. Noise discrimination was accomplished using several AE attributes, primarily a high value of energy and amplitude in the resonant frequency. The authors also pointed out that *loading noise and normal airframe reactions, although sometimes loud enough for a human to hear, did not have high amplitudes and energies in the ultrasonic range.* The second application was on a Vickers VC-10 pressurization proof testing, with the aim of detecting the presence of growing cracks in order to prevent serious damage to the aircraft. The AE system consisted of the channel lights on the front panels of the AE instruments, and graphs of signal amplitude and signal arrival rates. A sensor spacing of 1.8 m was used, which makes the system prone to large attenuation and dispersion. On the whole, these two applications, although successful, involved a very basic analysis of AE signals and not an in-flight situation.

4.7 Summary

In this chapter, a detailed description of the past and current studies on the application of AE to the damage characterisation was given. Stemming from the review of these works, it is believed that a purely AE features approach relies too much on the subjectivity and the sensitivity of the equipment, and cannot lead to effective and complete characterisations (§4.1). Most of the information contained in an acoustic emission lies within its frequency spectrum, and the studies which retain it seem to be the most successful (§4.2). The application of neural networks to AE damage characterisation appear effective, but not capable of generating universal results (§4.3). On the other hand, the results achieved with purely

mathematical models (§4.4) are of scant usefulness: they are limited to very simple cases — too simple for a realistic enough description — otherwise they cannot be mathematically, nor numerically, solved. They are not versatile enough to be applied to complex real structures.

Since any attempt to characterise the acoustic emissions in a composite material must deal with the anisotropy of the medium, which poses serious problems for the location of the events, a review of this aspect (§4.5) has been presented as well. The in-flight aspect of this works resides in the limitations that it poses, and works as an inspirational source (§4.6).

The AE characterisation examined in this thesis has the real-time monitoring of flying composite structures as primary scope of application, and thus versatility and flexibility is a requirement. The modelling of all the features thereof would be not only extremely difficult but also impracticable. Therefore, in this work a purely theoretical modelling approach will be discarded and the focus will be put on developing an experimental testing strategy to extract and characterise the acoustic emissions from composite panels.

This literature survey has suggested an experimental approach, questioned the the validity of the AE parameters, which will be verified in the chapters dedicated to the experimental campaign. Also, the spectra of the acoustic emissions will be retained, and the analysis will be focused on them. Although difficult, if not impossible, with commercial AE equipment, the localisation features of AE will be used to filter out those events that, coming from outside the sensors, are likely to be extraneous (noise, reflections from the edges). Also, the effect of the anisotropy on the collected waveforms will be investigated.

CHAPTER

FIVE

System and sensors used in this work

Give us the tools and we will finish the job.

Winston Churchill

5.1 Physical Acoustics' AE System

The AE system used in this research is manufactured by Physical Acoustic Corporation, 195 Clarksville Road Princeton Jct, NJ 08550, USA. It uses two PAC PCI-2 boards for a total of four AE channels and two parametric channels. They are referred to as C1, C2, C3 and C4 throughout this work. The PCI-2 AE System is a 2-channel data acquisition and digital signal processing system on a single full-size 32-bit PCI-Card. It has got a 18-bit 40 MSamples/sec A/D architecture.

Through the PCI (Peripheral Component Interconnect) bus and Direct Memory Access (DMA) architecture, significant AE data transfer speeds can be attained, assuring a wide bandwidth bus for multi-channel AE data acquisition and waveform transfer. Waveform data streaming capability is achieved within the board, allowing waveforms to be continuously transferred to the hard disk. Four high-pass and six low-pass filter selections are possible for each channel, under software control.

The system used is very simply illustrated in Fig. 5.1. Compared with the generic system of Fig. 3.5, some simplifications come from the missing filter, which is integrated into the

preamplifier, and from the missing amplifier and event detector, integrated into the main computer chassis.

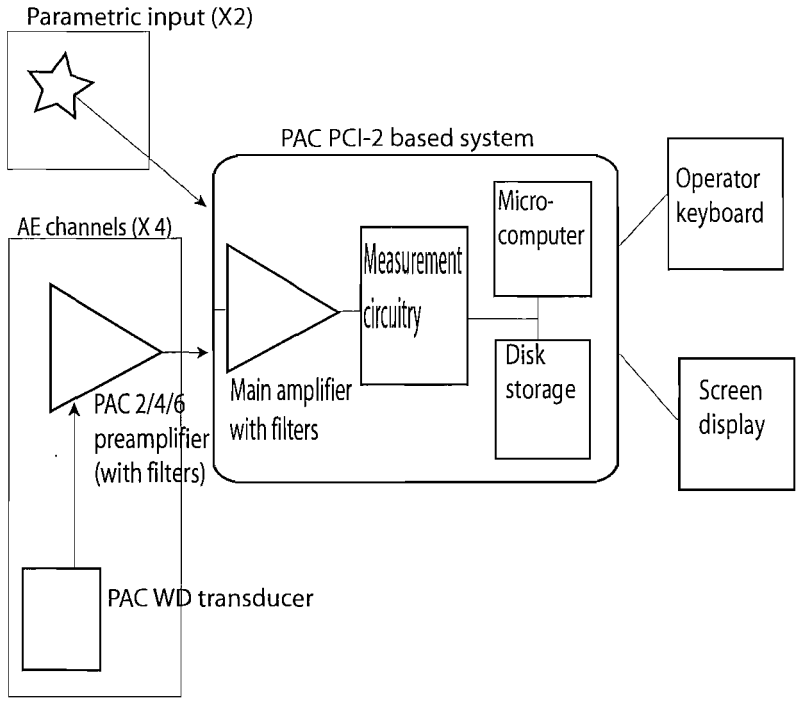

Figure 5.1: Simple schematic of PAC system

5.1.1 General experimental procedure

Although the experimental procedure followed for the tests described in this thesis generally varies with each experiment, some aspects are certainly in common and shall be described here, with the exception of the software setup, illustrated in §5.3.1.

Generally, either one, two, or four sensors (§5.2) are used at the same time, each connected to a preamplifier (§5.4) and next to the PCI acquisition system. Each preamplifier is set to a common gain, usually 40 dB, and this value is then set in the software (§5.3).

The sensors are always acoustically coupled with Vaseline to the samples. In the case of metal plates, horizontal during the testing, this coupling is sufficient to hold the sensors in position. In the case of composite strips mounted in the tensile testing machine (§8.2), their vertical position requires electric tape to hold the sensors firmly in position. In either case, with or without tape, the correct coupling is always verified, after each mounting, by checking that a PLB in close proximity of the sensors is detected with a hit amplitude of 90 dB or greater.

The two "parametric channels" built in the PAC system are generally connected to two output channels of the testing machine, that provides indication of load and, when an extensometer is mounted and connected, strain. At the beginning of each test, the correct multiplication factors are individuated, so that the readings displayed in the AE software coincide with those displayed by the software of the tensile machine.

5.2 PAC sensors

Although resonant sensors are the standard choice in commercial applications, for this work broad-band sensors are used. Resonant sensors can maximize the output of the acoustic emissions of interest, but they must be known in advance; this work needs broad-band sensors because the frequency range is not known *a priori*. Thus, the commercially available sensor used in this work is the PAC WD, which is a wide-band sensor supplied with integral cable and a dual BNC end connector. The cylindrical (18 $\varnothing \times 17$ mm) stainless steel housing is sealed with epoxy to a ceramic face.[1] Other features are reported in Table 5.1.

Table 5.1: PAC WD sensor's features (PAC, 2003)

Operating temperature	−65 to +177°C
Shock limit	10 g
Peak sensitivity	−62.5 dB (Ref. 1 V/μbar)
Operating frequency range	100 to 1000 kHz
Resonant frequency	650 kHz

According to the Nyquist theorem, all the frequency information in a signal will be retained if the signal is sampled at a rate greater than two samples per period of the highest frequency component present. This does not pose a problem with the current equipment as the sensors do not respond to frequencies greater than 1 MHz, so in this work the signals are sampled at 2 MHz. For an easier referencing throughout the tests, the sensors used (four PAC WD's) were labelled as in Table 5.2. The frequency responses[2] of these four PAC WD sensors are shown in Figures 5.2 – 5.5 and may pose a real problem for this work. In fact, notwithstanding their being four nominally identical wide-band sensors, they are not identical (Fig. 5.6 shows them superimposed on a single chart) and show conspicuous

[1] This sensor can only withstand a very limited removal force between the housing and the mounting plate, so it cannot be adhesively bonded to the specimens.

[2] The calibration methodology is based on ASTM standard E976.

Table 5.2: Sensors labels

Sensor S/N	Label
AJ51	S1
AJ49	S2
AJ57	S3
AJ60	S4

resonant peaks, although not at the 650 kHz quoted by the manufacturer.

The comparison shows that the curves differ considerably and that at certain frequencies the difference is as great as 10 dB. The plot is divided into three frequency ranges labelled as A (ranging up to 300 kHz), B (covering from 300 to 650 kHz) and C (over 650 kHz). Although the AE from composite materials is broadband, the literature indicates that most of the activity occurs at frequencies in the range covering regions A and B. It is clear from Fig. 5.6 that the response of the sensors differs in these regions. In A the response of S2 differs from the most from the other sensors, although at approximately 0.28 MHz there is a peak in the response of S3 and S4 that is not evident in the other sensors. S3 and S4 present two resonant peaks (at about 0.28 MHz and 0.45 Mz), whereas S1 and S2 have only one peak at about 0.26 MHz. In region B the response of S3 and S4 is practically identical, however the response S1 is around 5 dB less and S2 10 dB less. Above 0.30 MHz and below 0.65 MHz the sensor sensitivity is constantly in the order S2, S1, S3, S4, from the least to the most sensitive. Interestingly, across the spectrum shown in Fig. 5.6, the order of the four sensors sensitivities is not the same. Although the sensors are sold as wide-band between 100 kHz and 1 MHz, there are areas (especially the low frequencies) within this range where the sensors are *relatively* blind: for example between 0.10 MHz and 0.28 MHz there is a difference of approximately 10 dB, in other words the signal detected would result *ten times more powerful at 0.28 MHz than at 0.10 MHz.*

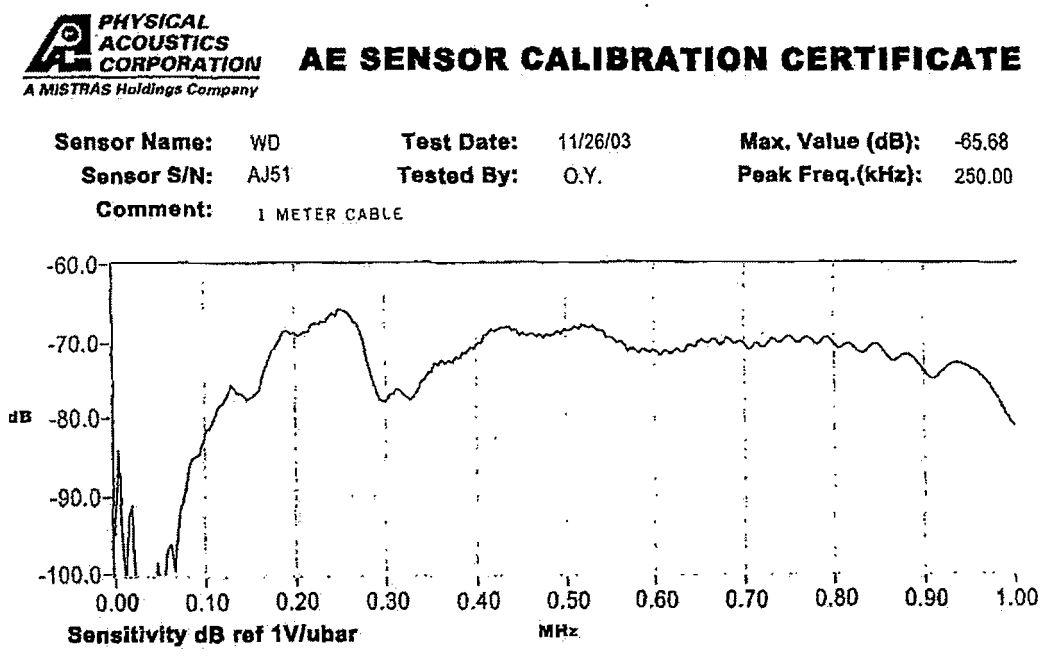

Figure 5.2: Calibration certificate for S1

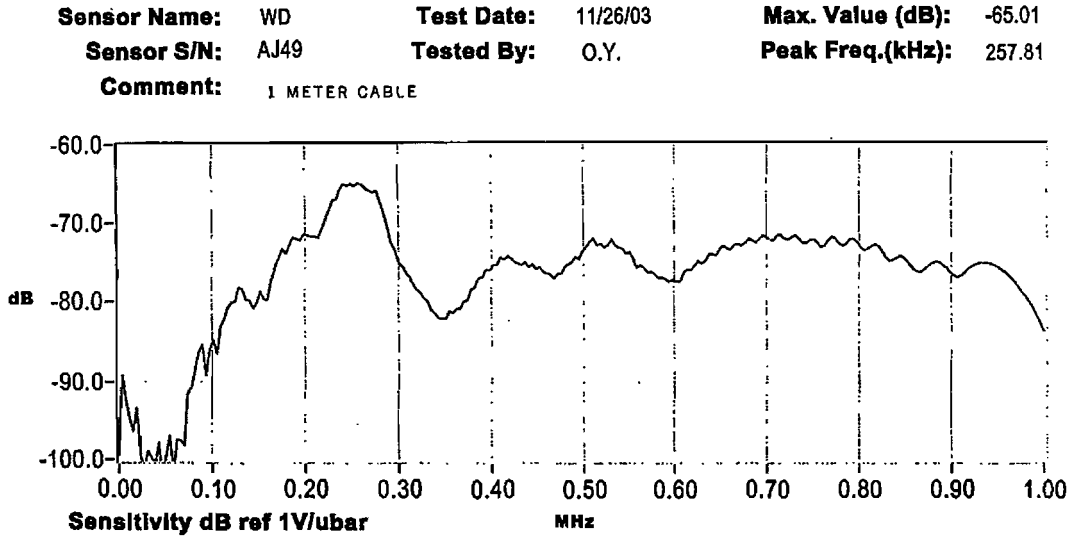

Figure 5.3: Calibration certificate for S2

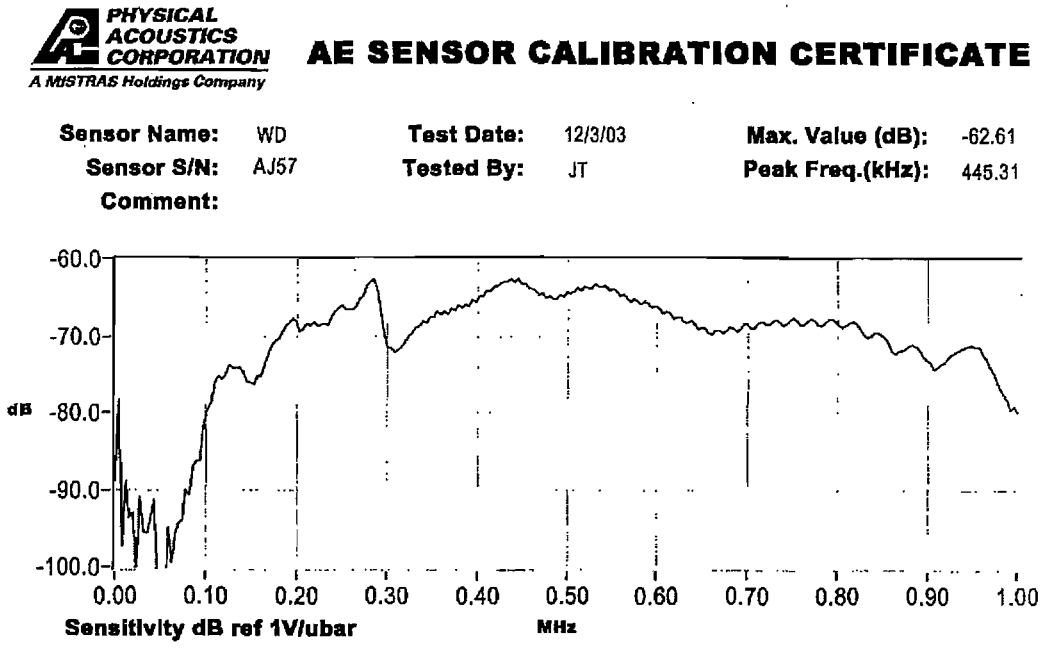

Figure 5.4: Calibration certificate for S3

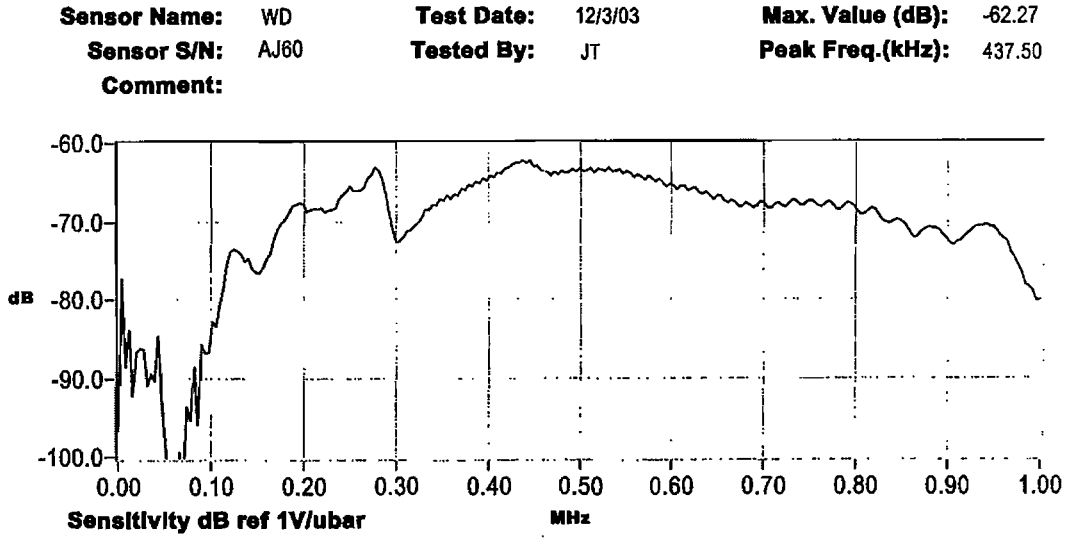

Figure 5.5: Calibration certificate for S4

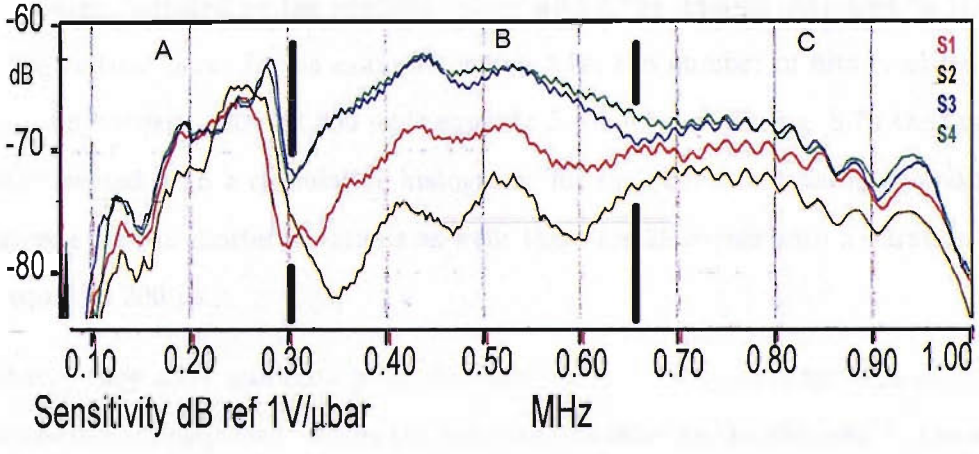

Figure 5.6: All the four calibration certificates are superimposed and shown here in different colours

5.3 PAC AEWin 2.0 software

PAC PCI-2-based system comes with a proprietory software, AEWin®, necessary for the acquisition of the data, and which also allows the operator to do some basic data analysis. The software can digitally record the waveforms and, independently,[3] extract real-time features of the acoustic emissions, such as: duration, counts, energy, amplitude, rise time, threshold, average frequency, etc. These features can be plotted against each other in many combinations during the "play-back" of the data recorded during the tests. Parametric inputs, such as the load applied by the test machine, can be mixed with these features as well.

The most used visualisation modes offered by AEWin in this work are three:

Histograms: they normally account for the number of hits recorded having the value of the parameter indicated by the abscissa falling within the interval indicated by the width of the vertical bars. In the example of Fig. 5.7a, the number of hits recorded with a duration between 100 and 200 μs is equal to $5 + 3 + 1 = 9$. In Fig. 5.7b the same data are presented with a cumulative histogram: for each bar, the total is not zeroed and accounts for the shorter durations as well: there are 25 events with a duration shorter or equal to 200 μs.

Point plots: they show one data point for each hit (or event), and for each of them two parameters are displayed, one by the ordinate, the other by the abscissa. In the example of Fig. 5.8, there is one event having 60 dB of amplitude, and happening 111 s after the start of the test.

Power spectra graphs: they are of limited usefulness, because the user has no direct control over the sampling time of the signals, nor the parameters for the calculations are transparent.

An essential feature to this work is the ability to export, as ASCII data files, the acoustic emission waveforms which will be eventually input into Matlab routines. Another important function implemented in the software under the name of "Waveform filtering and extraction utility" is that of post-processing the data in order to alter the acquisition parameters such as PDT, HLT, etc.; unfortunately when using this tool it was found that processing data

[3]The circuitry assigned to the waveform transient recording is not the same as that extracting the AE features. This means that the AE features can be extracted even if the transient recording is deactivated.

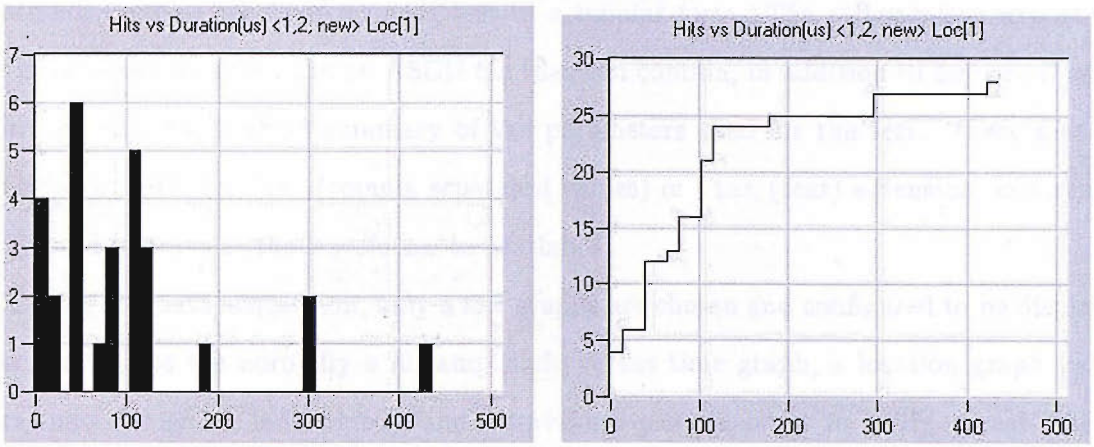

(a) Non-cumulative (b) Cumulative

Figure 5.7: Two examples of histograms

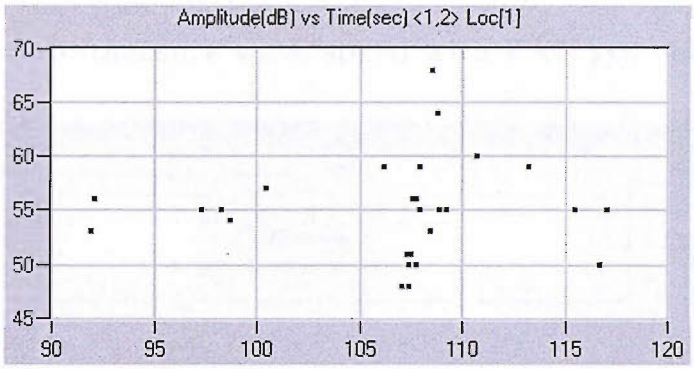

Figure 5.8: An example of a point plot

files repeatedly with the same parameters produced different outputs. Therefore this tool will not be used for this work.

In the following two sections (§5.3.3 and §5.3.2) are described two procedures essential to this work, set-up by means of AEWin: those of, respectively, measuring the wave speed in a given medium and setting-up a location.

5.3.1 General set-up procedure for AEWin software

The configuration of the PAC AE system is entirely done through its AEWin software, with the only exception of the preamplification gain, which is user-selectable through a physical switch on the preamp unit. Since each acquisition is often executed with a different set of parameters, these are normally stored in a *layout file* (`.lay`) accompanying each data set for a subsequent *replay* of the data file (`.dta`) during the analysis stage. The parameters that affect the testing, such as the timing-related ones (HDT, PDT, HLT) and the frequency

thresholds, will be reported for each test in a tabular form. The software can export the raw data of the waveforms in an ASCII file that can contain, in addition to numerical series expressed in volts, a short summary of the parameters used for the test. These files are identified by either a `.csv` (comma separated values) or `.txt` (text) extension, and can be easily used to transfer the waveforms to Matlab.

During the data acquisition, only a few graphs are chosen and configured to be displayed on screen: these are normally a hit-amplitude versus time graph, a location graph (when more than one sensor is involved), and a waveform plot, in order to verify in real-time — and possibly act to correct — respectively the collection of the signals, the correctness of the location setup, and the adequacy of the transient recording parameters.

5.3.2 Procedure to measure wave speed with PAC system

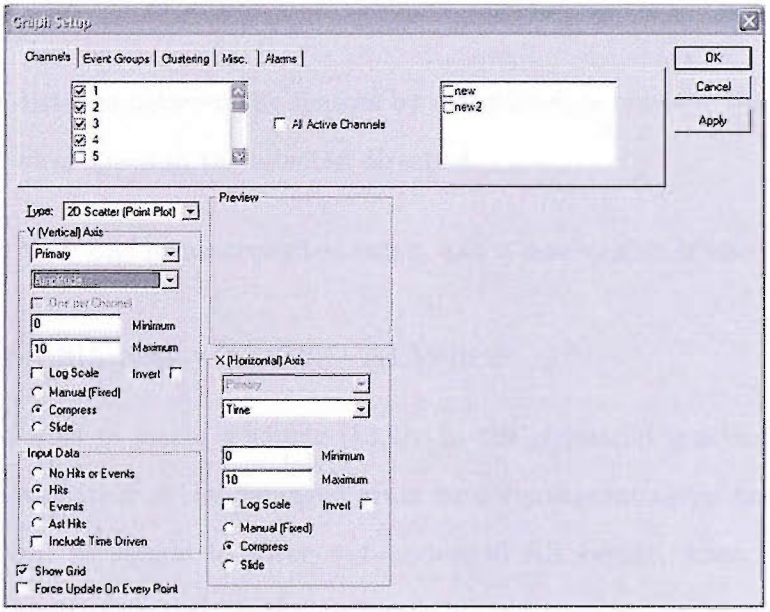

Figure 5.9: Graph setup window

In order to use the location capabilities of the PAC system (§5.3.3), it is necessary to know the wave speed in the given medium.

It can be easily evaluated through the following procedure.

1. Set up any 2D point plot graph, e.g. amplitude versus time is a good choice (like the graph in Fig. 5.8) because it provides an indication of the correct acoustic coupling as well.

2. In the `Graph Setup` window (Fig. 5.9), choose `Hits` as `Input Data`; the hits in fact need to be examined individually and not as a single located event.

3. Activate two channels and place two sensors enough apart on the structure; 10 cm is a good choice in such the resulting hits are so sufficiently separated in time, so that the calculation at point 6 is not dominated by numerical error.

4. Perform a pencil lead break, onto a position ideally aligned with the two sensors, and outside of them.

5. Locate on the graph of point 1 the two hits corresponding to the same event (usually the ones with the highest amplitudes), and read the two arrival times. These two hits are easily identified in the graph, in such they are minimally spaced in time, but consistently in amplitude, because of the large distance difference between the PLB and each sensor.

6. Divide the distance between the sensors by the difference between the arrival times to obtain the wave speed in the selected direction.

Usually more than one measurement is taken, and a mean value is chosen.

5.3.3 Location filtering with PAC AEWin

An AE system is able to locate a source (§3.9). In the industrial practice, this is usually aimed at the identification of the damaged areas for a consequent easier inspection. In this thesis, location will be sought to *filter out* undesired AE events, when they come from outside an area of interest and cannot be but extraneous sources. In what follows, two approaches to location filtering will be described, in view of an implementation in the PAC system.

5.3.3.1 Guard sensors

A guard sensor is an AE sensor used exclusively to discriminate from sources originating outside the area of interest. The most typical guard technique consists of a *data* sensor placed on the area of interest surrounded by several *guard* sensors (Fig. 5.10). AE waves from the area of interest will hit the data sensor before hitting any of the guards. Waves from outside will hit at least one of the guards before hitting the data sensor.

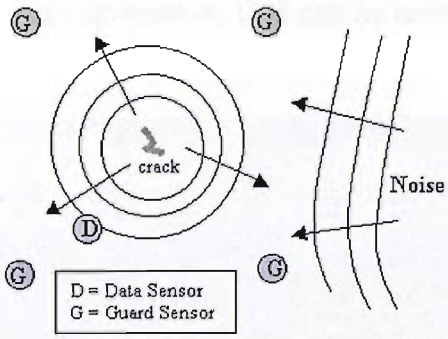

Figure 5.10: Guard sensor principle (Diederichs and Ginzel, 1999)

The PAC system only has four channels, which are insufficient for the guard strategy depicted in Fig. 5.10 on a panel. One substantial advantage of guard sensors, compared to the spatial filtering technique described in the next paragraph, would be that it can be used even when a good knowledge of the sound propagation in the medium lacks, like in composite structures.

5.3.3.2 Spatial filtering

Spatial filtering is essentially the use of the traditional localisation features of modern AE systems, but not with the aim of locating the damage but of accepting only those signals coming from an (approximate) area of interest. It is the technique used for all the tests described in §8. Spatial filtering requires only four sensor to describe and analyse a rectangular area of interest, compared to the five required by the guard sensor technique illustrated in the previous section. It is therefore possible to adopt this technique with the PAC system.

It should be emphasized that, in order to gain a reasonably good accuracy in the localisation, an equally good knowledge of the sound speed and timing strategies is needed; in spite of that, this is not fully true, given the anisotropy and inhomogeneity of composites (see §4.5). Nevertheless, since the goal of the localisation process in this step of the present research is just to include only the signals coming from an area of interest, it does not matter if this area is further reduced and less well approximated, as long as it includes only a defined inner portion of the panel.

5.3.3.3 Implementation in AEWin

Fig. 5.11 shows the location set-up window in the software. The following is a description

of the settings in the location set-up window, that can be used in order to achieve location filtering.

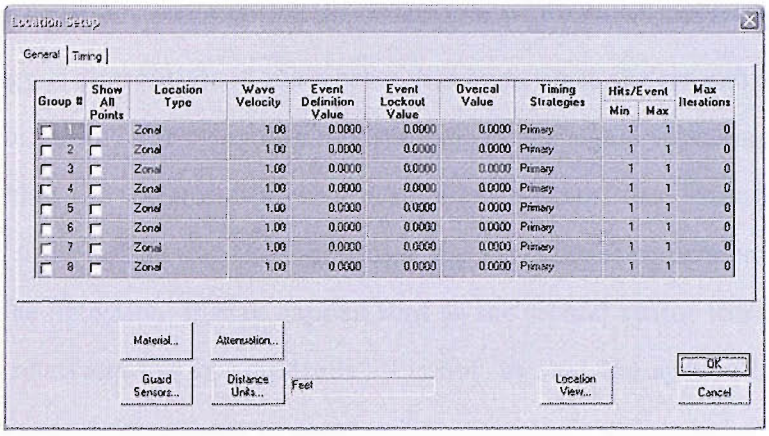

Figure 5.11: Location Setup window in PAC AEWin 1.53

- Group # Selects which predefined groups of channels are to be used for location purposes. It is possible to group together some or all channels from Acquisition Setup > Channel Group Setup. Then, the adjacent columns consent to specify a different timing strategy for each group or, if desired, the same strategy for all of them.

  There can be various reasons for grouping the channels; perhaps the most typical being to assign a different wave speed for sensors located in different areas (of possibly different material) of the structure.

- Show all points Displays points (hits, events) coming from all the timing strategies defined.

- Event Definition Value (EDV) Is the maximum distance between the sensors (within the selected group); this of course coincides with the distance between the sensors, when two sensors are used.

- Event Lockout Value Equal or lesser that EDV, is the distance between the sensors to consider for location. This can be substantially lesser than EDV to ensure that no events coming from outside the sensors are considered.

- Overcal Value Is a sort of tolerance on the EDV. Traditionally it is set to $\approx$ 10% EDV, but can be set equal to zero to better exclude external events.

- Timing Strategies Refers to what is defined in the next tab (Timing), with Secondary being either 1, 2, 3 or 4. Primary stands for FTC (First Threshold Crossing), i.e. a signal is detected as arrived at one sensor as soon as it passes the acquisition threshold. This strategy is appropriate in most cases, but sometimes the sensors may be far apart from each other and the attenuation/dispersion of the signal travelling the medium so significant that the waveforms arrived at different sensors are substantially modified in shape, and if for instance at the first sensor the extensional component is large enough to trigger the detection, it may happen that at the second sensor the same component — usually relatively low in amplitude — is not, so that the system has to "wait" for the larger flexural component to come, which nevertheless does not correspond to the same time-scale position.

  Opposite to Primary, selecting Secondary it is possible to select Peak Timing (PT) instead of FTC. In this way the system can derive the arrival time from the waveforms, modifying the waveform threshold. PT sets the arrival time at the detected waveform peak.

  Each timing strategy can have a different wave velocity.

- Hits/Events Min/Max Are relative to planar location, and tell the system how many sensors must be hit to obtain an event. The usefulness of setting Max lesser than the total number of channels is primarily to lower the CPU load. Max iterations Are somehow related to the computing accuracy, 256 being a fine first attempt.

5.3.3.4 Description of a typical set-up

The steps illustrated in §5.3.3.3 will be exemplified in this section for the case of the test on a tensile strip, likewise the tests described in §8.

The strip has a gauge length of 30 cm, but the two sensors, connected to channels 1 and 2, are placed 21 cm apart. This can be seen in Figures 5.12 (the two numbers on top represent the channel numbers, and their distance can be read on the abscissa), 5.13 (the intra-sensors distance, expressed in metres, coincides with the Event Definition Value, and the wave velocity, measured as in §5.3.2 along the direction of the strip, is 5050 m/s), and 5.14 (the positions of the sensors is input into a "free structure", with only one meaningful coordinate, X, expressed in metres). In order Fig. 5.12 displays events and not unlocated

hits, a few more steps are necessary in the graph setup window (Fig. 5.15): "Events" is selected in the "Input data" section, and the "linear location group" consisting in channels 1 and 2 is activated ("On").

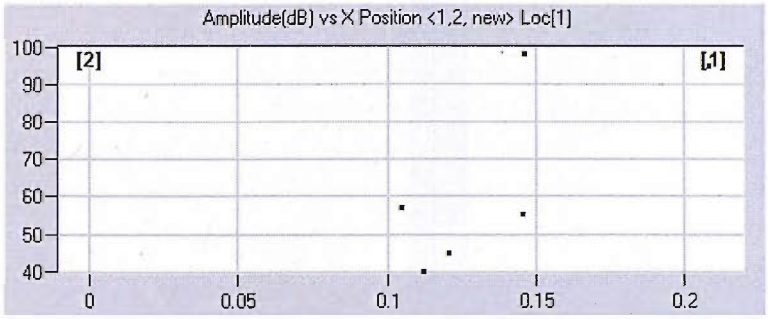

Figure 5.12: Location example: the events located in an amplitude versus position point-plot

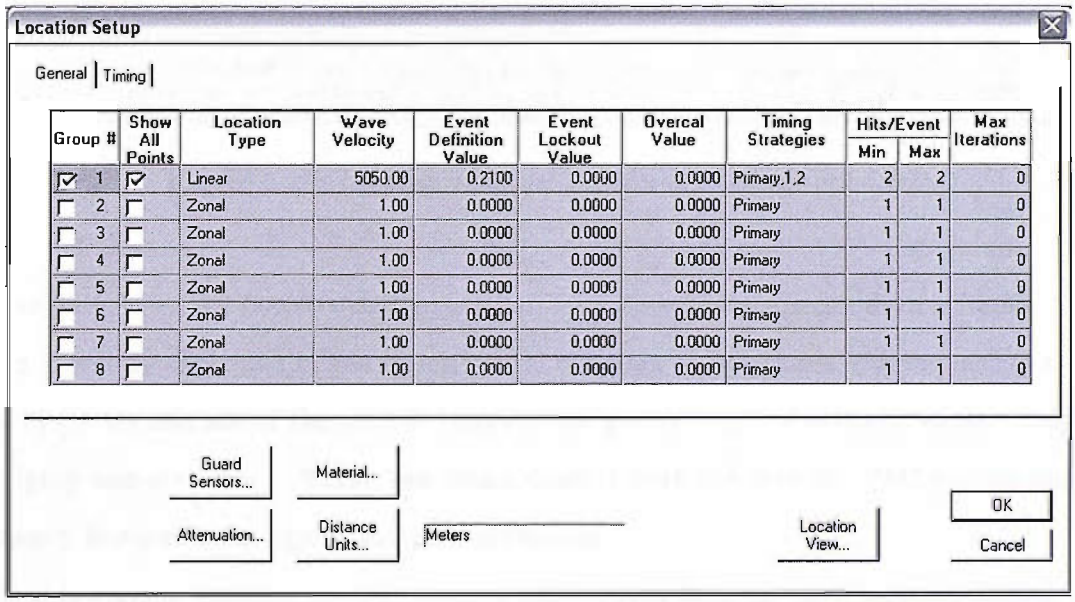

Group #	Show All Points	Location Type	Wave Velocity	Event Definition Value	Event Lockout Value	Overcal Value	Timing Strategies	Hits/Event Min	Hits/Event Max	Max Iterations
☑ 1	☑	Linear	5050.00	0.2100	0.0000	0.0000	Primary,1,2	2	2	0
☐ 2	☐	Zonal	1.00	0.0000	0.0000	0.0000	Primary	1	1	0
☐ 3	☐	Zonal	1.00	0.0000	0.0000	0.0000	Primary	1	1	0
☐ 4	☐	Zonal	1.00	0.0000	0.0000	0.0000	Primary	1	1	0
☐ 5	☐	Zonal	1.00	0.0000	0.0000	0.0000	Primary	1	1	0
☐ 6	☐	Zonal	1.00	0.0000	0.0000	0.0000	Primary	1	1	0
☐ 7	☐	Zonal	1.00	0.0000	0.0000	0.0000	Primary	1	1	0
☐ 8	☐	Zonal	1.00	0.0000	0.0000	0.0000	Primary	1	1	0

Figure 5.13: Location example: the location setup window

5.3.4 Frequency calculations

Associating the acoustic emission with single numbers (the parameters) is not the only choice of analysis: the whole digitized signal, recoded in the time space, can be used to perform calculations in the frequency domain. In this way, another series of quantities can be associated with the acoustic emissions, derived from their power spectrum. In this thesis, the frequency centroid will be most used, defined as the first-order statistics of the

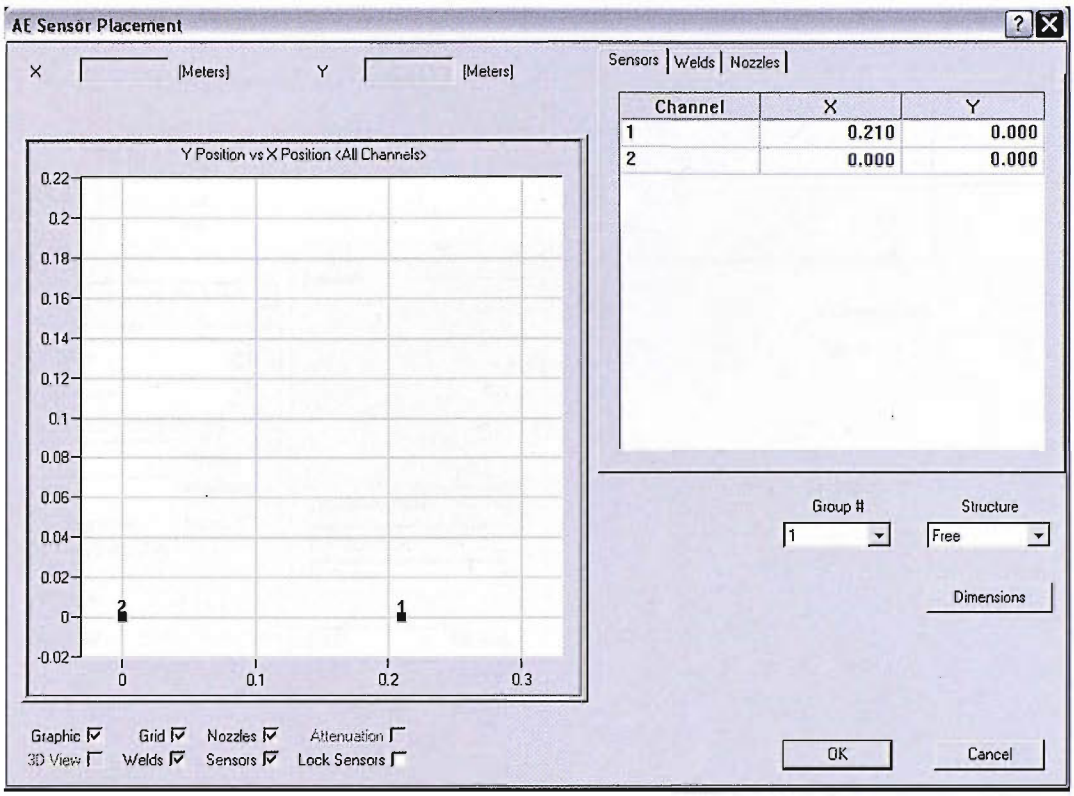

Figure 5.14: Location example: the sensor placement window

spectrogram,[4] i.e. the power-weighted median frequency of the spectrum in a frame.

As it will be explained in the experimental chapters of this thesis, (i) frequency calculations of the signals are of the utmost importance, and (ii) typical acoustic emission signals are highly non-stationary. These two issues conflict with the way the PAC system obtains frequency features from signals sampled differently.

In this system, the frequency features are calculated from the waveform associated with the hit. The length of the collected waveform depends on parameters, and the interactions thereof, like HDT, PDT, HLT, pre-trigger length and, most importantly, the maximum byte length, which does not have a duration associated with it if a sampling rate is not specified as well. The problem here is that if the waveform length is greater than 1 kbyte, the FFT that is used for the frequency features calculations is a result of averaged 1 kbyte FFTs (Bradshaw, 2006). Typical signals have a large intensity initially and then rapidly decrease and are therefore non-stationary, so this way of averaging the frequency features calculations is highly inappropriate. In fact:

1. the results strongly depends on the total length of the signal that has been sampled,

[4] A graphic representation of a spectrum.

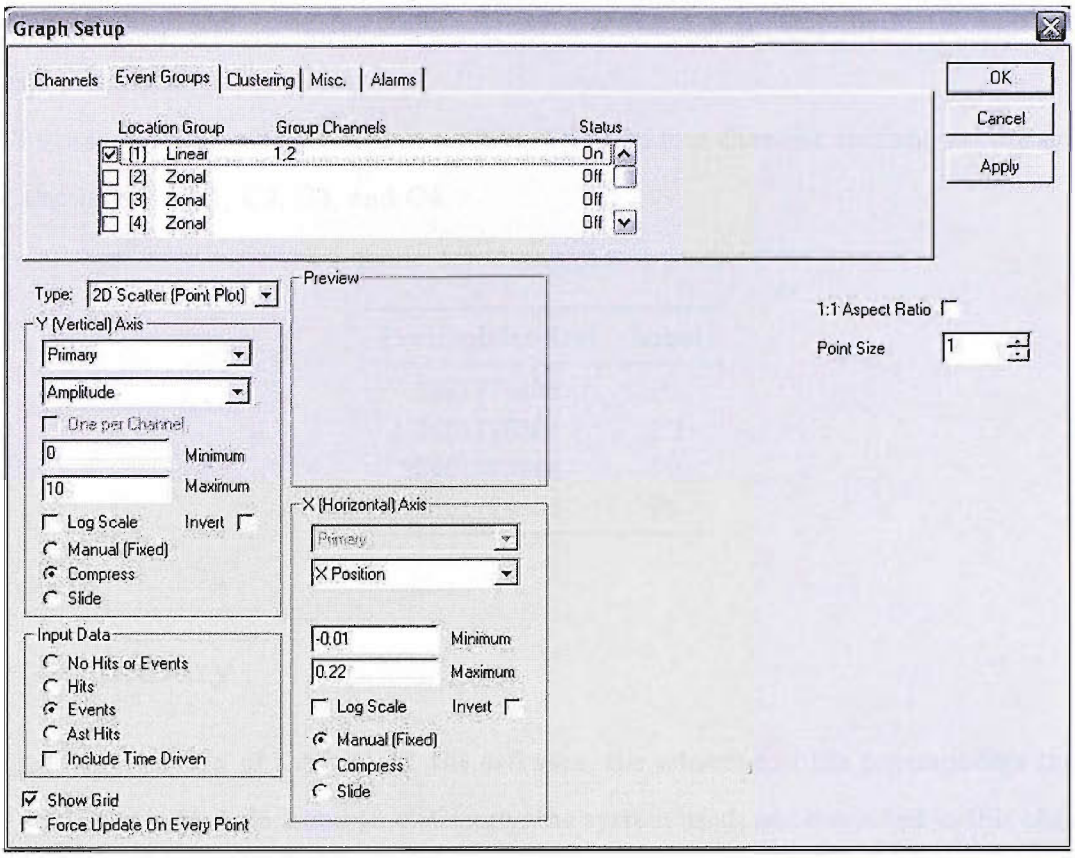

Figure 5.15: Location example: the graph setup window

2. this total length is not directly selectable by the user, but is rather the result of the interaction of the parameters mentioned before,

3. a signal that extends itself for 2 kbyte, for instance, will be treated differently from a signal contained within 1 kbyte, and will normally be associated to a different frequency centroid, even in presence of an identical spectrum.

In the rest of the thesis, some of these calculations will be executed by Matlab routines, as it shall be explained in the experimental chapters.

5.4 The preamplifiers

The four PAC "2/4/6" preamplifiers used were designed to be used with all available AE systems that have their power supplied via the output signal BNC. The preamplifiers have a switch-selectable gain providing 20/40/60 dB gain (switch selectable), and operate with either a single-ended or differential sensor. Plug-in filters provide the possibility to optimize

sensor selectivity and noise rejection. These are "voltage preamplifiers", as opposed to "charge preamplifiers".

The preamplifiers were labelled as in Table 5.3. The four channels available on the system were also labelled C1, C2, C3, and C4.

Table 5.3: Preamplifiers labels

Preamplifier S/N	Label
2461775406	P1
2461776406	P2
2461773406	P3
2461774406	P4

5.5 Summary

§5.1 gave an overview of the system, the software, the sensors and the preamplifiers thereof were described in §5.3, §5.2 and §5.4. Clearly, the system used, and described in this chapter, is not flawless, nor immune from defects. Some of these were unexpected (the bugs in the software, the far-from-high-fidelity response of the sensors, the way of calculating frequency features), others were known *a priori* (the limited number of channels).

The wide variation in the response of the sensors must have some effect on the results, particularly the calculated hit/absolute energy and other AE features. Therefore series of experiments will be designed to establish the effect this variability has on the results and on the frequency spectrum; they will be described in §6.2. It should be noted that these differences in sensitivity cannot be adjusted by preamplification as the sensors are broadband and have a non-uniform frequency response.

The issues described about the frequency calculations prompt the use of alternative tools: some Matlab routines will be written and used on raw data files exported from AEWin; they will be presented throughout chapter 6 and 7.

CHAPTER

SIX

Consistency of AE parameters

I didn't think; I experimented.

Wilhelm Roentgen

An AE characterisation of a damage is ultimately the characterisation of a signal produced by an acoustic source and propagated through a medium. This chapter will describe several experiments conducted using a pencil lead break (PLB) as a source, and metal plates of different shapes and sizes, or composite panels and strips, as a travelling medium. The PLBs are not related to the actual acoustic emissions generated from a damage, and they represent an almost impulsive source that therefore introduces a broadband spectrum of frequencies in the structure. This is particularly suitable to verify the performance of a broadband sensor like the PAC WD.

The aims of the experiments contained in this chapter are:

1. showing the variability of the collected signals with parameters such as equipment, geometry, position, etc., and by doing so validating the consistency of AE parameters,
2. suggesting testing parameters for the subsequent tests,
3. emphasizing what can and cannot be achieved when undertaking a study of characterisation of a source in terms of AE,
4. assessing the effect of different sensor sensitivity.

6.1 The pencil lead break source

A pencil lead break on a specimen is an easy and effective way to simulate an out-of-plane excitation which produces an acoustic emission rich in the flexural mode. These "simulations" have already been carried out in literature to investigate the waveform propagation in composite panels (Banerjee and Mal, 2005).

In a standard pencil-lead break test (§3.6), the AE source should originate from the fracture of the lead, and not from the impact of the pencil onto the surface. The stress release is then transmitted through the lead to the specimen. A teflon guide ring is used to ensure that it is the break signal, and not the subsequent impact of the pencil on onto the specimen, that will be detected. Globally, the Hsu-Nielsen source depends on three parameters: the lead length, the angle of the lead on the surface, and the impact.

A modified version of the test is adopted in this chapter,[1] which aims at reducing the variables to one: the length of the lead only. To do this, the pencil leans on the surface (as in Fig. 6.1) and the break is obtained by gently rotating the pencil around the point where the metallic sleeve is in contact with the surface. In this way sufficient energy is released into the material but there is no impact and the only variable is the length of the lead, maintained at about 3 mm throughout the tests.

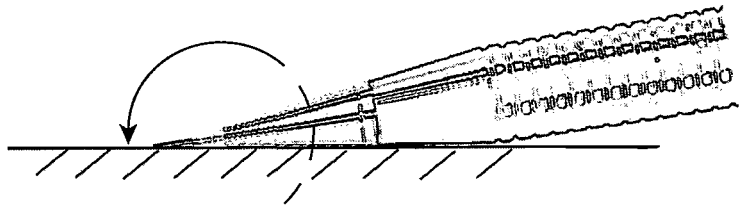

Figure 6.1: Modified pencil lead break test: starting position and indication of the movement

6.2 The response of the sensors

A necessary condition for a signal characterisation is that, for the same source, the system (considered here as a combination of sensor / preamplifier / acquisition system) responds with the same output. Verifying the extent to which this may be true is the aim of the tests described in this section. This verification is achieved by conducting a series of tests designed so that the results coming from each sensor are nominally comparable and thus

[1] With the only exception of the tests described in §6.2, where a standard PLB is used

permit the study of the response of the system to the source. The aspects under scrutiny during the following experiments are what is usually referred to as "AE features" or "AE parameters" (hit energy, hit amplitude, hit duration, hit counts, etc.) i.e. those that have been traditionally used to study structural performance.

It is well known that there is significant attenuation of the signal with distance (Ni *et al.*, 2001), and this is normally measured by hit amplitude. The tests described in this section are designed to verify the dependence of the other AE features (duration, counts, etc.) on the recorded amplitudes, and whether there are unacceptable variations for nominally identical sources. A further consideration is thus the accuracy and the effectiveness itself of the AE features in the description of the sources.

The tests described in this section will investigate:

- the performance of the system,
- the relation between the system sensitivity and the results,
- how the performance of single sensors affects the location of the source, executed with the information of two or more sensors.

Two main groups of tests (here called "Y" and "J") are reported here. They consist of several pencil lead breaks on an aluminium plate, 6 mm thick, upon which the four sensors are arranged in a 200 mm square pattern, as shown in Fig. 6.2. Each set consists of readings taken from four pencil lead breaks in the centre of the specimen as shown in Fig. 6.2. During

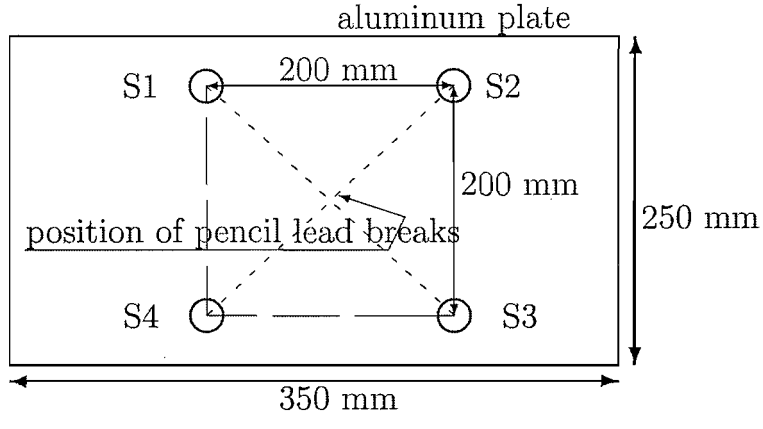

Figure 6.2: Simple layout for tests J and Y

Y tests, the preamplifiers (P) were fixed to the same channel (C) and only the sensors (S) positions changed as shown in Table 6.1. In the J tests the preamplifiers (P) were fixed to the same sensors (S) throughout the tests; only the channels (C) moved their positions over

the preamplifier/sensor couples as defined in Table 6.2.[2]

Table 6.1: Y tests layout

Test Y1	S1 P1 C1	Test Y2	S1 P2 C2
	S2 P2 C2		S2 P1 C1
	S3 P3 C3		S3 P4 C4
	S4 P4 C4		S4 P3 C3
Test Y3	S1 P3 C3	Test Y4	S1 P4 C4
	S2 P4 C4		S2 P3 C3
	S3 P2 C2		S3 P1 C1
	S4 P1 C1		S4 P2 C2

Table 6.2: J tests layout

Test J1	S1 P1 C1	Test J2	S1 P1 C2
	S2 P2 C2		S2 P2 C1
	S3 P3 C3		S3 P3 C4
	S4 P4 C4		S4 P4 C3
Test J3	S1 P1 C3	Test J4	S1 P1 C4
	S2 P2 C4		S2 P2 C3
	S3 P3 C2		S3 P3 C1
	S4 P4 C1		S4 P4 C2

The symmetry of the geometry and the isotropy of the material should yield consistent and similar results for each channel within each single test. From one test to another, the sensors are not moved. This situation is ideal for checking the consistency of the system output.

6.3 Absolute energy

The "Absolute Energy" readings are analysed to provide a first benchmark of the system response. Table 6.3 summarises the average absolute energy values for each channel and single Y test, and illustrates the position of each sensor within each test. Common cell styles in the table denote results coming from the same experimental configuration and then, row by row, correspond to the same pencil lead break.

Each cell displays the arithmetic mean (μ, fifth row) and the standard deviation (σ, sixth row) of the four hits for the specified triplet of sensor, channel and preamplifier. The arithmetic mean (μ_μ) and the standard deviation (σ_μ) of the means of all the results from

[2]Tests Y1 and J1 are nominally identical. For test J4, only three valid breaks were found.

Table 6.3: Results for "Y" tests (Absolute energy, aJ)

	C1/P1	C2/P2	C3/P3	C4/P4	
S1	827.202E+03 (I) 787.912E+03 885.466E+03 732.184E+03 μ = 808,191 σ = 55,949 (7%)	592.504E+03 902.855E+03 989.450E+03 1.040E+06 μ = 881,221 σ = 173,762 (20%)	1.554E+06 976.107E+03 616.338E+03 827.907E+03 μ = 993,604 σ = 347,925 (35%)	1.854E+06 964.823E+03 1.728E+06 994.894E+03 μ = 1,385,289 σ = 408,004 (29%)	μ_μ(S1) = 1.0171e+06 σ_μ(S1) = 2.2261e+05 (22%)
S2	2.968E+06 4.400E+06 5.340E+06 5.587E+06 μ = 4,573,604 σ = 1,027,449 (22%)	3.857E+06 3.495E+06 4.141E+06 3.345E+06 μ = 3,709,658 σ = 310,988 (8%)	8.559E+06 4.293E+06 7.751E+06 4.405E+06 μ = 6,251,853 σ = 1,924,927 (31%)	6.704E+06 4.320E+06 2.668E+06 3.708E+06 μ = 4,350,061 σ = 1,481,818 (34%)	μ_μ(S2) = 4.721e+06 σ_μ(S2) = 9.3883e+05 (20%)
S3	22.701E+06 10.555E+06 21.516E+06 10.104E+06 μ = 16,219,046 σ = 5,906,562 (36%)	16.637E+06 9.139E+06 5.766E+06 8.351E+06 μ = 9,973,481 σ = 4,044,582 (40%)	9.954E+06 (II) 8.634E+06 10.589E+06 8.374E+06 μ = 9,387,692 σ = 916,570 (10%)	5.881E+06 9.709E+06 10.885E+06 11.999E+06 μ = 9,618,337 σ = 2,304,613 (24%)	μ_μ(S3) = 11.2996e+06 σ_μ(S3) = 2.8479e+06 (25%)
S4	10.245E+06 5.341E+06 3.346E+06 4.541E+06 μ = 5,868,145 σ = 2,624,649 (45%)	11.017E+06 5.195E+06 11.193E+06 5.062E+06 μ = 8,116,681 σ = 2,989,311 (37%)	2.846E+06 4.816E+06 5.676E+06 6.375E+06 μ = 4,928,338 σ = 1,323,122 (27%)	4.420E+06 3.956E+06 4.943E+06 3.545E+06 μ = 4,215,948 σ = 521,294 (12%)	μ_μ(S4) = 5.7822e+06 σ_μ(S4) = 1.4696e+06 (25%)
	μ_μ(C1/P1) = 6.8672e+06 σ_μ(C1/P1) = 5.7102e+06 (83%)	μ_μ(C2/P2) = 5.6703e+06 σ_μ(C2/P2) = 3.5806e+06 (63%)	μ_μ(C3/P3) = 5.3904e+06 σ_μ(C3/P3) = 3.0111e+06 (56%)	μ_μ(C4/P4) = 4.8924e+06 σ_μ(C4/P4) = 2.9743e+06 (61%)	

the same sensor, and of those from the same couple channel/preamplifier, are displayed respectively on the right and at the bottom of the table. The percentages refer to the ratio of σ over μ.

Similarly, Table 6.4 summarises the average absolute energies for each channel and J test, and illustrates the position of each sensor within each test. Here, the S1/P1 couple always gives the lowest readings, S3/P3 always the highest. A comparison of the two tables in terms of averages and standard deviations shows that the sensors play the most important role and both sets of results show similar trends. Therefore the remaining analysis concentrates on the results in Table 6.3.

Table 6.4: Results for "J" tests (Absolute energy, aJ)

	C1	C2	C3	C4	
S1 P1	1.665E+06 1.280E+06 961.003E+03 925.415E+03 μ = 1,207,682 σ = 297,699 (25%)	1.140E+06 679.856E+03 849.578E+03 674.340E+03 μ = 835,998 σ = 189,241 (23%)	960.409E+03 739.816E+03 773.890E+03 855.593E+03 μ = 832,427 σ = 85,029 (10%)	1.094E+06 2.086E+06 997.507E+03 N/A μ = 1,392,545 σ = 492,044 (35%)	μ_μ(S1/P1) = 1.0671e+06 σ_μ(S1/P1) = 2.4195e+005 (23%)
S2 P2	4.678E+06 2.897E+06 3.392E+06 2.829E+06 μ = 3,449,340 σ = 742,132 (22%)	6.836E+06 4.770E+06 4.299E+06 4.062E+06 μ = 4,991,842 σ = 1,095,075 (22%)	3.302E+06 6.722E+06 3.013E+06 N/A μ = 4,345,446 σ = 1,684,332 (39%)	2.746E+06 2.170E+06 2.497E+06 2.444E+06 μ = 2,464,192 σ = 204,561 (8%)	μ_μ(S2/P2) = 3.8127e+06 σ_μ(S2/P2) = 9.5193e+005 (25%)
S3 P3	9.310E+06 14.977E+06 8.043E+06 N/A μ = 10,776,767 σ = 3,014,753 (28%)	8.748E+06 6.835E+06 6.886E+06 7.901E+06 μ = 7,592,319 σ = 791,205 (10%)	20.016E+06 12.769E+06 10.206E+06 10.285E+06 μ = 13,318,840 σ = 4,001,349 (30%)	10.835E+06 6.619E+06 8.120E+06 6.550E+06 μ = 8,031,014 σ = 1,736,110 (22%)	μ_μ(S3/P3) = 9.9297e+06 σ_μ(S3/P3) = 2.3061e+006 (23%)
S4 P4	4.802E+06 3.768E+06 3.952E+06 4.476E+06 μ = 4,249,417 σ = 411,262 (10%)	5.812E+06 9.994E+06 5.038E+06 N/A μ = 6,948,112 σ = 2,177,069 (31%)	5.856E+06 3.727E+06 4.539E+06 3.656E+06 μ = 4,444,316 σ = 885,926 (20%)	10.653E+06 6.981E+06 5.313E+06 5.230E+06 μ = 7,044,408 σ = 2,197,618 (31%)	μ_μ(S4/P4) = 5.6716e+006 σ_μ(S4/P4) = 1.3269e+006 (23%)
	μ_μ(C1) = 4.9208e+006 σ_μ(C1) = 3.5600e+006 (72%)	μ_μ(C2) = 5.0921e+006 σ_μ(C2) = 2.6372e+006 (51%)	μ_μ(C3) = 5.7353e+006 σ_μ(C3) = 4.6137e+006 (80%)	μ_μ(C4) = 4.7330e+006 σ_μ(C4) = 2.8516e+006 (60%)	

The results in Table 6.3 show that for the same sensor, four separate pencil lead breaks yield four different responses with standard deviations in the range 7 to 45%. This shows that a PLB is not a constant source (in terms of absolute energy) and cannot be used for absolute calibration. However, the average results for each sensor show in a clear and evident way, S1 consistently gives the lowest readings, S3 the highest ones. Within each cell, the reported standard deviation values mostly account for a poor overall uniformity of the source, but for these tests and the following analyses the homogeneity of the source from test to test would not be an issue. No trend is shown in the response over the different channels/preamplifiers: the averages μ_μ reported in the fifth row are substantially the same, especially if compared to the high variability of the other quantities.

The intention of the analysis is to understand why the Absolute Energy values are so different over the four sensors which are nominally identical. There is no indication of any faulty sensor, but rather of a poor overall homogeneity amongst the four sensors. By examining the collected data, it is possible to see that the average absolute energy values for each sensor over all Y tests are in order, from Table 6.3: $\mu_\mu(S1) = 1.0171 \times 10^6$ aJ, $\mu_\mu(S2) = 4.721 \times 10^6$ aJ, $\mu_\mu(S4) = 5.7822 \times 10^6$ aJ, $\mu_\mu(S3) = 11.2996 \times 10^6$ aJ. Dividing the highest by the lowest gives $\mu_\mu(S3)/\mu_\mu(S1) = 11$, which is very close to the maximum amplitude difference[3] in dB (10) found over the calibration certificates (Fig. 5.6), which accounts for a signal ratio of $\sqrt{10}$ and then for a power (or energy) ratio of 10.

A starting point for a possible explanation is the comparison of two hits picked from the test Y1 (from S1C1P1 and S3C3P3), and labelled in Table 6.3 as (I) and (II). These readings have been acquired from the same pencil lead break by two different sensors, and are chosen because their AE features are reported very differently by the system. Table 6.5 displays the features as reported by the PAC system for these two hits.[4]

Table 6.5: Comparison between hits I and II

	Rise time (μs)	Counts	Energy	Durat. (μs)	Ampl. (dB)	Frequency centroid (kHz)	Maximum peak frequency (kHz)
(I)	22	2000	676	13482	82	337	222
(II)	70	2926	2478	20821	90	388	537

Fig. 6.3 permits the visual analysis of the two hits I and II: the two power spectra displayed have a strong resemblance; the only major difference lies in the overall intensity. The large frequency distance of the reported maximum peak positions does not account for two power spectra which are substantially the same in shape (although different in overall intensity). On the other hand, this similarity is suggested by the similar frequency centroid values (Table 6.5).

The next step of the analysis would be to check if the different results provided by the two sensors could be explained by their sensitivity as reported by the calibration certificates (shown in Figures 5.2 and 5.4) which, at a first glance, appear identical. In Fig. 6.4, hit I is displayed superimposed over the calibration certificate for its sensor (S1), and in Fig. 6.5,

[3]The same ratio is a little smaller over the J tests.

[4]The "energy", as used by AEWin, is a dimensionless parameter, and the maximum peak frequency is simply indicated as peak frequency.

hit II is displayed over S3's frequency response.[5] These figures show that (i) the pencil lead break spreads over almost all the available frequency range, without concentrating on any sensitivity peak of the sensor, (ii) although the sensors are still quite sensitive at high frequencies, most of the activity of the pencil lead breaks falls below 750 kHz, (iii) in the low-frequency range, the spectrum of the input practically follows the sensitivity of the sensor.

The comparison of the spectra of the PLBs with the calibration certificates of the four sensors does not seem to provide an adequate explanation of the order found in the results. The calibration certificates show a different order for most (zones B and C of Fig. 5.6)

[5]The vertical units are not displayed because the calibration graph cannot be directly compared with the power spectrum of the waveform.

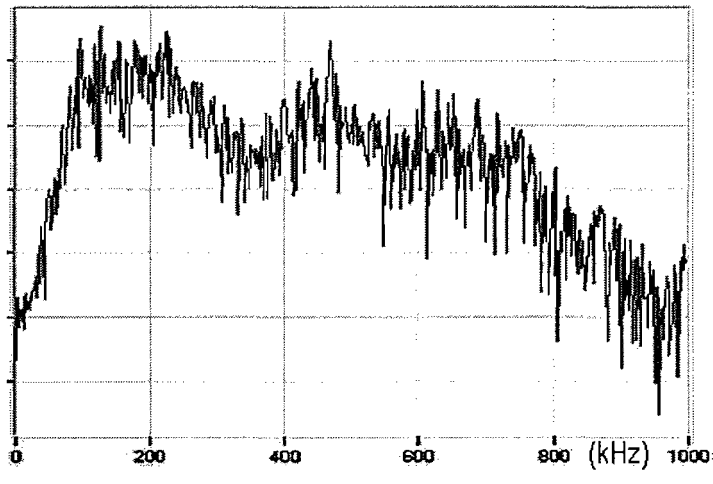

(a) Power spectrum of hit I from S1

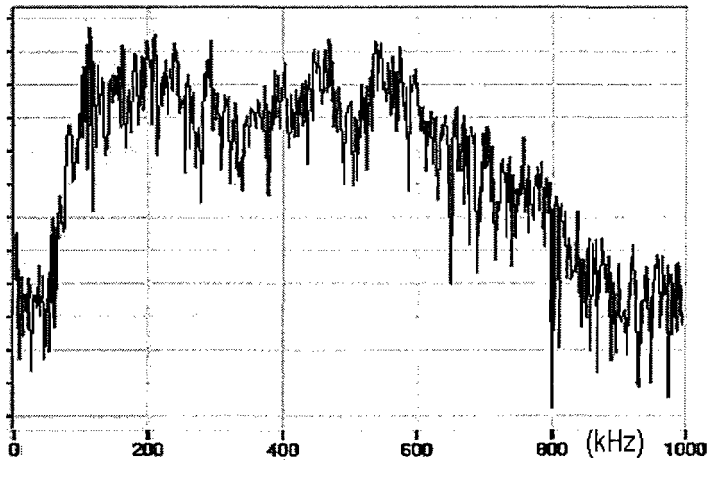

(b) Power spectrum of hit II from S3

Figure 6.3: Normalised power vs frequency (kHz) for the very same event detected as hits I and II by sensors S1 and S3, as generated by AEWin

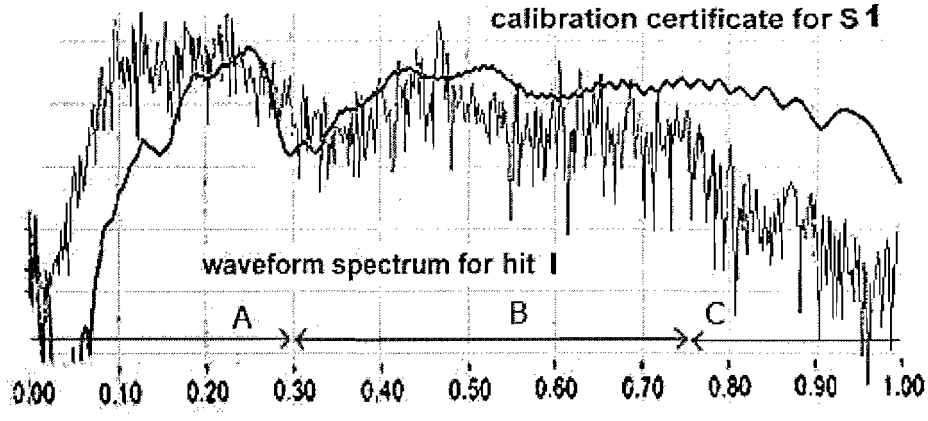

Figure 6.4: Hit I over S1's calibration certificate, normalised power vs frequency (kHz)

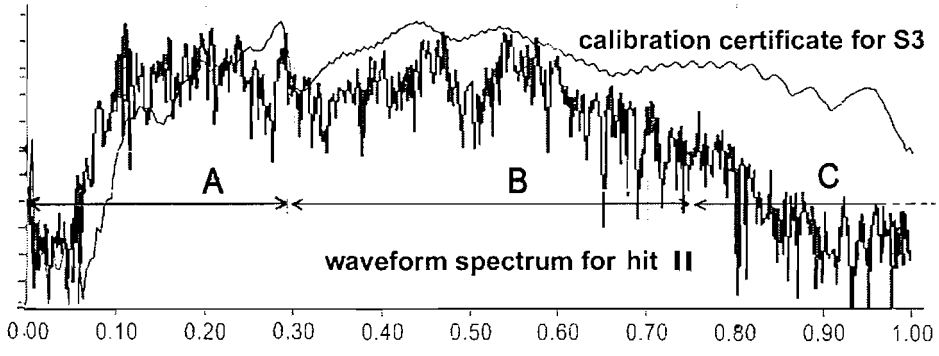

Figure 6.5: Hit II over S3's calibration certificate, normalised power vs frequency (kHz)

of their working band of 100–1000 kHz. The region that matches the order found in the absolute energy readings (S1, S2, S4, S3) is around 0.28 MHz. It is thus likely that a more plausible explanation is deeper than the spectra presented by AEWin: Figure 6.6 considers one waveform from test Y1, and truncates it after, respectively, 25, 50, 100 and 300 μs; in each of the four frames, the waveform and the corresponding raw nondimensional power spectrum are displayed, as computed by external Matlab routines. Differently from the spectra displayed by AEWin (for example Fig. 6.5), the scale is linear, and so it is easier to see that the activity is not really spread over all the spectrum. It is also possible to observe that the resulting spectrum of Fig. 6.6 tends to that of Fig. 6.5 when the signal truncation is delayed. In relation to the previously mentioned issue of the order of the outputs, the following considerations can be made:

1. The algorithm used by the PAC system to generate hit amplitudes and absolute energy is not public, but it clearly has to include some sort of integration of the signal over

the time and/or the frequencies. The extremes of these ranges are not known, but Fig. 6.6 clearly indicates that they can have a significant effect on the final results.

2. When the signal is truncated relatively soon, it almost contains only frequencies in the range indicated as A in Fig. 5.6. Within this range, the order shown by the calibration certificates is different from that in zones B and C.

3. The "black box" nature of the specific algorithms used for calculating the AE features, together with the significant differences that different algorithms would have on the outputs, further deprive these features of significance.

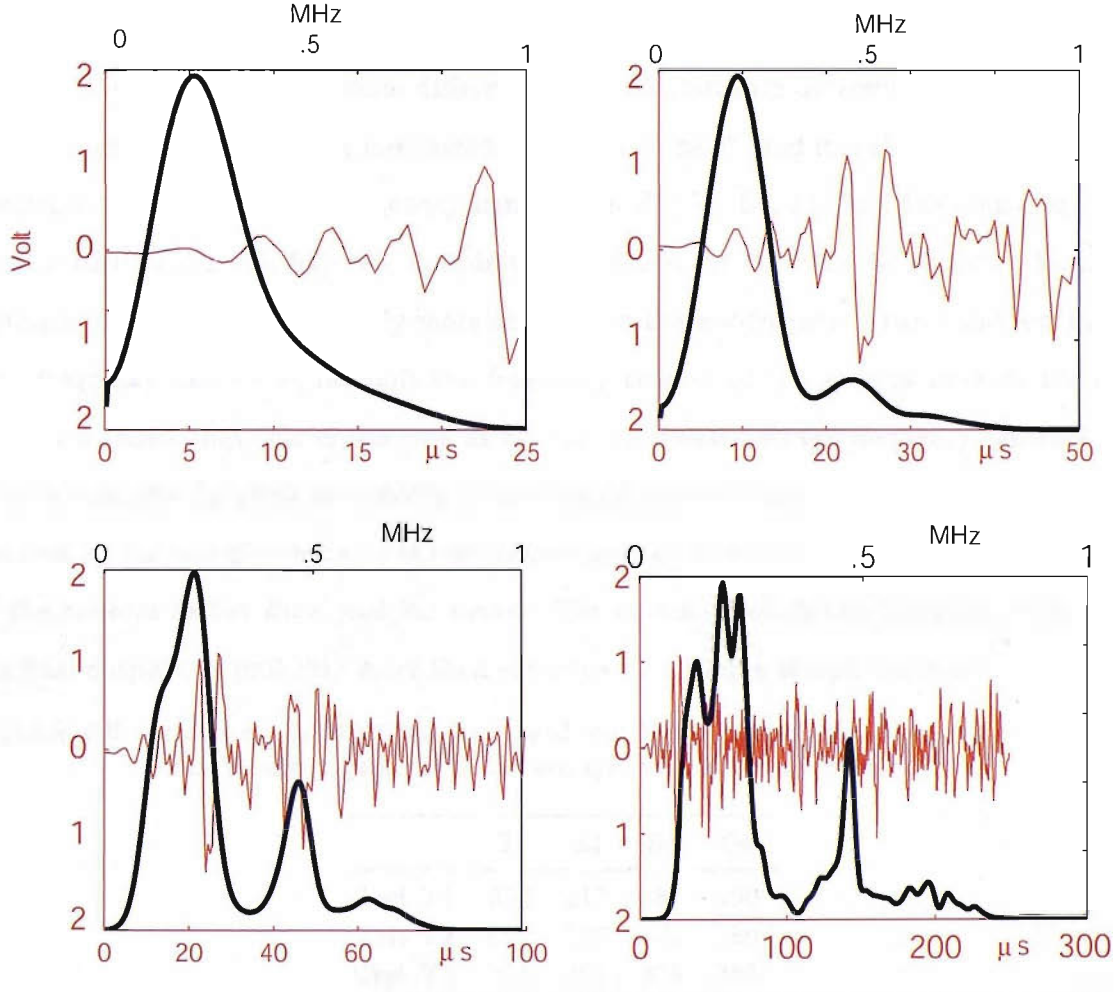

Figure 6.6: An acoustic emission from test Y1 truncated after 25, 50, 100 and 300 μs, displayed in time (V,μs) and frequency domain (normalised spectra)

The principal conclusion from this analysis is that *the Absolute Energy readings provided by the PAC system are directly affected by the sensitivity of each sensor, and describe them rather than the real event.* Also, the combination source / sensor is a fun-

damental determinant of the values obtained; different sources can excite differently different sensors and affect the final readings.

6.4 Frequency spectra

Table 6.6 provides the frequency centroids of the hits from Y tests and shows that all hits are similar from the point of view of the frequency centroid. An explanation of the trend shown thereby may be found in Figure 5.6, where the superimposition of all the four calibration certificates shows that the biggest difference in the sensor response is about 10 dB in the frequency band 350 – 650 kHz. In this band, the order, from the lowest to the highest in sensitivity, is: S2, S1, S3, and S4; nevertheless, there is another narrower band about 0.28 MHz with again a maximum difference of 10 dB, but in a different order: S1, S2, S4, S3. Though, the centroid only indicates the "centre of mass", and it is clear that most of the spectra fall both in the low-frequency band (order S1, S2, S4, S3) and the high-frequency band (order S2, S1, S3, S4). So, examining Fig. 5.6 again, it would be expected that, for example, S2 — which is relatively more sensitive in the low-frequency band and less in the high-frequency one — would shift the frequency content of the spectra towards the left. Table 6.6 shows that this is the case as S2 has the lowest average frequency centroid. In other words, *the different sensitivity of nominally identical sensors affects the frequency content of the waveforms, and therefore partially characterises the frequency response of the sensors rather than just the source.* The extent to which this happens, in terms of the final outputs, is probably more than expected by a simple sample variation.

Table 6.6: Frequency centroids (kHz, averaged over the four pencil lead breaks of each test) from Y tests, together with the average over all tests for each sensor

	S1	S2	S3	S4
Test Y1	336	317	387	400
Test Y2	322	297	375	380
Test Y3	321	304	378	385
Test Y4	321	297	368	385
Average	325	304	377	388

6.5 Hit amplitudes

Table 6.7 shows that the maximum amplitude difference is 10 dB over all the tests (although referred to different breaks). This amount is also the maximum difference in sensitivity found in the calibration certificates. Table 6.8 shows in full detail the results for the hit amplitudes, together with the averages (μ) and the standard deviations (σ) over each sensor and within each test. It is clear that the four sensors consistently provide hit amplitudes in the order (from the lowest): S1, S4, S2, and S3, with sensors S2 and S4 having a similar performance. A similar trend is shown in Fig. 5.6, and it can be seen how the different sensitivities of the sensors (in different frequency bands) translate into an averaged difference in the hit amplitude recordings. In other words, if the calibration curves show a maximum difference of 10 dB at some frequencies, the hit amplitudes show an averaged maximum difference of 7 dB, which is the result of the spectra covering a wide frequency band. Although other factors can play a role in the final output (acoustic coupling, system settings, characteristics of the source) in the main *the hit amplitude reflects the characteristics of the sensors rather than those of the real event.*

Table 6.7: Minimum and maximum recorded amplitudes over the four breaks of each Y test

	Minimum recorded amplitude (dB) / Associated sensor	Maximum recorded amplitude (dB) / Associated sensor	Maximum amplitude difference (dB)
Test Y1	82 / S1	91 / S3	9
Test Y2	80 / S1	90 / S3	10
Test Y3	82 / S1	92 / S3	10
Test Y4	84 / S1	94 / S3	10

Table 6.8: "Y" tests results (Amplitude, dB)

	C1 / P1	C2 / P2	C3 / P3	C4 / P4	
S1	82	80	85	85	
	83	83	83	84	
	83	84	82	84	$\mu = 83.06$
	82	83	82	84	$\sigma = 1.25$
	$\mu = 82.5$	$\mu = 82.5$	$\mu = 83$	$\mu = 84.25$	
	$\sigma = 0.5$	$\sigma = 1.5$	$\sigma = 1.22$	$\sigma = 0.43$	
S2	89	87	90	89	
	89	86	88	88	
	89	88	90	85	$\mu = 88.25$
	89	88	89	88	$\sigma = 1.3$
	$\mu = 89$	$\mu = 87.25$	$\mu = 89.25$	$\mu = 87.5$	
	$\sigma = 0$	$\sigma = 0.83$	$\sigma = 0.83$	$\sigma = 1.5$	
S3	94	92	90	88	
	90	90	89	90	
	93	88	91	90	$\mu = 90.19$
	90	90	89	89	$\sigma = 1.59$
	$\mu = 91.75$	$\mu = 90$	$\mu = 89.75$	$\mu = 89.25$	
	$\sigma = 1.79$	$\sigma = 1.41$	$\sigma = 0.8292$	$\sigma = 0.83$	
S4	90	89	n.a.	88	
	88	88	89	87	
	85	90	89	88	$\mu = 88.13$
	88	88	88	87	$\sigma = 1.2$
	$\mu = 87.75$	$\mu = 88.75$	$\mu = 88.67$	$\mu = 87.5$	
	$\sigma = 1.79$	$\sigma = 0.83$	$\sigma = 0.47$	$\sigma = 0.5$	

6.6 Time-related features (duration, counts)

Table 6.9 reports a summary of the statistics about the time-related features. These are derived by averaging the values reported directly by PAC AEWin and then. It is clear from Table 6.9 that there is proportionality between the reported average hit duration and the sensitivity of each sensor. The order (from the shortest to the highest: S1, S2, S4, S3) is the same shown at about 0.28 MHz in the calibration curves (Fig. 5.6). *Therefore it seems that there is not a characteristic duration for a pencil lead break, because this value also depends on the sensitivity of the sensors* (other that on the set amplitude threshold above which the duration of a waveform is recorded: see §6.7).

The same can be said for the ring-down counts, which are proportional to the sensitivity of each sensor and thus to the duration. This is demonstrated by the ratio of the two values as

Table 6.9: Average duration (1st row, μs), ring-down counts (2nd row) and their ratio (μs), on the right, for each sensor/test

	S1		S2		S3		S4	
Test Y1	13139 *1922*	6.8	15955 *2394*	6.7	20130 *2796*	7.2	18211 *2448*	7.4
Test Y2	13668 *1792*	7.6	16831 *2256*	7.5	20414 *2564*	8.0	19234 *2298*	8.4
Test Y3	14003 *1951*	7.2	16696 *2403*	6.9	20222 *2776*	7.3	19538 *2437*	8.0
Test Y4	14320 *1978*	7.2	17961 *2408*	7.5	21545 *2770*	7.8	20571 *2456*	8.4

being practically identical for all tests. So for these tests *the ring-down counts do not add any information.* Again, the reported values for the rise times (Table 6.10) seem dependent on the sensitivity of the sensor around 0.28 MHz, and they characterise the latter, rather than the actual AE event. The rise-time values do not show a proportionality with the sensors as consistent as the duration and the counts values. This certainly reflects the fact that, for the definition of rise time, very short times are considered, and a relatively-unpredictable single peak in the signal can play an important role.

Table 6.10: Average rise times (μs) for each Y test / sensor

	S1	S2	S3	S4
Test Y1	21.50	185.00	270.50	57.75
Test Y2	20.75	200.00	388.25	158.00
Test Y3	21.75	59.00	241.75	61.75
Test Y4	20.50	64.50	521.50	294.75

6.7 Dependence of hit durations on threshold settings

The duration of a hit is defined as the time the signal remains over a defined threshold. The signal (function of time) is usually expressed in mV, whilst the threshold (constant) in dB. In the PAC system, the acquisition threshold expressed in dB is then transformed in a voltage threshold expressed in mV. Using a threshold is necessary, because the system needs to know when the recording of the signal has to start, and to exclude weak and uninteresting acoustic emissions that usually represent noise.

A test, named T1, was designed and executed to determine how the *hit duration* of the

hits depends on the sensitivity of the sensors used. Sensors S1 and S3 (i.e. the two with the widest gap in sensitivity) were chosen.

Sensors S1 and S3 are placed on the same aluminum plate used for tests J and Y, §6.2. The distance between the two sensors is 28 cm, as shown in Fig. 6.7. S1 was connected to C1 through P1, and S3 to C3 through P3. Pencil lead breaks were carried out equidistant to each sensor.

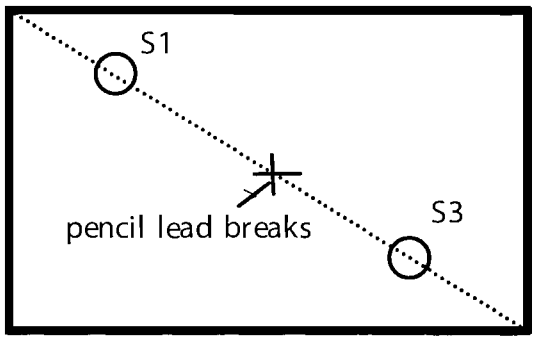

Figure 6.7: Simple geometry lay-out for test T1

A high acquisition threshold (80 dB) was selected. Seven breaks were performed but S1, because of its lower sensitivity, records only six of them. The minimum possible sampling rate (1 MHz) and the maximum byte length (15 kb) are used; these values correspond to a maximum duration of 15 ms collected and displayed by the system.

6.7.1 Results and analysis

Table 6.11 shows the statistics for test T1: the substantial difference in the recorded amplitude and duration values is evident. This shows that the duration of a hit is directly dependent on the threshold: the less sensitive the sensor, the less threshold crossings and hence the less duration. There is in fact an equivalence between the sensor sensitivity and the threshold, and the measured duration depends on both of them: the PAC system takes a 1 μV signal as reference; this undergoes to a preamplification of 40 dB (in this test), manually set in the preamplifiers via the apposite switch, which is equivalent to a multiplication by $10^2 = 100$ and hence becomes 0.1 mV. The 80 dB threshold of test T1 corresponds to a signal which is $10^{80/20} = 10^4 = 10\,000$ times 0.1 mV and then 1000 mV; a threshold of 60 dB corresponds to a signal of $0.1 \times 10^{60/20} = 100$ mV.[6]

[6]This comes from the definition of decibel that to express amplitude ratios is defined as $20 \log_{10}$ (ratio).

Table 6.11: Amplitudes and durations in test T1

	S1	S3
Average duration (μs)	903	2197
Average amplitude (dB)	87	91
Number of hits	6	7

As an example, two hits from test T1, one from each sensor, are considered, with their associated waveforms and AE features. Fig. 6.8 shows the two waveforms associated to the same event chosen as reference with their corresponding reported durations. It can be easily observed that the reported duration is clearly linked to the position in time of the last threshold-passing, and thus strongly related to the position of the latter *and* to the intensity of the waveform. The waveform coming from S1 is less intense and *therefore* shorter.

From the waveforms in Fig. 6.8 it can also be seen that the system stops recording and analysing after 800 μs of inactivity (i.e. a signal below the threshold); 800 μs being the HDT (hit definition time) set for this test. Whereas the HDT is another arbitrary factor in the analysis and computing of the hit duration, it must be noted here that the definition itself of HDT relates again to a set threshold and therefore to a sensor sensitivity.

There is proportionality between the duration-based parameters and the sensitivity of each sensor. Indeed, it is possible to roughly simulate the effect of a lower sensitivity with a higher threshold, as indicated by some typical data waveform shown in Fig. 6.9. A "new" threshold, drawn on a waveform, is obtained from the "old" (original) one by multiplication by 3.16, (i.e. 10 dB, to represent an order of magnitude of the difference in the sensitivities of the sensors). The hit duration is obtained from the last point where the waveform crosses the threshold, a reduction is observed (in this simulated case the system would report a duration just below 1500 μs) in the duration of the same order as the difference between the durations given in Table 6.9 for S3 and S1, which have a 10 dB difference in sensitivity at the peak in region A of Fig. 5.6.

It has been shown that the so-called duration of a hit is related more to the measured intensity of the waveform than to its length. From this point of view, the duration is strongly correlated not only to the acquisition threshold of the system, but to the sensitivity of the sensor as well. Unfortunately, the latter is much less controllable than the threshold itself.

Changing sensor, i.e. changing the sensitivity, is equivalent to amplifying the waveform, and then to shifting down the threshold and eventually to modify the reported "duration"

of the hit. *The hit duration is therefore not absolute, and is a characteristic of the acquiring sensor,* once the system threshold has been set.

Reducing the threshold might seem an easy solution to this problem, because it would mean more threshold crossings for sensors with lower sensitivity. However, it should be noted that the dependence of the response of the sensors on the frequency content of the acoustic emission is not linear, nor is it predictable in absence of the knowledge of the exact frequency content itself; hence the response of the sensors cannot be corrected by a simple shift factor.

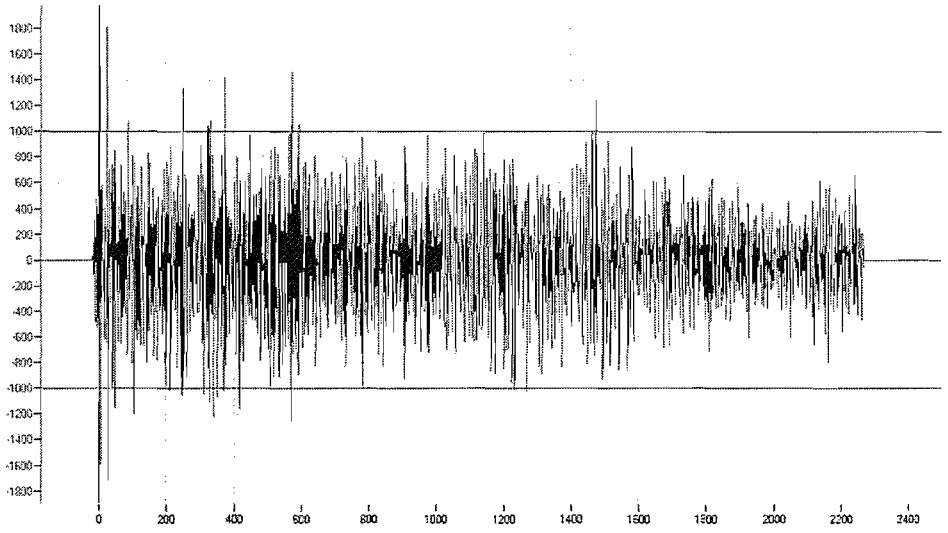

(a) S1: 88 dB, 1470 μs

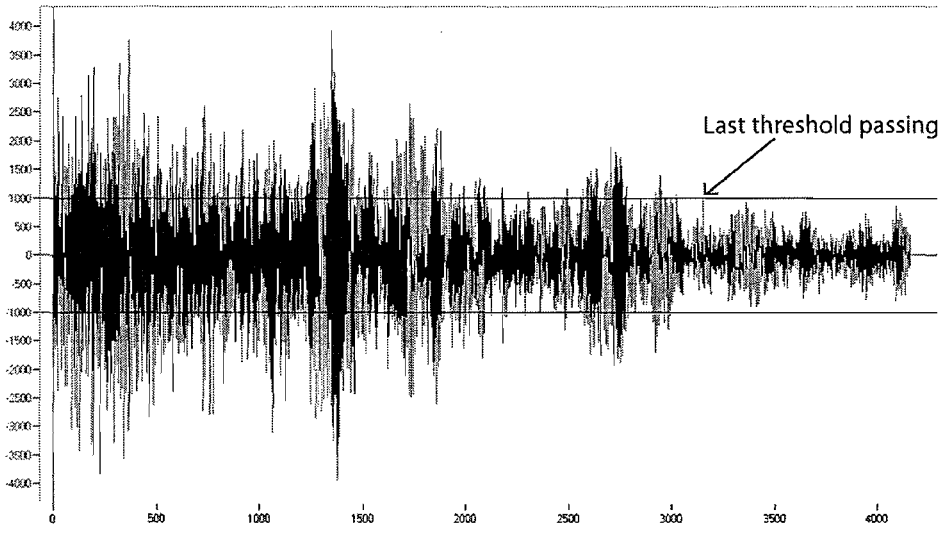

(b) S3: 94 dB, 3359 μs

Figure 6.8: Waveforms from sensors S1 and S3 corresponding to the same event. Time (μs) vs. voltage (mV). The threshold (1000 mV) is shown, and the amplitude and duration reported by the system is indicated. The scale is different for the two waveforms.

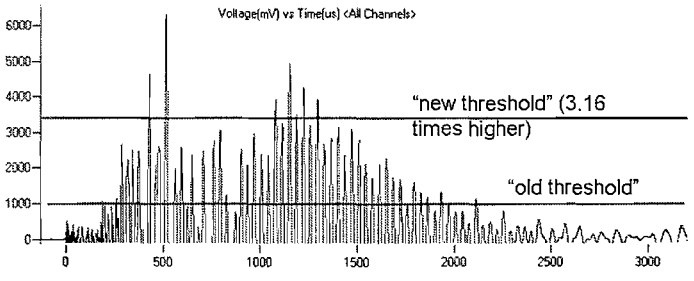

Figure 6.9: Half of the same waveform from Fig. 6.8b with a new threshold 10 dB bigger

6.8 Location capabilities

A test, named T2, with the same set-up and geometry depicted in Fig. 6.7, was conducted to assess how the difference in the sensor response affects the location capabilities of the system. Although the ability of locating the damage is not directly related to its characterisation, location is very important for filtering out spurious hits coming from outside the examined area.

The wave speed in the aluminum plate is measured at 4929 m/s following the procedure described in §5.3.2. The distance between the two sensors is 279 mm, and the pencil lead breaks are executed in the middle (0.1395 m), with an accuracy of ± 1 mm. Fourteen breaks were performed, twelve of them were recognised as events by the system.

6.8.1 Results and analysis

The histograms in Fig. 6.10 show a vertical bar (indicating the cumulative hit amplitude of all the events detected in that position) in correspondence of where the events are located (the abscissa represents the distance between the two sensors, placed 280 mm apart). The location is not accurate, and the system shifts the located position mostly towards the most sensitive sensor (S3). Table 6.12 summarises the location results for test T2, the percentage being such that 50% corresponds to the centre of the specimen and 100% to the whole distance between the sensors.

Table 6.12: Positions located for test T2

Nominal centre [m]	Average location [m]	St. dev. (σ)	6σ
0.1395	0.1526 (54.70%)	0.0049	29mm (11%)

As it may be expected, the recorded arrival times indicate that the hit is *always* triggered at S3 before than at S1. Table 6.13 summarises the differences in arrival times, and also translates this average time difference in a linear distance based on the measured wave speed in the medium. The average distance corresponding to the difference in arrival times (28 mm) is the same as 6σ shown in Table 6.12.

It can be concluded that the location capability of the system heavily relies on the homogeneity of the sensors (in terms of frequency response) employed, and that *its discrepancies can be directly related to the difference in sensitivity.*

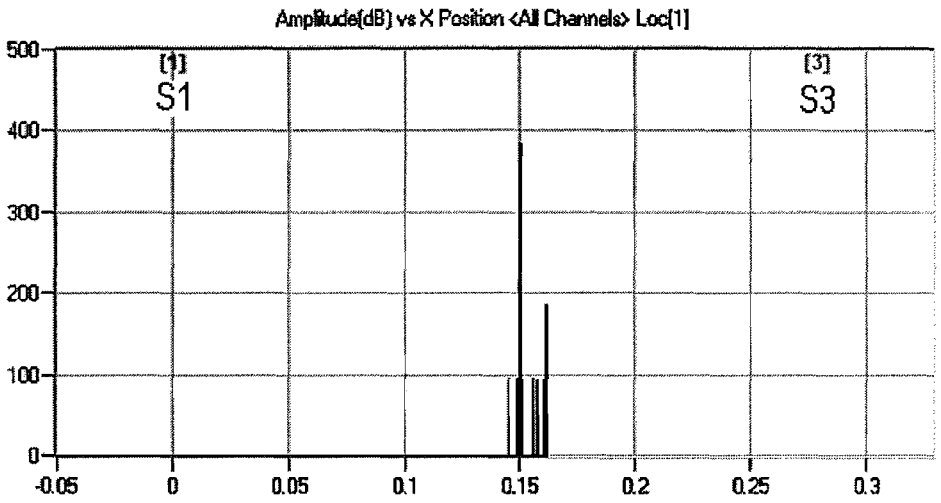

(a) Whole plot (the position of the sensors is shown)

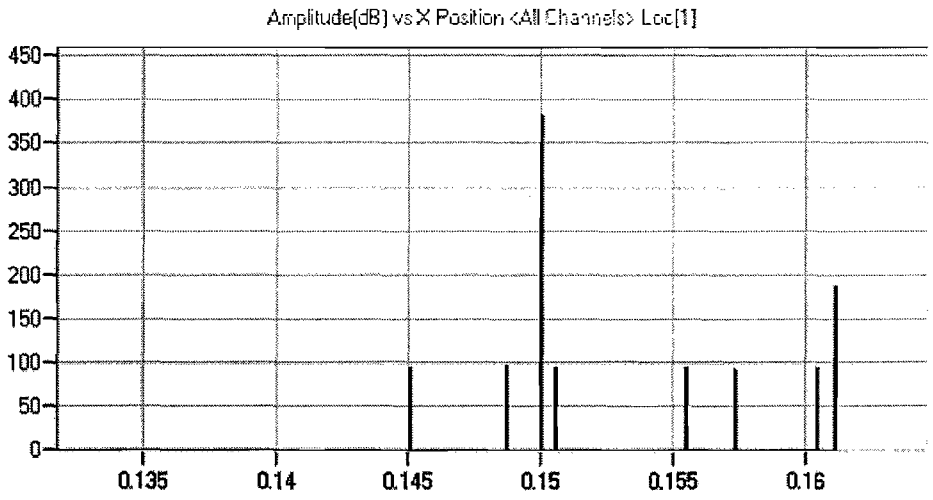

(b) Zoom about the located position

Figure 6.10: Amplitude versus position plot for test T2

Table 6.13: Arrival time differences Δt in test T2 (a positive difference means an arrival at S3 before S1); the last row reports the average and the standard deviation σ

Δt [s $\times 10^{-7}$]	Corresponding distance [mm]	σ [s]
42	21	
65	32	
87	43	
43	21	
43	21	
45	22	
23	11	
87	43	
73	36	
85	42	
38	19	
42	21	
56	28	21.2

6.9 Overall considerations

All the classic AE features (energy, amplitude, duration, counts) are strongly dependent on the sensors used to perform the test, and characterise these rather than the actual physical event.

This implies two things at least: 1. All the sensors used in a test should have practically identical calibration certificates and characteristics: being of the same nominal type is not adequate. 2. A reference sensor as suggested by technical standards cannot exist, and because the classic AE features seem to strongly depend on the characteristics of the sensors, this can seriously undermine the very idea of characterising damage with the use of AE features.

Even without the aim of characterising damage with the use of classic AE features, it is important that all the sensors used in a test be identical, because the location features of AE systems not only rely on the arrival times, but also on the position of the peak within the waveform, which has been shown (from the analysis of the rise times) to strongly depend on the sensors.

The standard deviations of the quantities measured during these tests (see Table 6.3 for instance) appear to be of no statistical usefulness because of the non-Gaussian distribution of AE parameters (Shiryaev *et al.*, 1990). On the other hand, as it has been shown for the two hits I and II, the power spectra do not change substantially in shape and features with the sensor; only the intensity seeming to be affected. Thus the waveform-based approach is probably the best one — if not the only possible — to characterise damage, because it is much less dependent on the used sensors.

There does not exist a good reason for attempting a serious characterisation of the damage through a pure parametric analysis. Quantities such as duration, amplitude, counts may be useful in some respects; for example, for classifying — within the same test — the events closer to the sensors from those further, those stronger from those weaker, and so on. But, for their intrinsic nature, and for their being relative quantities rather absolute, *these parameters cannot be successfully used to extrapolate any general characterisation from very specific experiments, nor attain universal laws.*

AE parameters are not adequate characterise a source. The results shown in §6.2, together with the concluding remarks drawn in §6.9, exclude them as a valid tool for describing objectively a source, if not used in conjunction with other aids. The only approach

to a characterisation of the acoustic emissions has to take in consideration the full spectrum of frequencies of the source, and the rest of this thesis will follow this direction. The next chapter will investigate the variability of a characterisation in terms of frequency with parameters (dimensions, material, positions) that have not been considered previously in the context of characterising acoustic emissions.

CHAPTER

SEVEN

Frequency analysis

There are no such things as applied sciences, only applications of science.

Louis Pasteur

In this chapter, several experiments are described, involving pencil lead breaks on different specimens. The samples are chosen to study the effect of the diversity of the material, specimen geometry, and lay-up on the transmission of the elastic wave to the sensor.

The experiments described in the previous chapter suggested to discard the AE parameters to describe a signal, and to focus on frequency characteristics. Therefore, since the use of frequency calculations will be extensive, and the software provided by PAC is not flexible enough for these purposes, some Matlab code is written and used.[1]

7.1 Effect of different media on AE signals

7.1.1 Test specimens

In total, three different specimens are used for the five tests described in this section. Two are metallic (a $450 \times 400 \times 9$ mm aluminium plate and a $31 \times 470 \times 11$ mm steel bar), one is a composite panel, detailed as follows. The variability of the geometry will be eliminated in tests appearing further on in this thesis.

[1] The Matlab code appears in the Appendix.

A 305 × 460 mm, $[0/90]_5$, carbon/epoxy panel, is made from a prepreg roll of 920cx-FT300(12k)-5-42% manufactured by Hexcel Composites. One face of the panel has a rough texture due to the peel ply used during the curing process, whereas the other face, directly in contact with a smooth aluminum plate, has a smooth finish. These two faces will be called respectively R and S, and the 0° direction coincides with the longest side. The layup of this panel is evidently non-symmetrical, but the manufactured panel was perfectly flat. The composite panel was purposely prepared in this non-symmetrical fashion to study the differences between a pencil lead break on a rough and smooth surface, with different orientation of the fibres in contact with the sensors.

7.1.2 Sensor placement and test procedure

The test configuration is similar to the one described in §6.7 for T1 and T3. Amongst the four PAC sensors available, the two with the most similar characteristics were chosen (S3 and S4), according to the the calibration certificates (§5.2) and tests described in §6.2 (Table 6.6). For each test, at least ten pencil lead breaks were performed. Of these, the ten most representative (chosen, after visual examination of the spectra displayed by AEWin, for best consistency within the whole test and the two sensors) were eventually saved for further analysis.

The parameters used in the tests are listed in Table 7.1. Vaseline was used as acoustic couplant. Sensors S3 and S4 were connected to channels C3 and C4 respectively. They were fixed to the specimens by strips of insulating tape, which can be stretched to get a small but sufficient pretension; this would not be necessary on smooth surfaces, where Vaseline itself would provide adequate adhesion, but is used thorough all the tests for uniformity. The distance between the centres of the sensors was of 270 mm (Fig. 7.1 illustrates this generically for all the five tests); this is used as reference distance to calculate the wave speed (as described in §5.3.2), and in the location setup of the PAC AEWin software (see §5.3.3). The breaks were always performed equidistant to each sensor. The location capabilities of the PAC system were used in order to identify real events.

7.1.3 Description of the tests

Sensors S3 and S4 were used on the three previously described specimens arranged in the following five tests:

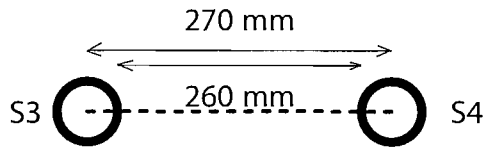

Figure 7.1: General sensor setup

Table 7.1: Parameters adopted for tests Comp1, Comp2, Comp3

Acquisition threshold	65 dB
Preamplifier gain	40 dB
Analogue Filter (software)	100 kHz–1 MHz
Sample rate	2 MHz
Pre-Trig	128 bytes
Waveform length	14 kbytes
PDT	200 μs
HDT	800 μs
HLT	1000 μs
Location type	Linear
Structure type	Free
Event Definition Value	0.25
Event Lockout Value	0.2
Overcal Value	0
Timing strategy	First Threshold Crossing

1. Test "Al", centrally positioned onto the aluminium plate.

2. Test "Steel", centrally positioned onto the 31 × 470 face of the steel bar.

3. Test "Comp1": the sensors were placed on face S of the composite panel, along an axis parallel to the 0° direction of the panel and to the fibres on the surface in contact (Fig. 7.2).

4. Test "Comp2": the sensors were placed on face R of the composite panel, along an axis parallel to the 0° direction, and orthogonal to the fibres on the surface in contact (Fig. 7.3).

5. Test "Comp3": the sensors were placed on face S of the composite panel, along an axis parallel to the 45° direction of the panel (Fig. 7.4).

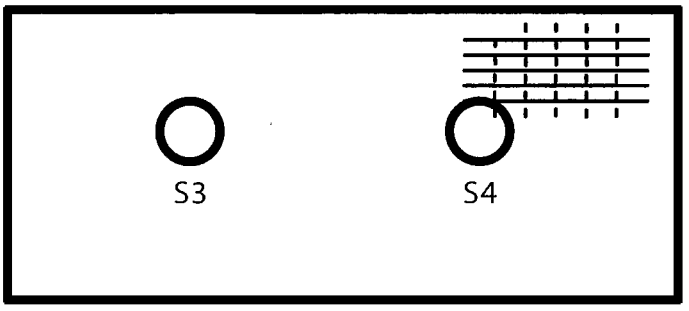

Figure 7.2: Set-up for test Comp1

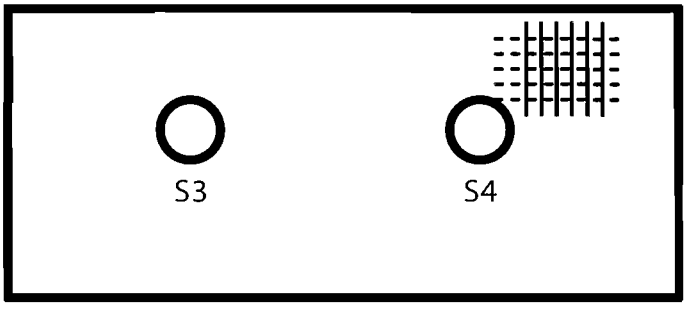

Figure 7.3: Set-up for test Comp2

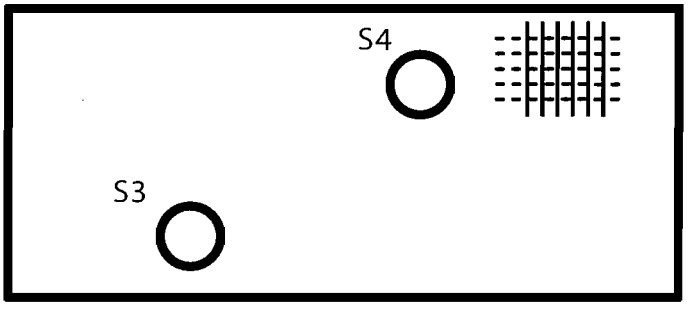

Figure 7.4: Set-up for test Comp3

7.1.4 Results and analysis

The wave speeds measured and used for location are reported in Table 7.2.[2] The velocity in Comp3 is considerably less than that in Comp1 and Comp2. The events recorded from Comp2 are a little weaker than that of Comp1: the rough texture of face R (Comp2) is likely to be the cause, for a different acoustic coupling has been probably achieved.

Table 7.2: Wave speed measured for the five tests

Test	Speed [m/s]
Al	5100
Steel	4800
Comp1	6330
Comp2	6430
Comp3	4440

For each test the following was obtained:

1. the power spectrum calculated as the *geometric mean* of twenty spectra (ten from each channel);

2. the average and the standard deviation of the frequency centroids of all the spectra and, for comparison, the frequency centroids of the geometric-mean spectrum and of the arithmetic-mean spectrum.

Figure 7.5 shows the geometric means of the power spectra for each test, superimposed, after normalisation. Encouragingly enough, the power spectra detected within each test are quite consistent and differ very little from event to event. At this stage it was decided to use a known routine to determine the frequency spectra rather than use that provided by the PAC software. The core of the power spectra computation program is the Matlab's `pwelch.m`, which estimates the power spectrum of the sequence using the Welch method of spectral estimation. The FFT length adopted here is 4096 or higher; this value being chosen for providing a spectrum that visually appears detailed but not too noisy. This value determines the number of different frequencies at which the power spectrum is estimated (a power of 2 is specified for faster execution). Following the approach of Ferreira *et al.* (2004), the spectra in this thesis are shown normalised. This is needed because the pencil lead breaks on steel clearly undergo a smaller attenuation when compared with those on

[2]These detected wave speeds may correspond to the group velocities of different modes, that are detected differently by the first threshold passing.

composite, and the power spectra thereof are of different scale, which would make their comparison not immediate. The normalisation is done by dividing each spectrum by a local (computed for each individual spectrum) maximum; then the averages and the statistics are computed for these normalised spectra. Finally, a last normalisation is again performed on the geometric mean. For the analysis of the power spectra, the geometric mean was used to bring the images from the two channels to a single one.

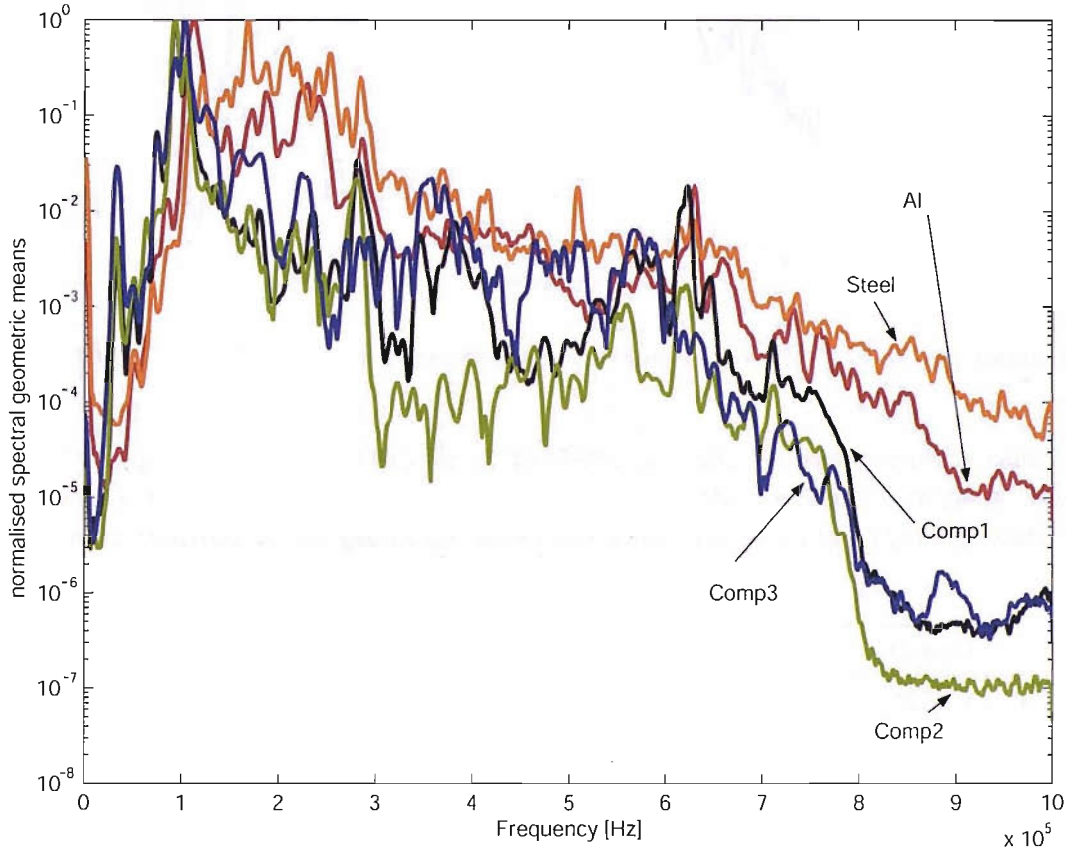

Figure 7.5: The geometric means of the power spectra coming from all the five tests, normalised

It is easy to group together the tests involving a metallic specimen (Al and Steel, Figures 7.6 and 7.7) and those on the composite panel (tests Comp1–Comp3, Figures 7.8, 7.9 and 7.10), because they show some common features. The spectra from the cross-ply panels (Comp1 and Comp2) and that from the Al panel also have one peak at about 630 kHz, which is not present in the test on the angle-ply panel and the steel bar.

Table 7.3 shows a summary of the frequency centroids for all the tests: on metals the waveforms from the pencil lead breaks are slightly higher in frequency than in composites.

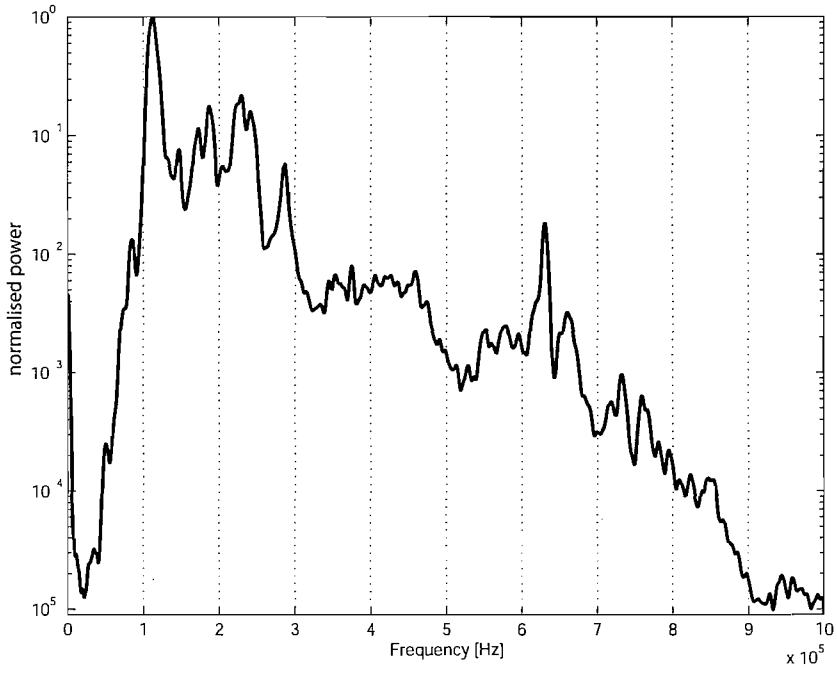

Figure 7.6: The geometric mean of the power spectra from the twenty hits of Al test, normalised

Table 7.3: Frequency centroids (Hz) for all the tests: μ is the average frequency centroid of all the twenty waveforms; σ is the standard deviation of the frequency centroids; GMS is the frequency centroid of the geometric mean spectrum; AMS is the frequency centroid of the arithmetic mean spectrum

	Al	Steel	Comp1	Comp2	Comp3
μ	181063	217972	158040	114515	157809
σ	25997 (14%)	16637 (8%)	49665 (31%)	11963 (10%)	42187 (27%)
GMS	173727	214718	131170	108980	137111
AMS	190101	217917	169841	116798	170850

7.1.5 Standard deviation of the spectrum

An attempt to display the range of variation in terms of the standard deviation (for example, the interval $[\mu - \sigma, \mu + \sigma]$) is unsuccessful because the standard deviations found are very high, and such intervals would spread over negative values as well — making a logarithmic plot meaningless. It is likely that this is due to the sensitivity difference of the two sensors: in fact, the averages shown before are not only the result of many acoustic emissions, but also of two different sensors. To show this, the same data from Comp3 have been processed again, with those from S3 separated from those from S4.

The standard deviation has been calculated from the non-normalised spectra, and then normalised respect to the average normalizing factor from all the ten spectra. The results,

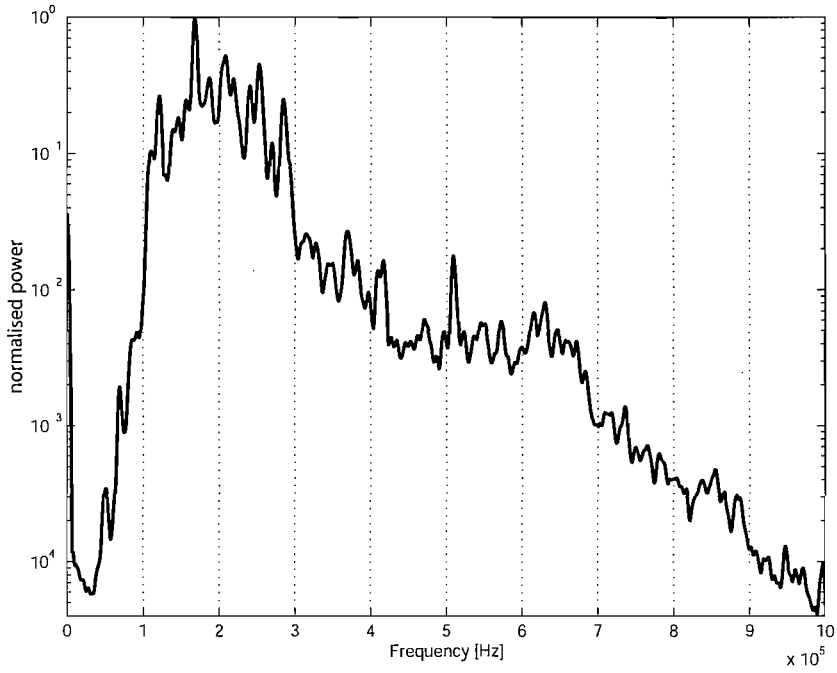

Figure 7.7: The geometric mean of the power spectra from the twenty hits of Steel test, normalised

displayed in Figures 7.11 and 7.12, show that:

- it is indeed possible to obtain a reasonable standard deviation of the spectra, provided that the data are collected from the same sensor, and
- spectra from S3 are visibly different from spectra from S4: S4 is relatively more sensitive between 300 and 400 kHz.

7.1.6 Summary

The tests performed in this section have the purpose to assess how differently the very same AE source can be detected by the sensors, at the same distance, after travelling through a different material, or the same material organised in a different way. The main relevance of the results from tests Comp1–Comp3 is their difference: they simply suggest that an acoustic emission generated will be detected differently according to the angle between the travelling path to the sensor and the fibres.

On the whole, as expected, the two metallic media have provided similar results and, although with some difference due to the orientation, the acoustic emissions detected from the composite look substantially different from those recorded from the metals. More gen-

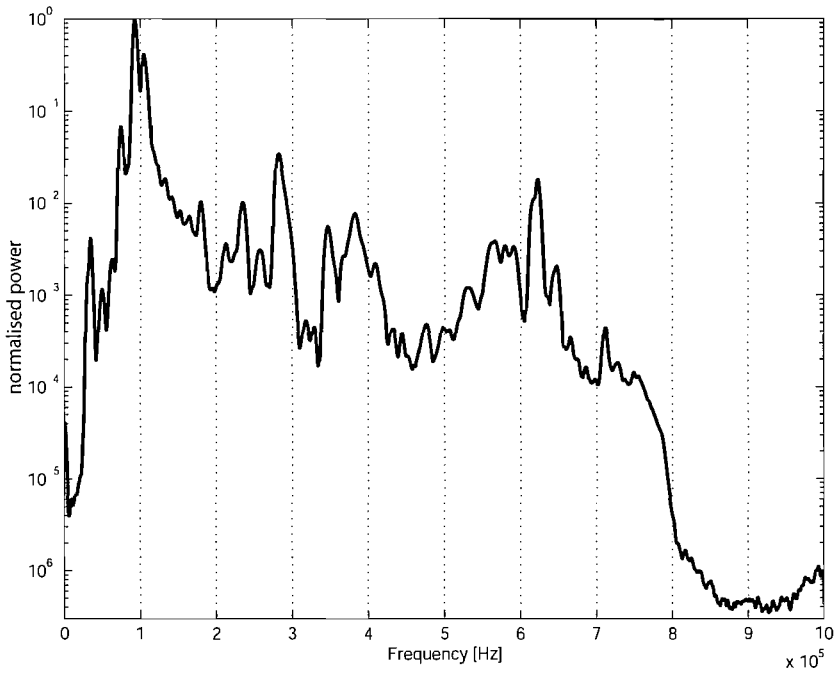

Figure 7.8: The geometric mean of the power spectra from the twenty hits of Compl test, normalised

erally, it seems not possible to talk of a "characterisation of the damage" without referring to the travelling medium. In fact the travelling media affect the way the waveform is detected at the sensor or, in other words, a characterisation through the AE cannot leave out of consideration the travelling medium.

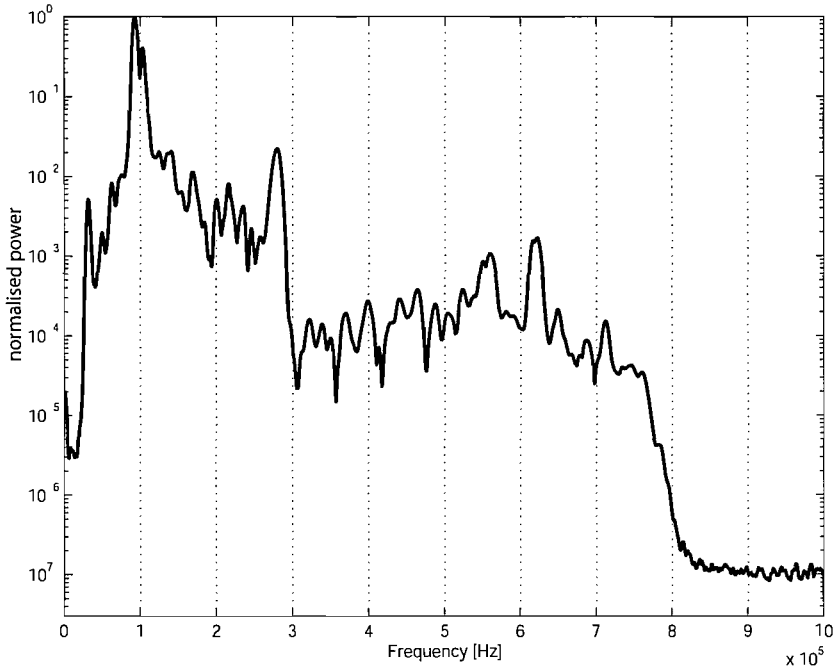

Figure 7.9: The geometric mean of the power spectra from the twenty hits of Comp2 test, normalised

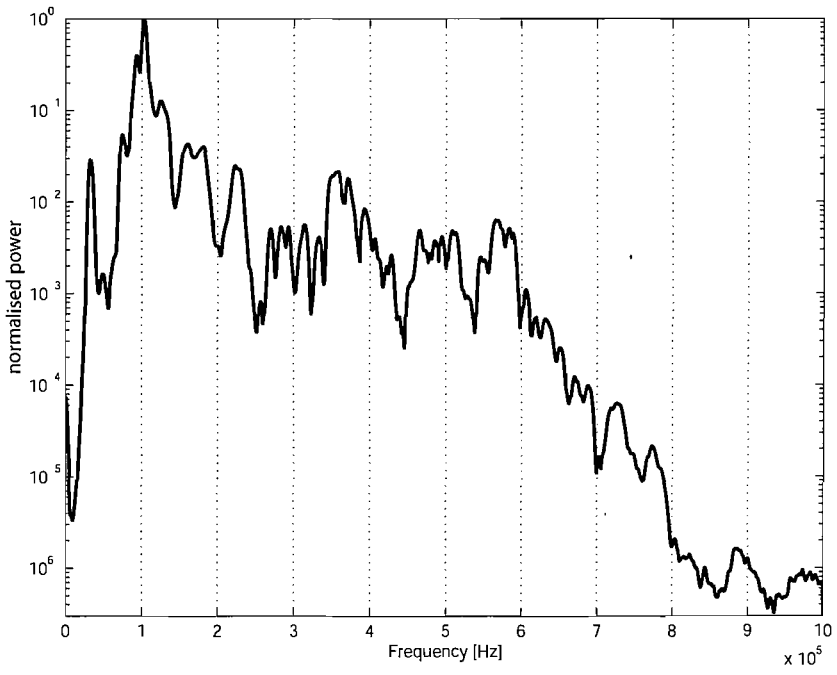

Figure 7.10: The geometric mean of the power spectra from the twenty hits of Comp3 test, normalised

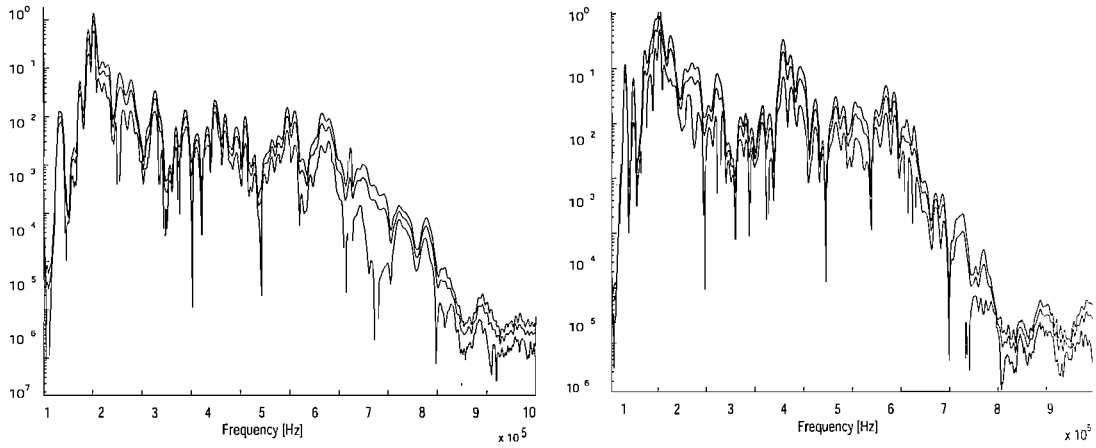

(a) S3 (b) S4

Figure 7.11: Spectral arithmetic mean (μ) and standard deviation ($\mu + \sigma, \mu - \sigma$), normalized, of data from Comp3 separated over the two channel

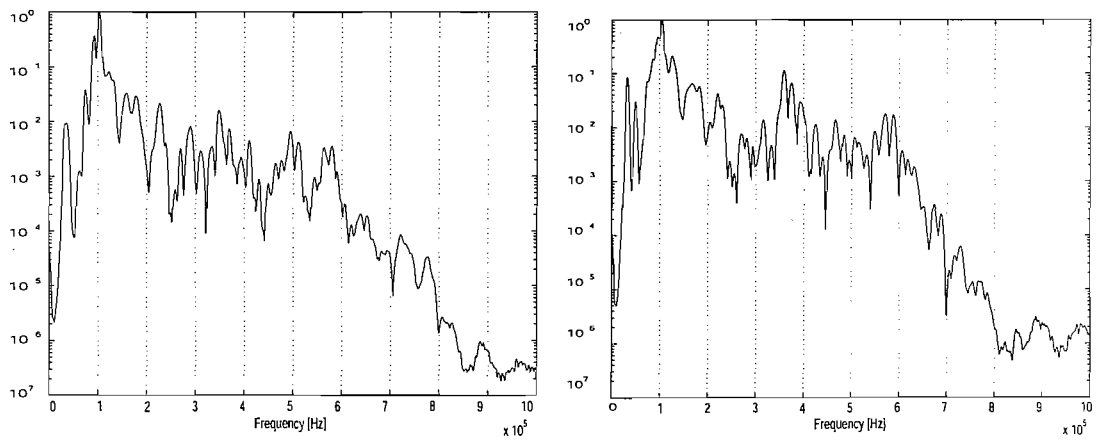

(a) S3 (b) S4

Figure 7.12: Spectral geometric means for Comp3, with the data separated over the two channels S3 and S4

7.2 Effect of anisotropy and position of sensor and sources relative to the edges on the waveforms

Any real attempt to characterise a source in a composite panel must take into account that the waveforms detected by the sensors will have travelled through a heavily anisotropic[3] and non-homogeneous medium. The alterations introduced by the anisotropy will be added to the dispersive effects of the Lamb waves — effects that exist regardless of the homogeneity of the material — and to the boundary effects that are inevitable with a panel with finite dimensions.

In composites, location of the damage and, more generally, of a source originating on them is imprecise (§4.5). Without an exact location of the source, an array of sensors distributed on a panel does not know *a priori* the direction the acoustic emission will come from, nor the orientation of the travelling path respect to the fibres. A consequent further unknown is that the source could originate from the middle of a panel, as well as from close to the edges, and this could result in a signal that is detected differently. In the following tests, PLBs are used to investigate the effect of the variable orientation and proximity to the border.

7.2.1 Descriptions of the tests

Two tests were conducted in this section of work. In both tests, sensor S3 was placed on the smooth side of a $[0]_{20}$ 470 × 300 mm CFRP panel and connected to P3 and eventually to C3 of the PAC system, using Vaseline as acoustic couplant. The panel was supported by a sheet of foam. The first test (named "O", for orientation) investigated the effect of the orientation of the fibres with respect to the travelling path. The positions of the PLBs are identified as A, B, C, D in Figure 7.13, and are characterised by different angles between the travelling path and the fibres.

On this panel, the highest wave speed is measured along the direction of the fibres, 8475 m/s. At this speed, a signal originating from A takes 11 μs to travel from S3 to the left edge and, with the assumption that the reflected wave travel at the same speed, further 11 μs to go back to S3. In other words, an eventual reflection should arrive in S3 22 μs after the main signal.

[3] An isotropic wave speed would produce results not good even in first approximation.

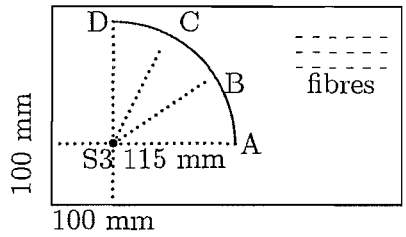

Figure 7.13: Positions A, B, C, D for test O (not in scale)

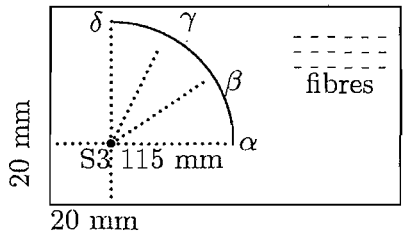

Figure 7.14: Positions α, β, γ, δ for test E (not in scale)

A time of 22 μs is usually too short for a waveform be recorded *and* the combination of HDT and HLT stop the recording *before* the reflection comes back to the sensor. So it must be assumed that the recorded waveforms contain the reflections too. These considerations lead to the test E ("E" for edge) that investigates the effect of the edge on the acoustic emissions, where the positions A, B, C, D are shifted respect to the edges of the panel, and denoted as α, β, γ, δ as illustrated in Fig. 7.14.

Ten or more breaks are executed for each position, but only ten are considered for the analysis, chosen from their parameters and from a visual inspection of their power spectra for the best consistency. The acquisition parameters adopted are summarised in Table 7.4.

Table 7.4: Acquisition parameters for tests O and E

Acquisition threshold	60 dB
Preamplifier gain	40 dB
Analogue Filter (software)	100 kHz–1 MHz
Sample rate	2 MHz
Pre-Trig	128 bytes
Waveform length	15 kbytes
PDT	200 μs
HDT	800 μs
HLT	1000 μs

7.2.2 Results and discussion

The four graphs shown in Figure 7.15 represent both the results from tests O (solid line) and E (dashed line). Each curve is the normalised geometric mean of ten power spectra. The scale of the vertical axis is logarithmic, whereas the abscissas represent the frequency. The same results are compared differently in Fig. 7.16.

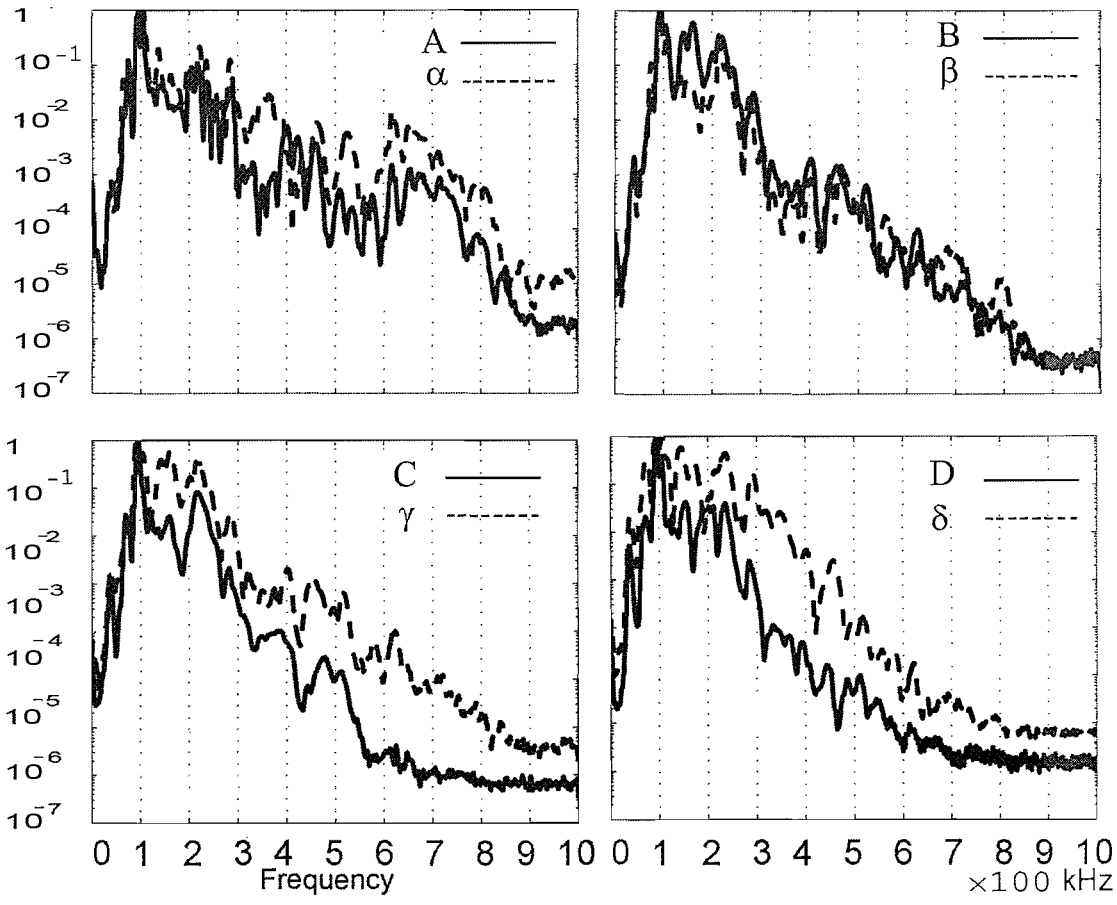

Figure 7.15: Normalised geometric mean of power spectra from tests O and E

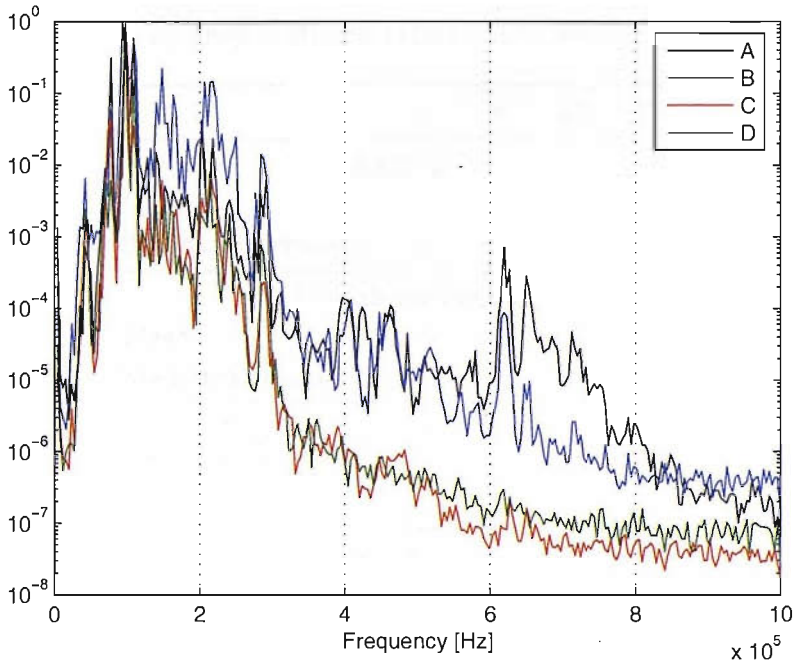

(a) Test O

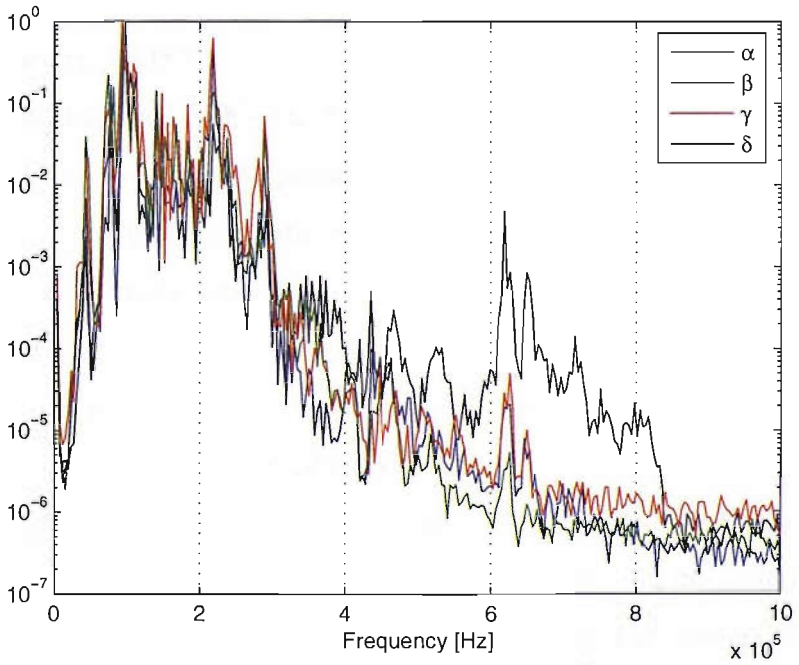

(b) Test E

Figure 7.16: Normalised geometric mean of power spectra from tests O and E

An approximate numeric estimate of these spectra can be obtained by means of the frequency centroids. Table 7.5 reports, for each test A, B, C, and D, the statistics on the frequency centroids of the ten events computed from the hits by the PAC system; together

Table 7.5: Frequency centroids (kHz) of the ten events for test O

	A	B	C	D
AEWin				
Mean	213	178	153	157
Standard deviation	12	7	12	8
Matlab routines				
Mean	137	153	128	120
Standard deviation	27	13	25	17
	α	β	γ	δ
Matlab routines				
Mean	160	137	176	159
Standard deviation	29	24	13	17

with the same data but computed from the waveforms by external Matlab routines.[4] The difference in the frequency centroid can be probably explained by the irregular fashion the PAC system does these calculations (see §5.3.4). The overall numerical comparison of the tests is then shown in Table 7.5.

All the spectra displayed look — as they should, since they all belong to the same type of source — similar in the features (position and relative magnitude of the peaks), and this makes even clearer the differences with the fibre orientation and edge distance.

Results from test O show that the waveforms appear different when detected at a different orientation between the travelling path and the fibres. Waveforms travelling along the direction of the fibres contain some activity at higher frequencies that is lost at higher inclinations. Results from test E indicate that the frequency centroid of the waveforms collected closer to the panel edges is larger than that of the waveforms collected far from the edge. The only exception seems to be the B/β positions, where the frequency centroid does not increase with the proximity to the border. This suggests that other factors, other than inclination respect the fibres and distance from the edge, can play a role: the tests described in §7.4, by means of a more sophisticated series of experiments and analysis techniques (that

[4]Further in this chapter, some observations will be made on the length of the signal used for the computation of the power spectra. For these tests O and E, the whole signals were used, that naturally decay after 1.5 ms.

will first be presented in §7.3), will investigate the reflections and the effect of the edges.

7.3 PLBs on a carbon strip at different distances from the sensor

The previous tests have shown that the same source (a PLB, in particular), originated or detected in different conditions or positions, may either look identical, or different, according to the level of detail of the analysis technique. Starting a simile with a magnifying lens, it may be said that a low-power lens will show the signals A and α as both PLBs (peaks in the same positions, of similar relative magnitudes), whereas a higher-power lens will show more (different) details and make them look different (for example, by comparing the two spectra by normalization respect to the peak at 100 kHz) and tell something about their different positions.

The experiment in this section serves the purpose of presenting techniques that will increase the level of detail of the analysis, by adding some time-related information, thus showing that signals originating from the same source can "hide" some variability that depends on factors not directly linked to the source mechanisms, such as position and acquisition parameters.

7.3.1 Testing setup

One [90/0_4/90] CFRP strip is used, with four steel end-tabs for easy mounting in the tensile test machine. The choice of the layup was not dictated by any particular reason. Figure 7.17 illustrates the schematic of the specimen and test setup: one sensor (S3) is placed close to one end-tab, and two positions characterised by different distances are identified on the strip for the PLBs. The sensor is coupled with Vaseline and held in place with electric tape; the strip is mounted in an Instron tensile test machine with a load of 700 N, to simulate the boundary conditions of a tensile testing. Table 7.6 summarises the AE acquisition setup for both the positions "A" and "B." At least ten PLBs are executed and recorded for each position.

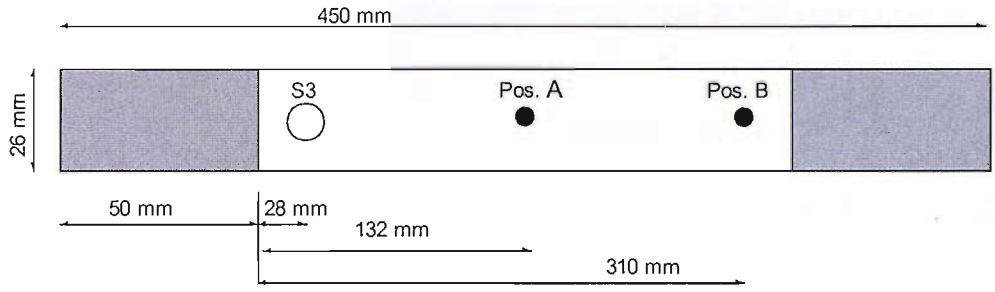

Figure 7.17: Schematic of the specimen and test setup, not in scale

Table 7.6: Parameters adopted for the test in the positions A and B

Acquisition threshold	60 dB
Preamplifier gain	40 dB
Analogue Filter (software)	1 kHz–1 MHz
Sample rate	2 MHz
Pre-Trig	128 bytes
Waveform length	10 kbytes
PDT	200 μs
HDT	800 μs
HLT	1000 μs

7.3.2 Results and discussion

All the waveforms collected are first visually analysed with PAC AEWin software; both the raw waveforms and their power spectra, as displayed by AEWin, are considered for this preliminary visual analysis. Any waveform looking the result of an error in the acquisition is discarded.

Because all the collected signals look consistent and similar within the same originating position, only one waveform for each position was chosen and carried forward for further analysis. They are displayed in Figure 7.18. These waves look qualitatively similar in the time domain (a first short low-amplitude part, and then two identifiable groups), but present a small time-shift, due to the different travel distance. This is reasonable, since the originating type of the source is the same.

Figure 7.19[5] shows a frequency content shifted between positions A and B: the normalisation is intended to concentrate the attention to the frequency centroid only. It is difficult to tell the one from the other, because they present the same trend and positions of the

[5]The thickness of the lines hide the fact that the two peaks below 100 kHz do coincide at a maximum normalised value of 1.

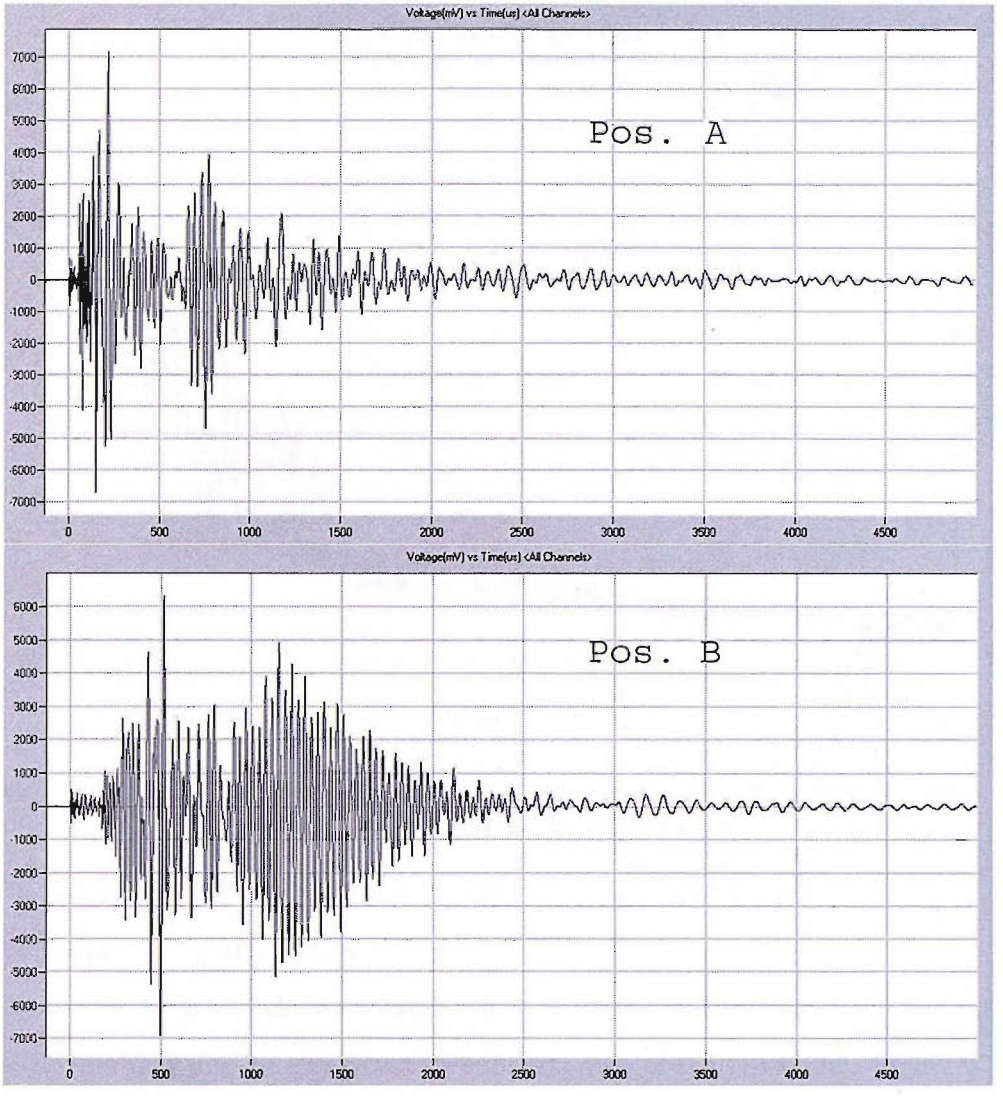

Figure 7.18: Waveforms "A" and "B"

major peaks; nevertheless, the spectrum for the wave A emerges and elevates (one order of magnitude) from that of the wave B, which appears as a sort of baseline. It is clear that wave A has a higher frequency centroid.

From the point of view of characterising the source, an attempt to use the normalised spectra would fail, as it would lead to the conclusion that A and B belong to different sources; Figure 7.20, by zooming on the previous graph, emphasizes this difference.

7.3.3 Analysis: development and building-up of the waveform

The following analysis stems from the idea that, behind the different content in the high-frequency range, *the transient building-up of the waveforms (as indicated in §6.3) with*

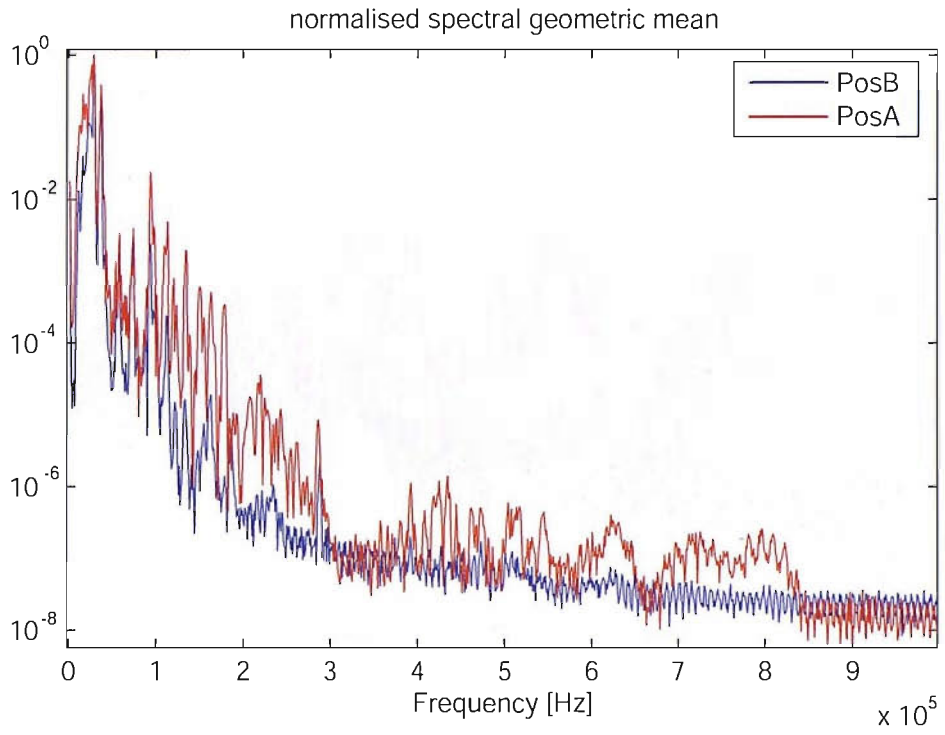

Figure 7.19: Normalised spectra for the two waves A and B; the normalisation point corresponding with the very-low frequency peak

the time plays an important role.

Using the full length of the waveforms collected by the PAC system is not compulsory: a power spectrum may also be computed on subparts only of the full signal. Figure 7.21 illustrates this concept with the waveform from position B:[6] the subgraphs display the subpart of the waveform and the corresponding normalised power spectrum.[7] The sample times (30, 160, 270, 450, 800, 2000 μs) were chosen after a visual inspection of the signal in the time space: they seem to correspond to identifiable features. The following considerations derive from the observation of this graph:

1. It is evident that the power spectrum changes substantially with the considered part of the waveform.

2. The first parts of the waveform consist of low-amplitude high-frequency extensional modes, and this is evident from the corresponding spectra.

3. As the time allowed for the waveform to grow increases, lower-frequency slower antisymmetrical modes arrive at the sensor, higher in amplitude because of the out-of-plane nature of the PLBs, and the power spectrum changes accordingly, shifting its frequency

[6]The trend illustrated is representative of all the waveforms collected.

[7]The spectra are displayed normalised for a better comparison of their frequency centroids.

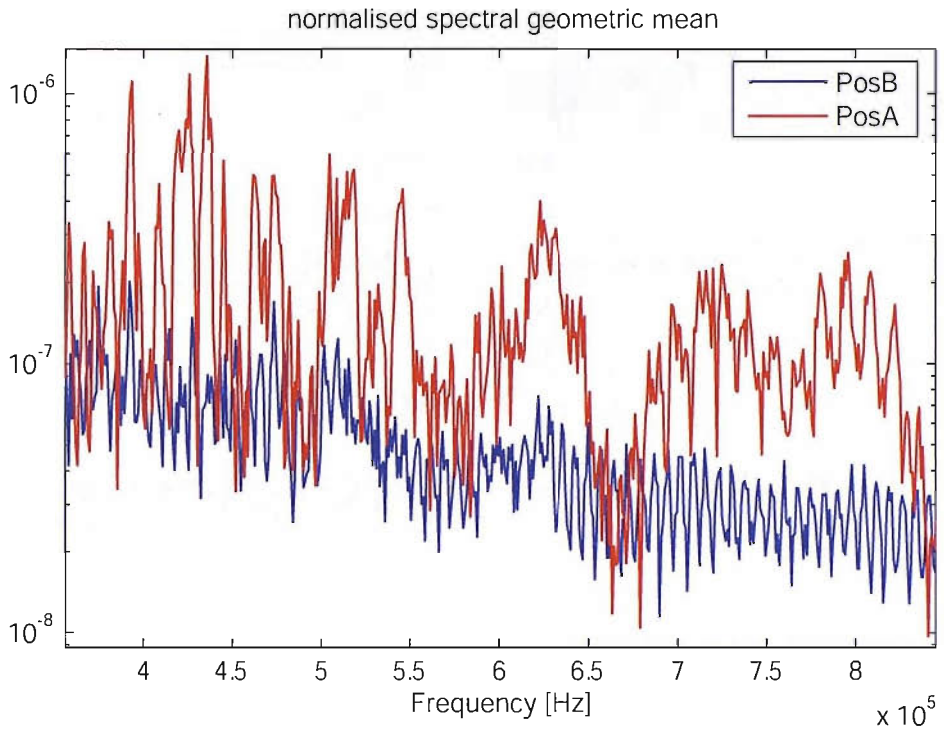

Figure 7.20: Zoom on Figure 7.19

centroid towards left.

Another way to look at waveform B is by subdividing it according to its three main inhomogeneities: a first tract from 0 to 180 μs, a second tract including the next 800 μs, and the third tract continuing until the end of the signal. These three segments of signal, together with the respective power spectrum, are shown in Fig. 7.22. Here, the spectra show that the only tract containing high frequencies is the first one. Whereas the second tract still contains an almost imperceptible fraction of high frequencies, these are not present in the third tract. The same is confirmed by simple visual inspection of the waveform again, better windowed to include up to the maximum of the third tract only (Fig. 7.23): the third tract is "smooth" and clearly at a low and constant frequency. Given the physical nature of the signal (two distinct modes, S and A, of different frequency and amplitude, that travel forth and back along the specimen), it is not difficult to identify in the waveform something not too dissimilar from a beating wave.

From the point of view of the characterisation of the signal, the following observations can be made:

- the frequency content indicates that the signal is stationary after about 900 μs. In other words, recording and/or analysing a longer tract does not add any information.

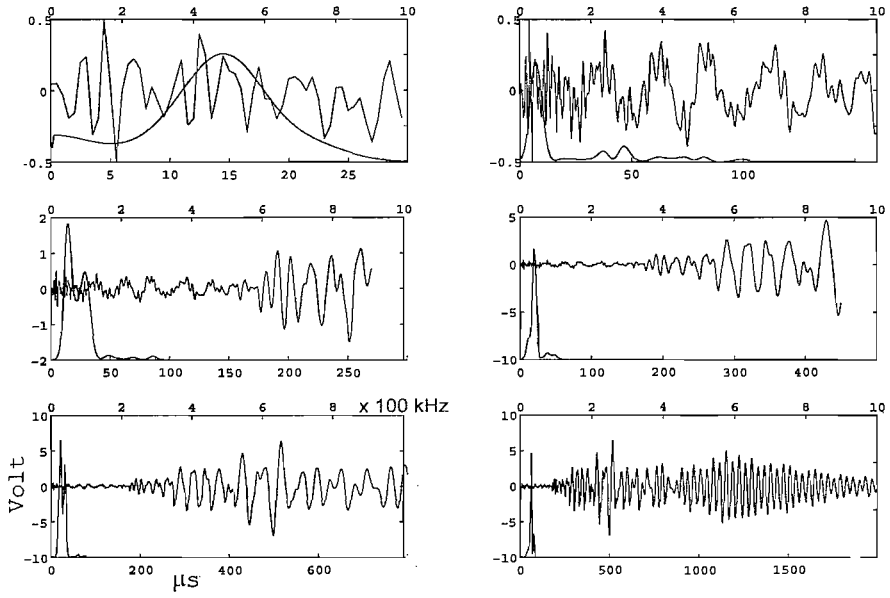

Figure 7.21: Subpart of waveform B and its corresponding normalised power spectrum, after: 30, 160, 270, 450, 800, 2000 µs

- Power spectra of longer signals tend to show only a very low frequency activity. This can be interpreted either as the beat frequency (equal to the absolute value of the difference in frequency of the two waves) or as the vibrational mode of the structure; in either case, and whatever the underlying physical reality, what is observed in the signal after a relatively long time is little correlated to the mechanism of the source.

Figure 7.24 proposes an aid to this analysis: for each sample time, indicated on the abscissa, after which the same signal is truncated, it plots the frequency centroid of the corresponding spectrum on the ordinate. This graph explains the relative influences of the modes and number of reflections, and by its inspection, it is possible to compare and distinguish the waves coming from the two distinct positions. In fact:

1. the waveform from position A starts with a higher frequency centroid: being further than B from the sensor, it benefits for a longer time of the faster extensional modes,

2. the waveform from position B converges slower to the final value.

A physical interpretation of the reason for these two spectra differ can help to identify a better analysis procedure as follows:

1. because of the well known dispersive nature of Lamb waves, the higher-frequency symmetrical mode travels faster than the lower-frequency antisymmetrical mode, so

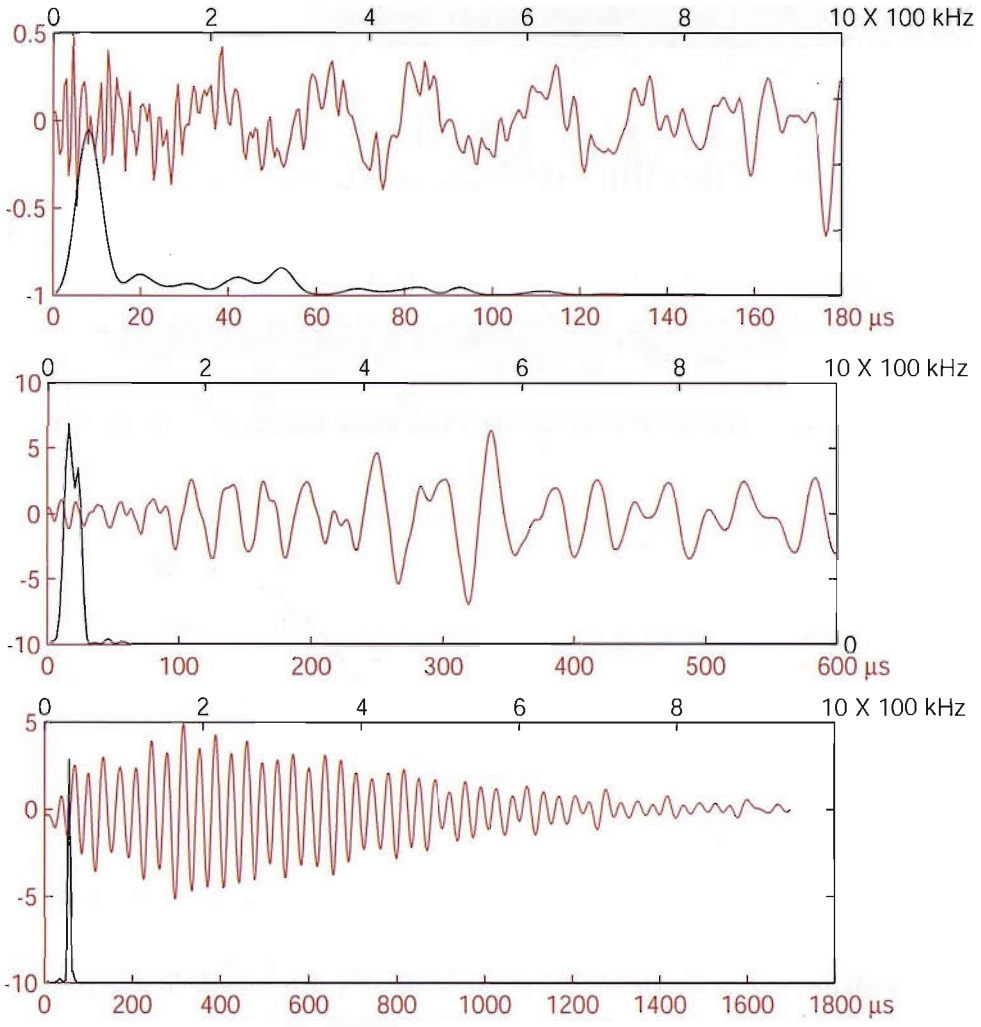

Figure 7.22: Three sections of the waveform from position B with relative normalised power spectrum

2. within the same time-window that the AE system uses to record the wave, the fastest mode reflects more within the specimen, and so is counted more than the other mode, resulting in an overall higher high-frequency content (until 80 µs, Fig. 7.24).

3. Due to the essentially out-of-plane nature of a PLB, the strongest mode contained in the elastic wave is the antisymmetrical one, that is the mode characterised by lower frequencies as the higher frequencies are attenuated. This appears in the spectra, where the highest intensities occur at the lowest frequencies (Fig. 7.19).

4. This strongest mode is the one destined to count relatively more after a while, when the fastest — but weakest — high-frequency mode has been greatly attenuated (after 80 µs in Fig. 7.24).

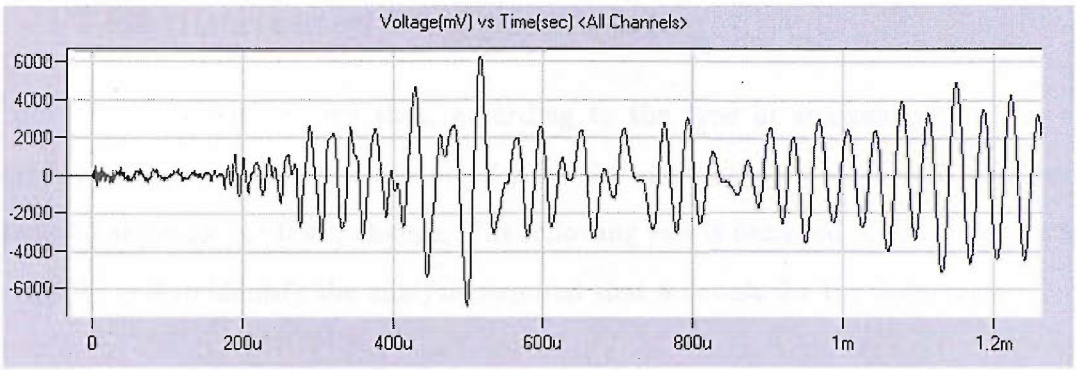

Figure 7.23: Different zoom and scale on the waveform from position B

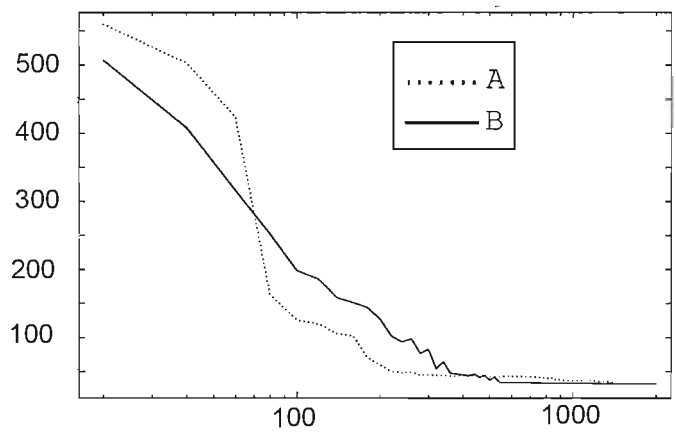

Figure 7.24: Plot of the frequency centroid (kHz) VS the length of the waveform considered (μs, logarithmic), for waves A and B

7.3.4 Overall comments

In this section, frequency centroid versus sampling time curves have been introduced. They take into account that a proper characterisation must consider the development and the building-up of the waveform, *because what is recorded by an AE system is not a snapshot at a fixed moment, but actually a series of reflections, the number thereof increases with the time.* These curves seem to carry some positional information about the sensor and the source. Although the tests do not indicate what sampling time is best suited for a given analysis purpose, they do suggest that this choice may be critical: it is in fact evident that some details and features of the power spectra are visible only with a given choice of sampling time. The experiments described in the next section will investigate all these issues by using a larger data set of PLBs and a differently designed exp0eriment.

7.4 PLBs distributed on a steel plate

The previous tests have shown that, according to the type of analysis performed, same sources may appear different if the position of the source itself on the specimen, or the position of the sensor, or both, change. The following test is designed to examine this topic more deeply and to identify the analysis required that accounts for the differences.

7.4.1 Test setup

Several PLBs were executed on a steel plate of dimensions $18.2 \times 25.4 \times 1$ mm, in the position shown in Fig. 7.25. Sensor S3 with the letters from A to L as shown in the same Fig. 7.25. For each position of the sensor, two PLBs were executed.

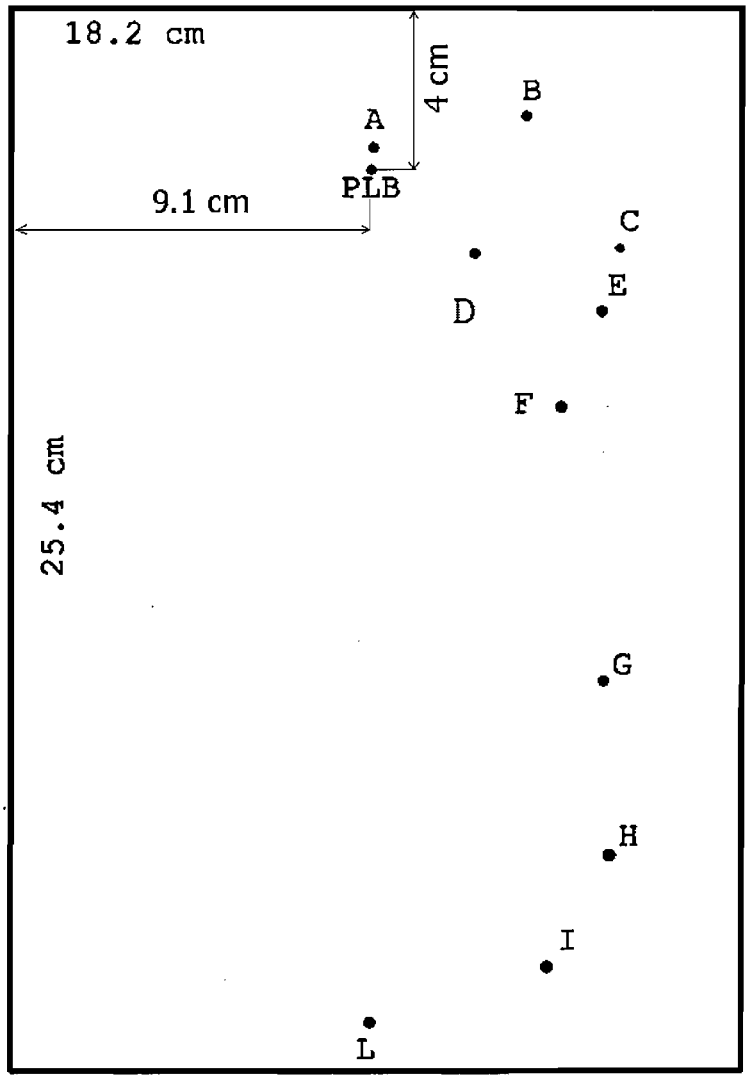

Figure 7.25: Schematic of the steel plate with the identification of the positions

The detected wave speed is 5000 m/s. The details of the acquisition for this test, named "S" for "scattered", are summarised in Table 7.7. The PAC system was set-up to collect a 10 kbytes-long waveform sampled at 2MHz, for a total of 5 ms each (including the pre trigger time).

Table 7.7: Parameters adopted for test S

Acquisition threshold	65 dB
Preamplifier gain	40 dB
Analogue Filter (software)	1 kHz–3 MHz
Sample rate	2 MHz
Pre-Trig	128 bytes
Waveform length	10 kbytes
PDT	200 μs
HDT	800 μs
HLT	1000 μs

7.4.2 Results and analysis

A typical waveform ("typical" because they look similar in the time domain) from this test is displayed in Fig. 7.26.

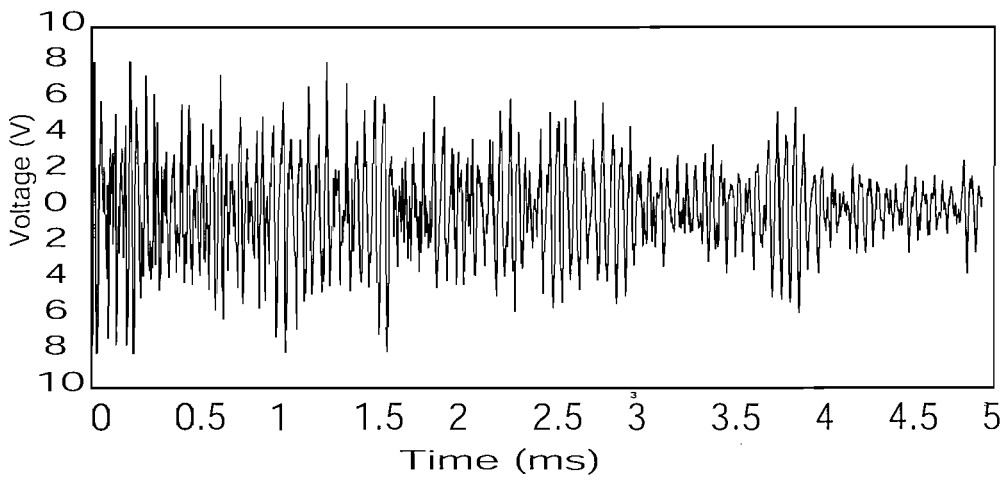

Figure 7.26: Typical waveform for test S as detected in A

Figure 7.27 shows the normalised mean of the spectra for the twenty waveforms collected for test S, and the spectrum of the waveform given in Fig. 7.26; it is evident that the frequency spectrum does not provide unique information about the positions of the PLBs. In Fig. 7.28 the calculated frequency centroid value is given for waveforms truncated after a

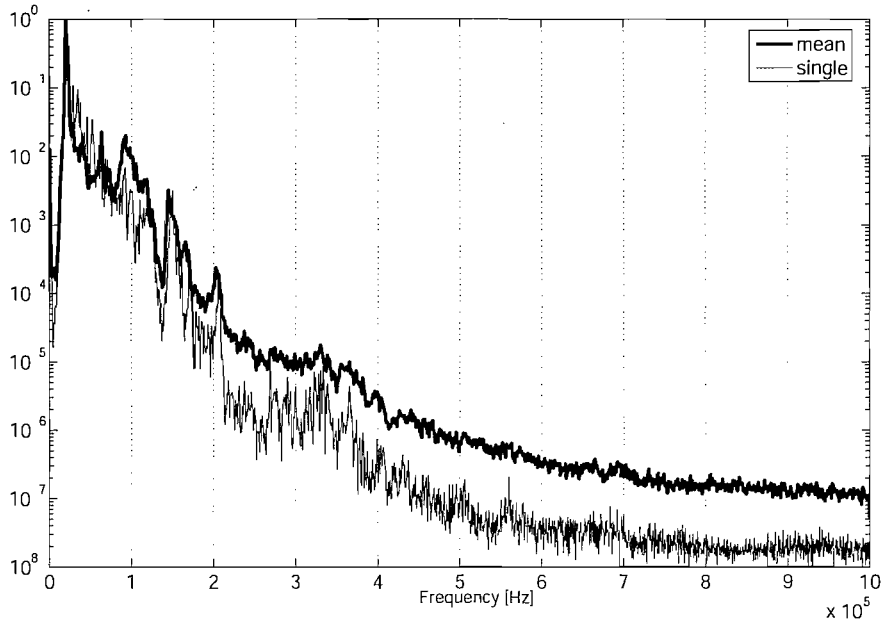

Figure 7.27: Spectrum from position A ("single") plus the geometric mean spectrum for all the twenty signals, both normalised

given sample time. It is clear that for sample times greater than around 350 μs the frequency content of each signal does not change. This can be attributed to the dominating effect of the large frequency peak shown in Fig. 7.27. The same figure also shows that, generally, the pairs of signals detected from the same position have similar curves. Although only a pair of PLBs is performed for each position, the repeatability is generally good, as exemplified in Fig. 7.29 by three randomly picked pairs, detected in positions G, H and L, for instance.

Table 7.8 reports frequency centroids values for each position, from the highest frequency to the lowest, at two different sample times: 100 μs and 5 ms. It is worth noting that, starting from the closest position to the PLBs, and then proceeding to the furthest, the order as dictated by the distance would be: A, D, B, C, E, F, G, H, I, and L. This order is not matched in the frequency centroids, indicating a more complex dependence, perhaps on the reflection patterns, rather than simply on the distance.

As it has already been hypothesized in §7.3.3 for a carbon strip, a possible explanation for this dependence of the results on the sampling time is the role played by edge-to-edge reflections together with the dispersion characteristics of Lamb waves. Prosser *et al.* (1999) suggest that PLBs on a panel may generate different detected signals because of different reflection paths. Some variability of the results is due to the time window the AE systems

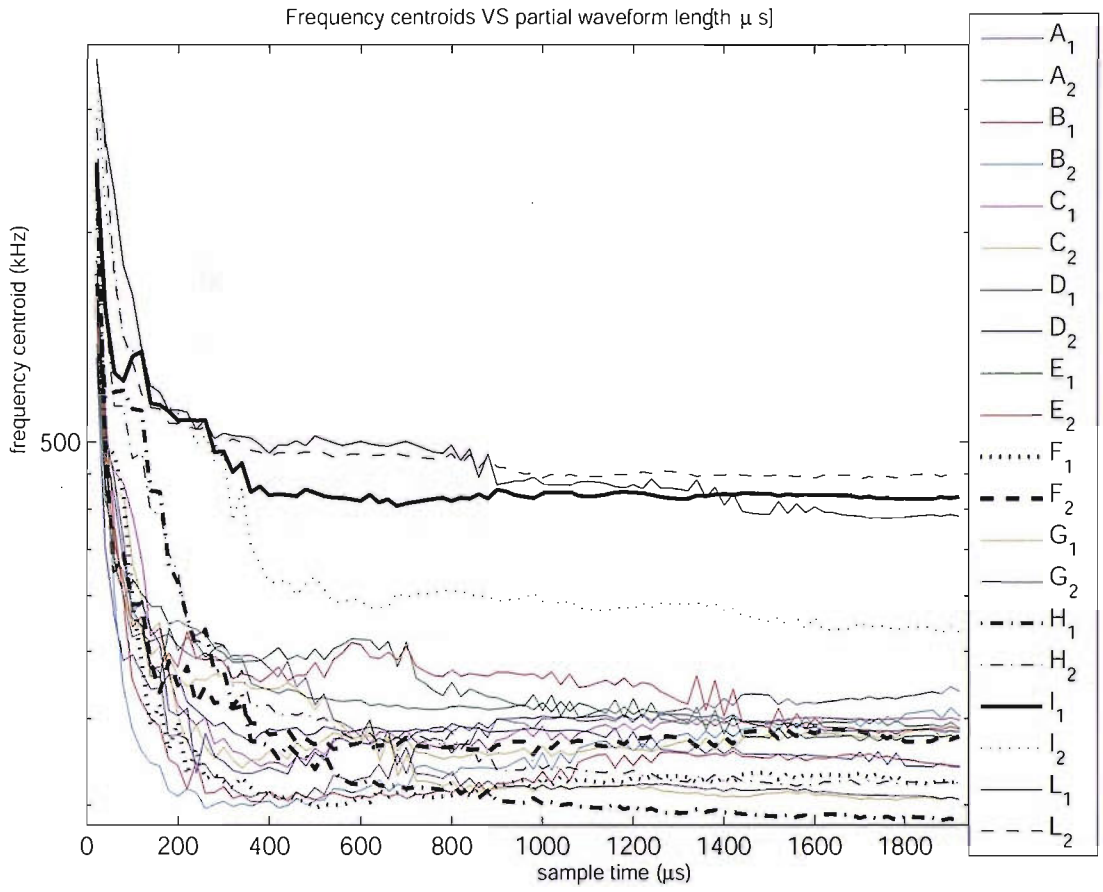

Figure 7.28: Frequency centroids (kHz, logarithmic) VS partial waveform length (μs, linear) for test S

uses to record the waveforms, and this dependence is ultimately dependent on the number and intensity of the reflections against the edges that this time window would allow.

In structures like those tested (a strip and a small plate), the presence of reflections is inevitable, and is detected differently according to the positions of the sensor and the source on the sample. In what follows, numerically realistic values for a reflection-less time window will be presented, for the assumption of a panel where the wave speed is isotropic.

7.4.2.1 Mathematical model for the reflections

The scheme in Figure 7.30 puts a sensor ("Se") and a source ("So") on a generic plate of which one edge is at an infinite distance from the source and the sensor and thus will not limit the reflection-less time window, and the other three, the two lateral edges are named "side" edges, and the other is named "rear" edge.

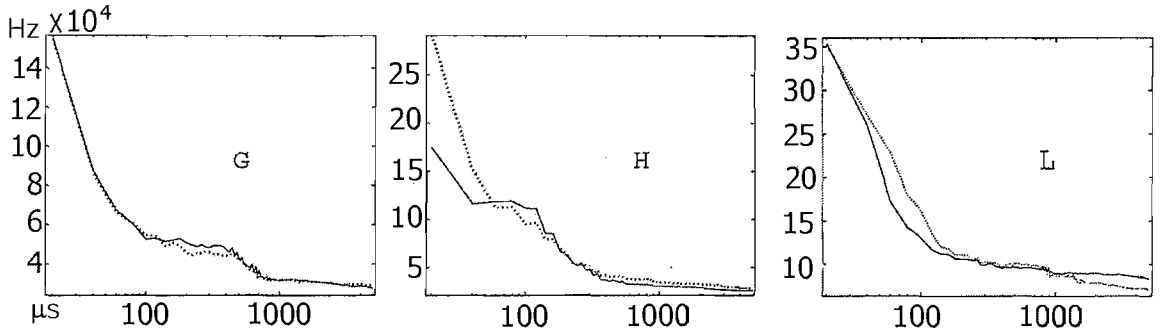

Figure 7.29: Graphs of the frequency centroids versus the partial waveform length for two PLBs detected respectively in positions G, H, L

Table 7.8: Frequency centroids (f.c., kHz) for each position at two different partial waveform lengths, and distance sensor–source (cm)

f.c. at 100 μs		f.c. at 5 ms		distance	
L	163	I	75	A	0.8
I	133	L	70	B	3.9
H	112	D	47	C	6.4
C	78	C	35	D	3.2
F	60	E	31	E	6.2
E	58	B	30	F	7.3
D	56	F	30	G	13.3
G	55	A	29	H	17.4
A	49	G	28	I	19.4
B	46	H	25	L	20.3

Figure 7.31 illustrates the schematic of a source (So) and a sensor (Se), where the reflection occurs from an edge on the side (in other words, the wave does not have to travel back and then forth to arrive at the sensor). According to the laws of reflection, the incident and reflected angle (θ) are the same for the *shortest reflection,* and this permits some simple calculations, that are shown in Appendix A.

To illustrate the effects of the above, two examples are provided, using $v = 10\ 000$ m/s.[8] Only half of the panel / strip, the semi plane where $x > 0$, is represented, because the results are symmetric. One example is a narrow and long strip of width 2 cm, the other is a large plate of width 50 cm. The latter is chosen to show that even for a large plate the values obtained are very short.

Figure 7.32 shows the results for the narrow strip, with $e = 1$ cm and $e_1 = 5$ cm. The

[8]This value is chosen because the linearity of the problem means that the final reflection-free times are linearly inversely proportional to the adopted wave speed, and a round value (10 000 or its half, 5000) makes quick calculations easier when comparing the wave speed with other values, more typical of real structures.

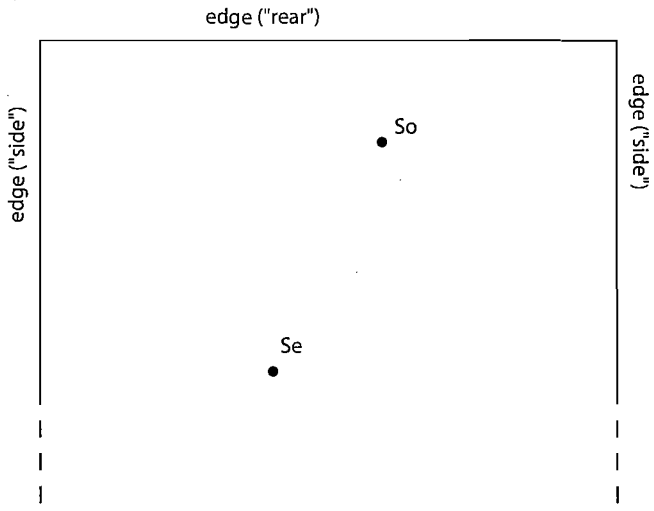

Figure 7.30: Schematic of a sensor and a source on an open plate

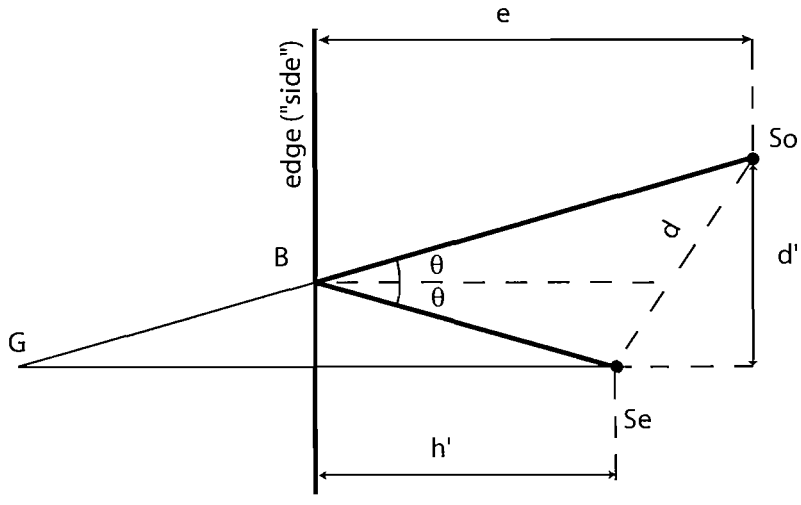

Figure 7.31: Schematic of a side reflection

time window plots are shown up to where $y = y_{max} = 6$ cm. Each point in the graph provides the value for the reflection free time if the sensor was placed in that point. As it is obvious, these time windows go to zero at the edges, and are everywhere extremely short.

Figure 7.33 refers instead to a large panel ($e = 25$ cm, $e_1 = 20$ cm, and $y_{max} = 20$ cm). The values are notably higher, but still incredibly shorter than the time windows commonly used in AE.

A map of the reflection-free times, calculated over half of the plate of test S, with a wavespeed of 5000 m/s, is displayed in Fig. 7.34, and shows that these times are 12 μs at the most, so *all the waveforms collected include a substantial amount of reflections.*

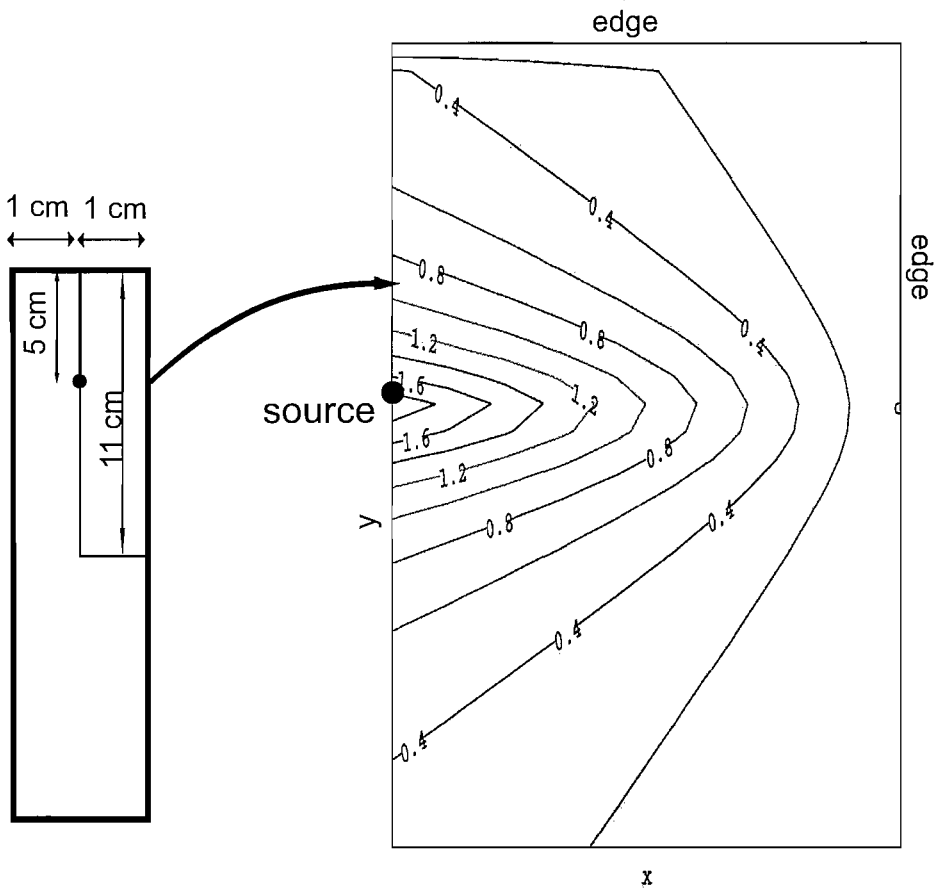

Figure 7.32: Time windows (microseconds) for a narrow strip: schematic and contour map (not in scale)

7.4.2.2 Conclusions

The maps shown indicate that:

1. the reflection-less time windows are extremely short to be adopted (they are so short that the collection of the "whole" waveform could be prohibited), thus leading to AE recordings always containing reflections,

2. these values vary over the panel, indicating that the number of reflections collected, the effect of dispersion, and thus the aspect of the waveform depend on where the sensors and the sources are.

With the typical sound speeds, panel dimensions, and time parameters, multiple reflections are inevitable: the system will record them. What is more important in view of a characterisation, though, is that *a definable reflection-less time window is* not only very short, but most importantly *highly dependent on the positions of the sensor and AE*

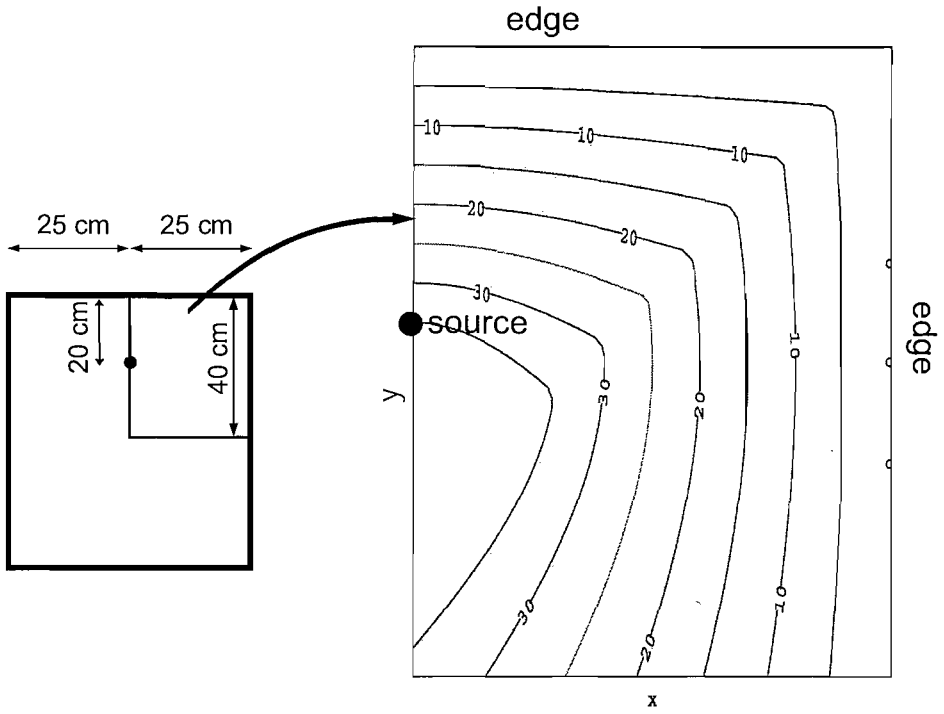

Figure 7.33: Time windows for a panel (microseconds): schematic and contour map

source.

7.4.3 Comments

The results shown in this section enlighten the following points:

1. Power spectra alone cannot distinguish the same source when detected at different positions on a plate.

2. Choosing the sampling time of the signal greatly affects the results.

3. Fourier analysis is originally designed for stationary signals; acoustic emissions typically are not, and the frequency centroids depending on the sampling time clearly show that.

4. Certain sampling times may be more appropriate to detail signals than others.

5. Frequency centroids versus sampling time curves may give information about where the same signal is detected on a panel.

From the point of view of a characterisation, one evident conclusion is that the spectra of identical PLBs, detected on different positions, differ substantially, as long as the frequency

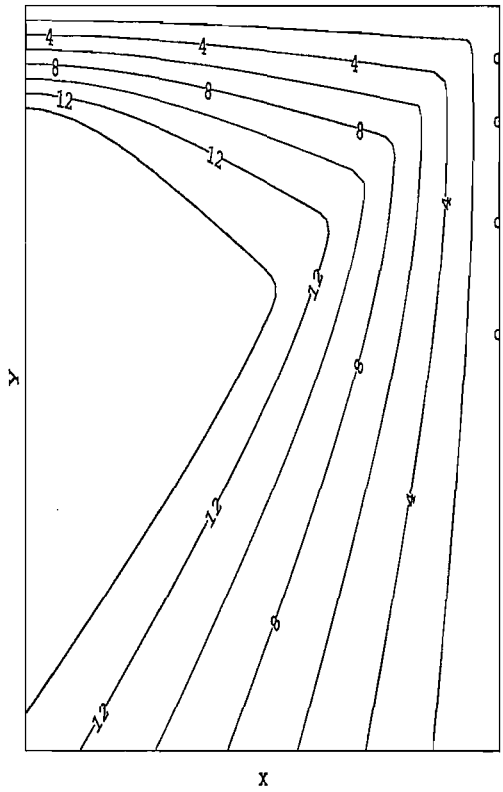

Figure 7.34: Reflection-free times (μs) on half of the plate of test S

centroid is used as their descriptive parameter.

7.5 Relationship between spectral features and position of the source on the panel

The previous experiments, particularly the one with the PLBs distributed over a steel plate, have emphasized that the position of the source and of the sensor affect the recorded signal. It has also been suggested that frequency centroids versus sampling times curves may contain some information about the different locations of the sensor. In this section, a test is designed with two aims:

1. providing a simple scheme of positions over which PLBs are detected, so simple that they can all be described with a single measure, the distance source – sensor;
2. inventing a new technique for an easy visualisation of the spectral features, that would allow an easy interpretation for a rapid matching of the spectra with the positions.

7.5.1 Test setup

PLBs are executed on an aluminium plate of dimensions 1100 × 185 × 5 mm, at one fixed position, and detected in five positions (A, B, D, E, F) by a single sensor (S3). The dimensions of the plate were chosen so to be sufficiently large and thus able to represent relatively larger reflection-less time windows. Two PLBs for each sensor location are considered. The acquisition parameters are summarised in Table 7.9, whereas the geometry is in Fig. 7.35. The plate is supported by a foam sheet and Vaseline is used as acoustic couplant.

Four of the five positions are designed to be easily described with a single parameter (the distance sensor – source): they vary their positions with respect to one pair of plate edges only. The fifth position, F, creates with the source location an oblique pattern on the plate.

Table 7.9: Parameters adopted

Acquisition threshold	66 dB
Preamplifier gain	40 dB
Analogue Filter (software)	1 kHz–3 MHz
Sample rate	2 MHz
Pre-Trig	128 bytes
Waveform length	10 kbytes
PDT	200 μs
HDT	800 μs
HLT	1000 μs

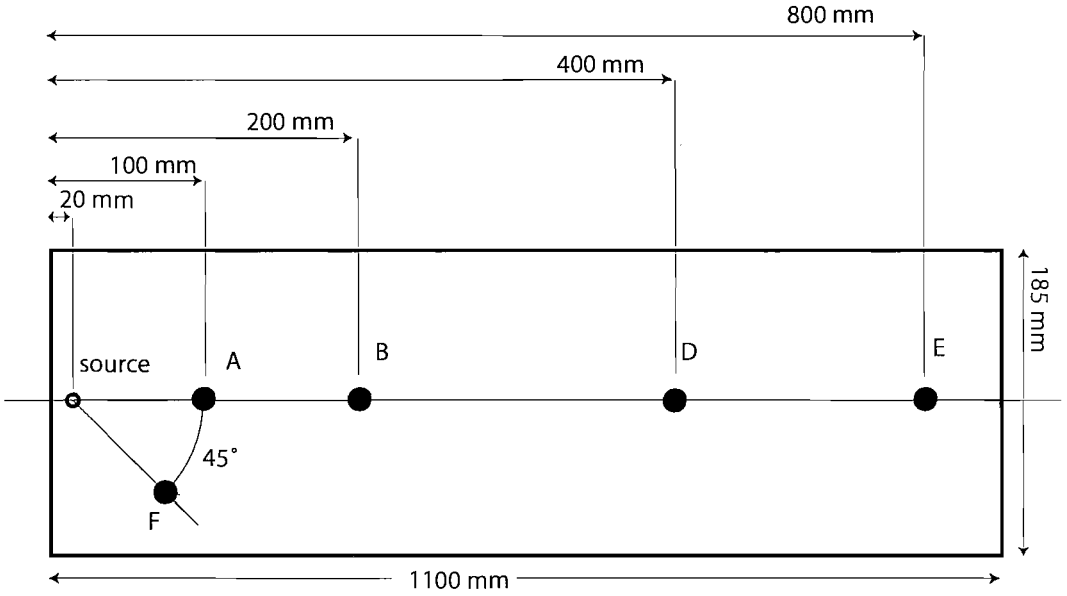

Figure 7.35: Schematic of the aluminium plate and the positions

In this way, there are two positions (A and F) with the same sensor-source distance, but with different orientation, and different configuration of wave reflections against the edges of the plate.

7.5.2 Results

All the spectra look substantially the same, and are undifferentiated to the naked eye. The following technique is thus devised so to emphasize the most important spectral features, i.e. the positions of the local maxima in the spectra.

Such spectra, especially when observed with AEWin, are extremely noisy and "spiky", and this results in an almost impossible task of objectively identifying the peaks. On the other hand, as it has been suggested previously in §7.3 and §7.4, the signals are non-stationary, and considering the power spectra at different sampling times makes sense.

The technique adopted here consists of the following steps:

1. A number of sampling times are considered, e.g. 30, 120, 220, 300, 450, 1000 μs.

2. For each sample time, and for each signal, the `pwelch` Matlab routine is used, with the default parameters (`pwelch(signal,[],[],512)`).

3. A graph is generated, for a single signal, where the normalised spectra of the chosen sampling times are plotted together (Fig. 7.36) and *local* maxima identified as shown

in the Figure.

4. These spectra are smooth (some of them are calculated on a very small number of data points), so it is easy to identify the local maxima. Each maximum is indicated by a vertical bar on the top of the graph (Figure 7.36), provided that the normalised amplitude of the spectrum at that point exceeds a chosen threshold (0.01 in the example). Local maxima too close to each other are excluded for better clarity.

5. Each sampling time provides a different set of maxima, that would otherwise be hidden by the spiky and irregular aspect of the whole spectrum.

6. Taking advantage of the fact that now the spectra have been reduced to a short list of numbers (the local maxima), a graph like that in Fig. 7.37 can represent all the ten signals detected during this experiment: each horizontal row represents the local maxima (vertical bars) of a single signal.

7.5.3 Discussion

Figure 7.37 summarises all the signals detected in this experiment: each row refers to one waveform, and reports the peaks found at different sample times. From the bottom to the top, the pairs of signals (two rows for each position) clearly show similarities. This technique is thus successful in enlightening spectral similarities between PLBs detected in the same position, similarities that would otherwise be lost or unnoticed in a simple power spectrum plot. Secondarily, these results show that the spectral features consistently vary with the detection position on the plate.

Although the signals presented would be characterised by roughly the same frequency centroid, the presence of the identified peaks may discriminate them. The exact number of these peaks does not have an absolute importance, since it depends on the subjectivity of the choice of the threshold. By means of an accurate fine tuning of this threshold, some features and similarities can be emphasised or even revealed.

In the test described, the two positions A and F can only be distinguished by the presence of an additional peak (a couple of lines in the graph) just below 100 kHz, that would not be observable in position F. Examining the scale of the graph in Fig. 7.37 reveals that all the peaks are closely packed together, and in fact the the choice of the threshold able to show

the differences was particularly critical. While the PLBs are described by low frequencies, different sources — such as damage in composites — may have a richer frequency content and the fine tuning of the threshold might have to be different. The following chapter will apply this technique to the acoustic emissions generated by failure in composites.

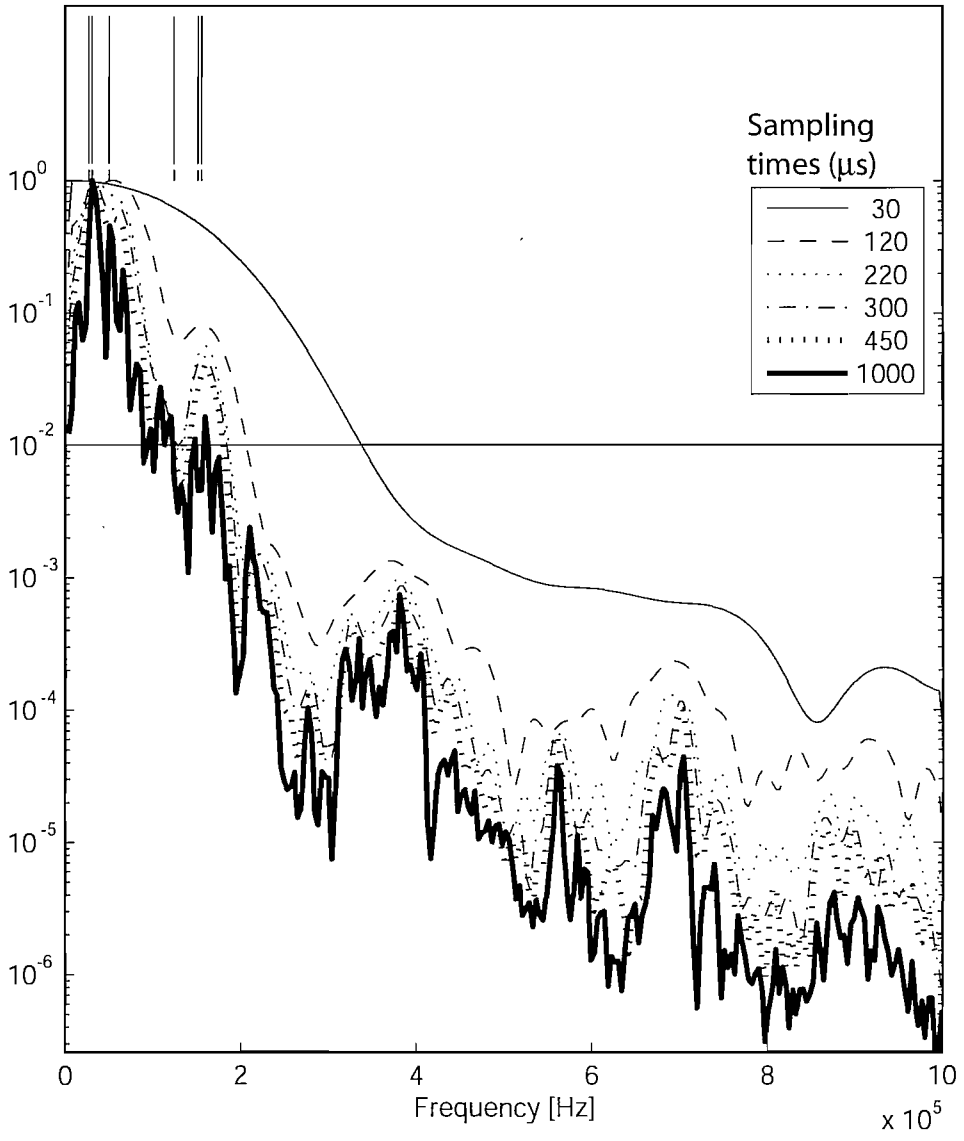

Figure 7.36: Superimposition of power spectra calculated at different sampling times (in the legend, in microseconds) and normalised, for a single signal detected in position F, with the indication of the local maxima and of the threshold. The semi-logarithmic scale makes the threshold clearly visible at $10^{-2} = 0.01$

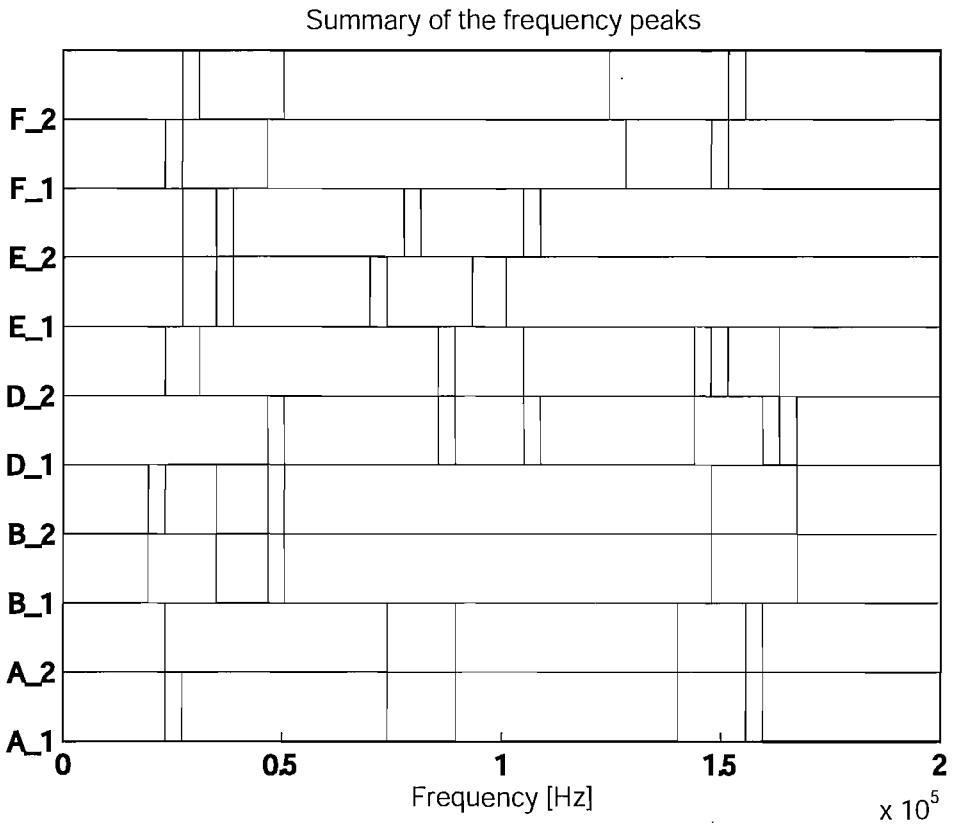

Figure 7.37: Summary of all the signals from this experiment — abscissa: frequency, ordinate: position of the sensor

7.6 Conclusions

The experiments reported in this chapter have addressed the attention to the following issues:

1. the suitability of the analysis of the full frequency content, for the same purpose,
2. whether it is appropriate to consider a characterisation of the source, regardless of the material and the structure that the acoustic emissions have to travel through,
3. how to summarise in a compact form the huge amount of data usually associated with the spectral analysis of a large number of signals,
4. how the spectral content of the signals can provide with information about the position sensor/source system on the structure.

These points will be summarised individually in what follows.

7.6.1 Suitability of a frequency analysis

The results presented in §7, §7.2, §7.3, §7.4 and §7.5 have indicated respectively that the frequency content can give information on the effect of different material, the anisotropy, the sensor-source distance, and the position relative to the edges on a plate.

In dealing with the frequency content of the acoustic emissions, however, it should be born in mind that Fourier analysis is not designed for highly non-stationary signals.

7.6.2 Characterising a source only

The acoustic emissions detected by the sensors carry information about: the AE system and the set-up (§6.2), the travelling media (§7), the orientation between the travelling path of the signal and the direction of the fibres in a composite (§7.2), the travelled distance after which the signals are detected (§7.3), where the sensor is placed on a large structure (§7.4 and §7.5). Of course, this does not necessarily imply that any information originating by the originating mechanism alone is lost; nevertheless these factors complicate any abstraction of the source characteristics from all the additional and extraneous factors. Therefore the implementation of a health-monitoring system will have to deal with the specificality of the structure where it is implemented.

7.6.3 Compacting the spectral information

Probably the most important advantage of the full spectral analysis of the data, compared to an AE parametrization, is that it retains a great deal of the information contained in the signal. The obvious drawbacks are:

- for visualisation purposes, at least one graph (a normalised power spectrum) is required for each signal,
- in view of the implementation of a real-time monitoring system, that matches the signals with an internal database, a signal power spectrum is compounded by too many data points for an effective comparison,
- the amount of data further increases if information about how the signal builds up with time has to be retained.

7.6.4 Positional information contained in the signals

Although the obvious way to obtain positional information from AE data is by triangulation of the acoustic emissions coming from *two or more sensors* (§3.9), an adequate processing of the signals coming from *one sensor* may provide information related to the position of the sensor on the structure, as commented in §7.5.3. Although the work done has not provided any way to precisely link the signal and the position, it has shown that some of its information can be used to help a location done with triangulation. Further research might be addressed to this aspect.

The next step in the course of this work is naturally that of applying the techniques illustrated in this chapter in the study of the acoustic emissions of failing composites. To the variability due to geometry and size, composites add those of the lay-up and the diversity of source itself. The investigation will try to assess how stable a possible characterisation of the source could be respect to the variations of parameters like geometry, size, lay-up.

CHAPTER

EIGHT

Acoustic emissions from composite tensile test specimens

Not everything that can be counted counts, and not everything that counts can be counted.

Albert Einstein

The lay-up of the strips used in the work described in this chapter is designed to produce a variety of damage: UD lay-ups, for instance, will *preferentially* produce fibre fracture. It should be noted however that "preferential" does not mean that a single type of damage only should be expected; quite the opposite may be true, and for example Kouvarakos and Hill (1996) reportedly find, in UD fibreglass epoxy tensile test specimens, seven failure "mechanisms", i.e. seven different types of AE activity recorded, without an independent verification of the failure types. Composite materials cannot be *perfectly* UD and cannot be loaded perfectly in uniaxial tension.

The choice of the form of the strips for the following tests has the clear advantages of providing a small cross section area, that can be damaged at low load with an applied tension, and a simple shape, where a 2D source location would work adequately, even in an anisotropic material. A pair of sensors will be used to achieve the source location on the strips, to discriminate extraneous noise from signals generated by damage (Bohse, 2000).

This chapter describes single tests on nine tests specimens with different lay-ups. The results presented are for single specimens and no attempt has been made to combine data from a number of similar specimens. It should be noted at this stage that the data presented in this chapter have been selected from a batch of data, generally involving three or more

identical test specimens. This selection was done for two reasons:

1. Not all the strips tested produce useful results: sometimes the failure was highly irregular, or it occurred between the sensors and the grips. Also, at other times most of the AE activity was recorded from a position too close to either one of the sensors.

2. Most of the preliminary analysis was carried out visually on a large number of waveforms and spectra (in some cases, hundreds for each test), either within a single test, or within the same batch. This part of the analysis cannot be accounted for in detail hereby in printed form.

Whenever power spectra are presented, they are provided in a dimensionless (normalised) form because their absolute intensity is greatly dependent on the distance of the source from the sensor, and the effect due to attenuation is much greater than any difference due to the diversity of the sources themselves.

8.1 Test specimens

Table 8.1 summarises the tensile tests on CFRP strips,[1] the results thereof are then listed and explained in this chapter.

Table 8.1: Tensile tests — Notes: † notched, 15 cm intra-sensors distance; ‡ notched, 25 cm intra-sensors distance — E: Young's modulus (GPa) in the direction of the load, σ_u: Ultimate stress (MPa) in the direction of the load

I.D.	Lay-up	Section	Thickness (mm)	Width (mm)	Notes	E	σ_u
Zero1	$[0_4]$	§8.3	0.70	15		84	835
Zero2	$[0_4]$	§8.3	0.70	25		100	1000
Zero3	$[0_6]$	§8.3	1.0	15		—	1000
CP1	[0/90/0/90/0]	§8.4	0.81	15		59	760
CP2	$[0/90_4/0]$	§8.4	0.95	15		42	435
CP3	$[90/0_4/90]$	§8.4	0.97	15	†	—	n/a
CP4	$[90/0_4/90]$	§8.4	0.97	15	‡	—	n/a
Ninety	$[90_6]$	§8.6	1.0	15		—	55
AP1	$[+45/-45]_3$	§8.5	1.0	15		9	196

All the tests described in this section use a Hexcel Fibredux 920 CX-TS-5-42% carbon/epoxy prepreg, based on HexPly 920 resin, cured in autoclave at 3 bar and 140°C for

[1] The Young's modulus and the ultimate stress are an anticipation of the results described later. They are measured from the tests reported here.

30 minutes with a heating ramp of 60°/min (approximately 30 minutes) and cooling at a natural rate at ambient pressure.

The cured panels were cut into strips with a diamond saw. Usually an accuracy of ± 1mm was achieved on the dimensions. Steel tabs (1 mm thick, 45 mm long, and as wide as the strip) were sanded and bonded at the ends of the carbon strips with Araldite 2015 adhesive. The notched specimens, indicated in Table 8.1, were "double edged notched" using the diamond saw, to give notches of 1 mm "thickness" and 6 mm length, leaving a central cross section of 3 mm.

8.2 Test procedure

Sensors S3 and S4 are used for the following tests, chosen for their similarity in the frequency response,[2] that should guarantee a better source location. They were mounted onto the strips by means of an insulating tape, stretched to achieve a pretension, and Vaseline was used as acoustic couplant.

For the tensile tests, the specimens were mounted into a screw-driven Instron 5569 testing machine. The specimens were gripped using mechanical wedge-type grips. The test machine is a screw-driven, dual column, table-top test machine with a capacity of 50 kN, a 0.001–500 mm/min speed range and a load accuracy of $\pm 0.5\%$. The machine has two strain channels so extensometers could be used during the test. Although the operational acoustic noise is much lower than that measured on servo-hydraulic test machines with hydraulic grips, the test machine transmits some noise to the sensors through the specimen that can affect the AE readings.

The PAC AEWin data streaming software can record the acoustic waves detected by the sensors even in absence of any acoustic emission that triggers the system. To assess the level of noise interference from the test machine, the data-streaming facility was used to record a continuous stream of data in absence of actual acoustic emissions. Some data were recorded at 2 MHz by sensors S3 and S4 placed on a UD carbon strip ($[0_6]$, 15 mm $\times$ 30 cm, of the same batch used for the tests described in §8) mounted in the machine and the recording was carried out while the machine was active at 1 mm/min. The recordings were repeated with each sensor mounted close to the top and to the bottom grip. Figures 8.1 and 8.2 show the power spectra of these signals.

[2] According to the the calibration certificates (§5.2) and tests described in §6.2 (Table 6.6).

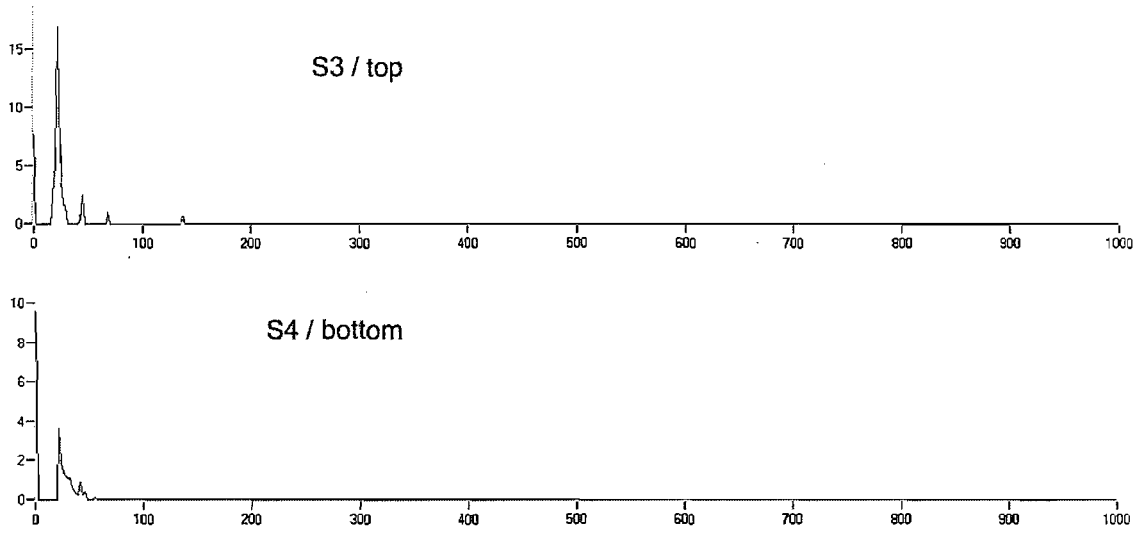

Figure 8.1: Power spectra (dB VS kHz) for sensors S3 (top grip) and S4 (bottom grip)

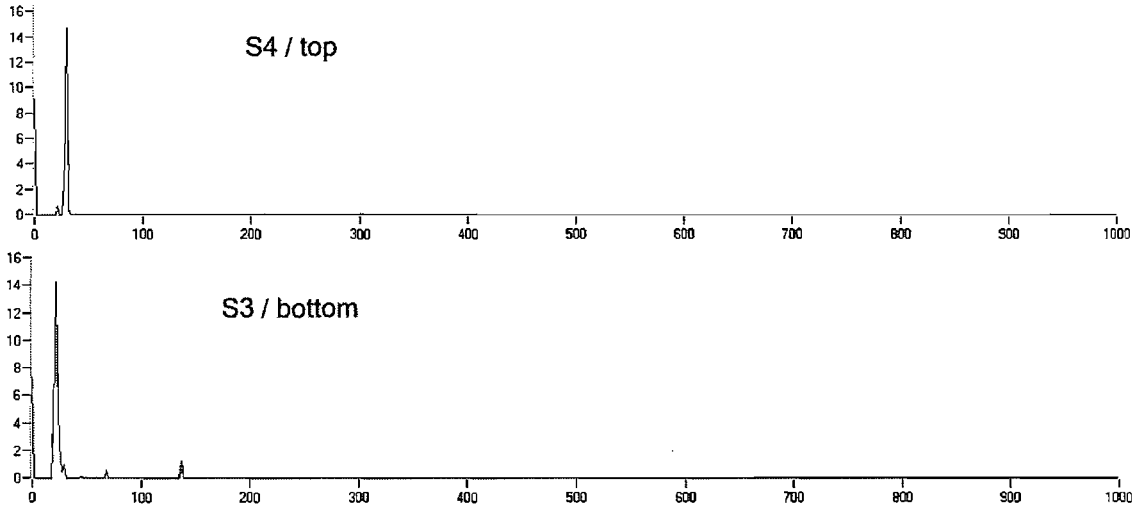

Figure 8.2: Power spectra (dB VS kHz) for sensors S3 (bottom grip) and S4 (top grip)

S3 appears sensitive to a high frequency noise (138 kHz); S4 does not. Overall, the machine noise is detected at: **22 kHz, 29 kHz, 44 kHz, 69 kHz, 138 kHz.** The four graphs do not show significant differences, so for the remaining tests the position of sensors (top or bottom) was not recorded. This analysis shows that the noise from the test machine does not extend significantly in the frequency range of interest for monitoring damage in composites so it will be ignored in the rest of the analyses.

During the tests an extensometer was also used to simultaneously monitor the strain in the specimen. The extensometer was mounted onto the specimens by positioning it above or below the sensors so that any acoustic emissions caused by clipping the extensometer to

the specimens could be easily filtered out by means of source location.

8.3 Unidirectional specimens

8.3.1 Description of the tests and basic AE features

The tests on unidirectional specimens are labelled Zero1, Zero2, and Zero3 and are summarised, in terms of sample geometry, mechanical characterisation, acquisition parameters, and test setup, in Tables 8.2 and 8.3. The timing parameters were chosen so to produce waveforms long enough to extract shorter sub-samples to examine separately.

Table 8.2: Test parameter summary for tests Zero

Parameter	Zero1	Zero2	Zero3
Young's modulus (GPa)	84	100	—
Ultimate stress (MPa)	835	1000	1000
Ultimate strain (%)	0.9	1.0	—
Lay-up	$[0_4]$	$[0_4]$	$[0_6]$
Gauge length (mm)	275	263	285
Width (mm)	15	25	15
Thickness (mm)	0.7	0.7	1.0
Notched	no	no	no
Cross-head speed (mm/s)	0.05	0.05	0.0167
Distance between sensors (mm)	173	165	205
Wave-speed used for location (m/s)	7700	7700	8540
Sensors used (Channels)	S3 (C1) & S4 (C2)		

Table 8.3: AE setup summary

Acquisition threshold (dB)	40
Preamplifier gain (dB)	40
Software analogue filter (kHz)	1–1000
Sample rate (MHz)	2
PDT (μs)	200
HDT (μs)	800
HLT (μs)	800

The selection of the acoustic emissions to be carried forward for further analysis was generally done by visual inspection of their power spectra as they were displayed by AEWin. This inspection examined the consistency of the data and excluded singular anomalies.

An overview of the AE activity of Zero1 is given in Fig. 8.3. Located AE events start

at a stress of 600 MPa and at 0.7% strain.[3] The one event identified at 0.55% strain was accompanied by a decrease in the load and can be attributed to slipping at the grips as it is clearly identified in the load VS time plot but not in load VS extension. No other irregular behaviour was recorded during the test. In Fig. 8.3, as in all the test data, a star indicates an event that will be analysed in full later. From the 36 events collected during

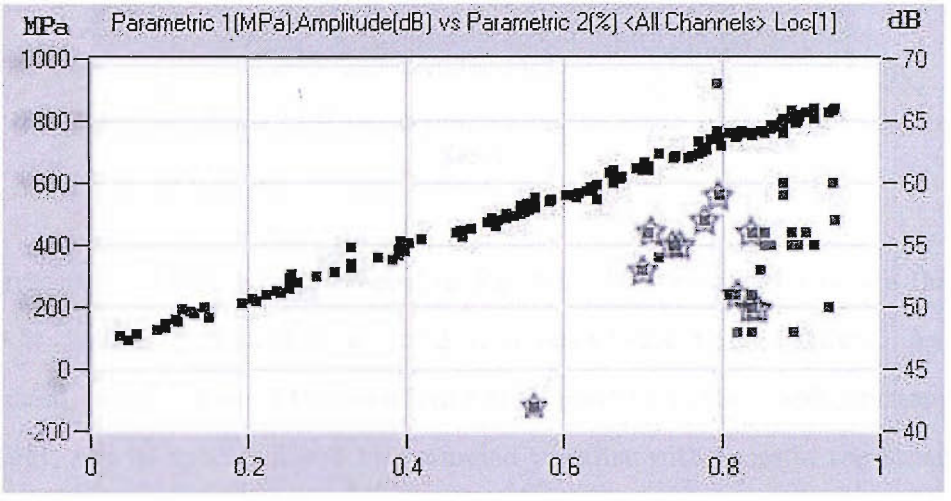

(a) Strain

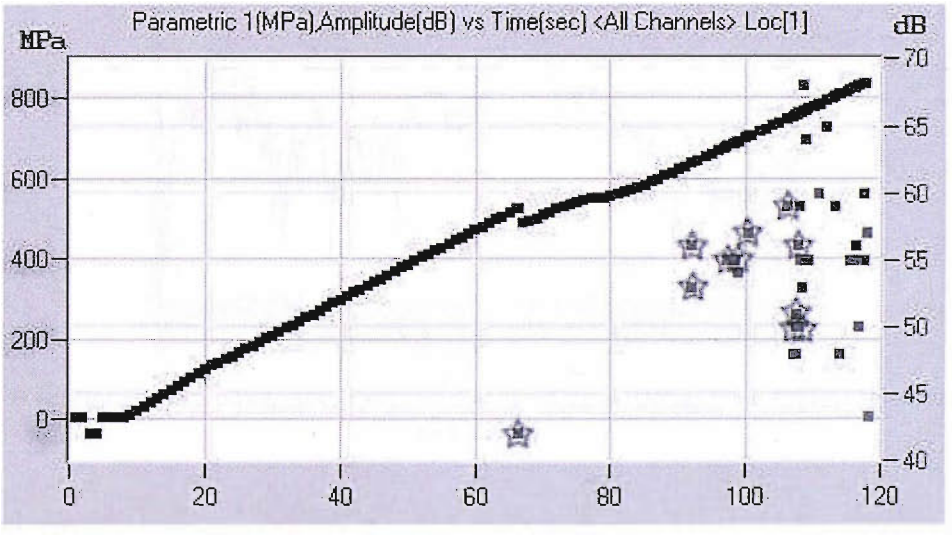

(b) Time

Figure 8.3: Overall AE activity for test Zero1, expressed as event amplitude, superimposed to the stress/strain (a) and stress/time (b) curves

test Zero1, ten[4] were chosen for further analysis. Figure 8.4 shows the AE activity over the length of the specimen; only one spatial group can be identified.[5] A visual inspection of their power spectra, conducted through AEWin, showed that most of the graphs have

[3]This suggests that the events recorded are related to fibre fracture.
[4]This number was chosen to be sufficiently small to present visuallt the data in a compact form.
[5]The sample failed in a position that is approximately the one suggested by this graph.

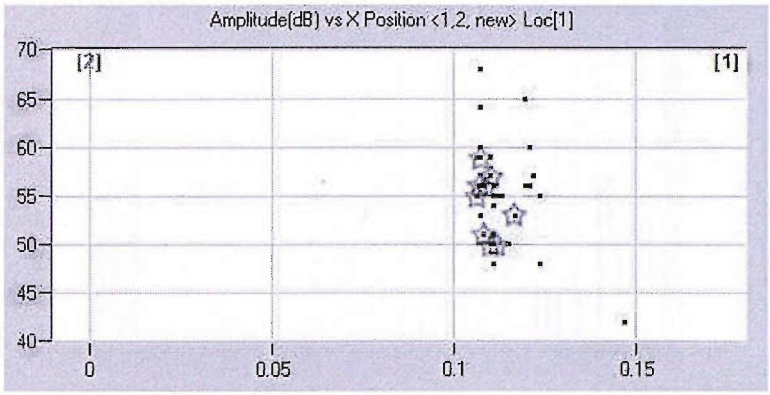

Figure 8.4: Event amplitude (dB) versus position on the length of the sensor (m) for sample Zero1

a strong resemblance to the one depicted in Fig. 8.5. The ten waveforms are thus chosen similar to it, and selected as they occurred at stresses below that of failure. An eleventh event is added, only because of the peculiarity of its position in the graph (corresponding to the slipping), and its spectrum will be examined together with those of the other acoustic emissions. Figure 8.6 shows the difference between (located) events and (unlocated) hits for

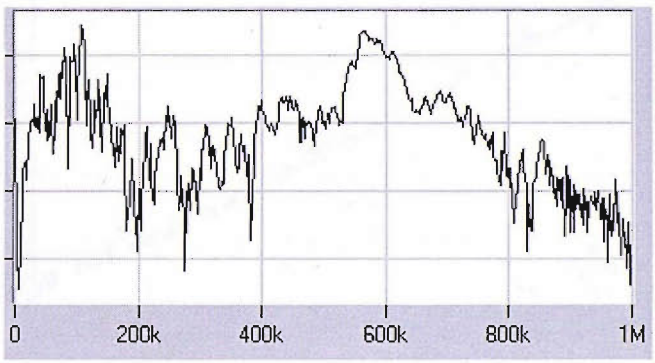

Figure 8.5: Normalised power spectrum, as displayed by AEWin, for a typical waveform from test Zero1

test Zero1: the logarithmic scale indicates an order of magnitude of difference, and no events are located for low values of time i.e. stress.

The AE activity for test Zero2 is given in Fig. 8.7. The sample had a width different from Zero1. At around 123 s an anomalous behaviour (slipping of the tabs) is visible, so only the events detected before 120 s are considered for further analysis. The first emissions are located at a stress of around 400 MPa and 0.43% strain. Figure 8.8 displays the AE activity over the length of the specimen for test Zero2: most of the activity is located close to the sensor S4, where the final failure occurred. In the figure, all the events collected during the

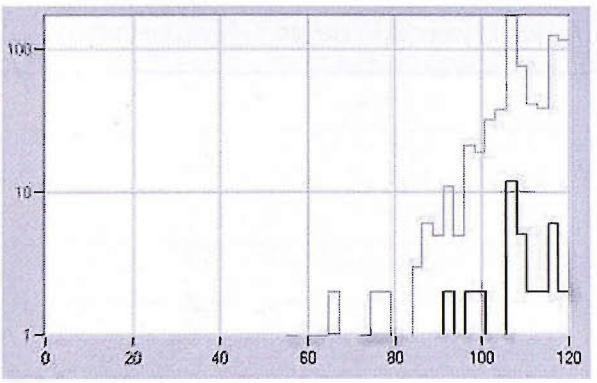

Figure 8.6: Histograms of hits (grey) and events (black) versus time, for sample Zero1

test are displayed. For test Zero2, not more than nine useful events were identified after a visual inspection, and after discarding several events as described before. The nine events are located within 6 cm from S4 and with stress below 380 MPa, and are visually consistent and similar to the event displayed in Fig. 8.9. They are marked with a star in Fig. 8.7b.

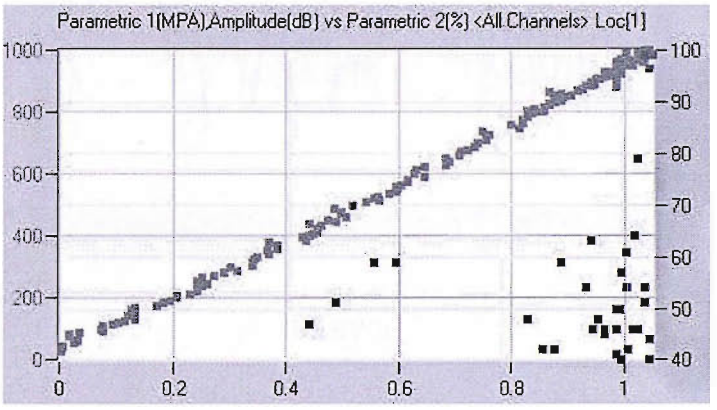

(a) Strain

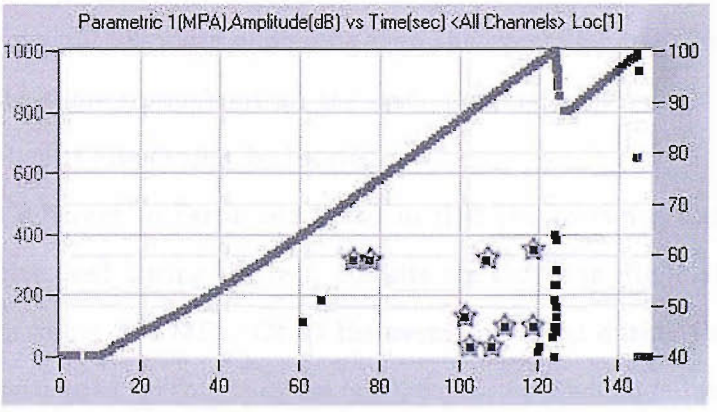

(b) Time

Figure 8.7: Overall AE activity for test Zero2, expressed as event amplitude, superimposed to the stress/strain (a) and stress/time (b) curves

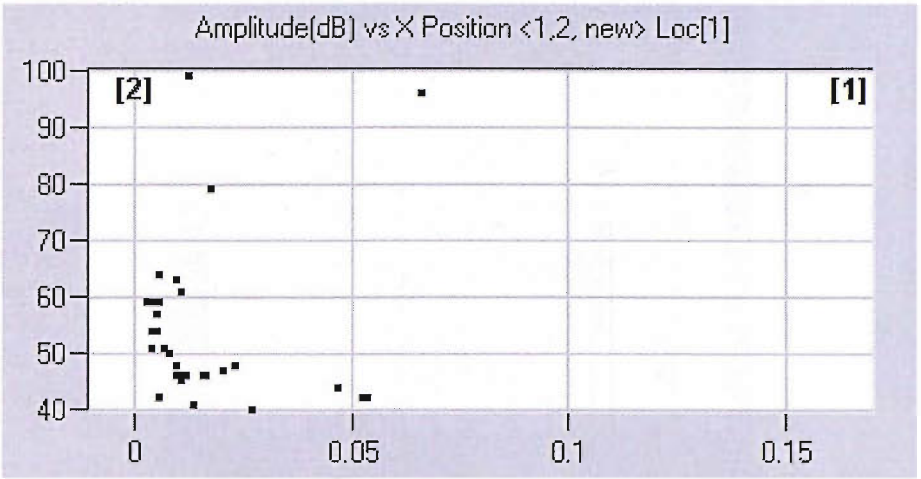

Figure 8.8: Event amplitude (dB) versus position on the length of the sensor (m) for sample Zero2

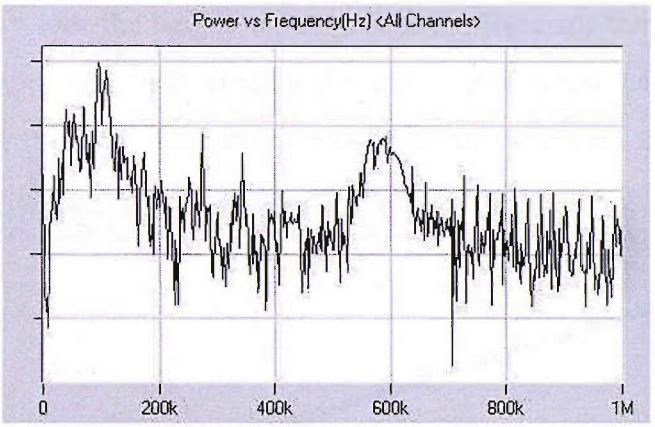

Figure 8.9: Typical spectrum (normalised) for the events from sample Zero2, as displayed by AEWin

Figure 8.10 accounts for the difference between events and hits for test Zero2. The hits are in one order of magnitude more numerous than the events for test Zero1, and this ratio is approximately the same throughout all the test. Especially during the first part of test Zero2, a large number of hits cannot be located.

Test Zero3 was different to Zero1 and Zero2 in that the specimen had six plies and an extensometer was not used during the test. Results are shown in Fig. 8.11. The first event occurs at a stress of about 500 MPa. Of all the events recorded during the test, only those before 330 s were considered, so that they are not too close to the final failure, which occurred four seconds later, at a load of 15.2 kN. In total, the events located in Zero3 before 330 s are 61. They are not identified by a star in Fig. 8.11, which would look overcrowded. The logic behind the selection of the events is illustrated in the location plot in Fig. 8.12, which

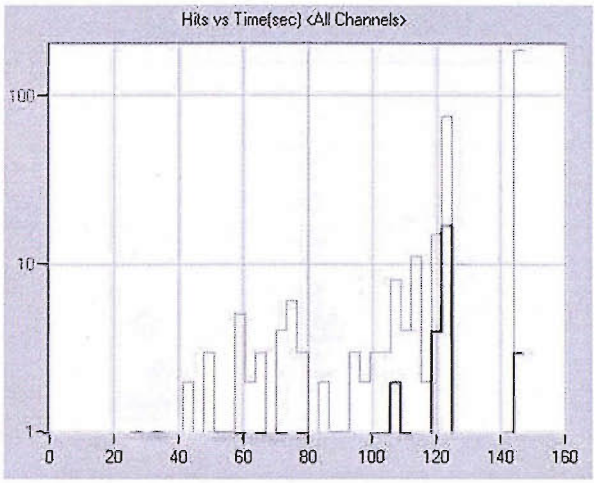

Figure 8.10: Histograms of hits (grey) and events (black) versus time, for sample Zero2

shows the AE activity over the length of the specimen. Although the results are obtained from an un-notched specimen, most of the activity is located at the centre of the strip, with only a minor part of the total AE activity located 6 cm away from S4. The existence of

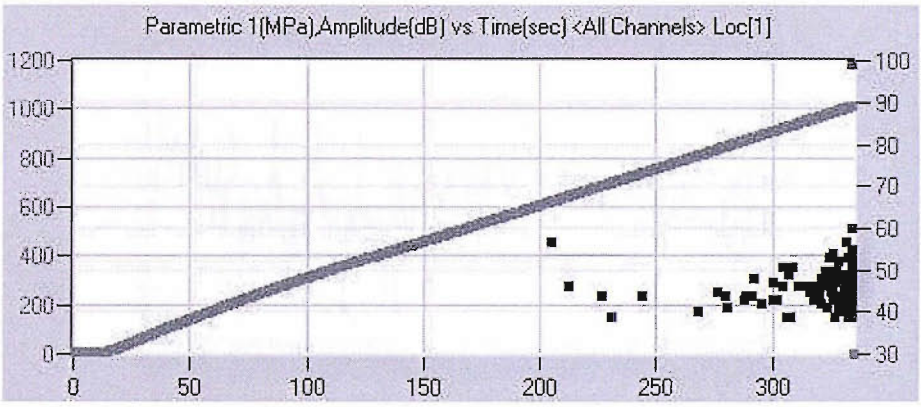

Figure 8.11: Overall AE activity for test Zero3, expressed as event amplitude, superimposed to the stress/time curve

two spatial groups of activity (one located around $x = 0.07$ and another one centered at $x = 0.11$, Fig. 8.12) makes the selection of the events to analyse further from test Zero3 a straightforward choice. Thus in the remainder of this section two sets of events will be considered: one group called "Six" and another called "Centre", respectively containing six and ten events. These two groups belong to two different positions on the specimen and therefore they are at a different distance from the sensor. The selection of the ten events for group Centre was done, as usual, by means of a visual inspection of the power spectra in AEWin. Figure 8.13 shows the similarity of the spectra obtained from the two groups

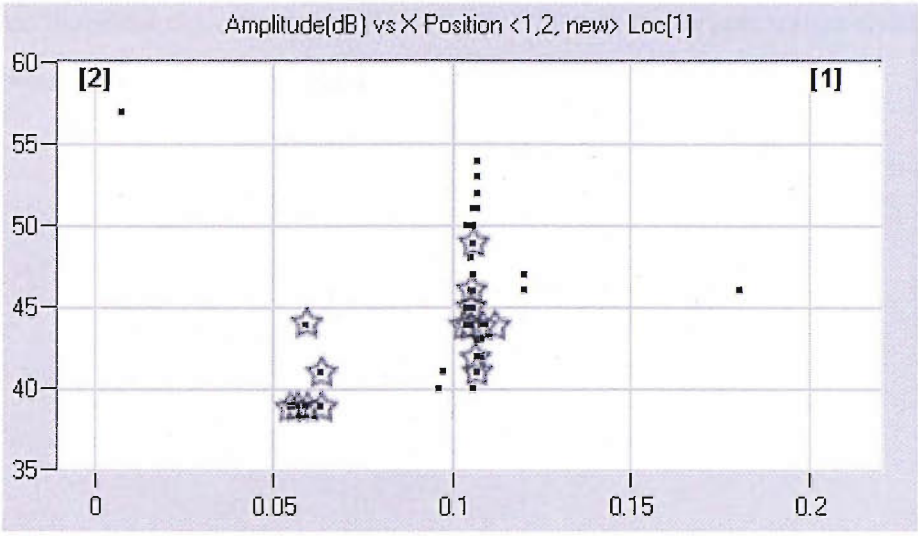

Figure 8.12: Event amplitude (dB) versus position on the length of the sensor (m) for sample Zero3

when examined with AEWin, indicating that a different analysis is necessary to see the information contained in the signals.

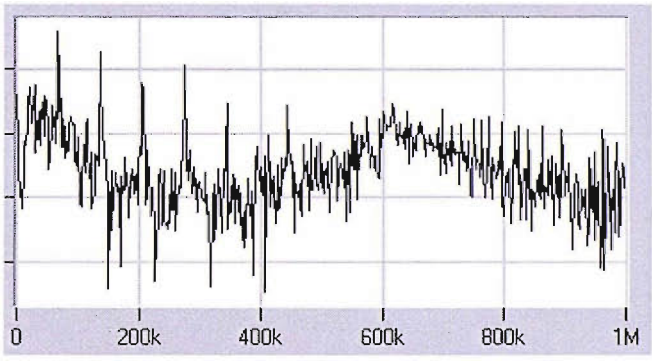

(a) From group Six

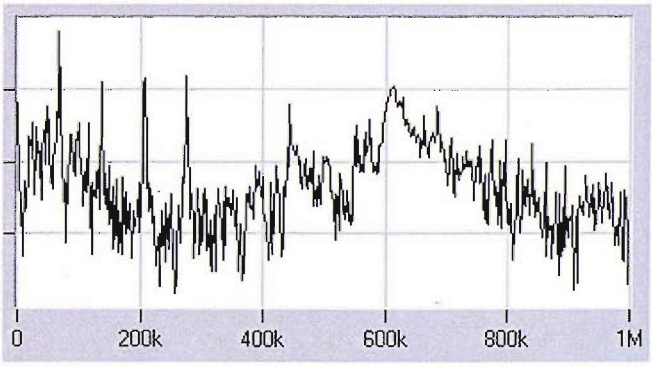

(b) From group Centre

Figure 8.13: Normalised power spectrum, as displayed by AEWin, for two typical waveforms from test Zero3

The AE activity does not show any characteristic grouping if examined with a visualisa-

tion analysis based on the classic parameters only. Therefore the spectral analysis described in the previous section will be applied.

8.3.2 Spectral analysis

The variation of the frequency centroids with the sampling time for the selected waveforms from test Zero1 is displayed in Fig. 8.14. All the ten waveforms show the same trend, although numbers 1 and 7 always keep a substantially higher frequency centroid. The start of the graph coincides with the detection of the major burst by the sensors. After about 40 μs the frequency centroids almost coincide around 550 kHz, then decrease. After 40 μs a second type of transient, at lower frequency, appears and modifies the spectrum and, consequently, the frequency centroid. Roughly speaking, these events are characterised by most of the activity concentrated around 580 kHz; a deeper analysis can show finer spectral details.

Using the technique presented in §7.5.2, of considering increasing sub-samples of the same signal, Fig. 8.15 links the power spectra to the various segments of the waveform 2 given in Fig. 8.14, chosen to exemplify the trend. In Fig. 8.16 the frequency spectra are colourised; the colour corresponds to the sample time that generates the spectra. If one sample time is responsible for a peak at the same frequency, then the longest sample time is displayed in the bars at the top of the plot.

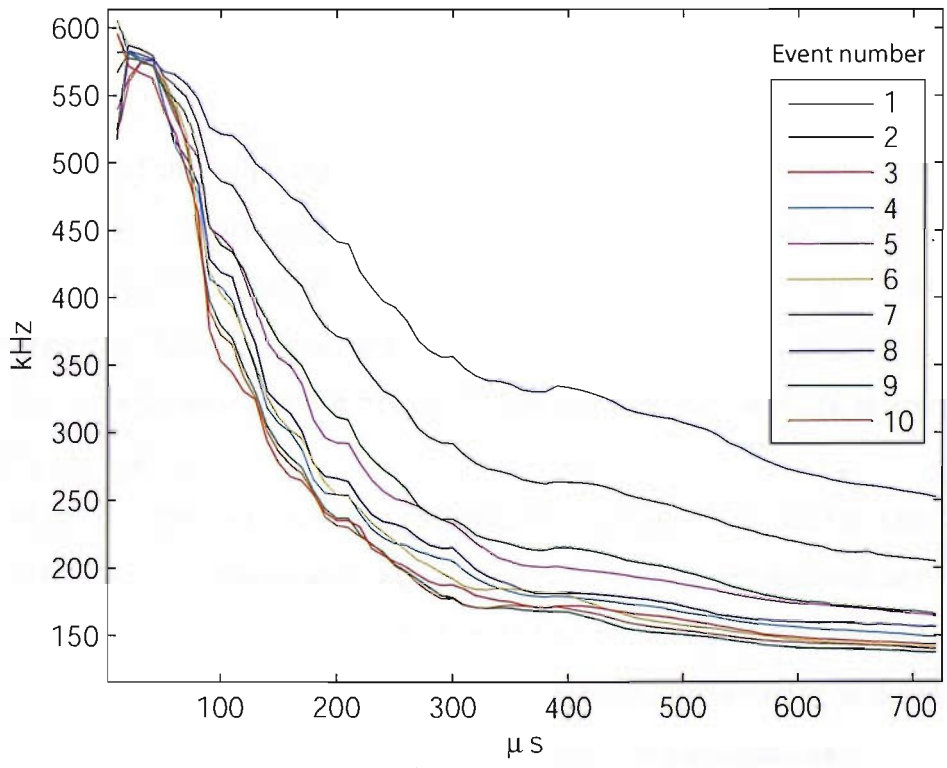

Figure 8.14: Frequency centroid (kHz) versus sample time (μs) for ten waveforms from test Zero1

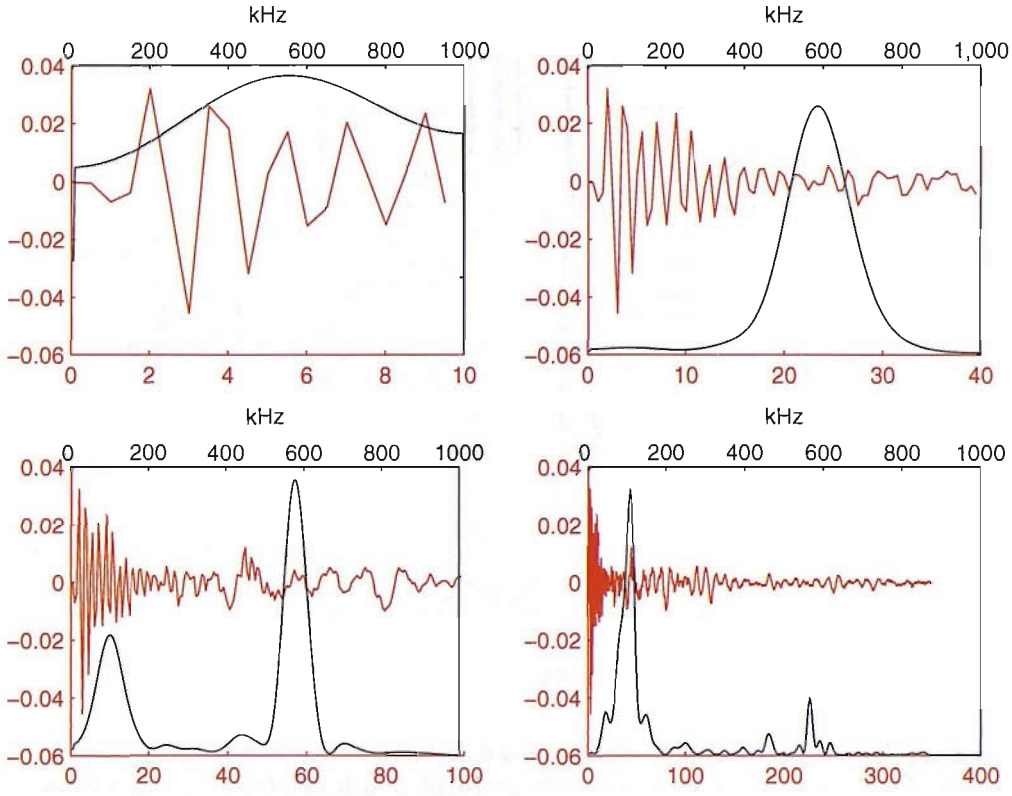

Figure 8.15: Normalised power spectra superimposed to the respective part of the waveform 2, for different sampling times — the lower abscissa is the sampling time (μs) and refers to the waveforms, measured on the ordinate in V; the upper abscissa is the frequency of the spectral density, nondimensional

The variation of the frequency centroids with the sampling time for the selected waveforms from test Zero2 is displayed in Fig. 8.17. According to this graph, two behaviours are clearly identifiable, and for instance waveforms 1 and 3 are of different types. Their spectra appear in Figure 8.18 and the most visible difference is the shift of large peaks from 600 to 800 kHz, that notably increases the frequency centroid, but only for short sample times, as indicated by the colours.

The variation of the frequency centroids with the sampling time for the selected waveforms from test Zero3 is displayed in Fig. 8.19, which show the existence of two frequency ranges: whereas for sample times longer than 150 μs the decay of the frequency centroid is relatively small and uniform, for shorter sample times the originating position (i.e. the group of events) seems to affect this decay ratio, that is less homogeneous.

Figure 8.20 illustrates the collection of the peaks for one waveform from test Zero3. A threshold slightly lower than for Zero1 and Zero2 was used to emphasise some relatively

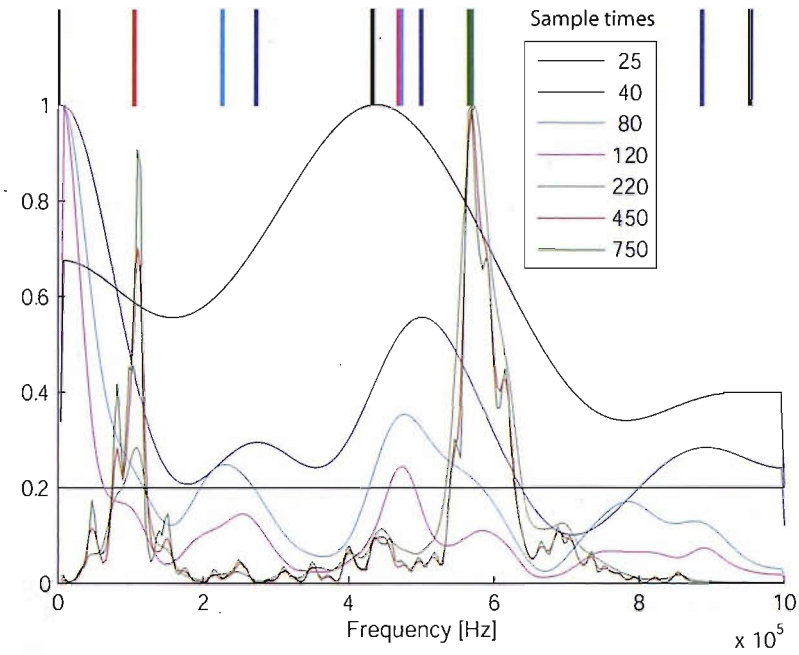

Figure 8.16: Spectral densities for different sampling times (in μs in the legend) for waveform 1 from test Zero1. A threshold of 0.20 identifies the local maxima as indicated by the upper bands

large peaks around 250 kHz.

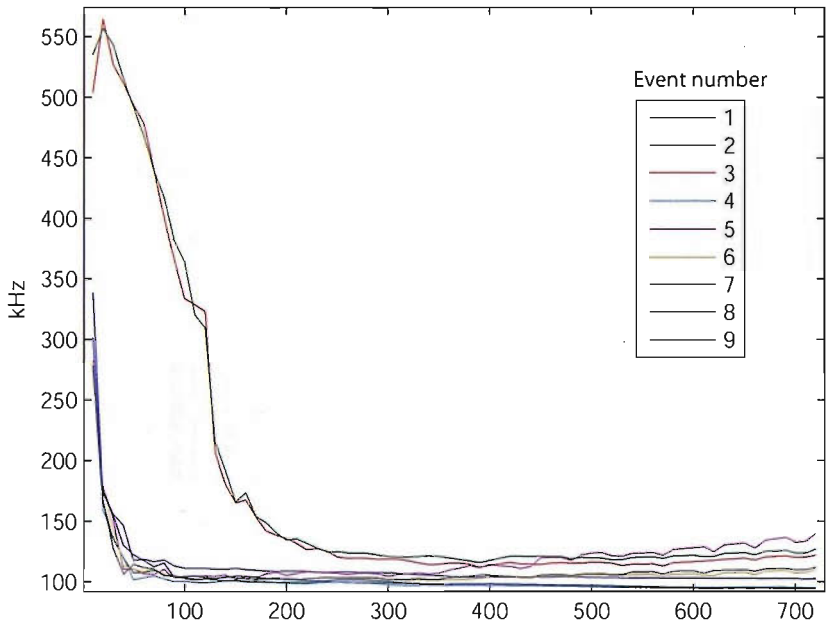

Figure 8.17: Frequency centroid (kHz) versus sample time (μs) for ten waveforms from test Zero2

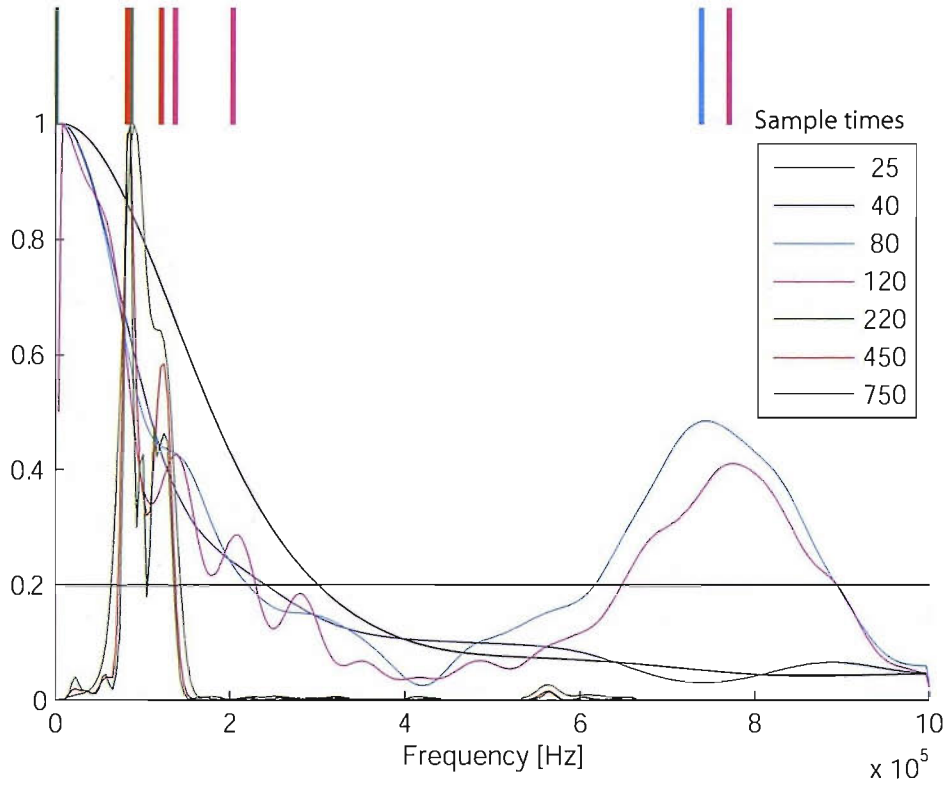

(a) Waveform 1

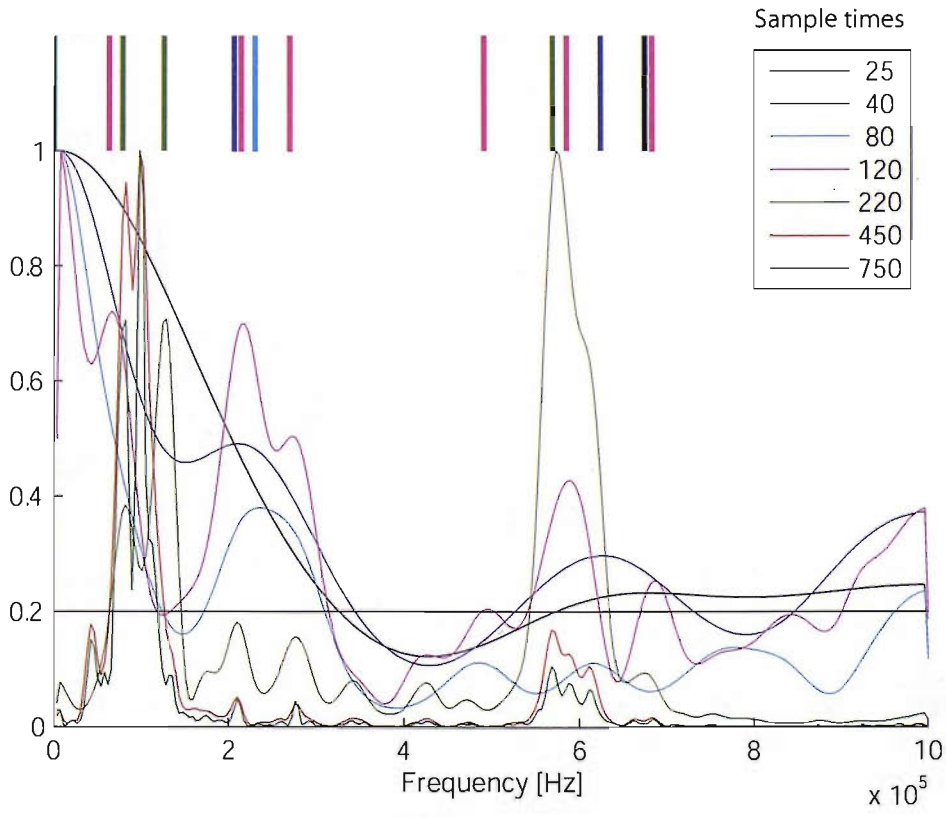

(b) Waveform 3

Figure 8.18: Spectral densities for different sampling times (in μs in the legend) for two waveforms from test Zero2. A threshold of 0.20 identifies the local maxima

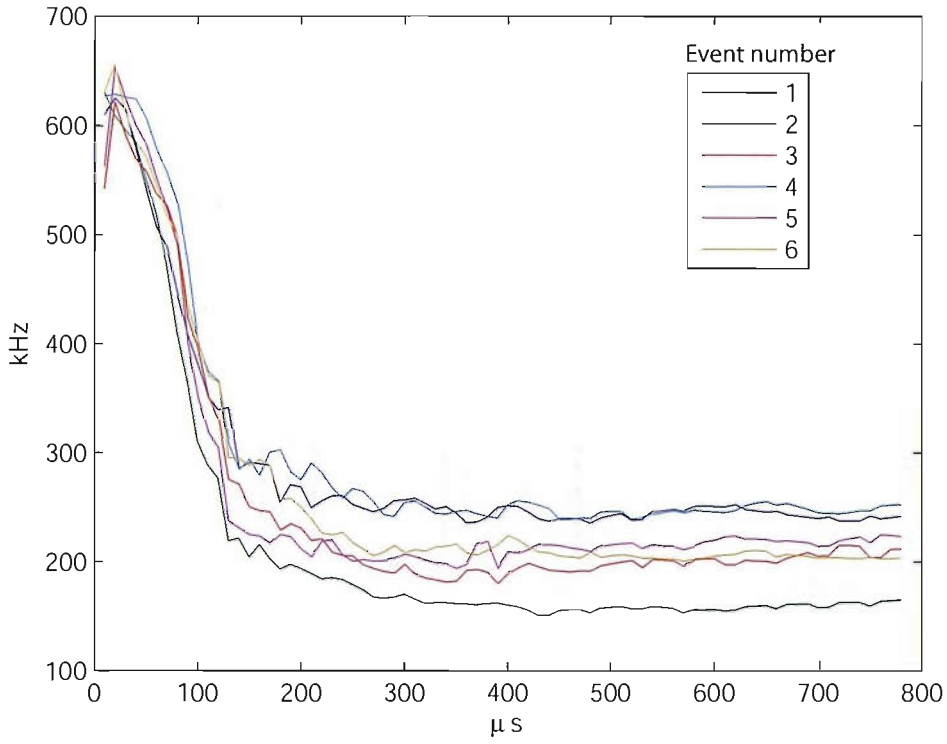

(a) From group Six

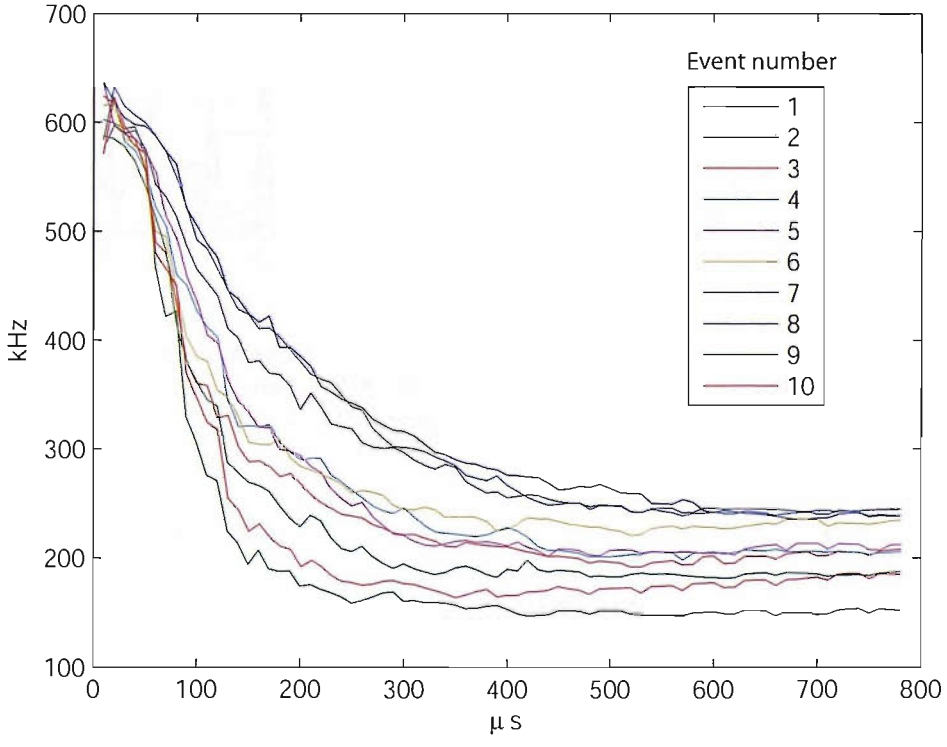

(b) From group Centre

Figure 8.19: Frequency centroid (kHz) versus sample time (μs) for the selected waveforms from test Zero3

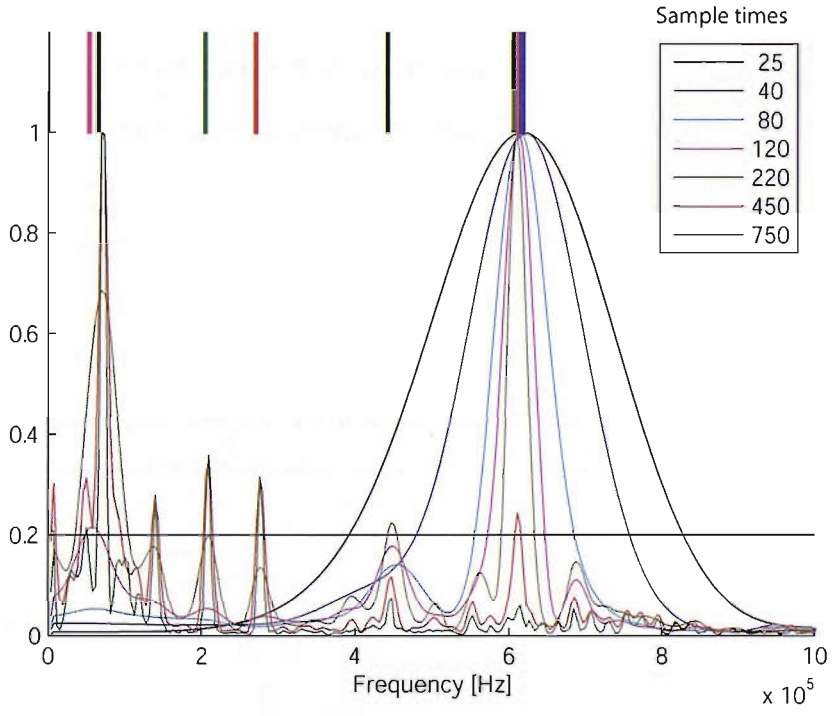

Figure 8.20: Spectral densities for different sampling times (in μs in the legend) for waveform 1 from group Centre, test Zero3. A threshold of 0.2 identifies the local maxima as indicated by the upper bands

8.3.3 Comparison of the frequency peaks and overall comments

Tests Zero are expected to produce mainly acoustic emissions due to fibre fractures. The following comparison, made with a waveform originated by a PLB on a similar specimen and at a similar distance from the source, show that Zero1's events originate from in-plane sources. Figure 8.21 plots the first part of a waveform collected from a pencil lead break on a specimen similar to Zero1. As should be expected, the extensional mode S_0 arrives first, at a higher frequency and — because the source (a PLB) induces an excitation which is mostly out of plane — also at lower amplitude than the flexural mode A_0. This waveform is displayed here for comparison: Figure 8.22 shows the first part of a waveform collected from Zero1. Beside the obvious difference in amplitude and scale (the break of a pencil lead introduces in the structure an energy greater than that of a single fibre breakage), by contrast, it is easy to see that the first segment of the waveform, clearly at higher frequency, has an amplitude larger than the rest at lower frequency (the waveform eventually decays without the rise in amplitude shown in Figure 8.21). This is consistent with the fact that fibre breakage introduces an in-plane excitation and so the extensional mode is the most excited, and in this respect the situation is the opposite as that of a PLB.

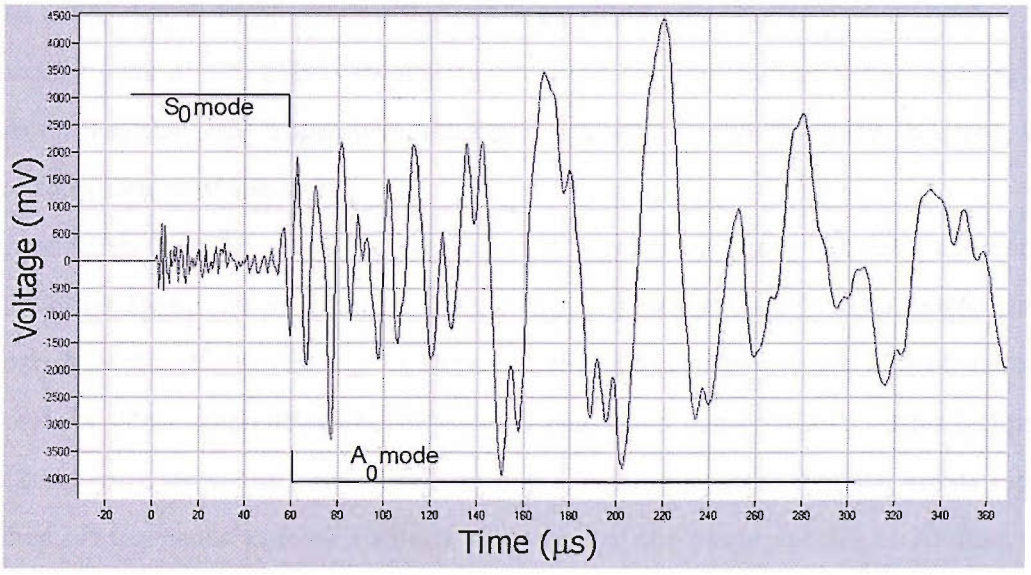

Figure 8.21: Waveform from a PLB on a specimen like Zero1; modes A_0 and S_0 are indicated

Using the technique described in §7.5.2, Fig. 8.23a displays the summary of the peaks of the ten waveforms from test Zero1, where a threshold of 0.20 over the normalised power density has been chosen to better identify the spectral features. Figure 8.23b displays the

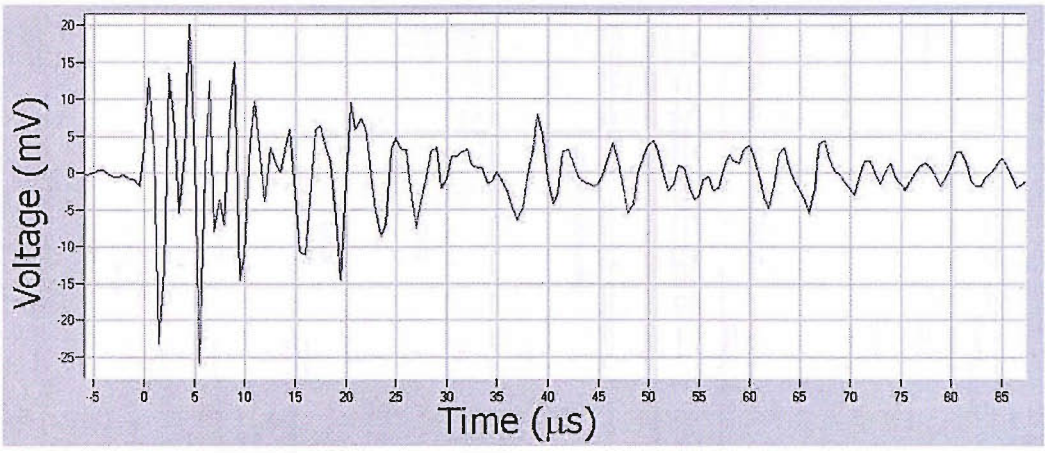

Figure 8.22: Beginning of a waveform collected from Zero1

summary of the peaks of the ten waveforms from test Zero2 and, finally, Figures 8.23c and d summarise the positions of the peaks in the power spectra of the waveforms from test Zero3. Perhaps the most evident feature shown by these four graphs is a stationary peak at about 600 kHz for tests Zero1 and Zero3. These peaks are not present in Zero2, involving a wider specimen. Qualitatively, the peak at 580 kHz in Zero1 is slightly different from the peak at 610 kHz in Zero3, which involves a slightly thicker specimen. Apart from the slight increase in frequency, these peaks differ in the sample times necessary to emphasise them. A secondary peak at 420 kHz is evident in Zero3 for medium sample times, although only from group Six; this peak appears sporadically, and with diverse intensity, in Zero1, Zero2, and in group Centre of Zero3.

Figure 8.23b (test Zero2) shows a graph that is relatively more cluttered and confused than the other three. Using a higher peak-defining threshold may help to better visualise the most characteristic peaks: this is shown in Fig. 8.24, with just the 25% of increase in the threshold. This graph shows better defined peaks and can provide a better comparison of test Zero2 with tests Zero1 and Zero3. In Fig. 8.24 it is apparent that the events recorded are not as homogeneous as from a simple inspection of the power spectra in AEWin.

During test Zero1, events were not located for low values of stress/strain (Fig. 8.3): any matrix crack possibly occurred at low stress levels could not be located by the system. Due to the lay-up and the high stress levels at which these events are detected, it is likely that they originated from fibre fractures, although it cannot be excluded that other mechanisms concurred simultaneously, such as pull-outs, fibre/matrix debonding and matrix cracks.

A peak at 580 kHz is a constant of the acoustic emissions from Zero1 (Fig. 8.23a).

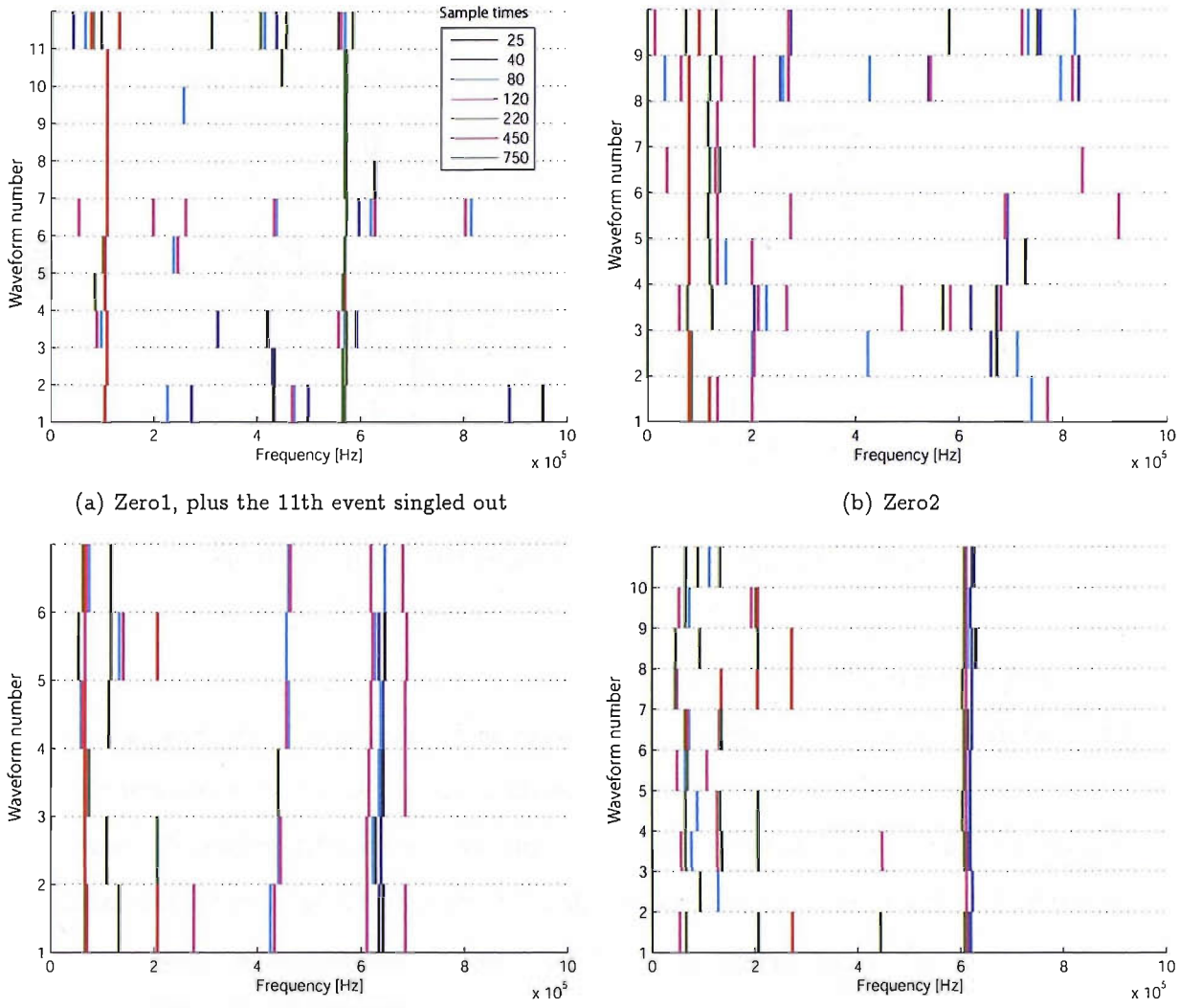

(a) Zero1, plus the 11th event singled out

(b) Zero2

(c) Zero3, group Six

(d) Zero3, group Centre

Figure 8.23: Spectral maxima for the waveforms selected, threshold = 0.20

This peak only appears for long sampling times, as indicated by the colours in the legend. The presence of this peak at long sampling times is also evident in Fig. 8.14: in fact, the decay of the curves is very slow (meaning the presence of high-frequency activity for long sample times), especially if compared with the similar curves from Zero2 in Fig. 8.17. Test Zero2 was designed to add *one* significant change in comparison of Zero1 — the specimen width — and it is exactly from this comparison that relevant comments stem for Zero2. In fact, although these two samples should have identical failure modes, the acoustic emissions detected show more differences than might be expected. In Fig. 8.17 the decay is faster and in fact Zero2's peaks at 580 kHz disappear for longer sampling times (Fig. 8.23b). According to Fig. 8.23b, Zero2's acoustic emissions do have peaks at high frequencies, but these only appear at short sample times, and this is evident in Fig. 8.17 too. Samples Zero1 and Zero2

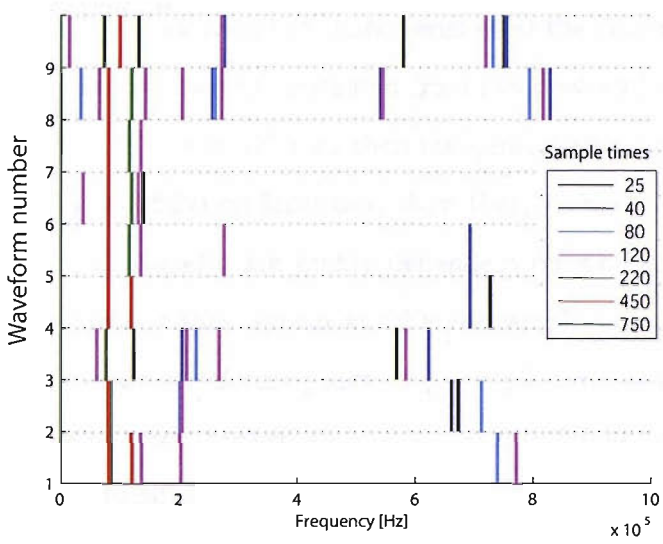

Figure 8.24: Spectral maxima for test Zero2, threshold = 0.25

were only different for their width: and *the results suggest that the recorded frequency activity depends on the proper of vibration of these structures (that is dictated by their dimensions), rather than on the characteristics of acoustic emission exciting the structures.* Geometric differences (here, the width of the specimen) can produce measurable dissimilarities in the output, and affect the measured signal more than the originating source itself. It should also be considered that the width of the sample has in fact a direct effect on the number of transverse reflections the elastic waves undergo to before arriving at the sensor.

In test Zero2, two types of event were identified (Figs. 8.17 and 8.18), that would be invisible to a traditional analysis, either conducted by means of AE parameters, or power spectra. While the "first" type (the one also appearing in the test Zero1) was relatively abundant, the "second" was not. Nevertheless, since the starting number of events available in test Zero1 was larger, and only a small fraction of events, visually selected, was carried forward, the presence of this second type in test Zero1 cannot be excluded. Waveforms 1 and 3 do not show, in Fig. 8.23b, the similarities that they showed in Fig. 8.17.

Specimen Zero3 was like Zero1, but thicker (six plies instead of four). Peaks at about 600 kHz appear in the events from Zero3, but they are different from those at 580 kHz found in Zero1: they only appears for medium-short sample times (Figure 8.23c); the same can be observed in Fig. 8.19a, where the decay of the curves is relatively fast before 130 μs. This difference of the results between Zero1 and Zero3 again suggests that the detected events

depend more on sample geometry than the characteristics of the acoustic emissions.

The fact that the acoustic emissions originated from two distinct locations in test Zero3, allows the analysis of events that only differ for their travelling distance to the sensor. Figures 8.23c and d (that refer to two different locations) show that, within the same sample Zero3, the quality of the peaks at 620 kHz are highly dependent on where on the specimen the emissions originate from: in fact they appear at different sample times in Figures 8.23c and d. *This suggests that in order to detect peaks, the sample time may have to be chosen according to the relative position sensor/source.* Another difference in the results from the two different positions is evident in Fig. 8.19, which shows that there is a significant decrease in the decay ratio of the frequency centroid when the originating location approaches sensor S3. The analysis of test Zero3 shows globally that the differences found in the events are due more to the geometric parameters (distance) rather then to the originating mechanism itself.

8.4 Cross-ply specimens

8.4.1 Description of the tests and basic AE features

Four tests involved four specimens of different types of cross-ply lay-up. These tests are labelled CP1, CP2, CP3 and CP4 and are summarised, in terms of sample geometry, mechanical characterisation, acquisition parameters, and test setup, in Table 8.4. The main reason for studying these specimens is the different layup, that would be more prone to a delamination failure and consequently provide a different type of damage and, eventually, a different data set upon which an analysis can be based.

Some test configurations resulted in no acoustic emissions, or provided not more than a single located event; this was the case for test CP2. When a lay-up shows little or no activity, it may be indicative of two facts:

1. The combination of the lay-up and the specimen size provides no acoustic emissions and shows no "warning" activity before the final failure.

2. The acoustic emissions are too weak to reach both sensors effectively and be located by means of the standard location algorithm designed for use on isotropic structures.

A correct explanation may reside in both these points.

Table 8.4: Test parameter summary for tests CP

Parameter	CP1	CP2	CP3	CP4
Young's modulus E (GPa)	59	42	—	—
Ultimate stress σ_u (MPa)	760	435	—	—
Ultimate strain ϵ_u (%)	1.3	1.0	—	—
Lay-up	[0/90/0/90/0]	[0/90$_4$/0]	[90/0$_4$/90]	[90/0$_4$/90]
Gauge length (mm)	380	305	270	350
Width (mm)		15		
Thickness (mm)	0.81	0.95	0.97	0.97
Notched	no	no	yes	yes
Cross-head speed (mm/s)	0.05	0.05	0.01	0.01
Distance between sensors (mm)	264	210	150	250
Wave-speed used for location (m/s)	6000	5050	7040	7040
Sensors used (Channels)	S3 (C1) & S4 (C2)		S3 (C3) & S4 (C4)	

An overview of the AE activity for test CP1 is given in Fig. 8.25. The first emissions are

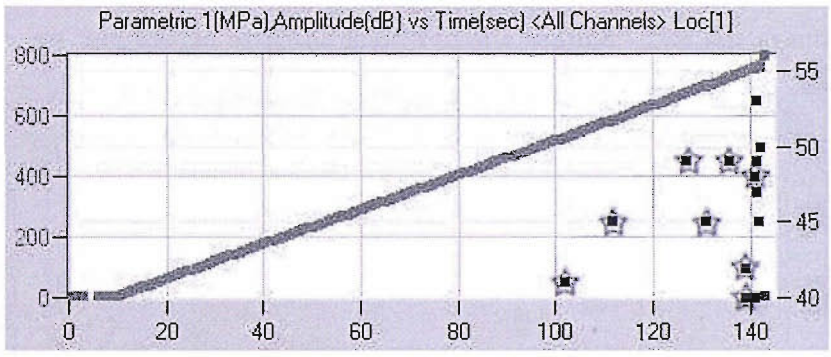

(a) Time

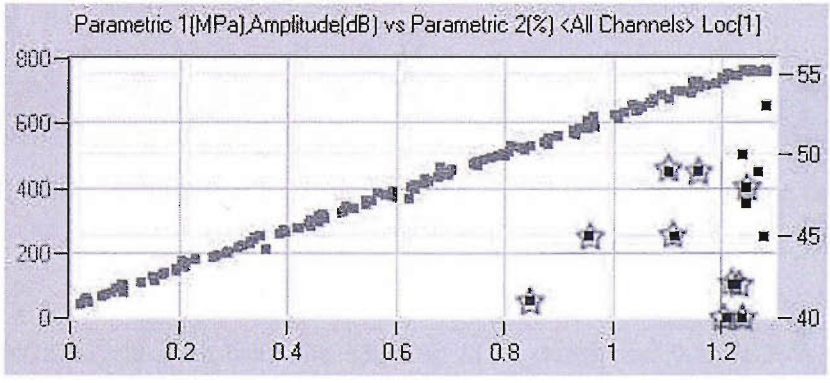

(b) Strain

Figure 8.25: Overall AE activity for test CP1, expressed as event amplitude, superimposed to the stress/strain (a) and stress/time (b) curves

located at a stress of 500 MPa and 0.85% strain. The activity intensifies right at the end of the test, making the exclusion of those hits that are caused by the major failure of the

specimen not straightforward. This is accomplished by the visual inspection of the spectra with AEWin. Using this visual inspection, roughly one kind of waveform can be identified, and Figure 8.26 provides a typical waveform displayed by AEWin.

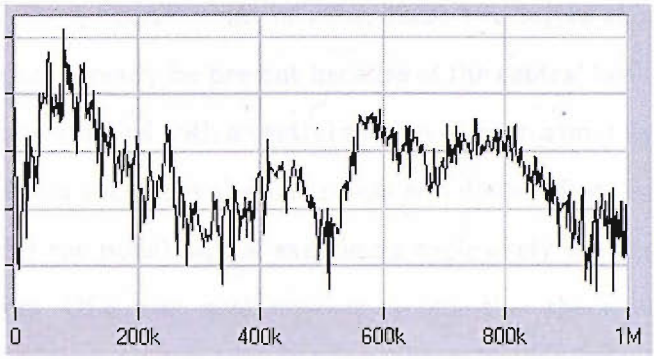

Figure 8.26: Normalised power spectrum, as displayed by AEWin, for a typical waveform from test CP1

The AE activity over the length of the specimen for test CP1 is localised in Figure 8.27: the events are few and sparse over the length of the sample. The ten events chosen from

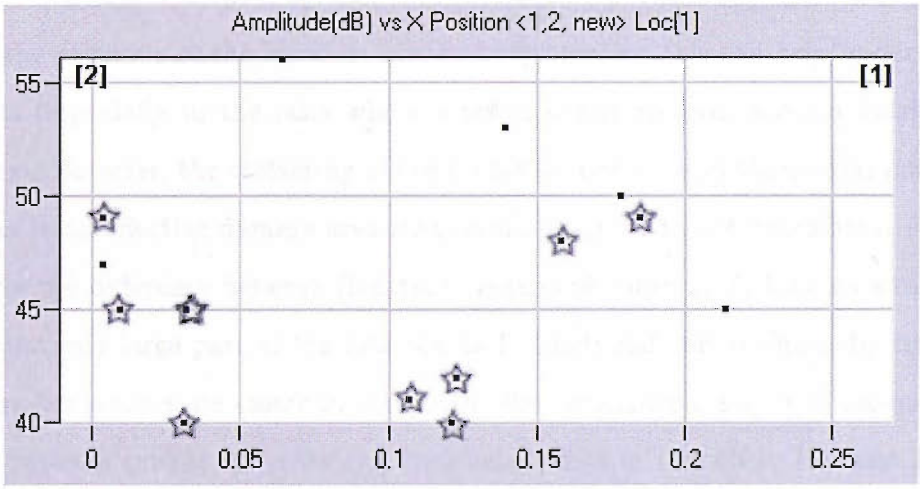

Figure 8.27: Event amplitude (dB) versus position on the length of the sensor (m) for sample CP1

CP1 for further analysis span over the 530–750 MPa stress and 0.85–1.25% strain ranges, and are not concentrated anywhere over the length of the specimen: they are identified with a star in Figures 8.25 and 8.27.

In the Zero specimens, the final fracture was such that the specimen violently disintegrated; this was not the case for the CP specimens. However, as there were so few located events in CP1 and none in CP2, it was decided to notch the specimens. The CP3 and CP4

specimens were notched quasi-uni directional CFRP strips. The "quasi" refers to the fact that, in addition to the central 0°-layers, these strips also have two outer 90°-layers, one for each side, that permits a more regular fracture of the specimens, by mitigating for the fibre discontinuities. From an AE point of view, these two layers should not add acoustic emissions that would not already be present because of the central layers.[6] Samples for tests CP3 and CP4 were edge notched with a central section of approximately 3 mm. The position of the pair of sensors was such that the notch was equidistant from each sensor. Notching the specimens provides the possibility of examining exclusively sources travelling the *same distance* to the sensors. Of course, such notches exclude that the acoustic emissions would be only due to fibre fracture. Load and strain data are not provided with these tests. In tests CP3 and CP4, the notched specimens provided a huge number of located events, so an individual analysis of all the events was not feasible. Ten events were inspected, chosen from the same position (i.e. the notch) and visually checked for consistency against their power spectra.

The AE activity over the length of the specimen is localised in Figure 8.28. It can be seen that the accuracy of the location is not always precise; this can help understand why several hits (especially in the tests where a notch is not applied) are not located by the PAC system. However, the scattering of the events located around the central position may also be due to an effective damage area that results larger than the notch area. Figure 8.29 accounts for the difference between (located) events and (unlocated) hits: as a result of the notch, a relatively large part of the hits can be located, and this is especially true for test CP3, where the sensors are closer to the notch. For comparison, Fig. 8.30 accounts for the difference between (located) events and (unlocated) hits in test CP1: this test included a large number of spurious acoustic emissions and only a small part of the hits are located as events towards the end.

As expected, the AE activity did not show any characteristic grouping if examined through a visualisation analysis based on the classic parameters only.

[6] Although the central UD layers are characterised by a fibre-dominated failure mode, other concurring damage types are to be expected.

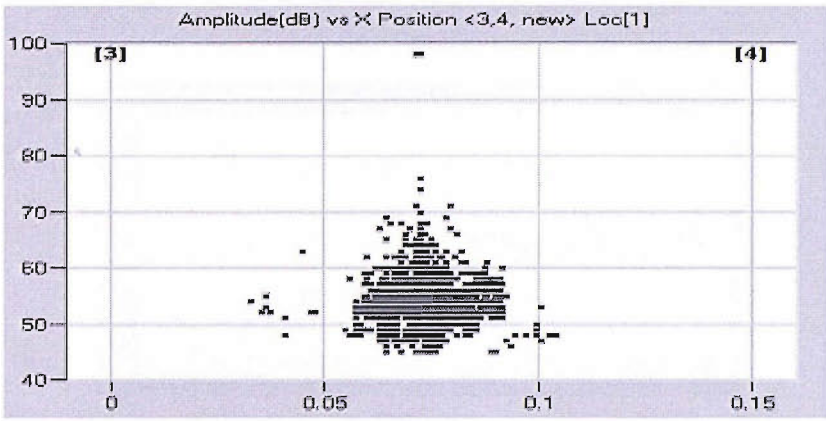

(a) Test CP3

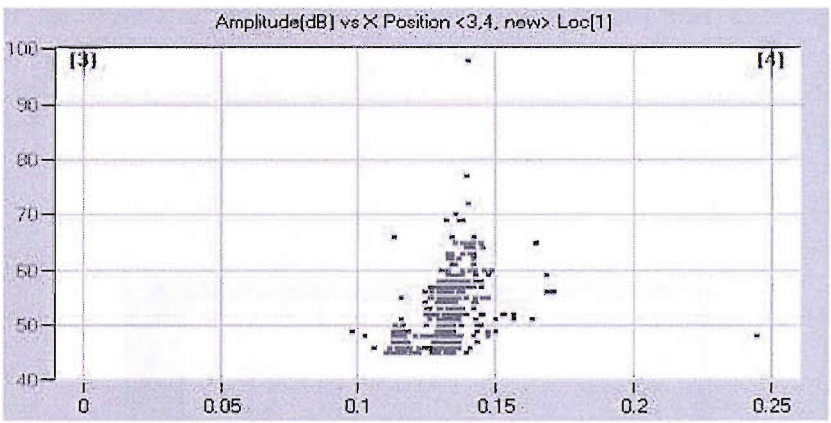

(b) Test CP4

Figure 8.28: Event amplitude (dB) versus position on the length of the sensor (m) for samples CP3 and CP4

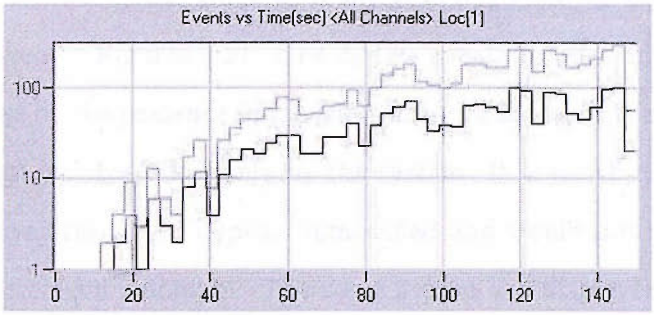

(a) Test CP3

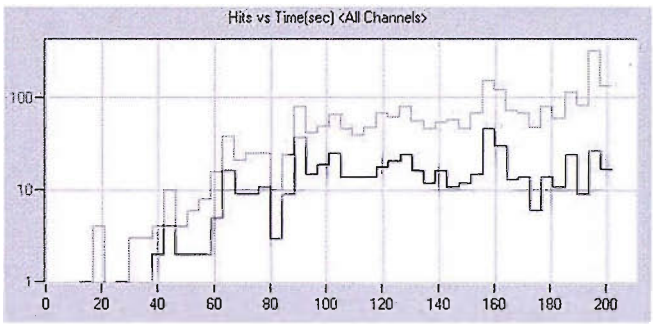

(b) Test CP4

Figure 8.29: Histograms of hits (grey) and events (black) versus time, for samples CP3 and CP4

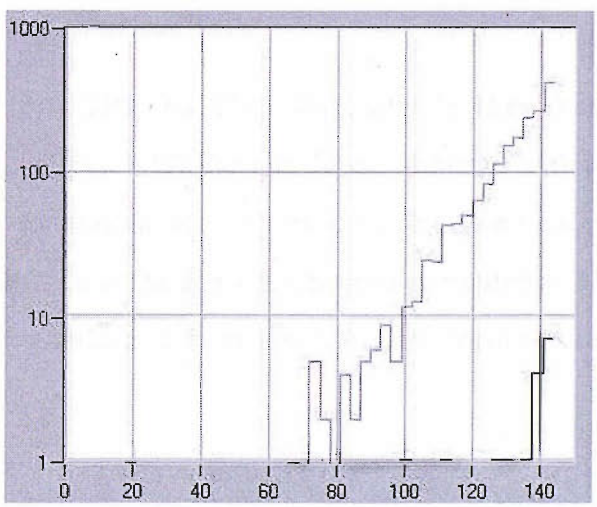

Figure 8.30: Histograms of hits (grey) and events (black) versus time, for sample CP1

8.4.2 Spectral analysis

The variation of the frequency centroids with the sampling time for the selected waveforms of test CP1 is displayed in Figures 8.31. One or two events present an irregular behaviour, that may be explained by the presence in the waveform of a second hit, extremely close to the first and therefore not isolated effectively by the system. It is worth noting that the power spectrum of such waveform would appear unmodified and would not show the presence of a second hit, in the frequency domain. The same graphs are displayed in Fig. 8.32 for the

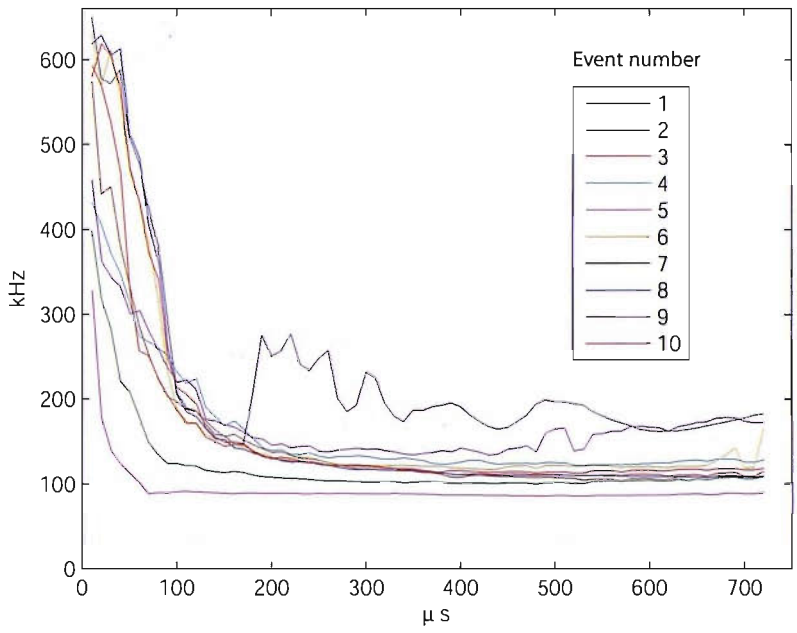

Figure 8.31: Frequency centroid (kHz) versus sample time (μs) for ten waveforms from test CP1

selected waveforms of tests CP3 and CP4. Qualitatively, they show the same trend as in Fig. 8.14 for test Zero1, or Fig. 8.19b for test Zero3, although with less scatter.

Figure 8.33 shows, for waveform 1 of test CP1, the selection of the local maxima by means of the superimposition of the spectral densities computed at different sampling times. Figure 8.34 shows, for waveform 2 from test CP3, the identification of the peaks with a threshold of 0.25.

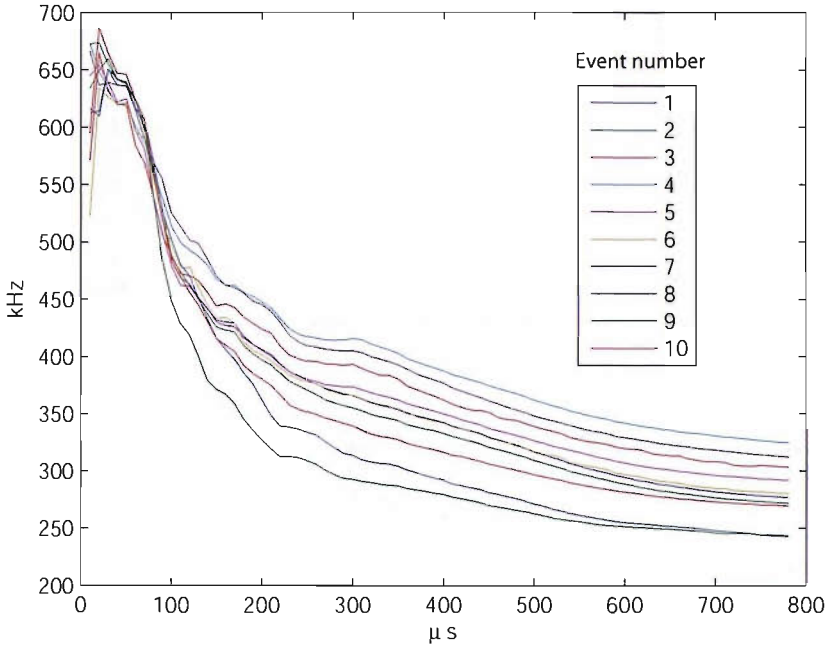

(a) Test CP3

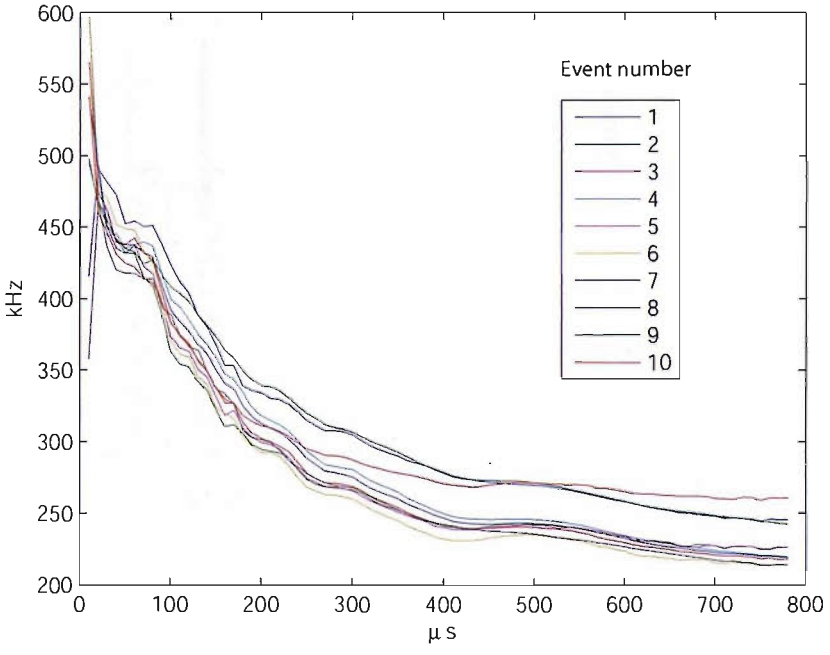

(b) Test CP4

Figure 8.32: Frequency centroid (kHz) versus sample time (μs) for ten waveforms from tests CP3 and CP4

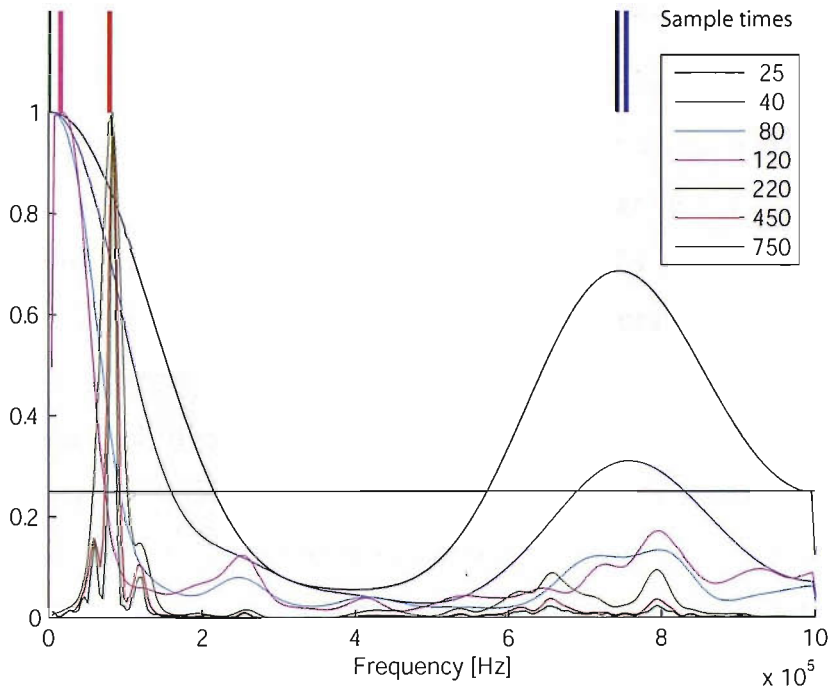

Figure 8.33: Spectral densities for different sampling times (in μs in the legend) for waveform 1 from test CP1. A threshold of 0.25 identifies the local maxima as indicated by the upper bands

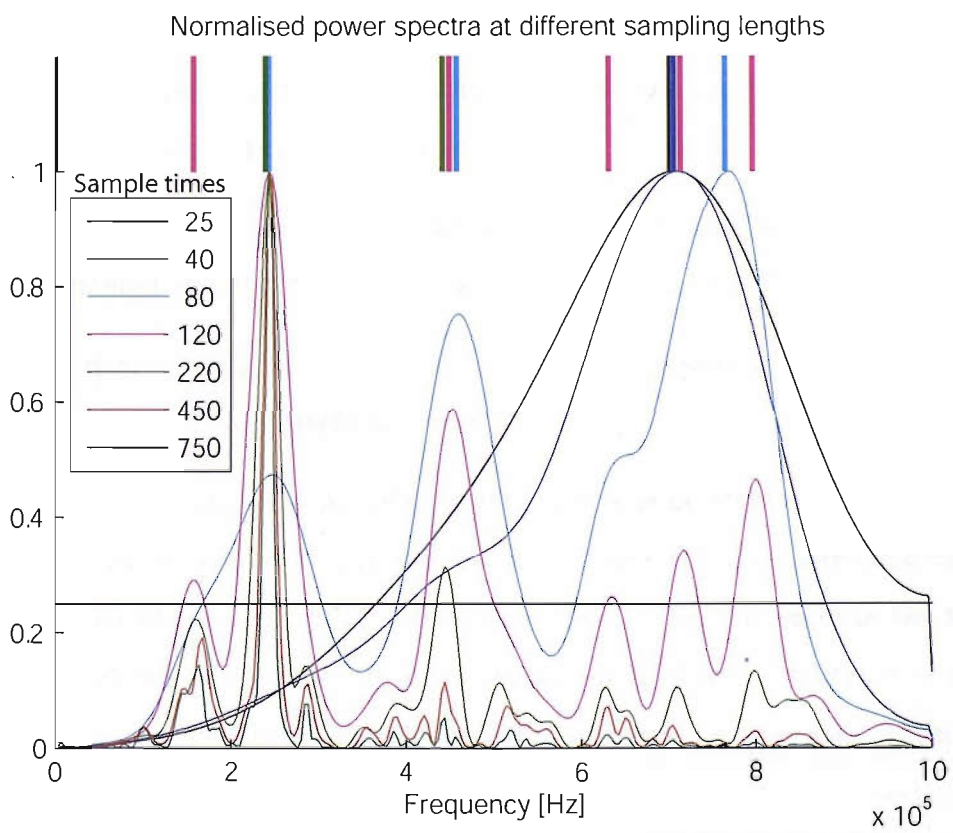

Figure 8.34: Spectral densities for different sampling times (in μs in the legend) for waveform 2 from test CP3. A threshold of 0.25 identifies the local maxima as indicated by the upper bands

8.4.3 Comparison of the frequency peaks and overall comments

The frequency positions of the local maxima of the power spectra calculated at different sampling times are shown in Fig. 8.35a for all the ten waveforms selected in test CP1, and in Figures 8.35b and c for tests CP3 and CP4. Although in Fig. 8.35 the use of the peak-defining threshold has been uniform, tests CP3 and CP4 seem to suggest the use of a higher threshold for a better identification of the relevant peaks; thus a further example is shown in Fig. 8.36 where, notably, the less important peak at 380 kHz disappears from CP4, as well as the peak below 200 kHz from CP3. This shows that the threshold can be "fine tuned" in order to obtain an amount of frequency peaks comparable amongst the tests. A lower threshold would result in too many peaks all lumped together and, *vice versa,* a higher threshold would account for a substantially lower number of peaks. So, in a way, the threshold used may be taken as a difference in the data itself, in such different data sets seem to require different thresholds in order to produce a comparable number of well separated peaks. In other words, a different peak-defining threshold may be appropriate for a different tests, exactly as a specific magnification may be indicated for the inspection of some samples under a microscope.

Figure 8.35a indicates that CP1's acoustic emissions are not homogeneous at all, with the existence of at least two types of signals:

1. a first type showing little or no activity at all outside the two important frequency bands centered at 100 and 650 kHz, i.e. waveforms 1, 2, 3, 4, 5, 6, 9 and 10,

2. a second type showing, on the opposite, an intense and peaked activity over a broader range of frequency, i.e. waveforms 7 and 8.

Fig. 8.27 suggests that the existence of different types may be attributed to the large variety of distances sensor–source, confirming that this parameter has greater importance than the characteristics of the originating sources themselves. The differences in the frequency response is not shown in Fig. 8.31. It is also worth noting that the existence of these two types of waveforms is only visible when looking at several sample times, and is therefore not visible in the spectra displayed by AEWin.

Another possible explanation for these two types of events may be that a cross-ply lay-up can favor damage generated by delamination, and such mechanism would introduce in the structure a strong out-of-plane component force: such excitation would be significantly

different from an in-plane force (see §8.3.3) and a spectral analysis, especially if conducted by looking at the building up of the signal with the time, is particularly apt to enhance differences between source mechanisms that are in-plane or out-of-plane.

Within CP samples, the most obvious comparison is to be made between CP3 and CP4, in such they mainly differ for the distance from the sensor to the source, that was easily controlled by means of the notch. The first apparent result is that *these acoustic emissions are different* (see Figures 8.35 and 8.36), and this again suggests that *the distance sensor–source changes significantly and coherently the detected events.* A high-frequency activity in 700–800 kHz is importantly present in CP3, but not in CP4: these peaks appear only for medium/low sample times. Another difference, also evident in Fig. 8.32, is that the frequency centroid of the acoustic emissions from CP3 is higher; this may indicate that *the events detected in smaller specimens have higher frequency.* Finally, the very-low frequency peaks, present in all tests, are lower in CP1 than in CP3 and CP4.

A cross-comparison can be made with Zero tests. When the peaks graphs are considered in their whole, and not on an event-by-event basis, the definite and consistent peaks of CP3 and CP4 (Figs. 8.35b and c) resemble tests Zero1 and Zero3 (Figs. 8.23 a, c and d). Specimens CP3 and CP4, notched, certainly generate fibre breakage, and in such they are similar to the Zero specimens, and different from CP1, which is likely to produce relatively more delamination and has a different peaks graph.

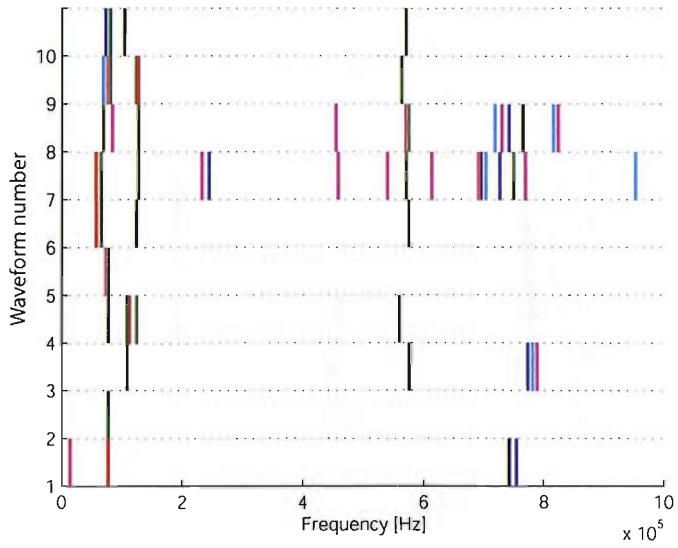

(a) CP1

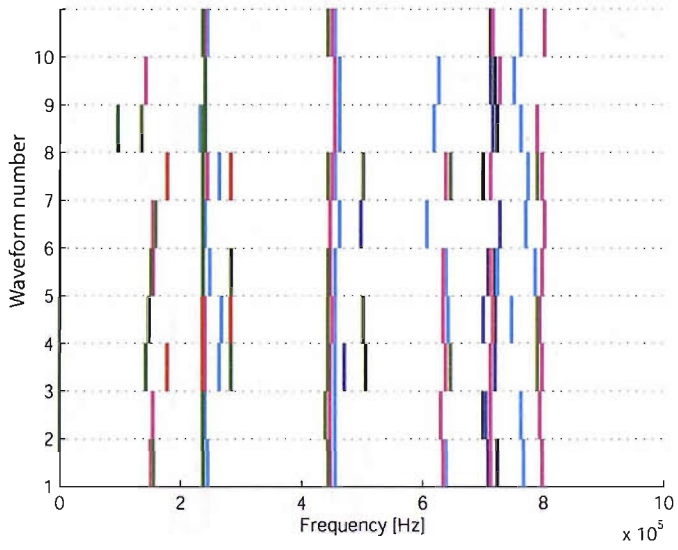

(b) CP3

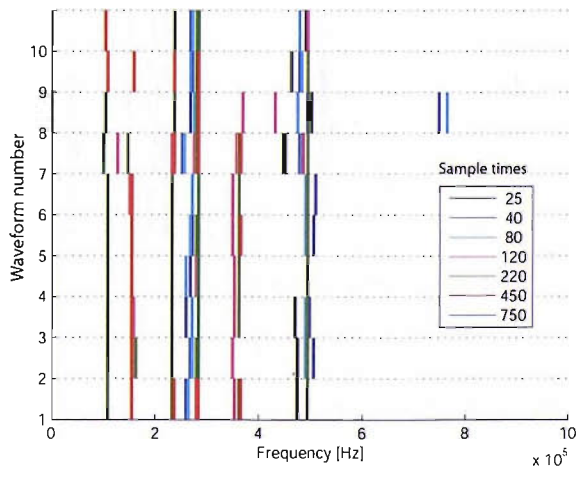

(c) CP4

Figure 8.35: Spectral maxima for CP tests, threshold = 0.25

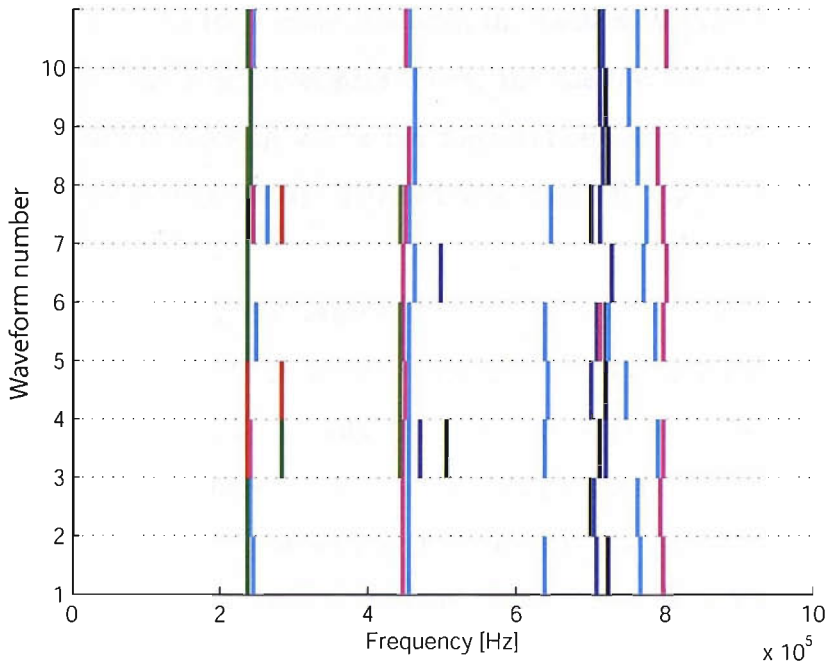

(a) CP3

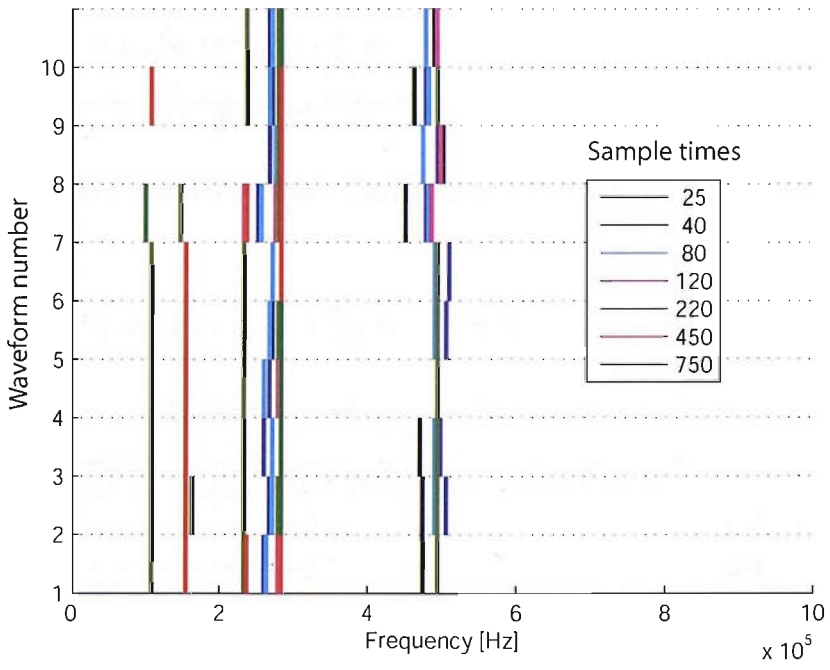

(b) CP4

Figure 8.36: Spectral maxima for CP3 and CP4 tests, threshold = 0.40

8.5 Angle-ply specimen

8.5.1 Description of the test and basic AE features

Table 8.3 and 8.5 summarise the sample geometry, the mechanical characterisation (sourced from the actual tests), the acquisition parameters, and the test setup for sample AP1. In angle-ply material, matrix cracking will be the dominant failure mode with some delamination at the edges. The first events are detected at a relatively low stress of 100 MPa with 4.5% strain.

The stress-strain data of Fig. 8.37 show that the material is far more "ductile" than either the UD or cross-ply specimens. The stress-strain curve has a significant discontinuity in it that indicates the onset of damage activity. The AE starts soon after the discontinuity. The material can strain much more prior to failure than in previous tests, so the whole test takes a relatively long time (1230 s), and tens of thousands of hits are recorded. Nevertheless, there is a huge discrepancy between the number of (unlocated) hits and (located) events, which are about two order of magnitude less. Figure 8.38 accounts for the difference between (located) events and (unlocated) hits. The ratio of hits recorded per unit of time increases almost exponentially till the end of the test. The fact that only a small proportion of hits is located accounts for (in this test even more than in the test of different configurations):

- spurious hits due to external noise (gripping, Instron) coming from outside the sensors area,
- hits that are too-weak to reach both the sensors,

Table 8.5: Test summary for sample AP1

Young's modulus (GPa)	9
Ultimate stress (MPa)	196
Ultimate strain (%)	16.4
Lay-up	$[+45/-45]_3$
Gauge length (mm)	375
Width (mm)	14
Thickness (mm)	1.0
Cross-head speed (mm/s)	0.05
Distance between sensors (mm)	275
Wave-speed used for location (m/s)	2800
Sensors used (Channels)	S3 (C1), S4 (C2)

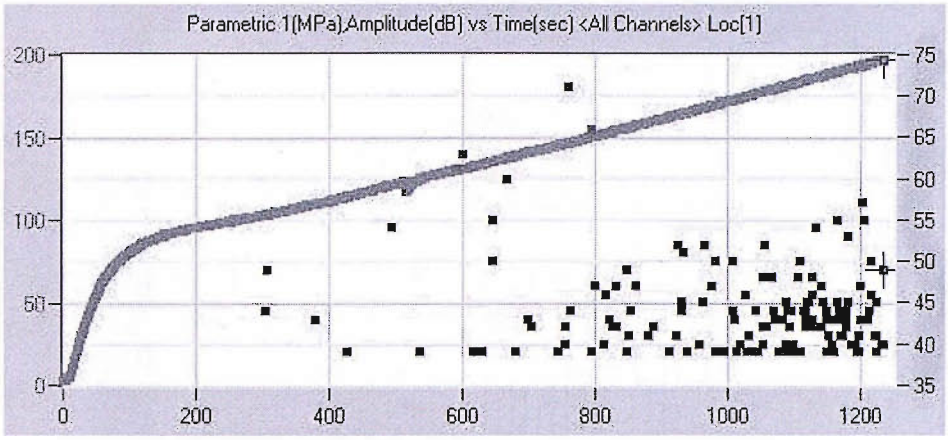

(a) Time

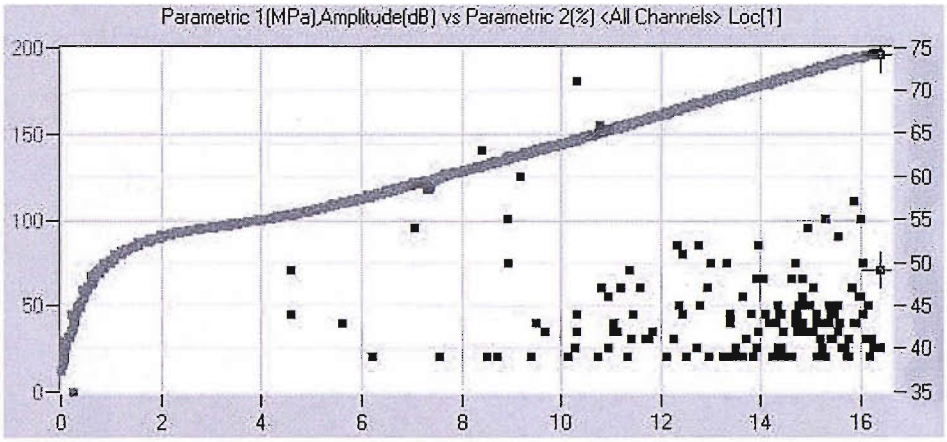

(b) Strain

Figure 8.37: Overall AE activity for test AP1, expressed as event amplitude, superimposed to the stress/strain (a) and stress/time (b) curves

- hits incorrectly located outside the sensors area, because the location algorithm was designed for isotropic material.

The choice of working with events only probably excludes some "good" hits due to damage, but also greatly reduces the chance of working with spurious hits.

The AE activity over the length of the specimen is localised in Figure 8.39. The damage does not originate from a single location: the sources appear evenly distributed over the distance between the sensors on strip, as would be expected from matrix cracking. The AE activity does not show any characteristic grouping if looked at through a visualisation analysis based on the classic parameters only.

Due to the huge number of events collected, a manual individual check of *all* the data is not feasible. The individual inspection then proceeds by focusing on the data collected in the middle of the test (temporally and spatially). This inspection of the spectra leads to the

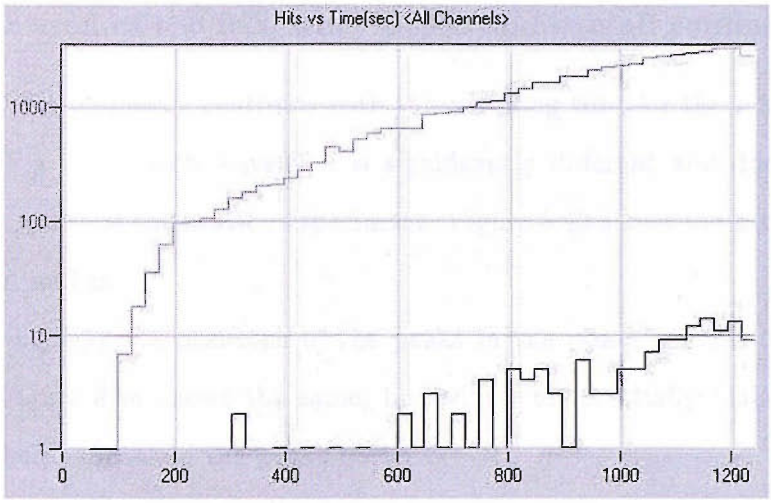

Figure 8.38: Histograms of hits (grey) and events (black) versus time, for sample AP1

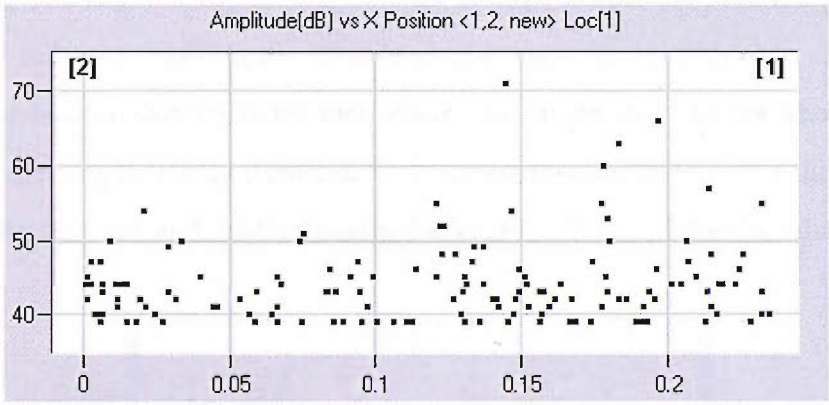

Figure 8.39: Event amplitude (dB) versus position on the length of the sensor (m) for sample AP1

visual identification of one type "A" of waveform that occurs frequently (Figure 8.40a) and to another type "B" which occurs slightly less frequently (Figure 8.40b) and also visually less defined (sometimes it has the resemblance of type A). These events and types are randomly distributed over Fig. 8.39. Since test AP1 provided many events over all the length of the specimen, it is possible to study waveforms located far from S3, in order to examine the effect of the distance between the source and the sensor. A third group of ten waveforms is then chosen for further analysis, called "C" and extracted from a position far from sensor S3.

8.5.2 Comparison of the frequency peaks and overall comments

The variation of the frequency centroids with the sampling time for the selected waveforms is displayed in Fig. 8.41; each waveform is significantly different and does not show the characteristic "cut off" of the previous specimens. Figure 8.42 shows the peak extraction for two waveforms A and B.

Figure 8.43 displays the positions of the peaks in the power spectra of the three sets of waveforms. Figure 8.44 shows the same, but with a substantially higher peak-defining threshold, that helps to isolate the peaks better.

The distribution of the events over all the length of the strips, together with their abundance (Fig. 8.39), immediately "characterises" angle-ply lay-ups and, for this load configuration, matrix cracking, thereby making this set of data completely different from the other sets described before in this chapter. This kind of characterisation, though, cannot be done on a hit-by-hit basis, individually for each event, but rather refers to the whole set of data.

The peak-defining threshold itself can be considered as characteristic of this test, since in order to display only few and relatively large peaks (Figs. 8.43 and 8.44) a value significantly

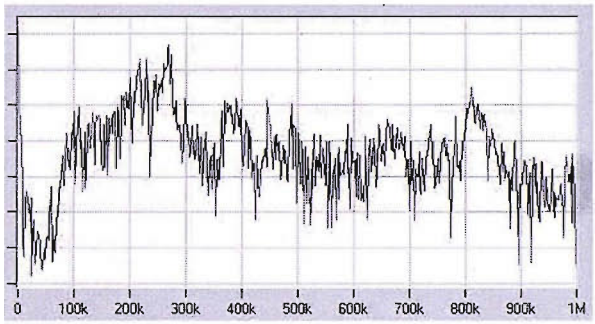

(a) Type A

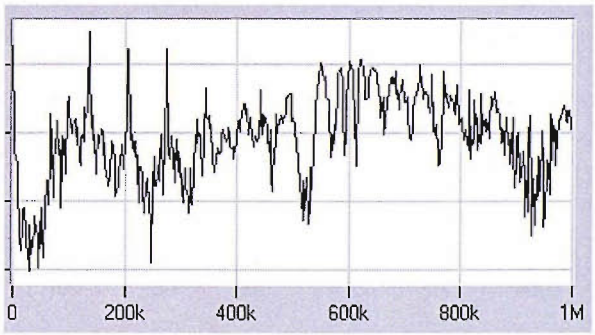

(b) Type B

Figure 8.40: Normalised power spectrum, as displayed by AEWin, for two typical waveforms from test AP1

higher than for the other tests (Zero, CP) was used.

Similarly to CP1, the fact that the acoustic emissions from AP1 originate from everywhere in the specimen yields to a large variety in the events (Fig. 8.44b), and might confirm that the acoustic emissions do not show similar features if they do not originate from the

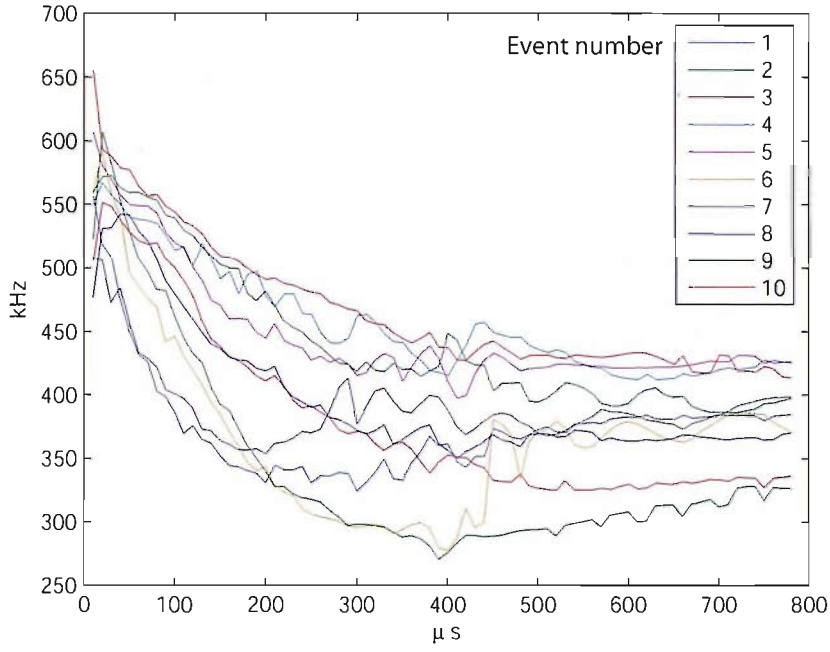

(a) Waveforms A

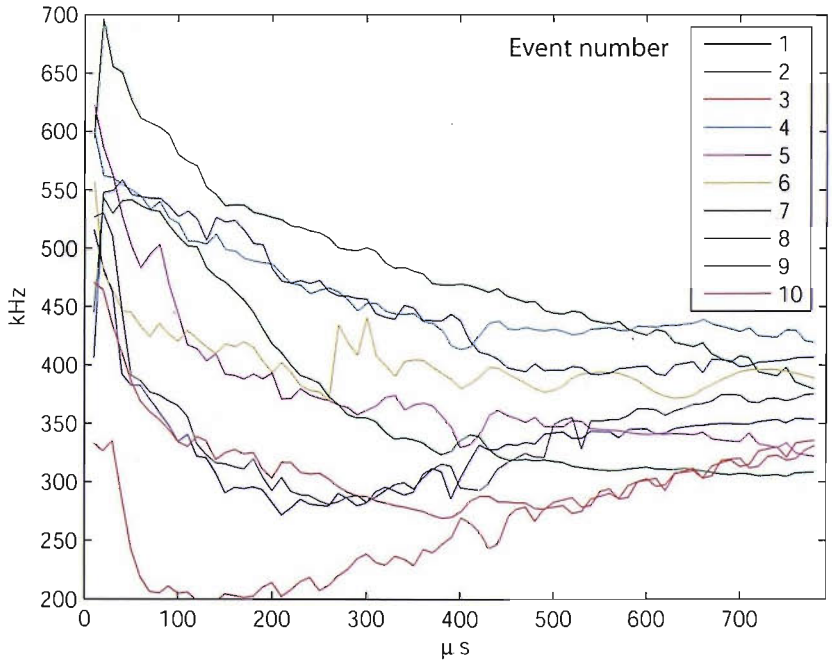

(b) Waveforms B

Figure 8.41: Frequency centroid (kHz) versus sample time (μs) for the selected waveforms from test AP1

same position. In general, most of the events peak at about 580 kHz, and it is necessary to use medium/low sample time in order to see them.

Although Figs. 8.44a and b would seem to indicate a strong and permanent characteristic of the acoustic emissions generated from an angle-ply layup, Fig. 8.44c contradicts this: the exam of type C shows that (with the exception waveforms 1 and 2) the patterns shown have a strong dependence on the position.

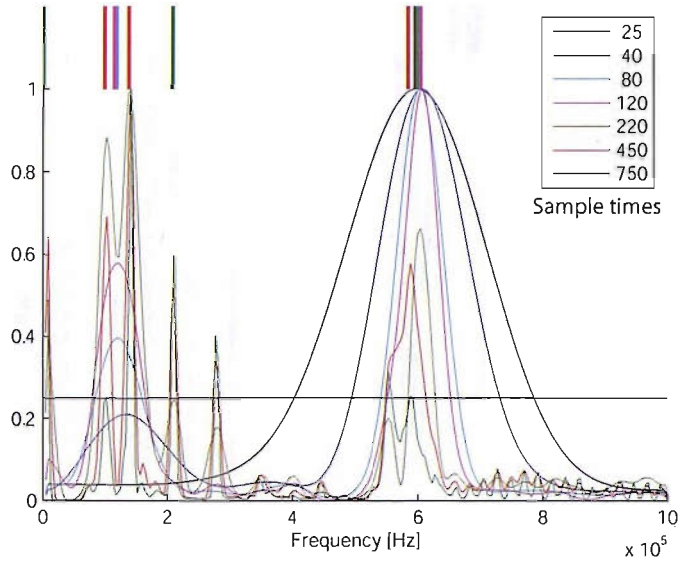

(a) Waveform 6, type A

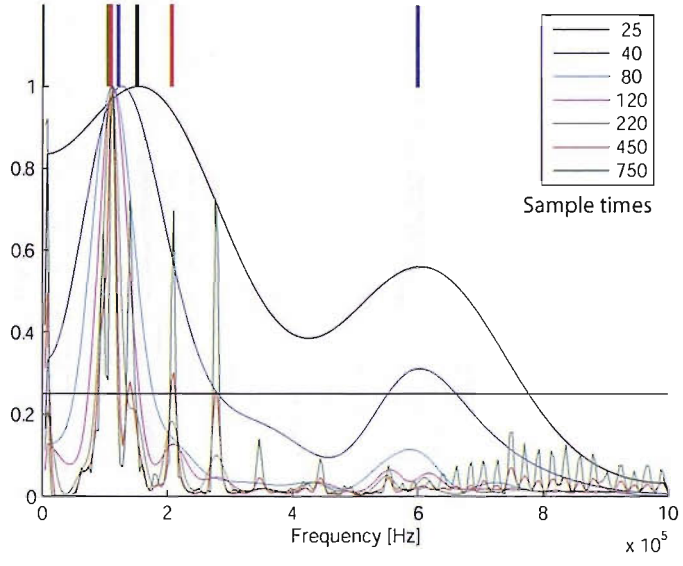

(b) Waveform 3, type B

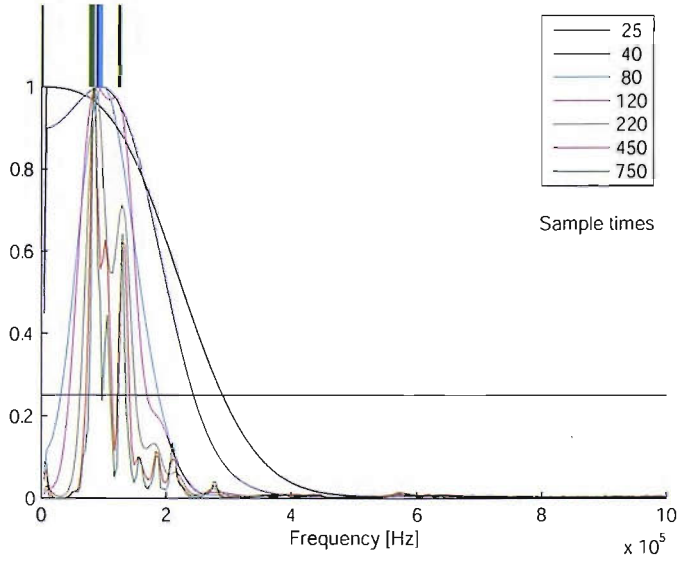

(c) Waveform 10, type C

Figure 8.42: Spectral densities for different sampling times (in μs in the legend) for three waveforms from test AP1. A threshold of 0.25 identifies the local maxima as indicated by the upper bands

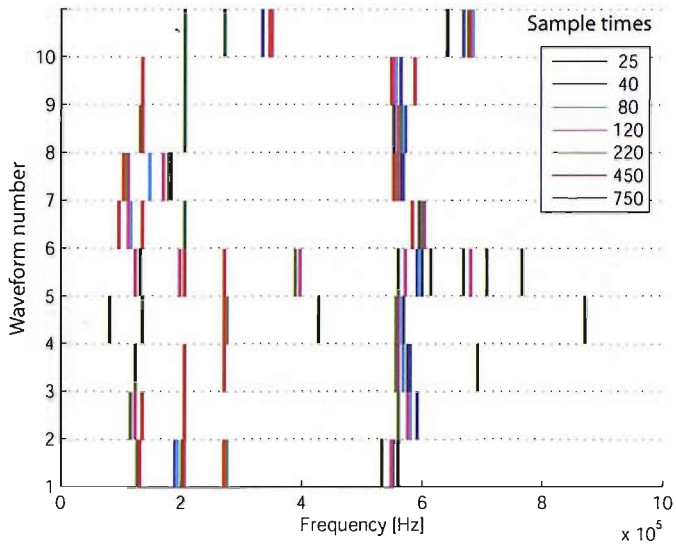

(a) Waveforms A

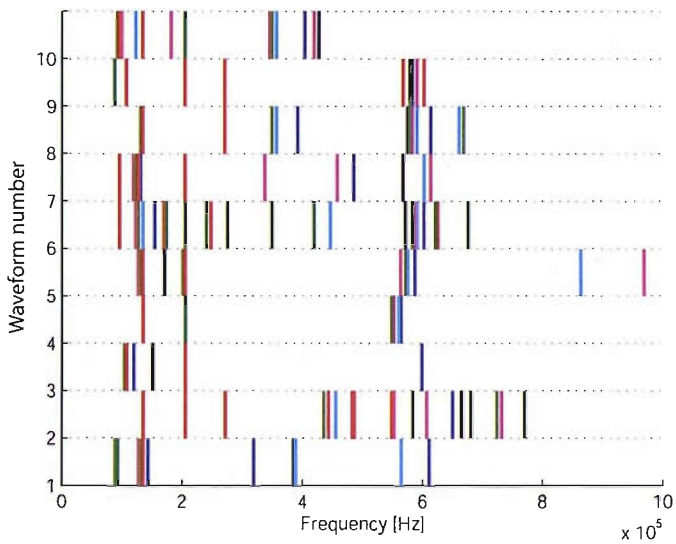

(b) Waveforms B

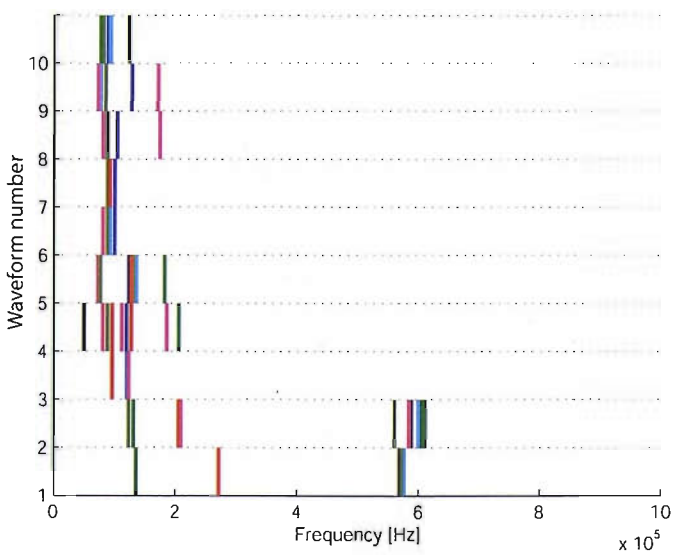

(c) Waveforms C

Figure 8.43: Spectral maxima for AP1 test, threshold = 0.25

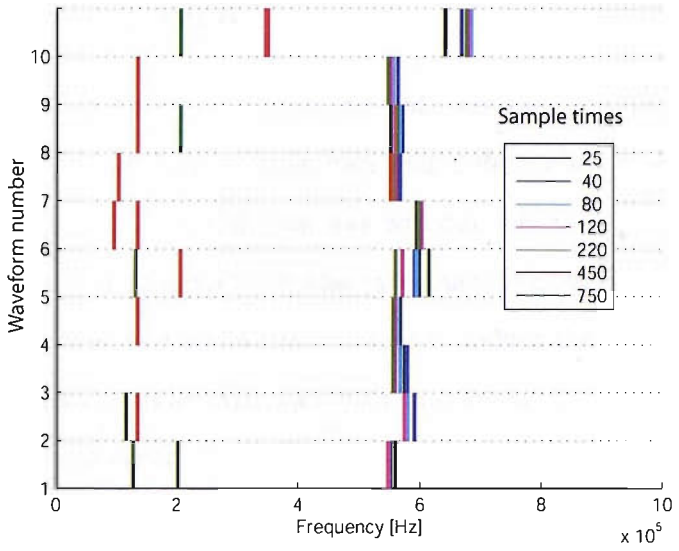

(a) Waveforms A

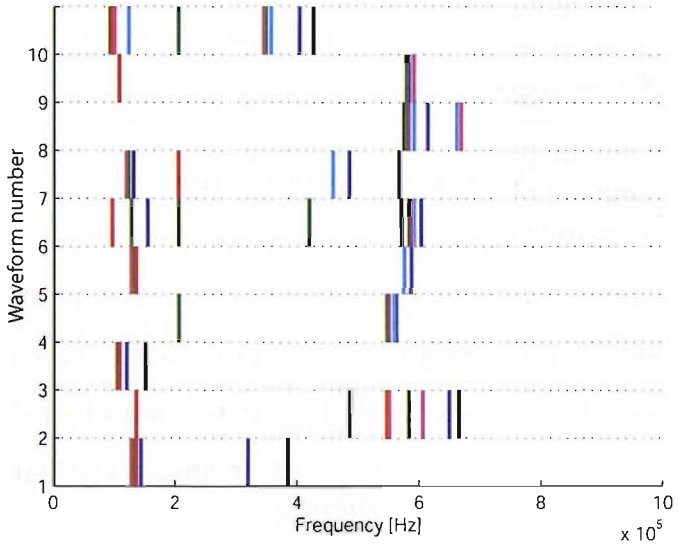

(b) Waveforms B

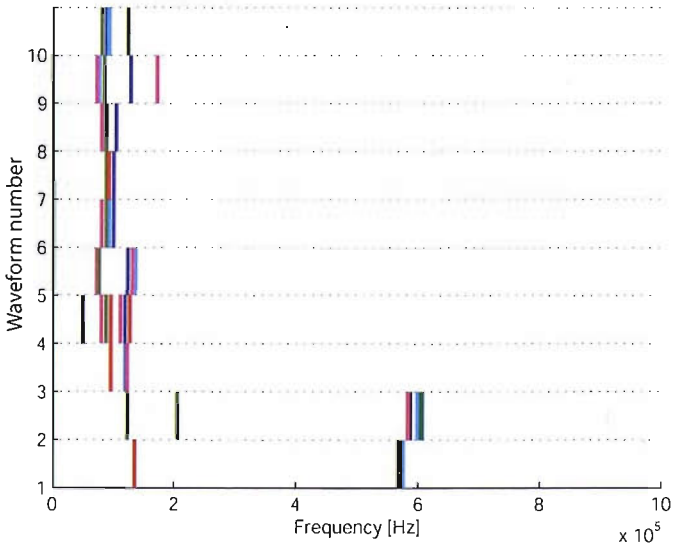

(c) Waveforms C

Figure 8.44: Spectral maxima for AP1 test, threshold = 0.60

8.6 Transverse specimen

In some tests no acoustic emission was detected; this was the case for test Ninety. Several tests were run with the same kind of specimen and different settings, in the attempt to collect acoustic emissions, but the outcome was without AE activity. In order to increase the capability of the system to detect low-energy acoustic emissions, the two sensors were also placed very closed to each other (4 cm) in order to reduce the attenuation of the signal, and the preamplifier gains were increased to their maximum (60 dB). However none of the tests yielded an acoustic emission.

Two reasons can explain the absence of AE events.

1. Acoustic emissions were generated by matrix cracking but, being characterised by a low energy content, were not able to reach both the sensors with enough amplitude to trigger the system, however the results from the AP test do not support this.

2. The final failure did not consist purely of a matrix cracking, but rather of a cracking that involves very little resin material (because of the interposed fibres that limit the cross sectional area) and the "debonding" of the corresponding fibres from the resin; and being this failure characterised by an ultimate stress lower than that corresponding from a full section of resin, the final failure would also be the only source of acoustic emission, because the cracking of the matrix would require a higher stress.

The samples, together with the conditions and the parameters under which they have been tested are reported in Tables 8.6.

Table 8.6: Test summary for sample Ninety

Ultimate stress (MPa)	55
Lay-up	$[90_6]$
Gauge length (mm)	185
Width (mm)	15
Thickness (mm)	1.0
Cross-head speed (mm/s)	0.0083
Distance between sensors (mm)	55, 120
Wave-speed used for location (m/s)	2170
Sensors used (Channels)	S3 (C1), S4 (C2)
Acquisition threshold (dB)	39
Preamplifier gain (dB)	40, 60
Software analogue filter (kHz)	100–2000
Sample rate (MHz)	2
PDT (μs)	200
HDT (μs)	800
HLT (μs)	800

8.7 Conclusions

The greatest limitation of the standard analysis tools provided by the PAC system is that the signals are considered as stationary. In this chapter, the AE events were analysed by means of frequency centroid versus sample time graphs and by frequency peak collection at several sample time. Both these tools consider the signals non-stationary and enlighten several features that would be otherwise invisible with a stationary analysis.

The set-up of these techniques is subjective up to some extent (e.g. in the choice of the peak-defining threshold) and can be fine-tuned to show, or hide, features. Clearly, the purpose of this type of analysis is finding enough similarities in the results to be able to infer a statistical proposition; at the same time, though, if the criteria for drawing such similarities are too broad, all the results may look the same or, at the exact opposite, if the magnifying lens of the analysis is too powerful, too many details will show up in the results and they will all look different.

In a way that is evident when examining the spectra, the signals do not generally present *substantial* differences that would allow for a sure discrimination in different types. The variations in the spectra are so large that any distinction, when exists, is too blurred. When these differences exist, and do seem to show a pattern, this pattern demonstrates more dependence on the specimen size, or the source position, rather than the lay-up and the

preferential damage it would produce. The next chapter will be able to introduce more significant variations in the specimen size by using a panel instead of a strip.

There are huge variations and scattering in the AE data, however the positions of the peaks in the spectra are relatively *stable* within each test, regardless of sampling time, especially if compared to the value of the frequency centroid itself. Nevertheless, when the frequency centroid value is plotted to show its variability with the sampling time, then it provides more useful information. The shape of these curves, and particularly their decay ratio, could tell something about the in- or out-of-plane nature of the originating damage.

A further consideration is the threshold used to define spectral peaks. This requires adjustment in order to produce results that show characteristic and well-defined peaks.

In view of a characterisation of the source based on the peak plots, the following global considerations can be drawn.

1. Although not on a hit-by-hit basis, the peak plots can describe some features characteristic of a lay-up on the whole. In fact, since they are able to show positional differences, they can help to identify lay-ups (like the matrix cracking in the angle-ply or the delamination in the cross-ply) that are characterised by events not concentrated in a single location, but are rather sparse over the specimen.

2. Because of their capability to associate the acoustic emissions to a time scale / sample length, and because of the dispersive nature of the Lamb waves and the different propagation speeds and interacting effects of the S- and A-modes, the peak plots can help to discern a damage strongly characterised by in-plane sources (like fibre fracture) from a damage that is mostly out-of-plane (like a delamination).

3. The peak plots cannot associate peak patterns to a specific type of damage, independently from other considerations (size, positions, distance).

CHAPTER

NINE

Acoustic emissions from a composite panel

There are two possible outcomes: if the result confirms the hypothesis, then you've made a measurement. If the result is contrary to the hypothesis, then you've made a discovery.

Enrico Fermi

In chapter §6 and 7, and particularly in §7.5, it is indicated that the detection of the acoustic emissions is greatly affected by size-related parameters. Verifying up to what extent this can be true for real damage in a composite structure follows quite naturally. Also, one advantage of testing composite panels instead of strips comes from the ability to exclude damage originating at the edges. This section will describe the AE testing of two CFRP panels.

A pair of sensors is generally sufficient to locate events in a unidimensional structure such as a strip. A two-dimensional structure like a panel will require at least three sensors to locate the events, with the condition that the material is isotropic and the wave propagation speed is uniform along all the directions. For the purposes of this thesis, enough sensors should be specified so that only data emanating from the region of interest are processed as relevant AE data, and the noise is filtered out (spatial filtering), according to the testing techniques described in §5.3.3.

9.1 Test set-up

Testing relatively large panels leads to the obvious requirement of a large tensile load. This would not be feasible with a standard traction test, because of the massive forces involved, too high for both the available tensile testing machines and their gripping jaws. A viable solution is applying the tension on the panel surface through bending, introducing another consequence, that the panels must be thick, since the applied bending moment and hence the stress are directly proportional to the thickness.

The requirements for the test described in this chapter ewre identified as:

1. The four sensors, arranged in a rectangular pattern, must surround the area where the damage is most likely to occur, i.e. the area with the highest bending moments.
2. The spacing between the sensors must be large enough to include most of the locations.
3. The sensors must not be placed too close to the edges, so that the signal reflections from the edges can be more easily detected as coming from outside the sensor area.
4. The load on the panel must not be exerted in the region within the sensors, otherwise extraneous noise would be introduced.
5. The rig must accommodate the large deflections associated with bending.

It was decided that a four-point bending test on a panel would be the optimal solution (Fig. 9.1).

A basic testing rig has been designed and manufactured in mild steel and used for the tests on panels. It consists of two halves, a lower and an upper one (Fig.9.2), to be clamped in an tensile machine.[1] The panel is loaded in the four-point-bend configuration by rollers. The rollers are mounted on long supports that are fixed on loading platforms. It is possible to move the supports to different locations on the platforms to produce different test parameters.

The generic set-up of a four-point-bending test is described in BSI (1998). Nevertheless, the standard cannot be fully followed in the current work. Referring to Fig. 9.1b, the standard would suggest $L = L'$. Instead, probably $L' \approx \frac{1}{3}L$ will be a more reasonable value, because here L must be enough large to comfortably accommodate the array of sensors, and because the overall panel dimension must fit in the test machine.

[1]The technical drawings are provided in the Appendix.

Denoting the panel thickness as h and its width as b, applying simple beam theory, some calculations can be done; nevertheless, a large panel can only in first approximation be modelled as a beam, especially because of the huge deformations involved. In a first approximation, the flexural stress σ_f is given by:

$$\sigma_f = \frac{3FL'}{bh^2} \tag{9.1}$$

Assuming $\sigma_f = 100$ MPa, $b = 250$ mm, $h = 1$ mm, $L' = 50$ mm, the load required to fail the panel would then be 1.7 kN.

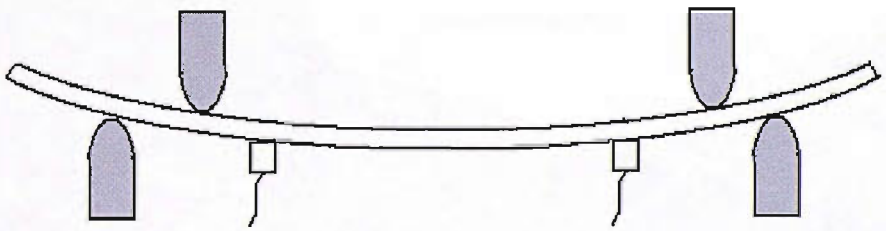

(a) 4-point bending test on the panel with sensors

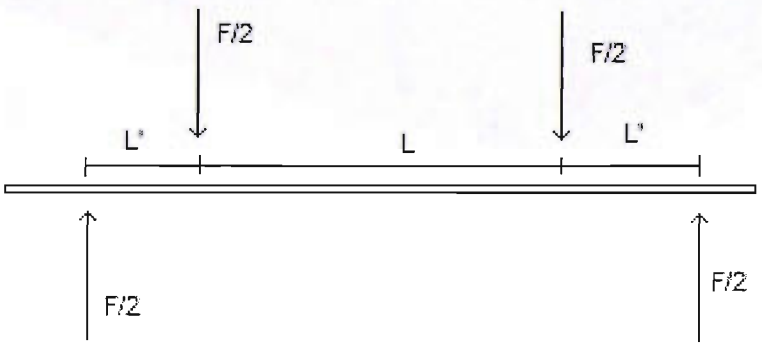

(b) The forces involved in a four-point-bend test

Figure 9.1: Schematic of the panel and the forces involved

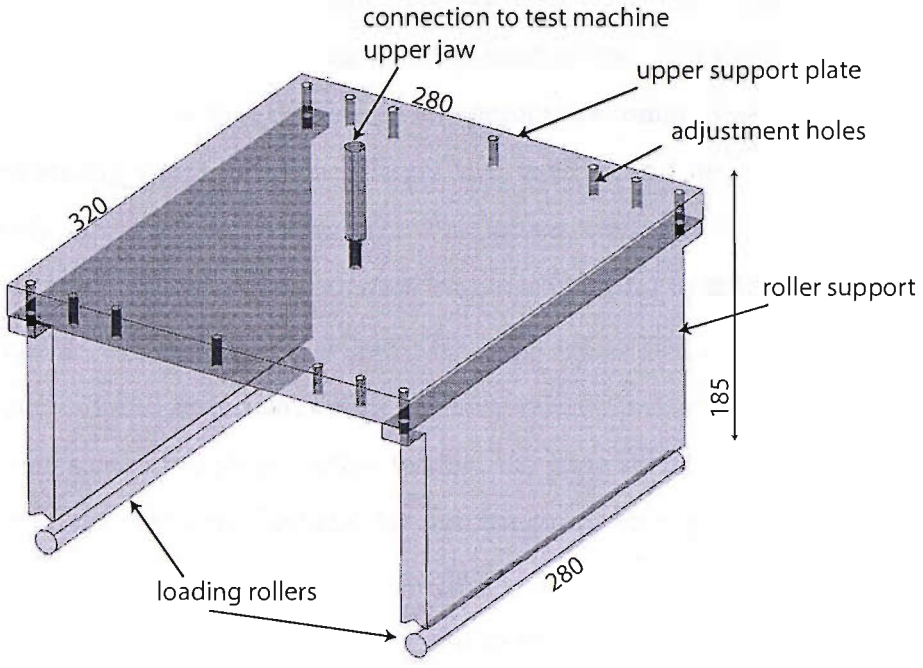

(a) Upper half

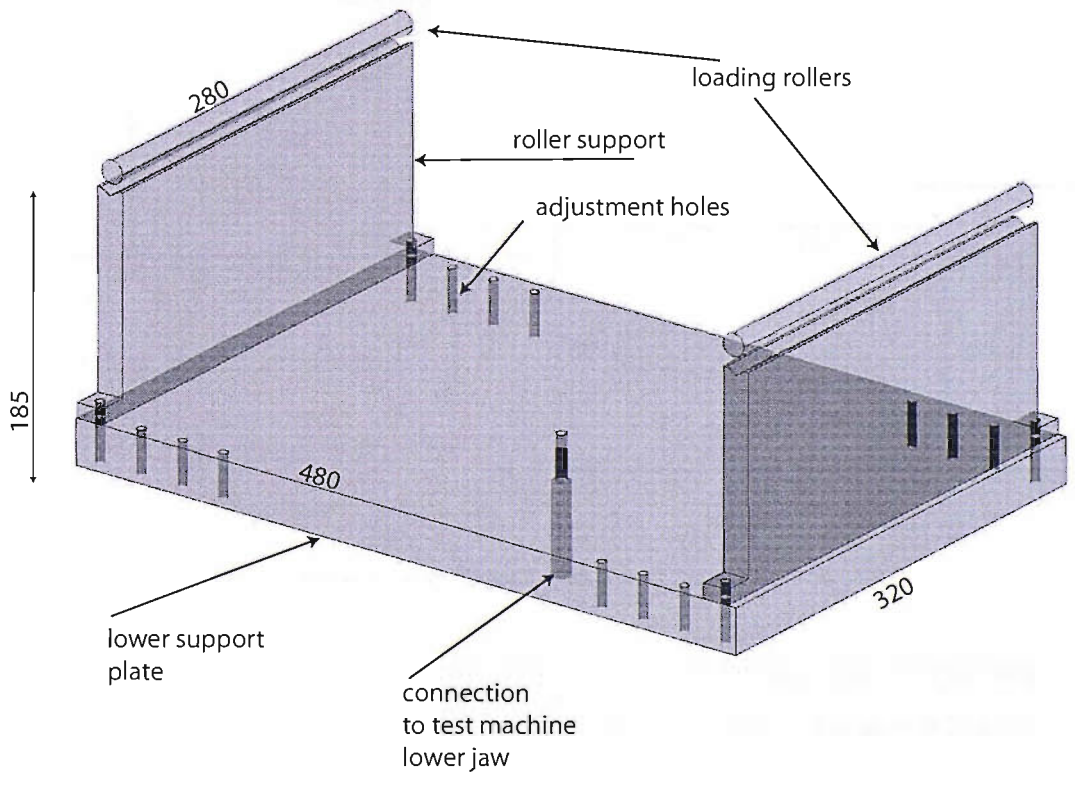

(b) Lower half

Figure 9.2: The four-point bending test rig — the main dimensions are quote in millimeters

9.2 Setup and results

A unidirectional $[0°]_{20}$, 300 × 470 mm, was prepared from carbon/epoxy prepreg, 920cx-FT300(12k)-5-42% from Hexcel Composites as used in the tests described in the previous chapters. The dimensions were considered an appropriate compromise between the contrasting needs of testing a structure much larger than a strip, and being able to accommodate it in an easily manufactured testing rig. The lay-up would introduce the variable of the anisotropy in the structure. The manufacturing was identical to that applied previously, so the panel had a "smooth" side that had been adjacent to the mould, and a "rough" side where the peel-ply had been removed. The fibres were orientated so that they were parallel to the 470 mm side of the plate. Before testing, the wave speed was measured along the 0° direction (parallel to the long side) and 90°, resulting respectively in 8475 m/s and 2280 m/s, showing that the panel is strongly anisotropic. The panel was mounted in the rig so that the tension caused by the bending moment was in the fibre direction (Fig. 9.3). The sensors were placed on the smooth side of the panel (see §7.1.1) for a better acoustic coupling and were secured in place using insulating tape.

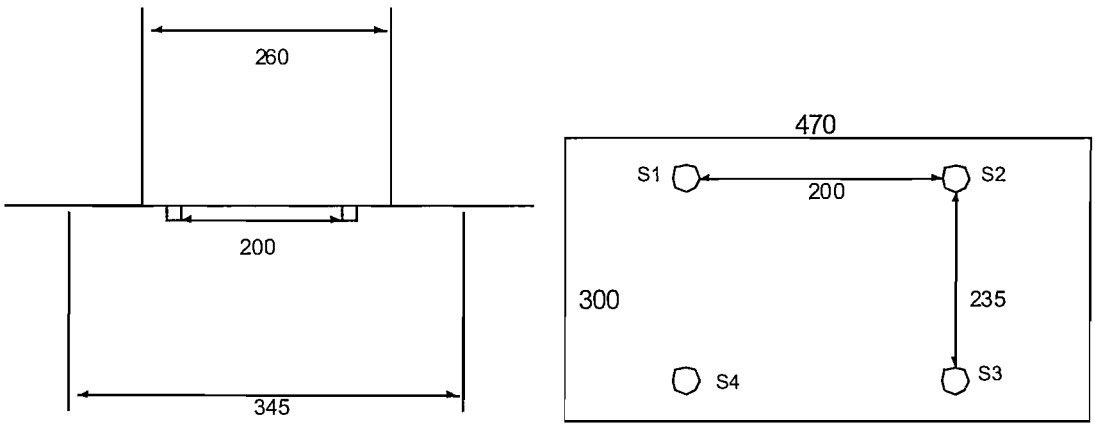

(a) Rig setup (b) Sensor setup

Figure 9.3: Sensor, panel and rig setup

The parameters of the test were as in Table 9.1. The test was stopped before any major failure of the panel. From a visual inspection, the panel contained a few tiny splits, randomly distributed on the panel, aligned along the fibres.

With this setup and such a strong anisotropy, the system barely identified five events out of the hundreds of hits recorded, clearly too few for an analysis. Representing the whole panel with one wave speed does not produce a satisfactory output, and the location of the

Table 9.1: Parameters adopted for the test of the panel

Acquisition threshold (dB)	35
Preamplifier gain (dB)	60
Software analogue filter (kHz)	100–1000
Sampling rate (MHz)	2
PDT (μs)	200
HDT (μs)	800
HLT (μs)	1000
Location type	2D Planar
Structure type	Plate
Event Definition Value	0.235
Event Lockout Value	0.19
Overcal Value	0
Timing strategy	First Threshold Crossing
Cross-head speed (mm/s)	0.0167

events on a composite panel in a standard setup is not accurate.

With the aim of collecting as many *valid* waveforms as possible, the sensors were subdivided in *groups* having the same wave speed. Sensors S1 and S2 are clustered in one group in AEWin, and sensors S3 and S4 in another group; the same wave speed of 8475 m/s was used for both sensors groups. By doing this, the source location becomes now *linear* rather than planar, working between a pair of sensors each, and the located events increase (Fig. 9.4). The total number of located events is greater, because with a linear type of

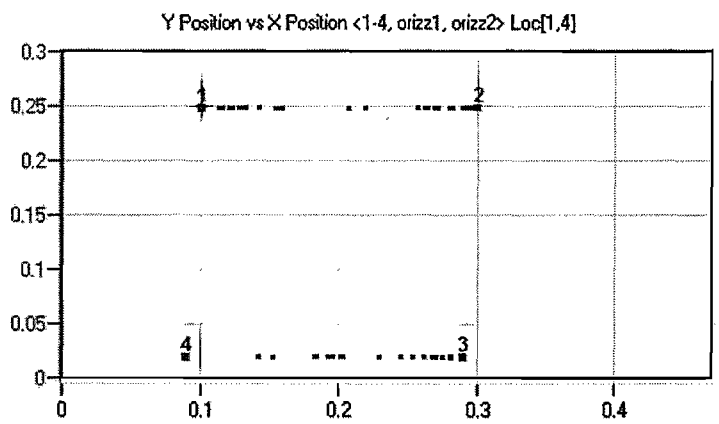

Figure 9.4: Located events, subdivided in two "horizontal" groups, for the panel

location, each event only needs to reach two sensors, rather than three, and the wave speed is more representative than the actual one, in such it would be the actual speed of the wave between the sensors in the x-direction.

Whilst Fig. 9.4 is useful to show the events according to their position, a graph like Fig. 9.5 allows the located events to be selected according to their amplitude. For uniformity

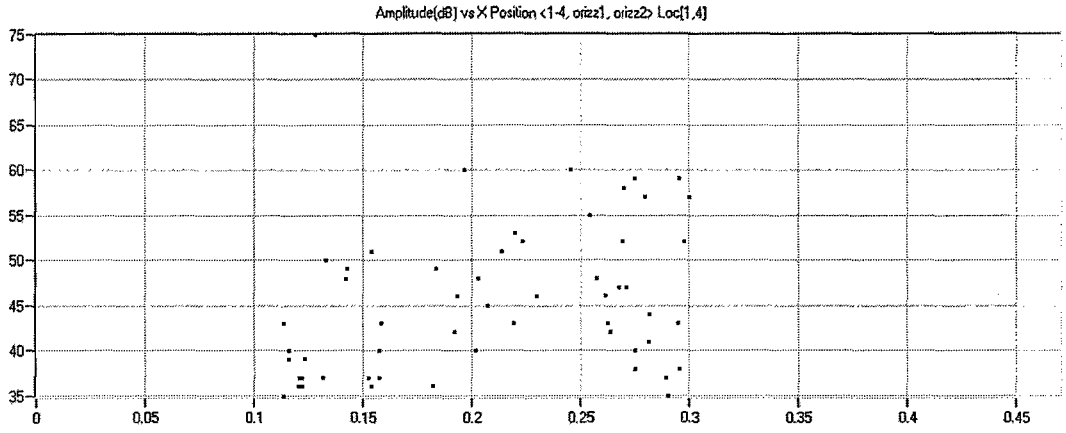

Figure 9.5: Amplitude vs X Position for events coming from the panel

with all the tests already described in this chapter, where only sensor S3 was considered, only the events located within sensors S3 and S4 are selected for further analysis.

There is a large variety in the power spectra displayed by AEWin: there is little uniformity (especially in comparison with the tests on the strips) and the identification of several "types" would be possible. For a simpler presentation of the results, two broad groups, named "α" and "β", are defined, characterised by some more visible similarity of their power spectra. Figure 9.6 shows two of these acoustic emissions, displayed by AEWin.

The variation of the frequency centroids with the sampling time for the waveforms is displayed in Fig. 9.7. Figure 9.9 summarises the positions of the peaks in the power spectra of the same waveforms. Both figures show a relatively large variety of signals. An example of the extraction of the peaks from the power spectra is illustrated in Fig. 9.8.

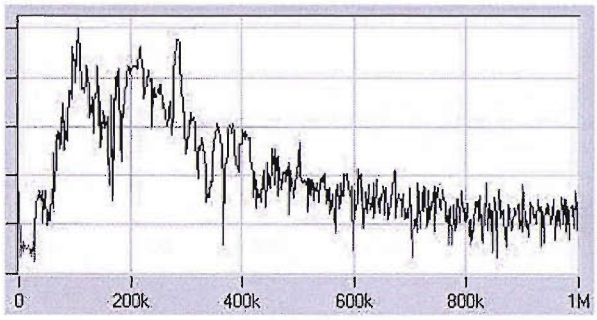

(a) From α

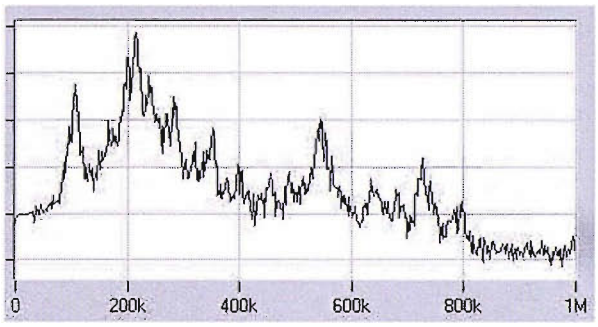

(b) From β

Figure 9.6: Power spectra of two waveforms collected during the test of the panel

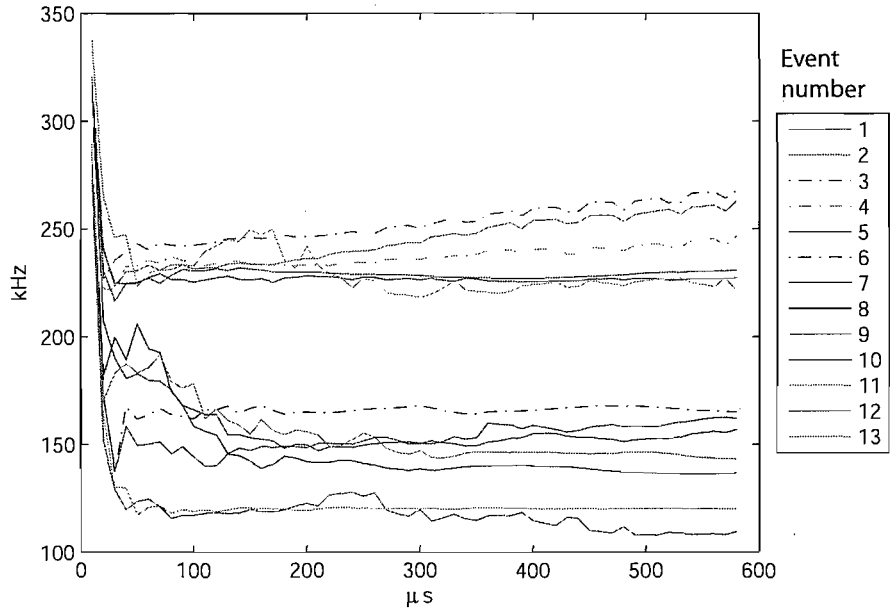

(a) Group α

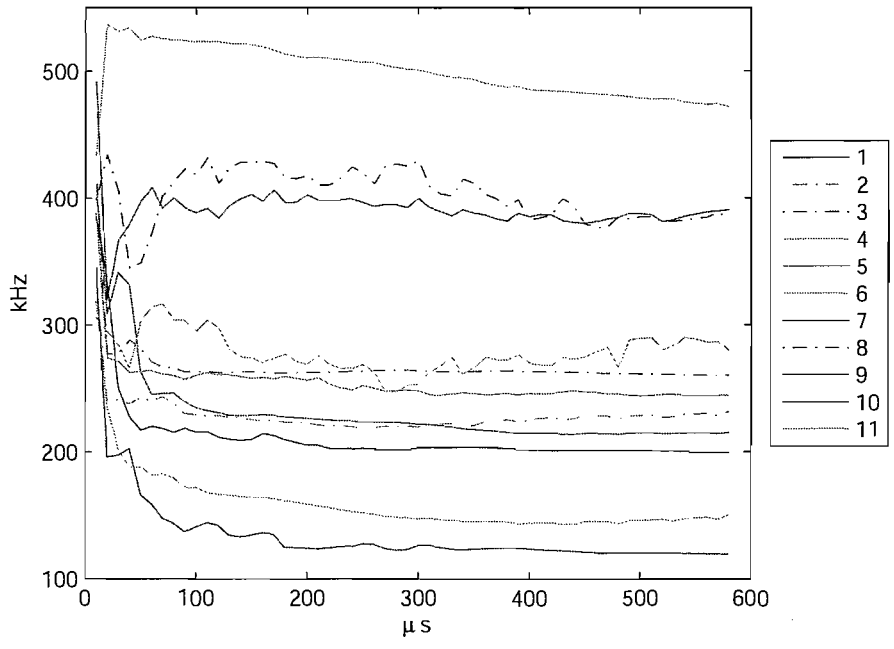

(b) Group β

Figure 9.7: Frequency centroid (kHz) versus sample time (μs) for the waveforms from the test on the panel

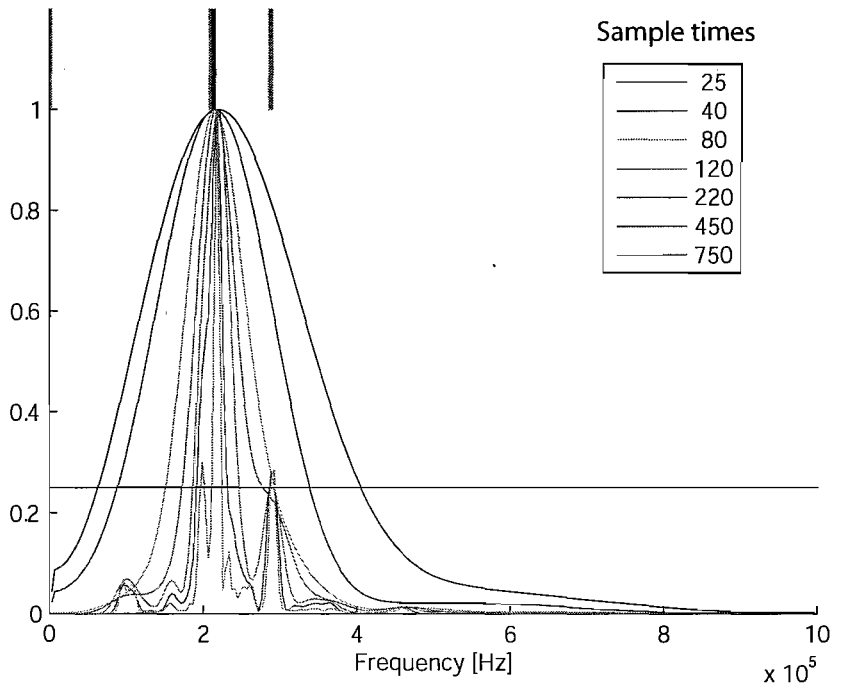

Figure 9.8: Spectral densities for different sampling times (in μs in the legend) for waveform number 5 from group α. A threshold of 0.25 identifies the local maxima as indicated by the upper bands

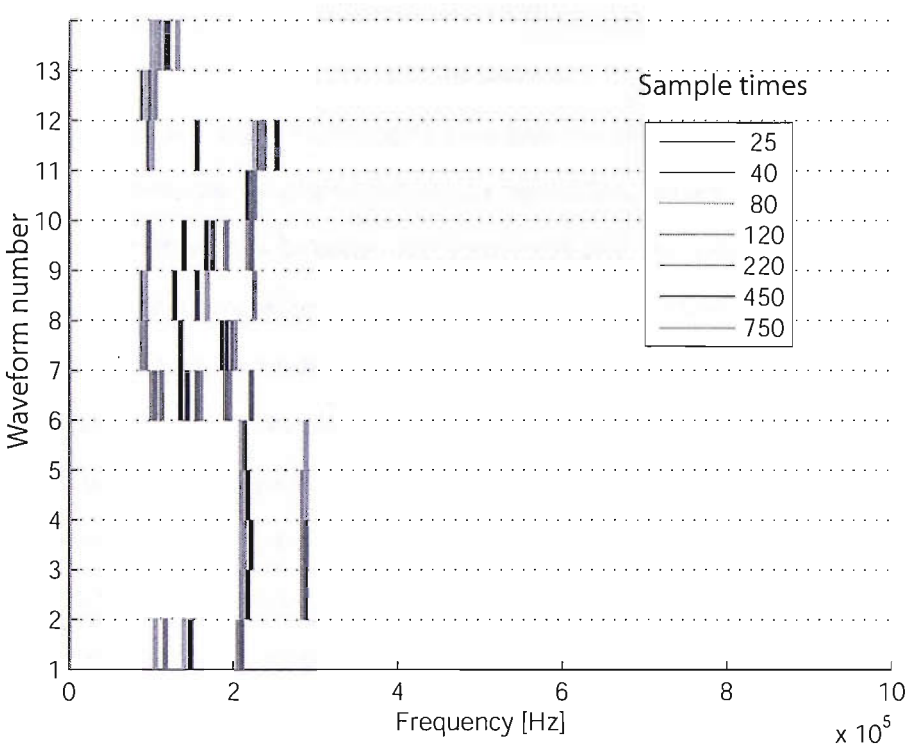

(a) Group α

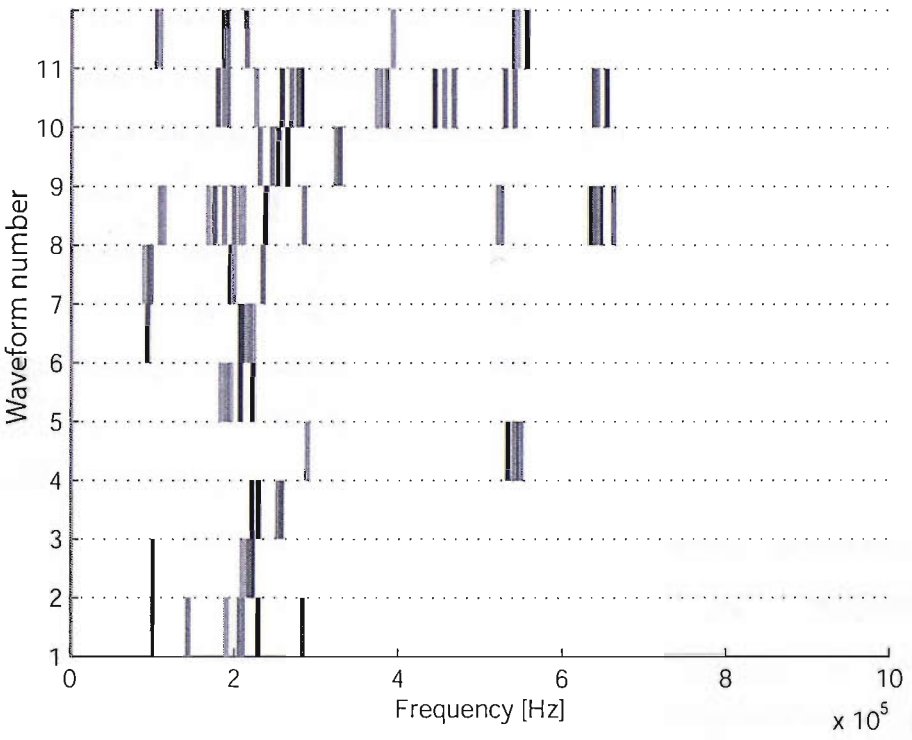

(b) Group β

Figure 9.9: Spectral maxima for the waveforms from the test on the panel, threshold = 0.25

9.3 Comments

Figure 9.7 shows several curves that increase with the sample time. This behaviour was not found in any test on strips. Since these curves depend on the different interactions between the reflections against the edges of the specimen and the dispersion of the Lamb waves, the increase of these curves can be attributed to the two-dimensionality of the specimen, which makes negligible the difference between the transverse and the longitudinal reflections that therefore assume equal importance and hence can cancel each other (a few curves are almost stationary) or yield to an increase or a decrease of the frequency centroid, depending on where on the panel, in respect to the edges, the acoustic source is located. In fact, the panel is highly anisotropic and the wave speed and the dispersion effects have a different relative weight on the transverse and longitudinal directions.

The collected signals can be broadly grouped into two categories (not necessarily coinciding with the aforementioned groups α and β): a first group with a relatively large frequency centroid (at all the sampling times) and a spectrum with activity and peaks all over the frequencies, and a second group with a low frequency centroid and an activity almost exclusively concentrated below 300 kHz. The existence of these groups is confirmed by both the types of graphs, in Figs. 9.7 and 9.9. The separation between these groups in terms of frequency centroid is not sharp, but certainly noticeable, especially when long sample times are considered (over 150 μs, Fig. 9.7).

Another dichotomy can separate the signals on the basis of how fast their frequency centroid reaches a stationary value. For example, the frequency centroids of waveforms 3 and 10 in Fig. 9.7a become stationary (at relatively high values) after very short sample times, whereas waveforms 8 (Fig. 9.7a) and 7 (Fig. 9.7b) need about 180 μs. As said previously about the tests on strips, the decay ratio of the frequency centroid may enlighten the different apport of the two Lamb modes, which have different wave speeds and are linked to in- or out-of-plane forces (as caused, respectively, by fibre breakage or delamination). On this basis, although it is not possible to demarcate a sharp distinction, it is possible to say that the graphs indicate the presence of both in- and out-of-plane damage types. Yet, strictly speaking, none of these signals coincide with any of the types encountered in the strips, confirming that variations in the dimensions of the sample greatly affects the results, more than the lay-up and consequently the likelihood of the same originating mechanism.

The graphs displayed in Fig. 9.7 present a large scattering. Together with the large scatter of the source positions on the panel, this fact sustains the hypothesis that such curves are strictly linked to positional effects between edges, sources, and sensor, and that positional differences have a much greater effect on the results than the possible originating mechanism.

The peak-defining threshold is substantially different (lower) from the one necessary with the tests on the strips.

This chapter concludes the description of the experiments. The geometry, lay-up, dimensions tested and described were not exhaustive of all the possible combinations; nevertheless, the purpose of this research not being the completeness of the tested configurations, but the completeness of the evidence necessary to achieve the aim described in the first chapter, no further tests were considered necessary. The next chapter will summarise the findings.

CHAPTER

TEN

Conclusions and future work

Facts are stubborn things; and whatever may be our wishes, our inclinations, or the dictates of our passions, they cannot alter the state of facts and evidence.

John Quincy Adams

The overall goal of this work, as stated in Chapter 1, was to assess the potential of using AE in composite structures, with the purpose of characterising damage. This broad goal has been fulfilled in this thesis by simplifying the matter in a laboratory and carrying out a detailed experimental programme on material that is representative of that used in the aircraft industry.

To achieve the overall goal, the study has included the understanding of the fundamental basis of AE, i.e. a study of elastic waves, an assessment of the equipment, i.e. that which senses and processes the elastic waves, an assessment of the feasibility using a "standard" AE source — the pencil lead break, and an application to composites.

To define the problem, Chapter 2 focused on the theory of the elastic waves governing the transmission of the acoustic emissions in thin bodies. This showed that the mathematical treatment of the acoustic emissions is complex. In Chapter 4 a review of literature demonstrated further that only a few papers that attacked the problem of acoustic emissions mathematically provided useful results. From this it could be concluded that an experimental approach, that would circumvent the difficulties in developing an exact mathematical solution, was necessary to assess the feasibility of the application of the AE technique to

damage characterisation of composite materials. The review of the literature showed that, by using an experimental approach, useful results can be obtained, as long as the goal is limited and the application is relatively narrow and specific in scope.

Two important reasons for achieving the aim of this research are the possibility of having a real-time in-flight system that could identify damage with AE, and a means of locating AE sources on a composite structure. To attain the aim, the characterisation would thus have to accomplish two tasks: (i) describing the source, in terms of AE, in the most accurate way, (ii) ensuring that this description would include parameters invariant with sample geometry. The literature survey showed that, although (i) has been extensively achieved, (ii) has never received enough attention, or led to success. For this reason, this work concentrated on showing the factors that modify the detected waveforms up to a point of making them not "characteristic" of a damage type.

Chapter 5, in describing the AE system used for this work, has also enlightened some of the limitations intrinsic to commercial AE equipments that, whereas perfectly suitable for industrial applications of damage detection, do not lend themselves to quantitative source characterisation of composites. Chapter 5 illustrated the low fidelity of even the best broad-band sensors, and the inhomogeneity of their response.

Chapter 6 has shown that the traditional AE parameters cannot be used to correctly describe a source and, by simulating signals with PLBs, that variations in the sensors, or more generally in the sensitivity and calibration of the system, may affect in a measurable way the detected signals. The main conclusion of this chapter has led to discarding the parameters throughout the rest of the thesis, and to focus on a frequency analysis, proven to be more stable.

Chapter 7 has presented two tools to present and visualise frequency AE data; it has achieved this by considering the signals as non-stationary, differently from the traditional way of processing AE signals. Measuring the way the signals build up with time — using the frequency centroids as estimator — curves were generated that qualitatively inform about the dimensionality of the structure, and permit a better visualisation of the peaks present in the power spectra. These, once identified, can represent compactly the spectral features of many signals.

Chapter 8, by applying the analysis techniques previously devised, has shown that the effect of the aforementioned variations in the structure, and particularly in its dimensions,

on the recorded signals of actual damage in composites may be larger that the variations due to the originating source itself. Despite the large variations and scattering in the AE data, the positions of the peaks in the spectra are relatively *stable* within each test. When the frequency centroid value is plotted to show its variability with the sampling time, then it provides more useful information about the in- or out-of-plane nature of the originating damage.

Chapter 9, by exaggerating the differences in the dimensions of the samples moving from a strip to a panel, emphasises the same conclusion of the previous chapter. So, if on one hand a good description of the sources can be achieved, on the other hand this description is not invariant with dimensional parameters and, as such, cannot be considered a characterisation. The graphs indicate the presence of both in- and out-of-plane damage types, consistent with the nature of the sample and the loading.

This work stressed the importance of the difference between a *description* and a *characterisation*. Emphasising the difference in the meaning leads directly to a better operational understanding of what is generally expected by a characterisation, and what is *instead* obtainable with a description. This was novel, together with the demonstration that the characteristics of the sensors affect the *description* of the damage more than it could be generally considered expected and acceptable. This demonstration went along with the investigation of the variability introduced by the system and the testing parameters. Finally, the importance of the non-stationarity of the signals was illustrated, and a new way to use this to yield to new information led to the conclusion that a characterisation can only have a weak meaning, where much of the desired generality, in terms of extrapolative data, must be abandoned.

Naturally, the fact itself that a characterisation of the damage is not achievable in the broad sense specified does not make the original need (implementing a real-time in-flight AE monitoring system) less important or needed. In this respect, it is suggested that the discrimination of the "useful" AE data from the operational noise should be done by locating the source rather than describing it; to such extent, the results presented in this thesis, and particularly those indicating a strong positional dependence of the source, might be used *pro* this purpose.

In view of an implementation of artificial neural networks (ANN), the peak graphs, i.e. the value of the frequency peaks collected at different sample times, may provide an

additional useful input for the training of the networks. Since ANN are usually implemented on a specific structure and do not have the goal of providing extrapolative characterising information, they would not be affected by the variability of the results due to different sizes, therefore the position of the peaks and more importantly the sample times at which they are detected may be used to train the networks, in view of a further aid to the source location and a better discrimination of the acoustic emissions generated by in-plane or out-of-plane forces.

A continuation of the work contained in this thesis could address the quantification of way the signals are modified because of the dimensional and positional differences. This thesis has demonstrated that, far from being just one (the originating damage type), the factors that alter the detected signals (positions of the sensors, travelling path from the source to the sensors, relative position of the edges, dimensions of the specimen, lay-up) are many. Yet, the quantification of these variations has not been investigated, since outside the scope of assessing the *validity* of a characterisation. The techniques provided can help to summarise the AE data and thus to quantify the variations, once they are introduced in a controlled fashion, possibly one at a time. Quantifying, for example, how much the frequency peaks shift when the sensor–source distance increase, or how the sample times must vary in order to resolve the same peaks when the specimen width increases, can yield to a better understanding of the signal processing of the acoustic emissions, and possibly to help extracting positional information from the analysis of the signals coming from a single sensor. It is likely that such variations should be introduced in the context of a non-dimensional model, and the investigation itself of the identification of these parameters and their relationships (for example, sample time times wave speed over a linear dimension) may constitute a significant project.

REFERENCES

Âberg, M., 2001. Numerical modeling of acoustic emission in laminated tensile test specimens. *International Journal of Solids and Structures*, **38**:6643–6663

ASTM, 1998. Standard guide for acoustic emission examination of small parts. ASTM Technical Standard E 1932 - 97

ASTM, 2002. Standard method for primary calibration of acoustic emission sensors. ASTM Technical Standard E 1106 - 86

ASTM, 2007. Standard guide for determining the reproducibility of acoustic emission sensor response. ASTM Technical Standard E 976 - 05

Auld, B. A., 1973. *Acoustic fields and waves in solids*, volume 1. John Wiley & Sons. ISBN 0-471-03700-1

Avdelidis, N., Almond, D., Dobbinson, A., Hawtin, B. and Ibarra-Castanedo, C. a. M., 2004. Aircraft composites assessment by means of transient thermal ndt. *Progress in Aerospace Sciences*, **40**:143–162

Awerbuch, J., 1997. On the identification of failure mechanisms in composite laminates through acoustic emission. *NDT&E International*, **30**(2)

Banerjee, S. and Mal, A. K., 2005. Acoustic emission waveform simulation in multilayered composites. *The Journal of Strain Analysis for Engineering Design*, **40**(1):25–32. Special Issue on Acoustic Emission

Beattie, A. G., 1983. Acoustic emission, principles and instrumentation. *Journal of Acoustic Emission*, **2**(1/2):95–128

Bhat, C., Bhat, M. R. and Murthy, C. R. L., 2003. Acoustic emission characterization of failure modes in composites with ANN. *Composite Structures*, **61**(3):213–220

Birt, E., 2000. Applicability of x-radiography to the inspection of composites. *Insight: Non-Destructive Testing and Condition Monitoring*, **42**(3):152–157

Blitz, J., 1963. *Fundamentals of ultrasonics.* Butterworths, London

Bohse, J., 2000. Acoustic emission characteristics of micro-failure processes in polymer blends and composites. *Composites Science and Technology*, **60**:1213–1226

Bradshaw, T. P., 2006. Personal communication. Physical Acoustics UK

BSI, 1998. Fibre-reinforced plastic composites — determination of flexural properties. British Standard. BS EN ISO 14125:1998

BSI, 2000. Non-destructive testing — terminology — part 9: Terms used in acoustic emission testing. British Standard. BS EN 1330-9:2000

BSI, 2001a. Non-destructive testing — acoustic emission — equipment characterization — part 1: Equipment description. British Standard. BS EN 13477-1:2001

BSI, 2001b. Non-destructive testing — acoustic emission — equipment characterization — part 2: Verification of operating characteristics. British Standard. BS EN 13477-2:2001

BSI, 2002. Non-destructive testing — acoustic emission — general principles. British Standard. BS EN 13544:2002

BSI, 2006. Draft EN 15495 non-destructive testing - acoustic emission - examination of metallic pressure equipment during proof testing - zone location of AE sources. British Standard. EN 15495

Carlos, M. F., 2003. Acoustic Emission: Heeding the warning sounds from materials. *ASTM standardization news.* Http://www.astm.org

Carlyle, J. M., Bodine, H. L., Henley, S. S., Dawes, R. L., Demeski, R. and Hill, E. v. K., 1999. Practical AE methodology for use on aircraft. *In* S. J. Vahaviolos (ed.), *Acoustic Emission: Standards and Technology Update*, ASTM STP 1353, pages 191–205. American Society for Testing and Materials, West Conshohocken, PA, USA

Castagnède, B., 1990. Acoustic emission source location in anisotropic composite plates. *In Proceedings of EUROMECH 289, Saint Etienne, France*, pages 433–441. Elsevier Applied Science, London

Ceysson, O., Salvia, M. and Vincent, L., 1996. Damage mechainsms characterisation of carbon fibre / epoxy composite laminates by both electrical resistance measurements and acoustic emission analysis. *Scripta Materialia*, **34**(8):1273–1280

Chahbaz, A., Mustafa, V. and Hay, D., 1996. Corrosion detection in aircraft structures using guided Lamb waves. *NDT.net*, **1**(11). Http://www.ndt.net/article/tektrend/tektrend.htm

Chalmers, B., 1944. The non-destructive testing of metallic components. *Proceedings of the physical society*, **56**(2):132–147

Cheeke, J. D. N., 2002. *Fundamentals and applications of ultrasonic waves.* CRC Press. ISBN 0-8493-0130-0

Chung, D. D. L., 2001. Structural health monitoring by electrical resistance measurement. *Smart materials and structures*, **10**:624–636

Cohen, P., 1997. Failing airframe speaks volumes to engineers. *New Scientist*, (2088):6. ISSN 02624079

Coleman, N., 2006. Dynamic defect detection — Part 1: Theory of vibrational analysis. *Sensors — www.sensorsmag.com.* Http://archives.sensorsmag.com/articles/0899/14/main.shtml

Cremer, L. and Heckl, M., 1973. *Structure-Borne Sound.* Springer-Verlag. ISBN 3-540-06002-2

Daniel, I. M. and Ishai, O., 1994. *Engineering mechanics of composite materials.* Oxford University Press. ISBN 0195075064

De Goeje, M. P. and Wapenaar, K. E. D., 1992. Non-destructive inspection of carbon fibre-reinforced plastics using eddy current methods. *Composites*, **23**(3):147–157

de Groot, P. J., Wijnen, P. A. M. and Janssen, R. B. F., 1995. Real-time frequency determination of acoustic emission for different fracture mechanisms in carbon/epoxy composites. *Composites Science and Technology*, **55**:405–412

Diederichs, R. and Ginzel, E., 1999. Nondestructive testing encyclopedia. Website http://www.ndt.net/article/az/ndtmain.htm

Dieulesaint, E. and Royer, D., 1980. *Elastic Waves in Solids.* John Wiley & Sons. ISBN 0-471-27836-X

Drouillard, T. F., 1996. A history of acoustic emission. *Journal of Acoustic Emission*, **14**(1):1–34

Dunegan, H. L., 1969. Ultrasonic acoustic emission from materials. *IEEE Transactions on Sonics and Ultrasonics*, **SU-16**(1, suppl.):32

Dunegan, H. L., 1996. Transducer performance terminology. *DECI newsletters and reports.* Http://www.deci.com/tpt.htm

Dunegan, H. L., 1997. Modal analysis of acoustic emission signals. *DECI newsletters and reports.* Http://www.deci.com/oct97.htm

Dzenis, Y. and Qian, J., 2001. Hybrid transient-parametric AE analysis of histories of damage micromechanisms in composites. *In* T. Kundu (ed.), *Advanced Nondestructive Evaluation for Structural and Biological Health Monitoring*, volume 4335 of *Proceedings of SPIE.* International Society for Optical Engineering

El Guerjouma, R., Baboux, J.-C., Ducret, D., Godin, N., Guy, P., Huguet, S., Jayet, Y. and Monnier, T., 2001. Non-destructive evaluation of damage and failure of fibre reinforced polymer composites using ultrasonic waves and acoustic emission. *Advanced engineering materials*, **3**(8):601–608

Ely, T. M. and Hill, E. v. K., 1993. Characterization of longitudinal splitting and fiber breakage in Gr/Ep using acoustic emission data. Technical Report CR-97-207214, NASA

Enoki, M., Fujita, H. and Kishi, T., 1997. Quantitative fracture mode analysis of composites by acoustic emission. *In* D. Thompson and D. E. Chimenti (eds.), *Review of Progress in Quantitative Nondestructive Evaluation*, volume 16. Plenum Press

Farrar, C. R., Sohn, H., Hemez, F. M., Anderson, M. C., Bement, M. T., Cornwell, P. J., Doebling, S. W., Schultze, J. F., Lieven, N. and Robertson, A. N., 2003. Damage prognosis: Current status and future needs. Technical report, Los Alamos National Laboratory

Ferreira, D. B. B., 2000. *Aplicaçao da técnica de emissão acústica na caracterizaçao dos mecanismos de falha em plásticos reforçados por fibras.* Ph.D. thesis, Universidade Federal do Rio de Janeiro, COPPE

Ferreira, D. B. B., da Silva, R. R., Rebello, J. M. A. and Siqueira, M. H. S., 2004. Failure mechanism characterisation in composite materials using spectral analysis and the wavelet transform of acoustic emission signals. *Insight: non-destructive testing and condition monitoring*, 46(5):282–289. ISSN 1354-2575

Ferrer, F., Faure, T., Goudiakas, J. and Andrès, E., 2002. Acoustic emission study of active-passive transitions during carbon steel erosion-corrosion in concentrated sulfuric acid. *Corrosion Science*, 44(7):1529–1540

Filipczynski, L., Pawlowski, Z. and Wehr, J., 1966. *Ultrasonic Methods of Testing Materials.* Butterworths, London

Frederick, J. R., 1965. *Ultrasonic Engineering*, chapter 2. John Wiley & Sons

Fuwa, M., Bunsell, A. R. and Harris, B., 1976. An evaluation of acoustic emission techniques applied to carbon-fibre composites. *Journal of Physics D: Applied Physics*, 9:353–365

Giordano, M., Calabrò, A., Esposito, C., D'Amore, A. and Nicolais, L., 1998. An acoustic-emission characterization of the failure modes in polymer-composite materials. *Composites Science and Technology*, 58(12):1923–1928

Graff, K. F., 1991. *Wave Motion in Elastic Solids.* Courier Dover Publications. ISBN 0486667456

Guild, F. J. and Adams, R. D., 1981. Detection of cracks in damaged composite materials. *Journal of Physics D: Applied Physics*, 14(8):1561–1573

Guo, D., Mal, A., Ono, K. and Gorman, M., 1997. Lamb waves from microfractures in composite plates. *In* D. Thompson and D. E. Chimenti (eds.), *Review of Progress in Quantitative Nondestructive Evaluation*, volume 16. Plenum Press

Halmshaw, R., 1991. *Non-destructive testing*, chapter 8. Arnold, 2nd edition. ISBN 0 340 54521 6

Haselback, W. and Lauke, B., 2003. Acoustic emission of debonding between fibre and matrix to evaluate local adhesion. *Composites Science and Technology*, **63**:2155–2162

Haugse, E., Leeks, T., Ikegami, R. and Johnson, P., 1999. Crack growth detection and monitoring using broadband acoustic emission techniques. *In SPIE Conference on Nondestructive Evaluation of Aging Aircraft, Airports, and Aerospace Hardware III. Newport Beach, California*, volume 3586, pages 32–40

Hill, R., Brooks, R. and Kaloedes, D., 1998. Characterization of transverse failure in composites using acoustic emission. *Ultrasonics*, **36**:517–523

Hill, R. and Stephens, W. B., 1974. Simple theory of Acoustic Emission — a consideration of measurement parameters. *Acustica*, **31**:224–230

Holroyd, T. J., 2000. *Acoustic emission & ultrasonics.* Coxmoor Publishing Company. ISBN 1-90189-207-7

Horvath, P. and Cook, F. J., 1982. Estabilishing signal processing and pattern recognition techniques for inflight discrimination between crack-growth acoustic emission and other acoustic waveforms. *In Proceedings of the 8th US Air Force/Defence Advanced Research Projects Agency — Symposium on quantitative nondestructive evaluation*, volume 1, pages 463–473. Boulder, CO, USA. 2–7 August

Huguet, S., Godin, N., Gaertner, R., Salmon, L. and Villard, D., 2002. Use of acoustic emission to identify damage modes in glass fibre reinforced polyester. *Composites Science and Technology*, **62**(10-11):1433–1444

Iwamoto, M., Ni, Q.-Q., Fujiwara, T. and Kurashiki, K., 1999. Intralaminar fracture mechanism in unidirectional CFRP composites — Part I: Intralaminar toughness and AE characteristics. *Engineering Fracture Mechanics*, **64**:721–745

Jemielniak, K., 2001. Some aspects of acoustic emission signal pre-processing. *Journal of Materials Processing Technology*, **109**:242–247

Jeong, H. and Jang, Y.-S., 2000. Wavelet analysis of plate wave propagation in composite laminates. *Composite Structures*, **49**(4):443–450

Joffe, R., Varna, J. and Berglund, L. A., 1995. Acoustic emission from composite laminates with simple damage characteristics. *In AECM-5. Fifth International Symposium on Acoustic Emission from Composite Material*, pages 179–186. American Society for Nondestructive Testing. Sundsvall, Sweden, 10–14 July

Johnson, M., 2003. Classification of ae transients based on numerical simulations of composite laminates. *NDT&E International*, **36**:319–329

Johnson, M. and Gudmundson, P., 2000. Broad-band transient recording and characterization of acoustic emission events in composite laminates. *Composites Science and Technology*, **60**(15):2803–2818

Johnson, M. and Gudmundson, P., 2001. Experimental and theoretical characterization of acoustic emission transients in composite laminates. *Composites Science and Technology*, **61**(10):1367–1378

Jones, B. E. and Yan, T., 2005. Acoustic emission traceable sensing. *The Journal of Strain Analysis for Engineering Design*, **40**(1):17–23. Special Issue on Acoustic Emission

Kino, G. S. and Shaw, J., 1972. Acoustic surface waves. *Scientific American*, **227**(4):50–68

Koo, J.-H., Enoki, M., Kishi, T. and Kim, B.-N., 1998. Three dimensional acoustic emission signal analysis in C/C composites with anisotropic structure. *Journal of Acoustic Emission*, **16**(1–4):269–276

Kouvarakos, M. and Hill, E. v. K., 1996. Isolating tensile failure mechanisms in fiberglass epoxy from acoustic emission signal parameters. *Materials Evaluation*, **54**:1025–1031

Krautkrämer, J. and Krautkrämer, H., 1983. *Ultrasonic Testing of Materials.* Springer-Verlag, 3rd edition. ISBN 3-540-11733-4

Lariviere, D., Krawczak, P., Tiberi, C. and Lucas, P., 2003. Acoustic emission applied to failure analysis of commingled yarn GF/PP composites in transverse tension and mode I delamination. *Advanced Composites Letters*, **12**(5):191–202

Liu, G. R. and Xi, Z. C., 2002. *Elastic Waves in Anisotropic Laminates.* CRC Press. ISBN 0849310709

Mal, A., 2000. Elastic waves from localized sources in composite laminates. *In* D. A. Sotiropoulos (ed.), *IUTAM Symposium on Mechanical Waves for Composite Structures Characterization*. Kluwer Academic Publishers

Marantidis, C., Van Way, C. and Kudva, J., 1994. Acoustic-emission sensing in an on-board smart structural health monitoring system for military aircraft. *In Proceedings of the SPIE — Conference: Smart Structures and Materials. Smart Sensing, Processing, and Instrumentation, 14–16 Feb 1994, Orlando, FL, USA*, volume 2191, pages 258–264. The International Society for Optical Engineering. ISSN 0277-786X

Matthews, F. L., 1999. Damage in fibre-reinforced plastics; its nature, consequences and detection. pages 1–15. Trans Tech Publications, Dublin. ISBN 0-87849-839-7

McBride, S. L., Pollard, M. D., MacPhail, J. D. and Bowman, P. S., 1991. Acoustic emission detection of crack presence and crack advance during flight. *ASTM Special Technical Publication*, (1077):146–155. ISSN 0066-0558. Symposium on Acoustic Emission: Current Pratice and Future Directions, Mar 20–23 1989, Charlotte, NC, USA

Mizutani, Y., Nagashima, K., Takemoto, M. and Ono, K., 2000. Fracture mechanism characterization of cross-ply carbon-fiber composites using acoustic emission analysis. *NDT&E International*, **33**(2):101–110

Mukhopadhyay, C., Jayakumar, T., Raj, B. and Ray, K., 2002. Correlation of acoustic emission with stress intensity factor and plastic zone size for notched tensile specimens of AISI type 304 stainless steel. *Materials Science and Technology*, **18**(10):1133–1141

NDT.net, 2007. NDT.net. Website. Http://www.ndt.net

NDTRC, 2007. NDT Resource Center. Website. Http://www.ndt-ed.org

Ni, Q.-Q., Kurashiki, K. and Iwamoto, M., 2001. AE technique for identification of micro failure modes in CFRP composites. *Materials Science Research International*, **7**(1):67–71

Nichols, R. W. (ed.), 1976. *Acoustic Emission*. Applied Science Publishers LTD, London. ISBN 0-85334-681-X

Nielsen, A., 1980. Acoustic emission source based on pencil lead breaking. Technical Report 80.15, SVEJSECENTRALEN The Danish Welding Institute

NTSB, 2003. Safety recommendation — september 4, 2003. Technical report, National Transportation Safety Board, Washington, D.C. 20594

O.U.P., 1989. *Oxford English Dictionary*, 2nd edition. Oxford University Press

PAC, 2003. *PCI-2 based AE system user's manual.* Princeton Junction, NJ. Rev 1a

Pappas, Y. Z., Kontsos, A., Loutas, T. H. and Kostopulos, V., 2004. On the characterization of continuous fibres fracture by quantifying acoustic emission and acousto-ultrasonics waveforms. *NDT&E International*, **37**:389–401

Pohl, J., Herold, S., Mook, G. and Michel, F., 2001. Damage detection in smart cfrp composites using impedance spectroscopy. *Smart materials and structures*, **10**:834–842

Pollock, A. A., 1976. Acoustic emission. *Machine Design*, **48**(8):72–76

Pollock, A. A., 1986. Classical wave theory in practical AE testing. *In Progress in Acoustic Emission III — Proceedings of the 8th international symposium, Tokio.* Japanese Society for non-destructive testing

Prakash, R., 1980. Non-destructive testing of composites. *Composites*, **11**(4):217–224

Prosser, W. H., 1996. Applications of advanced, waveform based AE techniques for testing composite materials. *In Proceedings of the SPIE — Conference on Nondestructive Evaluation Techniques for Aging Infrastructure and Manufacturing: Materials and Composites, December 2–5, Scottsdale, Arizona*, pages 146–153. The International Society for Optical Engineering

Prosser, W. H., 1998. Waveform analysis of AE in composites. *In Sixth International Symposium on Acoustic Emission from Composite Materials, San Antonio, Texas, June, 1998.* NASA Langley Research Center, Hampton, VA, 23681-0001

Prosser, W. H., Gorman, M. R. and Dorighi, J., 1992. Extensional and flexural waves in a thin-walled graphite/epoxy tube. *Journal of Composite Materials*, **26**(14):418–427

Prosser, W. H., Hamstad, M. A., Gary, J. and O'Gallagher, A., 1999. Reflections of AE waves in finite plates: finite element modeling and experimental measurements. *Journal of Acoustic Emission*, **17**(1–2):37–47

Prosser, W. H., Jackson, K. E., Kellas, S., Smith, B. T., McKeon, J. and Friedman, A., 1995. Advanced waveform-based acoustic emission detection of matrix cracking in composites. *Materials Evaluation*, **53**:1052–1058

Qi, G., 2000. Attenuation of acoustic emission body waves in acrylic bone cement and synthetic bone using wavelet time-scale analysis. *Journal of Biomedical Materials Research*, **52**(1):148–156

Qi, G., Barhost, A., Hashemi, J. and Kamala, G., 1997. Discrete wavelet decomposition of acoustic emission signals from carbon-fiber-reinforced composites. *Composites Science and Technology*, **57**:389–403

Rawal, S., 2001. Metal-matrix composites for space applications. *JOM*, **53**(4):14–17

Rhian Green, E., 1997. Surface response of an anisotropic laminate to acoustic emission sources. *In* D. Thompson and D. E. Chimenti (eds.), *Review of Progress in Quantitative Nondestructive Evaluation*, volume 16. Plenum Press

Scruby, C. B., 1987. An introduction to acoustic emission. *Journal of Physics E: Scientific Instruments*, **20**(8):946–953

Seo, D.-C. and Lee, J.-J., 1999. Damage detection of CFRP laminates using electrical resistance measurement and neural network. *Composite Structures*, **47**(1–4):525–530

Shiryaev, A. M., Golovinskii, A. G. and Kiselev, A. V., 1990. Possibility of evaluating the informativeness of acoustic-emission parameters. *Soviet Journal of Nondestructive Testing*, **25**(6):457–461. Translated from Defektoskopiya, No. 6, pp. 83–87, June, 1989

Silk, M. G., 1984. *Ultrasonic Transducers for Nondestructive Testing*, chapter 1. Adam Hilger Lmt, Bristol. ISBN 0-85274-436-6

Silva, F. E., Gonçales, L. L., Ferreira, D. B. B. and Rebello, J. M. A., 2005. Characterization of failure mechanism in composite materials through fractal analysis of acoustic emission signals. *Chaos, Solitons and Fractals*, **26**:481–494. Author Ferreira is mispelled as Fereira

Singh, S. K., Srinivasan, K. and Chakraborty, D., 2003. Acoustic emission studies on metallic specimen under tensile loading. *Materials & Design*, **24**(6):471–481

Surgeon, M. and Wevers, M., 1999. Modal analysis of acoustic emission signals from CFRP laminates. *NDT&E International*, **32**(6):311–322

Szilard, J., 1982a. *Physical principles of ultrasonic testing*, chapter 1. *In* Szilard (1982b)

Szilard, J. (ed.), 1982b. *Ultrasonic testing.* John Wiley & Sons. ISBN 0471279382

Tatiparthi, A. K., 2004. *Investigation of microcrack growth in* $[0/90]_s$ *graphite epoxy composite laminates using X-ray microtomography.* Master's thesis, Department of Mechanical Engineering, University of New Orleans

Tatro, C. A., 1976. *A welder's introduction to acoustic emission technology*, pages 1–9. *In* Nichols (1976)

Temple, J. A. G., 1988. Modelling the propagation and scattering of elastic waves in inhomogeneous anisotropic media. *Journal of Physics D: Applied Physics*, **21**:859–874

Terchi, A. and Au, Y. H. J., 2001. Acoustic emission signal processing. *Measurement + Control*, **34**:240–244

Tsai, H. H. and Hocheng, H., 2002. On-line identification of thermally-induced convex deformation of the workpiece in surface grinding. *Journal of Materials Processing Technology*, **121**(2–3):189–201

Tuikin, O. R. and Ivanov, V. I., 1985. Factorial analysys of stability for acoustic-emission parameters. *Soviet Journal of Nondestructive Testing*, **21**(8):554–558

Überall, H., 1973. Surface waves in acoustics. *In* W. P. Mason and R. N. Thurston (eds.), *Physical Acoustics*, volume X. Academic Press. ISBN 0-12-477910-7

Vallen, H., 2002. AE testing fundamentals, equipment, applications. *NDT.net*, **7**(9). Http://www.ndt.net/v07n09.htm

Viktorov, I. A., 1967. *Rayleigh and Lamb waves.* Plenum Press, New York

Vipond, R. and Daniels, C. J., 1985. Non-destructive examination of short carbon fibre-reinforced injection moulded thermoplastics. *Composites*, **16**(1):14–18

Wevers, M. and Surgeon, M., 2000. *Comprehensive Composite Materials*, volume 5, chapter Acoustic Emission and Composites. Elsevier

Williams, R. V., 1980. *Acoustic Emission.* Adam Hilger Ltd. ISBN 0852743599

Woo, S.-C., Kim, J.-H. and Choi, N.-S., 2004. Fracture processes and acoustic emission in continuos fiber reinforced composite laminates. *Key Engineering Materials*, **270–273**(111):1827–1832

Yamada, H., Mizutani, Y., Nishino, H., Takemoto, M. and Ono, K., 2001. Lamb wave source location of impact on anisotropic plates. *Journal of Acoustic Emission*, **18**:51–60

Appendices

Appendix A

Mathematical derivations from chapter 7

With reference to Fig. 7.31, the reflection free time can be calculated as follows:

$$t' = t'_2 - t'_1 \tag{1}$$

where t'_1 is the time for the acoustic emission to travel directly to the sensor and t'_2 is the time for the fastest reflection to reach the sensor. Then, from simple geometric relations:

$$\overline{SoB} + \overline{BSe} = \sqrt{d'^2 + (h' + e)^2} \tag{2}$$

$$d = \sqrt{d'^2 + (e - h')^2} \tag{3}$$

and then the times are:

$$t'_1 = \frac{\sqrt{d'^2 + (h' - e)^2}}{v} \tag{4}$$

$$t'_2 = \frac{\sqrt{d'^2 + (h' + e)^2}}{v} \tag{5}$$

$$t' = t'_2 - t'_1 = \frac{\sqrt{d'^2 + (h' + e)^2} - \sqrt{d'^2 + (h' - e)^2}}{v} \tag{6}$$

where v is the wave speed.

Similarly, Fig. 1 shows the schematic for a reflection from the rear (the wave must travel

back and then forth to reach the sensor). In a similar fashion,

$$d_1 = \sqrt{d''^2 + (h'' - e_1)^2} \tag{7}$$

$$\overline{SoB} + \overline{BSe} = \sqrt{d''^2 + (h'' + e_1)^2} \tag{8}$$

$$t''_1 = \frac{1}{v}\sqrt{d''^2 + (h'' - e_1)^2} \tag{9}$$

$$t''_2 = \frac{1}{v}\sqrt{d''^2 + (h'' + e_1)^2} \tag{10}$$

$$t'' = t''_2 - t''_1 = \frac{\sqrt{d''^2 + (h'' + e_1)^2} - \sqrt{d''^2 + (h'' - e_1)^2}}{v} \tag{11}$$

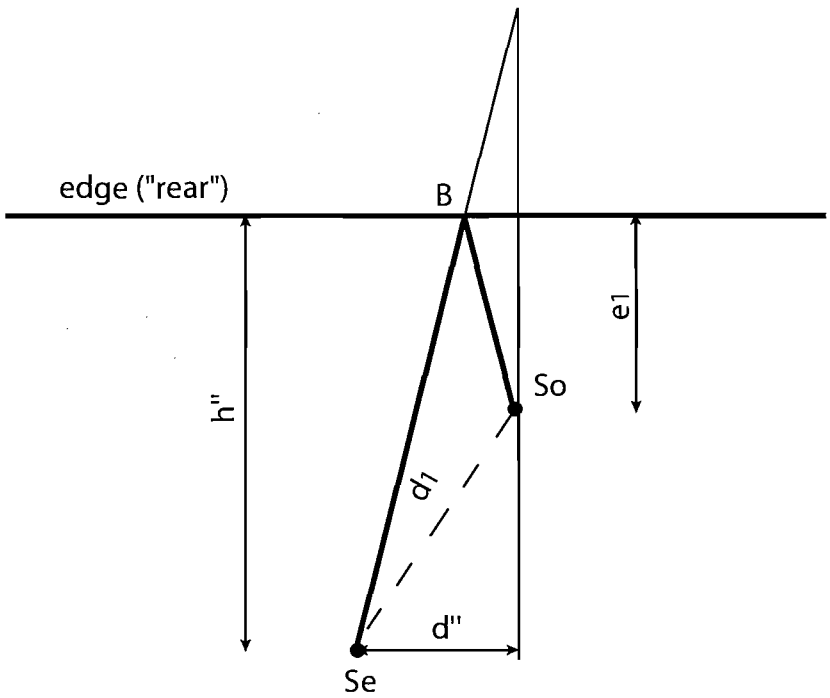

Figure 1: Schematic of a rear reflection

The reflection-less time window t^* is given by:

$$t^* = \min(t', t'') \tag{12}$$

In order to evaluate some grid computation on an (x, y) cartesian plane, the following relations apply, with reference to Fig. 2.

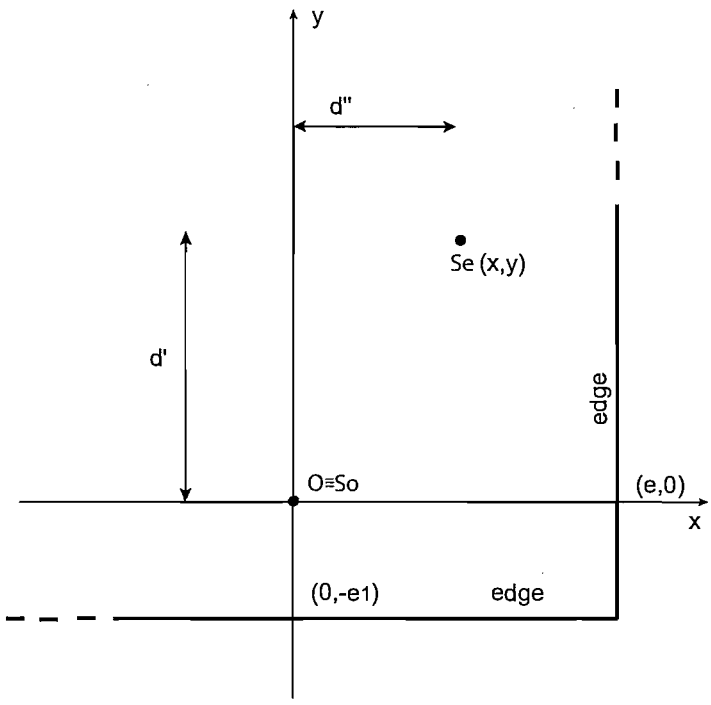

Figure 2: Transforming to cartesian coordinates

$$h' = e - x \tag{13}$$

$$d' = y \tag{14}$$

$$d'' = x \tag{15}$$

$$h'' = y + e_1 \tag{16}$$

$$d = \sqrt{x^2 + y^2} \tag{17}$$

$$\text{side reflection path length} = \sqrt{d'^2 + (h' + e)^2} = \sqrt{y^2 + x^2 + 4e^2 - 4ex} \tag{18}$$

and hence the times are:

$$t'_1 = d/v = \sqrt{x^2 + y^2}/v \tag{19}$$

$$t'_2 = \sqrt{y^2 + x^2 + 4e^2 - 4ex}/v \tag{20}$$

$$t''_1 = \sqrt{x^2 + y^2}/v \tag{21}$$

$$t''_2 = \sqrt{x^2 + (y + 2e_1)^2}/v \tag{22}$$

Appendix B

Matlab code

[GeometricMean.m]

```
% For Matlab 7.0
% Loads ascii waveforms and computes the geometric
% mean of the power spectra.
%
% It is assumed here that all the data files are of the same length.
%
% Uses some functions (C) by Frederico D'Almeida and (C) by Sergei Koptenko

%
% Initialization
%
clear all
%close all
%

%
% Program options
%
normalizespectra=1; % if 0 spectra are not normalized
displaywaveforms=0; % plots all the waveforms
displaygeometricmean=1;
aritmean=0; % display arithmetic mean with std devs
loadswaveformsfromtxts=0; % alternatively loads from MATlab file
%timeinterval=0.0000010000; % 0.000001 corresponds to 1MSPS
```

```
timeinterval=0.0000005; % [s] 0.0000005 corresponds to 2MSPS
% (*) timeinterval must be the time spacing between each data in nomefile,
% eg 0.000001, depending on the sample rate used.
% The frequency scale in the spectra will vary accordingly
PACpretrig=128; % value SET in PAC (number of bytes)
additionalpretrig=64 % value set manually (microseconds)
% (*) pretrig is the number of data recorded before the start of the hit
% e.g. 512. They will be discarded here, unless pretrig=0
microsec=4936; % if > 0 is after how many microsec the waveform is cropped
if microsec==0
    disp('Warning! The trailing zeros ...
    should be cropped out! No zero padding is desired!')
end
%


%
% Load data
%
% (*) nomefile1,nomefile2,etc must be strings with the name of the csv
% files; e.g. x = 'pippo.csv'.
% These files are obtained from
% AEWin Utilities->ASCIIWaveforms->Output file type: Simple.
% (Select Complete instead to gather the sampling rate.)
if loadswaveformsfromtxts
   numerofile=20; % Total number of input data files
   % NB All the input files must be the same length
   % NB All the input file names must be the same length
   nomefile(1,:)='A_1_1.csv';
   nomefile(2,:)='A_1_2.csv';
   nomefile(3,:)='B_1_1.csv';
   nomefile(4,:)='B_1_2.csv';
   nomefile(5,:)='C_1_1.csv';
   nomefile(6,:)='C_1_2.csv';
   nomefile(7,:)='D_1_1.csv';
   nomefile(8,:)='D_1_2.csv';
```

```
   nomefile(9,:)='E_1_1.csv';
   nomefile(10,:)='E_1_2.csv';
   nomefile(11,:)='F_1_1.csv';
   nomefile(12,:)='F_1_2.csv';
   nomefile(13,:)='G_1_1.csv';
   nomefile(14,:)='G_1_2.csv';
   nomefile(15,:)='H_1_1.csv';
   nomefile(16,:)='H_1_2.csv';
   nomefile(17,:)='I_1_1.csv';
   nomefile(18,:)='I_1_2.csv';
   nomefile(19,:)='L_1_1.csv';
   nomefile(20,:)='L_1_2.csv';
   %nomefile(20,:)='10Comp2_4_A.txt';
   for indice=1:numerofile
       data(indice,:)=csvread(nomefile(indice,:))';
       % data is a matrix which has nomefile(1,:)' as first row
   end
else
   load tenDs
end

%
% Cropping of the data (before and after)
%
pretrig=PACpretrig+additionalpretrig./timeinterval./1e6;
l=length(data(1,:));
if microsec>0
    afterwhat=pretrig+microsec./timeinterval./1e6;
else
    afterwhat=l;
end
for numerodatafile=1:numerofile
   newdata(numerodatafile,:)=data(numerodatafile,(pretrig+1):afterwhat);
end
disp('Cropped length of waveform (microseconds):'),disp(microsec)
```

```
data=newdata;
l=length(data(1,:));
%

%
% Plot of all the waveforms
%
if displaywaveforms
    maxtimesec=timeinterval*l; % full scale (seconds)
    timeaxis=0:timeinterval:(maxtimesec-timeinterval); % time axis
    if numerofile>1
        figure
        waterfall(timeaxis,(1:numerofile),data)
        colormap(white-1)
        xlabel('time [s]')
        ylabel('Hit #')
        zlabel('Volt')
        set(gca,'YTick',0:numerofile)
    end
    if numerofile==1
        figure
        plot(timeaxis,data)
    end
end
%

%
% Computing of Power Spectra
%
for indice=1:numerofile
    %Pxx=pwelch(signal,[],[],512);
    %Pxx=pwelch(data(indice,:),[],[],[]);
    Pxx=pwelch(data(indice,:),[],[],512);
   f=1:length(Pxx);
   f=(f./length(Pxx)./timeinterval/2)'; % frequencies axis
```

```
   PowSpDen(indice,:)=Pxx'; % a row
end
%

%
% Data saving
%
if loadswaveformsfromtxts % only if new data are read
    asc=length(data(1,:));
    waveascissa=1:asc; % ascissa per la waveform
    save PosF_700N_10eventi_FLT_3 data numerofile waveascissa
end
%

%
% Normalisation of Power Spectra
%
if normalizespectra
    mass=(max(PowSpDen'))'; % column vector
    for indice=1:numerofile
        PowSpDenNorm(indice,:)=PowSpDen(indice,:)./mass(indice);
    end
    PowSpDen=PowSpDenNorm;
    clear PowSpDenNorm
end
%

%
% Power Spectra Arithmetic mean
%
%
if aritmean & (numerofile>1) & normalizespectra
   MAS=mean(PowSpDen); % Arithmetic Mean of Normalised Spectra
   figure
   hold
```

```
   plot(f,MAS)
   devstand2=std(PowSpDen,1);
   % standard deviation of the non-normalised spectra
   mass2=(mean(mass));
   devstand2=devstand2./mass2;
   plot(f,MAS+devstand2)
   plot(f,MAS-devstand2)
   title('spectral arithmetic mean and ...
   std dev of the non-normalised spectra, normalized')
   grid
   xlabel('Frequency [Hz]')
   set(gca,'XGrid','off','YGrid','off','YScale','log')
   hold
   %
   freqcMAS=sum(f'.*MAS)/sum(MAS);
   disp('Frequency centroid for the Arithmetic Mean Spectrum [Hz]')
   disp(round(freqcMAS))
end
%

%
% Power spectra Geometric mean:
%
MGS=PowSpDen(1,:);
if numerofile>=2
   for indice=2:numerofile
      MGS=MGS.*PowSpDen(indice,:);
   end
   MGS=MGS.^(1./numerofile);
end
if normalizespectra
    MGS=MGS./max(MGS);
end
%
if displaygeometricmean
```

```
   figure
   plot(f,MGS);
   if normalizespectra
   title('normalised spectral geometric mean')
   else
       title('spectral geometric mean')
   end
   grid
   xlabel('Frequency [Hz]')
   set(gca,'XGrid','on','YGrid','off','YScale','log')
end
%

%
% Frequency centroid
%
disp('Frequency centroids for spectra')
for indice=1:numerofile

freqc(indice)=sum(f'.*PowSpDen(indice,:))/sum(PowSpDen(indice,:));
end
%
disp(round(freqc))
disp('Average Frequency Centroid [Hz]')
disp(round(mean(freqc)))
%
disp('Standard deviation of Frequency centroids [Hz]')
disp(round(std(freqc,1)))
%
freqcMGS=sum(f'.*MGS)/sum(MGS);
disp('Frequency centroid for the Geometric Mean Spectrum [Hz]')
disp(round(freqcMGS))
%
%
```

```
%
% information display
%
format bank
disp('Final Byte Lenght of the waveform:');disp(l)
disp('Initial part of the waveform eliminated, ...
including pretrigger (microseconds):'),disp(pretrig*timeinterval*1e6)
%
```

[FrequencyPeaks.m]

```
% Bands
% For Matlab 7.0
% Ver 2.0 (colour)
% Power spectra at different sampling lenghts
% It generates bands of maxima
% Uses function massimo.m
% It must be run individually on each single waveform datafile
% NB: delete bands.mat before a new analysis

%
% Initialization
%
clear all
close all
%

%
% Program options
%
nomefile='AP1vicinoCh2_1_A.csv'; % input data file
%
SAMPLErate=2; % [MHz] sampling rate of the input data file
PACpretrig=128; % value SET in PAC (number of bytes)
additionalpretrig=64;
summaryplot=1; % if 1 loads from savedatafile and plots the overall data
```

```
%
threshold=.25;
topbot=[1 1.2]; % vertical length of the bands for maxima
steps=[25 40 80 120 220 450 750];
% 7 steps (microseconds) considered after the pretrig
%
colore(1,:)=[0 0 0];
colore(2,:)=[0 0 1];
colore(3,:)=[.1 .6 1];
colore(4,:)=[1 0 1];
colore(5,:)=[.3 .5 0];
colore(6,:)=[1 0 0];
colore(7,:)=[0 .7 0];

%
% Program calculations
%
timeinterval=(SAMPLErate*1e6)^-1;
NOsteps=7;
%

%
% Load data
%
data=csvread(nomefile)';
%

%
% Cropping of the data (before and after)
%
orl=length(data); % original length
pretrig=PACpretrig+additionalpretrig./timeinterval./1e6; % total pretrig
afterwhat=steps./timeinterval./1e6; % is a vector of byte lengths
data=data((pretrig+1):(pretrig+max(afterwhat))); % delete before trig
l=length(data);
```

```
newdata=zeros(NOsteps,max(afterwhat));
for nnn=1:NOsteps
    tmp=zeros(1,max(afterwhat));
    tmp(1:afterwhat(nnn))=data(1:afterwhat(nnn));
    newdata(nnn,:)=tmp;
end
finl=length(newdata);
% newdata is a matrix, each row being a part of the waveform,
% growing row by row. For storage purposes, newdata has zeroes where
% there is no signal. Nevertheless the computation must be done
% on the signal without the zero padding.
%

%
% information display
%
format bank
disp('Original Byte Lenght of the waveform:');disp(orl)
disp('Final Maximum Byte Lenght of the waveform:');disp(finl)
disp('Whithout pretrig, available length of the waveform ...
(microseconds):'),disp((orl-pretrig)*timeinterval*1e6)
disp('Initial part of the waveform eliminated, including pretrigger ...
(microseconds):'),disp(pretrig*timeinterval*1e6)
%

%
% Power Spectra, normalised, with bands of maxima
%
for indice=1:NOsteps
    signal=shrink(newdata(indice,:));
    % the computation of the Spectral Density must be done
    % on the waveform without adding any zero to the signal!
    Pxx=pwelch(signal,[],[],512);
    Pxx=Pxx./max(Pxx); % power spectral density for one sample time
    matricemassimi(indice,:)=massimo(Pxx,threshold);
```

```
    PowSpDen(indice,:)=Pxx';
end
%
% compatta la matricemassimi in un solo vettoremassimi
vettoremassimi=zeros(1,length(Pxx)); % it has 1 where there is a maximum
for indice=1:NOsteps
    for scan=1:length(Pxx)
        if matricemassimi(indice,scan)==1
            vettoremassimi(scan)=1;
        end
    end
end
%

%
% Power Spectra Graphs
%
f=1:length(Pxx);
f=(f./length(Pxx)./timeinterval/2)'; % frequencies axis
%
figure('name','Normalised power spectra at different sampling lengths')
title('Normalised power spectra at different sampling lengths')
%
hold
for index=1:NOsteps
    plot(f,PowSpDen(index,:),'Color',colore(index,:))
end
legend(num2str(steps'))
%

%
% Graph of maxima
%
%frequenzecoimassimiv=vettoremassimi.*f'; % frequencies where maxima occur
for indice=1:NOsteps
```

```
    frequenzecoimassimim(indice,:)=matricemassimi(indice,:).*f';
end
%
for index7=1:NOsteps
    for indice=1:length(f)
        asc=[frequenzecoimassimim(index7,indice),...
            frequenzecoimassimim(index7,indice)];
        line(asc,topbot,'Color',colore(index7,:),'LineWidth',2)
    end
end
plot([0,f(length(f))],[threshold,threshold],'Color',[0 0 0])
axis([0 f(length(f)) 0 max(topbot)])
xlabel('Frequency [Hz]')
%

%
% Data saving/loading
%
if exist('bands.mat')==2
    load bands % it must contain a matrix "frequenze"
    frequenze=[frequenze;frequenzecoimassimim];
else
    frequenze=frequenzecoimassimim;
end
% each row is the vector of frequency maxima of a single sample time
%save savedatafile frequenze
save('bands.mat', 'frequenze')
%

%
% Summary plot
%
if summaryplot
    figure('name','Summary of the frequency peaks')
    %title('Summary of the frequency peaks')
```

```
    hold
    numerodati=min(size(frequenze))/NOsteps; % number of data sets
    ordinata=0:(1/numerodati):1;
    for scan=1:(numerodati*NOsteps)
        for indice=1:length(f)
            asc=[ frequenze(scan,indice) , frequenze(scan,indice) ];
            indicecolore=mod(scan,NOsteps);
            if indicecolore==0
                indicecolore=7;
            end
            line(asc,[ordinata(ceil(scan/NOsteps)) ...
                ordinata(ceil(scan/NOsteps)+1)],'Color',...
                colore(indicecolore,:),'LineWidth',2)
        end
    end
    axis([0 f(length(f)) 0 1])
    xlabel('Frequency [Hz]')
    set(gca,'ytick',0)
end
```

[massimo.m]

```
function massimi = massimo(x,threshold)
% Ver. 1.1
% Finds the local maxima in a vector which resembles a smooth function x
% Only considers those happening at high values (> threshold) of the function

%
% Parameters
%
lungh=length(x);

% generates segno vector
% segno is a vector which is 0 when x is decreasing and 1 when increasing
segno=zeros(lungh,1);
for scan=1:(lungh-1)
```

```
    if x(scan+1)>x(scan)
        segno(scan)=1;
    end
end
segno(lungh)=segno(lungh-1); % last element

% generates massimi vector
% massimi e' un vettore contenente 1 dove c'e' un massimo
massimi=zeros(lungh,1);
for scan=4:(lungh-4)
    if segno(scan+1)==0 & segno(scan)==1
        % possibile massimo
        if segno(scan+1)==segno(scan+2) & segno(scan+2)==segno(scan+3) ...
                & segno(scan+3)==segno(scan+4) & segno(scan)==...
                segno(scan-1) & segno(scan-1)==segno(scan-2) & ...
                segno(scan-2)==segno(scan-3)
            massimi(scan)=1;
        end
    end
end

%
% thresholding
%
for scan=1:lungh
    if x(scan)<threshold
        massimi(scan)=0;
    end
end
```

[FreqCentroidCurve.m]

```
% Ver 2.0.1
% For Matlab 7.0
% It works with  several waveforms
% It displays the variation in the frequency centroid
```

```
% in the building up of the waveform

%
% Initialization
%
clear all
%close all
%

%
% Load data
%
numerofile=10; % Total number of input data files
nomefile(1,:)='PosD_700N_10eventi_3_1.csv';
nomefile(2,:)='PosD_700N_10eventi_3_2.csv';
nomefile(3,:)='PosD_700N_10eventi_3_3.csv';
nomefile(4,:)='PosD_700N_10eventi_3_4.csv';
nomefile(5,:)='PosD_700N_10eventi_3_5.csv';
nomefile(6,:)='PosD_700N_10eventi_3_6.csv';
nomefile(7,:)='PosD_700N_10eventi_3_7.csv';
nomefile(8,:)='PosD_700N_10eventi_3_8.csv';
nomefile(9,:)='PosD_700N_10eventi_3_9.csv';
nomefile(10,:)='PosD_700N_10eventi_3_A.csv';
%nomefile(20,:)='10Comp2_4_A.txt';
for indice=1:numerofile
   data(indice,:)=csvread(nomefile(indice,:))';
end
%

%
% Program options
%
dispfitting=0; % displays polynomial fitting
dispder=0; % displays derivative
SAMPLErate=2; % [MHz] (sampling rate of the input data file)
```

```
PACpretrig=128; % value SET in PAC (number of bytes)
additionalpretrig=64;

stepresolution=10; % microsecond, coincides with the first step
finoa=2250-additionalpretrig; % maxlength considered [microsecond]



steps=stepresolution:stepresolution:finoa;
% microseconds considered after the pretrig
%

timeinterval=(SAMPLErate*1e6)^-1; % timeinterval of the original input file
NOsteps=length(steps); % total number of points where the freq cen is computed



%
% Cropping of the data (before and after)
%
orl=length(data(1,:)); % original length
pretrig=PACpretrig+additionalpretrig./timeinterval./1e6; % total pretrig (bytes)
afterwhat=steps./timeinterval./1e6; % is a vector of byte lengths
newdata=zeros(NOsteps,max(afterwhat),numerofile);
for ind=1:numerofile
   datatemp=data(ind,(pretrig+1):(pretrig+max(afterwhat)));
   l=length(datatemp);
   for nnn=1:NOsteps
       tmp=zeros(1,max(afterwhat));
       tmp(1:afterwhat(nnn))=datatemp(1:afterwhat(nnn));
       newdata(nnn,:,ind)=tmp;
   end
end
finl=length(tmp);
%

%
```

```
% Power Spectra
%
for ind=1:numerofile
   for indice=1:NOsteps
       signal=shrink(newdata(indice,:,ind));
       % the computation of the Spectral Density must be done
       % on the waveform without  any zero added to the signal!
       Pxx=pwelch(signal,[],[],512);
       f=1:length(Pxx);
       f=(f./length(Pxx)./timeinterval/2)'; % frequencies axis
       PowSpDen(indice,:,ind)=Pxx'; % a row
   end
end
%

%
% Frequency centroid
%
for ind=1:numerofile
   for indice=1:NOsteps
       freqc(indice,ind)=sum(f'.*PowSpDen(indice,:,ind))/...
           sum(PowSpDen(indice,:,ind));
   end
end
figure('name','Frequency centroids VS partial waveform length [microsecond]')
plot(steps,freqc)
legend(nomefile)
title('Frequency centroids VS partial waveform length [microsecond]')
%
figure('name','Norm Freq centr VS partial waveform length [microsecond]')
for ind=1:numerofile
   normfreqc(:,ind)=freqc(:,ind)./freqc(NOsteps,ind);
end
plot(steps,normfreqc)
legend(nomefile)
```

```
title('Norm Freq centr VS partial waveform length [microsecond]')
%
```

Appendix C

Technical drawings

This appendix (Figures 3–9) provides the technical drawings of the four-point bending test rig described in §9.

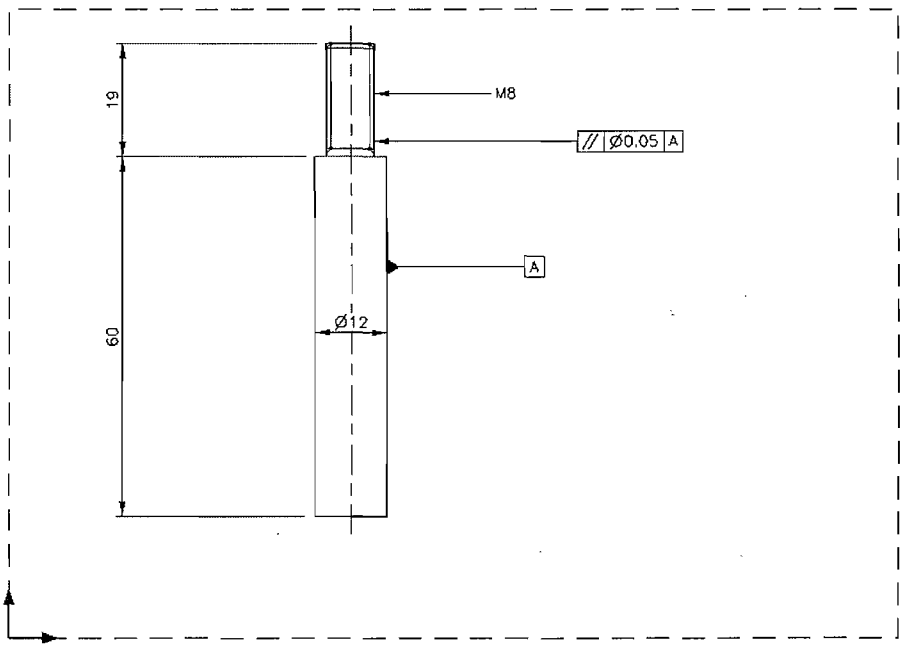

Figure 3: Central pin (interface with Instron machine)

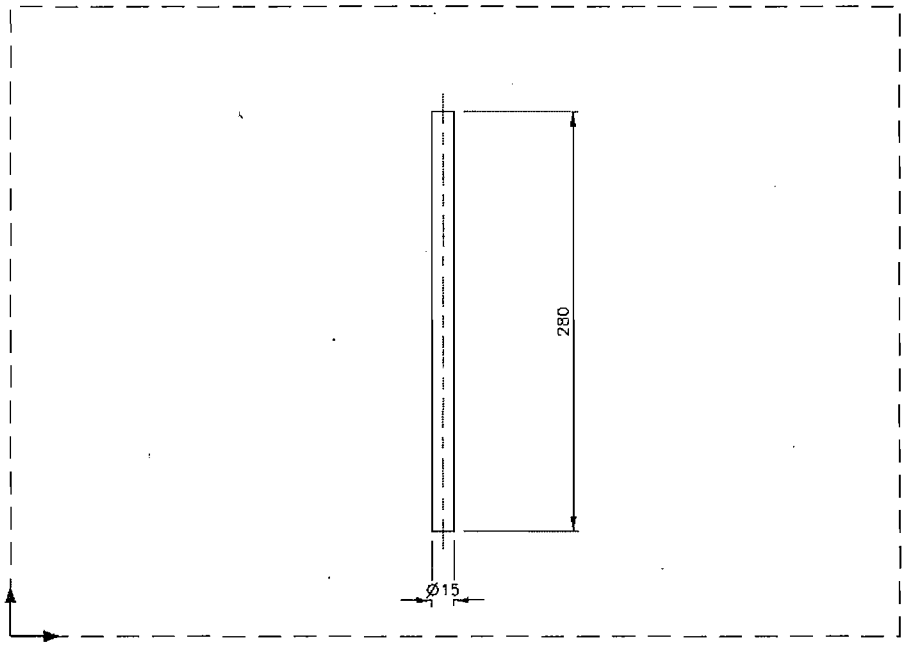

Figure 4: Roller

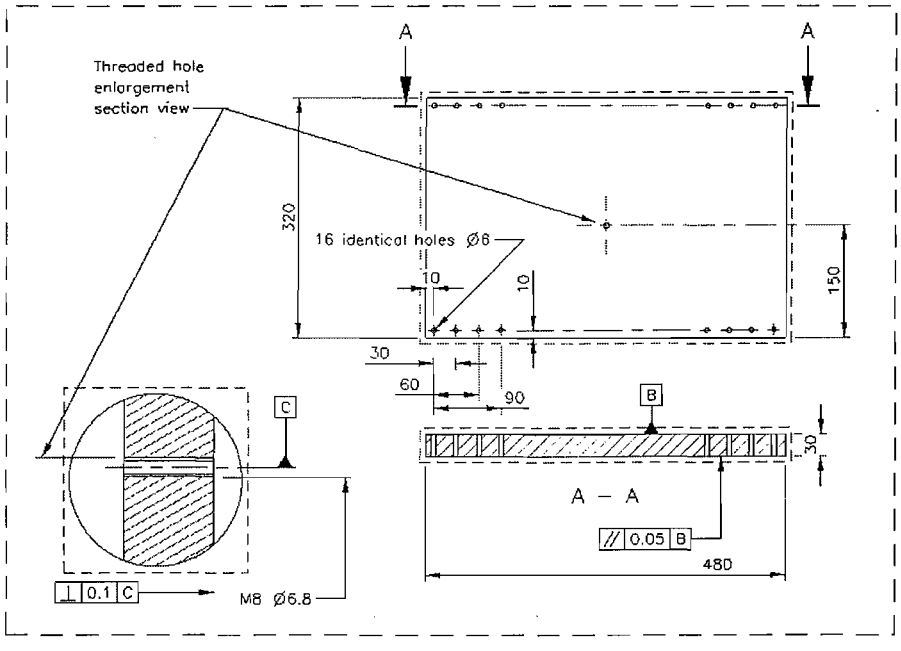

Figure 5: Lower half: plate

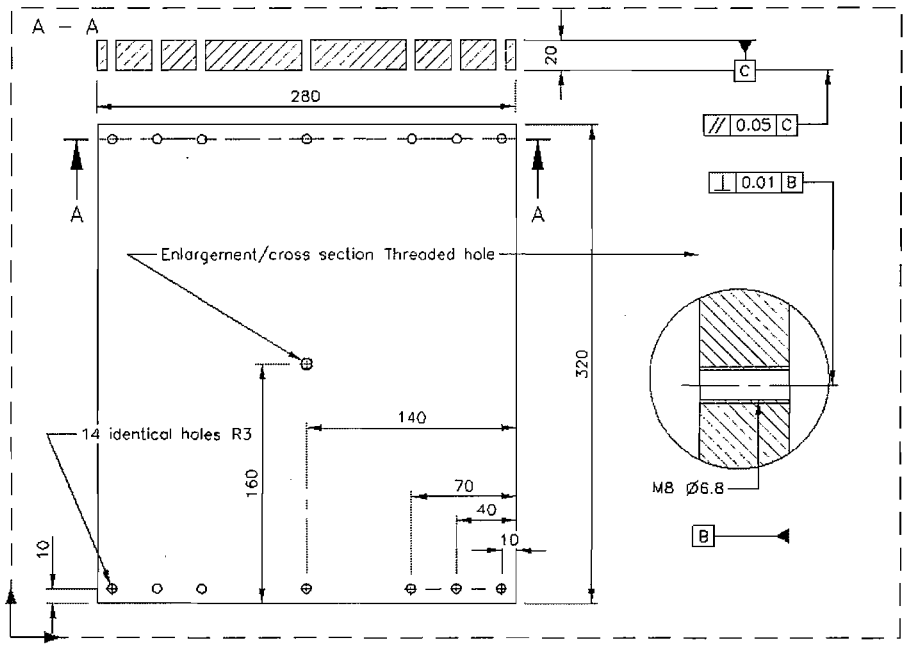

Figure 6: Upper half: plate

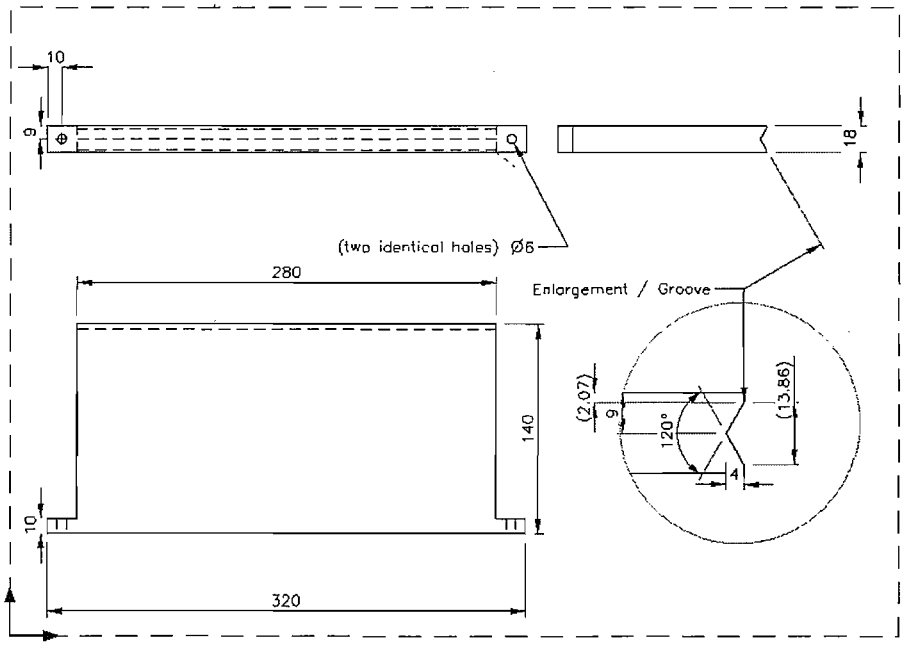

Figure 7: Vertical plates

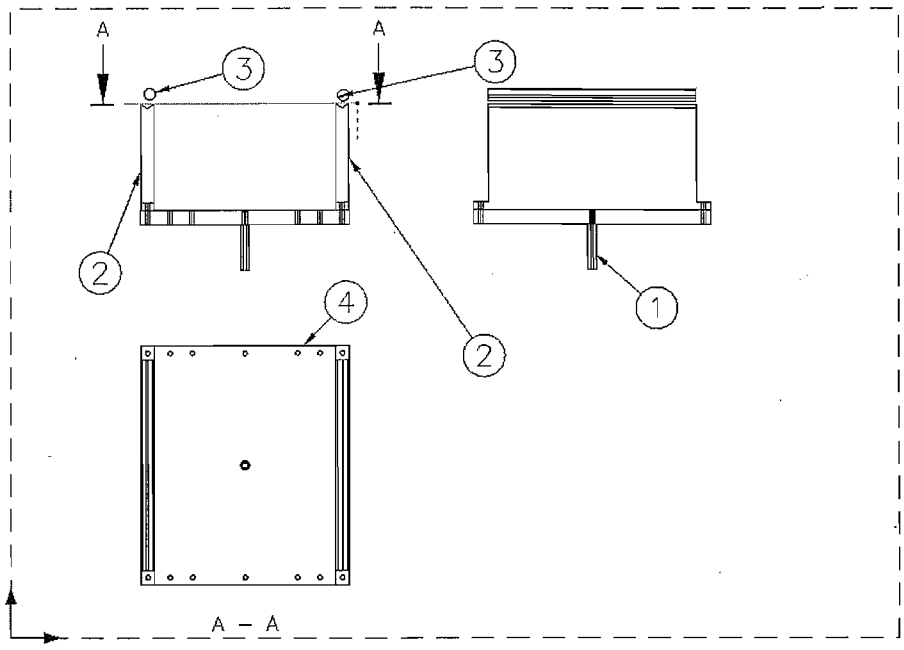

Figure 8: Upper half

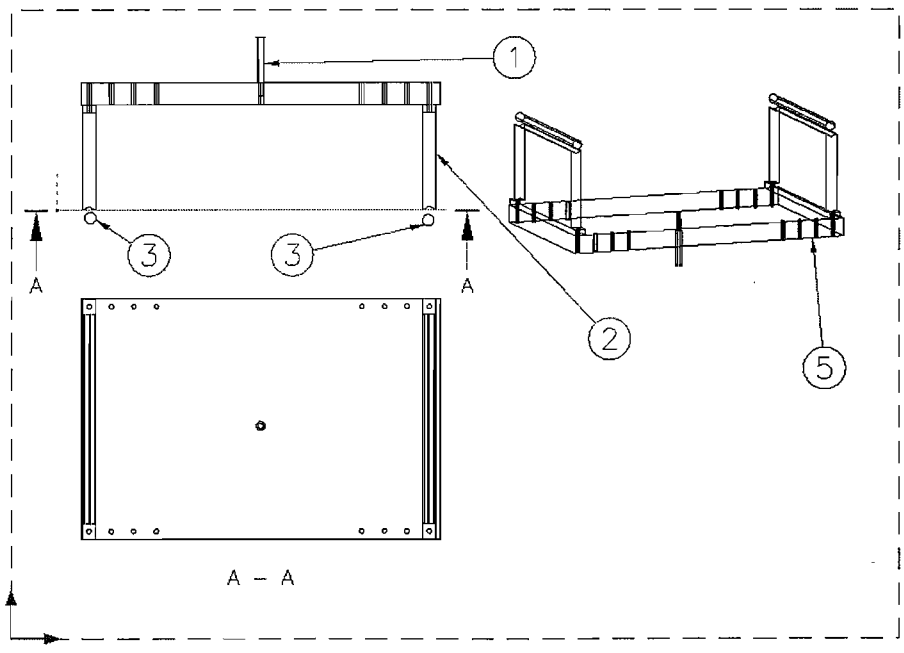

Figure 9: Lower half